FERMILAB-THESIS-2024-08

Imperial College London
Department of Physics

Measurement of Nuclear Dependence in Inclusive Antineutrino Scattering

Anežka KLUSTOVÁ

Submitted to Imperial College London in partial fulfilment
of the requirements for the degree of Doctor of Philosophy in Physics.

April 2024

Abstract

One of the fundamental questions in physics is the matter-antimatter asymmetry of the Universe, explored through charge-parity violation searches in neutrino oscillation experiments. Next-generation oscillation experiments like DUNE need to constrain the systematic uncertainties arising from our understanding of (anti)neutrino-nucleus scattering to within a few percent to achieve their physics goals. MINERvA, a dedicated (anti)neutrino-nucleus scattering experiment, plays a crucial role in constraining these uncertainties. This thesis presents MINERvA's first high-statistics direct measurement of nuclear dependence in charged-current inclusive antineutrino scattering on carbon, hydrocarbon, iron, and lead as a function of antimuon transverse momentum, p_{T}, and Bjorken x.

The analysis utilises interactions with a mean antineutrino energy of approximately 6 GeV, with reconstructed antimuons having a scattering angle of less than 17° relative to the antineutrino beam and an antimuon energy of 2–20 GeV. The measured per-nucleon differential cross-sections are reported with a precision of 7–9%, while the cross-section ratios of carbon, iron, and lead to hydrocarbon have uncertainties of 5% or less. The cross-sections for iron and lead indicate strong suppression at low p_{T} and Bjorken x, and an enhancement at high p_{T}. These effects are observed to be more pronounced with the increasing size of the target nucleus and are not reproduced by the underlying simulation prediction. Comparisons to alternative models used in current (anti)neutrino interaction generators show some improvements in modelling over the base prediction model, yet they are still unable to fully reproduce the observed nuclear dependence in this analysis.

Importantly, the analysis provides a direct test of nuclear effects in inclusive antineutrino scattering, with major contributions from resonant pion production, deep inelastic scattering, and the transition region between these channels, which will be significant in DUNE. This measurement also represents one of the largest antineutrino datasets in this energy regime analysed to date.

Statement of originality

The analysis described in this thesis is my own work as part of the MINERvA collaboration. The work of others and the inputs provided to the analysis are clearly and appropriately referenced.

Chapters 1 and 2 provide an introduction and summarise the current state of neutrino physics and the theory of neutrino interaction scattering. This work integrates contributions from numerous theorists and experimentalists in the field, all of which are appropriately referenced throughout. Chapter 3 describes the MINERvA experiment built upon more than a decade-long work of many of my MINERvA collaborators and supported by the Fermi National Laboratory Accelerator Division and the MINOS collaboration. Chapter 4 provides motivation for the measurement based on various cross-section results and other information from properly referenced and publicly available sources, as well as a general description of the binned differential cross-section extraction.

Chapter 5 describes the data sample collected by the MINERvA collaboration used in this measurement. It also details the corresponding simulation sample produced by the MINERvA collaboration based on the publicly available software provided by the GENIE collaboration. The changes I developed for the simulation are highlighted accordingly. They mainly involve the calculation of nuclear target fluxes, which uses MINERvA's newest flux constraints from Luis Zazueta and others, corresponding improvements and revisions to the 'daisy reweight' technique originally developed by Jeffrey Kleykamp, and the application of MINERvA's low four-momentum transfer squared tune to antineutrino scattering based on the analysis by Aaron Bercellie.

The reconstruction techniques outlined in Chapter 6 are also based on the work of many of my MINERvA collaborators. As part of the data and simulation sample production team, I participated in producing the analysis files used in this and other MINERvA measurements. My contributions to the reconstruction involving improvements to the application of calorimetric splines with the help of Andrew Olivier as part of MINERvA's data preservation efforts are marked accordingly.

Chapter 7 details my own work of extracting the inclusive antineutrino cross-section and cross-section ratios on carbon, hydrocarbon, iron, and lead. While the analysis framework is rooted in the public MINERvA analysis toolkit, the specific development and

implementation for this analysis were done by me, with key inputs and codes from Zubair Ahmad Dar, Amy Filkins and other MINERvA collaborators. The evaluation of the systematic uncertainties included in Chapter 8 is based on the analysis toolkit developed by the MINERvA collaboration. My development of new subdetector-by-subdetector evaluation of recoil uncertainties which was supported by David Last is emphasised. I also implemented the systematic uncertainty related to the machine-learning vertex reconstruction to account for differences between the data and simulation based on my own and Dipak Rimal's studies.

The results of this measurement are discussed in Chapter 9. The interpretation is my own, with valuable insights from Morgan Wascko, Abbey Waldron, Deborah Harris, Jeff Nelson, Jorge Morfin, and Rik Gran. Both the cross-section and cross-section ratios are compared to other simulation predictions produced by Dan Ruterbories. Chapter 10 provides a summary of the thesis, built upon all the preceding chapters.

Copyright declaration

'The copyright of this thesis rests with the author. Unless otherwise indicated, its contents are licensed under a Creative Commons Attribution-Non Commercial 4.0 International Licence (CC BY-NC). Under this licence, you may copy and redistribute the material in any medium or format. You may also create and distribute modified versions of the work. This is on the condition that: you credit the author and do not use it, or any derivative works, for a commercial purpose.

When reusing or sharing this work, ensure you make the licence terms clear to others by naming the licence and linking to the licence text. Where a work has been adapted, you should indicate that the work has been changed and describe those changes. Please seek permission from the copyright holder for uses of this work that are not included in this licence or permitted under UK Copyright Law.'

Anežka Klustová

Acknowledgements

This work was funded by the Imperial College London President's PhD Scholarship.

First and foremost, I would like to thank my supervisors Morgan Wascko and Abbey Waldron. Morgan, thank you for always being the sound (and fun!) voice cheering me on when needed. I wouldn't have ended up at Imperial having the best time during these past four years if it wasn't for you. Abbey, thank you for regularly listening to all of my physics and non-physics ramblings throughout this process, and always providing excellent insight and pushing me in the right direction. You were both indispensable in my journey to becoming an independent researcher while making sure I maintained the much-needed work-life balance. I struggle to imagine being matched with better supervisors.

The supervisor list, however, does not end there. My MINERvA work would be impossible without the excellent guidance of Deborah Harris and Jeff Nelson. Deborah, thank you for sharing your in-depth knowledge of MINERvA and beyond with me, and all the interesting studies our talks resulted in. They have made me a better scientist, and they have undoubtedly improved this analysis. Jeff, thank you for all your advice and endless expertise when it came to doing an inclusive measurement. While my work on DUNE is not included in this thesis, I would like to extend my thanks to Patrick Dunne, my honorary supervisor at Imperial. Patrick, thank you for giving me so much responsibility when it came to TOAD, and most importantly, for providing valuable advice in my efforts to navigate the academic environment. I also need to thank Cheryl Patrick who first introduced me to neutrinos and without whom I wouldn't have begun this journey.

It takes a village to produce a thesis on a neutrino cross-section. I feel so privileged to have been part of such a great and friendly family of scientists that make up the MINERvA collaboration. From trips to Fermilab with sing-alongs in the Users' Center to dinners at NuInt, I am so grateful for all the physics discussions and adventures with all of you. David Last, Andrew Olivier, Amy Filkins, Maria Mehmood, Zubair Ahmad Dar, Vaniya Ansari, Sayeed Akhter, Prameet Gaur, Christian Nguyen, Jeffrey Kleykamp, Dan Ruterbories, Kevin McFarland, Steve Manly, Laura Fields, Rik Gran, Jorge Morfin and many many others, thank you!

I would also like to thank my fellow students and other members of the Imperial group, both present and past, who made the day-to-day life at Imperial incredibly rewarding and

entertaining. Special thanks to Liban Warsame, Naseem Khan, Ed Atkin, Ioannis Xiotidis, Tiago Alves, Tailin Zhu, Yassine Alj Hakim, Charlie Naseby, Alie Craplet, Marvin Pfaff, Lauren Anthony, Minoo Kabirnezhad, Clarence Wret, and Mark Scott. I am looking forward to continuing my work at Imperial with you. Here is to more trips to Queen's Arms!

To all of my friends in London and around the world, thank you for supporting me throughout this endeavour and pretending so well to be interested in neutrinos almost as much as I am. A massive thank you also goes to everybody 'back home' rooting for me from the sidelines.

Denisa, while I do not expect you to read this thesis, I hope you know that I could not have done this without you. To be fair, you probably know as much as I do, having listened to all my presentations throughout the years anyway.

Finally, mum and dad, we made it! I owe you everything.

Contents

List of figures

List of tables

Glossary of terms, abbreviations, and acronyms

2p2h	Two-particle-two-hole interaction resulting in two nucleons in the final state
A	Mass number of a given nucleus referring to the number of nucleons (protons + neutrons)
***A*-dependence**	Nuclear dependence
ADC	**A**nalog-to-**D**igital **C**onverter of the signal
AGKY	**A**ndreopoulous-**G**allagher-**K**ehayias-**Y**ang model describing the hadronisation process in GENIE
Baffle	Graphite-aluminum tube designed to partially degrade missteered beams to protect other components of the beamline
Calorimetric spline	Piecewise calorimetric correction applied to reconstructed recoil energy to account for deposition in passive material, limited containment, and invisible energy deposits in the detector from particles such as neutrons
CC	**C**harged-**C**urrent interaction wherein (anti)neutrino exchanges a $W^{\pm}$ boson, converting into its coupled charged lepton
CP	**C**harge-**P**arity symmetry
DAQ	**D**ata **A**c**Q**uisition, the system that receives raw data from the detector, digitises them, and stores them on disk
'Daisy petal'	One of the 12 transverse bins in which the hexagonal cross-section of the scintillator tracker is divided for the flux and differential cross-section calculation

'Daisy reweight'	Linear combination of the scintillator distributions extracted in 12 'daisy petals' to match the flux of the scintillator tracker to that of a given nuclear target in cross-section ratios
DCNN	**D**eep **C**onvolutional **N**eural **N**etwork used in this work to reconstruct the interaction vertex
DIS	**D**eep **I**nelastic **S**cattering interaction channel in which a high-energetic (anti)neutrino interacts with the constituents of nucleons, producing a hadronic shower
Downstream	Relative position with respect to the (anti)neutrino beam referring to a position *in* the direction of the beam
DUNE	**D**eep **U**nderground **N**eutrino **E**xperiment, predominantly argon-based future neutrino oscillation experiment
ECAL	**E**lectromagnetic **CAL**orimeter designed to contain electromagnetic showers
EMC effect	**E**uropean **M**uon **C**ollaboration effect; one of the observed nuclear modifications to structure functions describing depletion in the bound nucleon cross-section ratio in the $0.3 \lesssim x \lesssim 0.7$
FEB	**F**ront-**E**nd **B**oard; electronics board attached on top of a PMT that digitises the output signal from the PMT
Fermi motion	Isotropic initial state movement of nucleons inside the nuclear environment
FHC	**F**orward **H**orn **C**urrent configuration of the magnetic horns in the beamline, resulting in neutrino-dominated beam
FSI	**F**inal **S**tate **I**nteractions that particles produced by (anti)neutrino interactions with nucleons inside the nucleus can undergo prior to exiting the nucleus
G4NuMI	**G**EANT**4** package for simulation of the **NuMI** beamline
Gate	MINERvA's data-taking period of 16 μs

GENIE	**G**enerates **E**vents for **N**eutrino **I**nteraction **E**xperiments; (anti)neutrino-nucleus interaction simulation, also known as event generator, used to model (anti)neutrino interactions and make predictions
GENIEXSecExtract	MINERvA's cross-section validation tool, which is external to the analysis framework
GEANT4	**GE**ometry **AN**d **T**racking software used for detector geometry and particle propagation through the detector modelling
HCAL	**H**adronic **CAL**orimeter designed to contain hadronic showers
Horn	Parabolic focusing and charge-sign selecting magnet used in the (anti)neutrino beamline setup
ID	**I**nner **D**etector
Inclusive	Considering all final states, i.e. all (anti)neutrino interaction modes
INTRANUKE	Intranuclear cascade simulation used in GENIE to model FSI
KNO	**K**oba-**N**ielsen-**O**lesen phenomenological model used in GENIE's AGKY hadronisation model to describe the hadronisation process for events with lower invariant mass
LE	**L**ow **E**nergy regime of the NuMI beam and corresponding MINERvA data-taking period with (anti)neutrino flux with (anti)neutrino energy peak of $\sim$3 GeV
LFG	**L**ocal **F**ermi **G**as model for the initial state of the nucleons inside the nucleus taking into account the local density at the interaction vertex
MAT	**M**INERvA **A**nalysis **T**oolkit used in MINERvA analyses mainly handling the propagation of systematic uncertainties
ME	**M**edium **E**nergy regime of the NuMI beam and corresponding MINERvA data-taking period with (anti)neutrino flux with(anti)neutrino energy peak of $\sim$6 GeV

MEC	**M**eson **E**xchange **C**urrent correlating nucleons inside the nuclear environment via an exchange of virtual mesons, often pions
MC	**M**onte **C**arlo simulation refers to the (anti)neutrino interaction simulation
Migration	Process of smearing of the reconstructed kinematics of an event from its true kinematics due to finite detector resolution and imperfect reconstruction described by migration matrix
MINERvA	**M**ain **I**njector **N**eutrino **E**xpe**R**iment to study ν–**A** interactions, a dedicated cross-section experiment
MINOS	**M**ain **I**njector **N**eutrino **O**scillation **S**earch, a neutrino oscillation experiment; in the context of this work often refers to its near detector only, which was positioned downstream of the MINERvA detector
ML	**M**achine **L**earning, refers to the technique used to reconstruct the interaction vertex
Module	MINERvA's detector tracking unit which refers to two planes of scintillator strips
MIP	**M**inimum **I**onising **P**article such as (anti)muon
NC	**N**eutral-**C**urrent interaction wherein (anti)neutrino exchanges a Z boson with no charge transfer and leaves the interaction without changing to its paired charged lepton
NEUT	Another (anti)neutrino event generator predominantly used in Japanese experiments, such as the neutrino oscillation experiment T2K
Nuclear target	Passive material interlaid between the active scintillator planes in MINERvA consisting of combinations of carbon, iron, and lead in the context of this work (there is also a water and helium target)
NuMI	**N**eutrinos ($\boldsymbol{\nu}$) at the **Main I**njection; (anti)neutrino beam production setup at Fermilab

OD	**O**uter **D**etector
PDFs	**P**arton **D**istribution **F**unctions describing the distribution of partons within the nucleus
PMNS matrix	**P**ontecorvo-**M**aki-**N**akagawa-**S**akata mixing matrix relating the neutrino mass eigenstates and the neutrino flavour eigenstates, describing neutrino oscillation
PMT	**P**hoto**M**ultiplier **T**ube with 64 channels converting the collected light into charge
Plane	MINERvA's detector tracking unit made of scintillator strips, with either X, U, or V orientation of the scintillator strips (parallel to the y-axis, 60° clockwise and anticlockwise, respectively)
Plastic	Refers to the hydrocarbon scintillator used to make the active tracker region or the scintillator planes in between the nuclear targets
Playlist	Lists of MINERvA runs and subruns that correspond to a specific detector configuration during a data-taking period
POT	**P**rotons **O**n **T**arget; a metric used to characterise the integrated luminosity of the (anti)neutrino beam
PPFX	**P**ackage to **P**redict the **F**lu**X** used to constrain flux predictions by external data and evaluate systematic uncertainties
PYTHIA/JETSET	Standard tool for generation of high-energy collisions, spanning models for few-body hard processes to complex multihadronic final states, that is used in GENIE's AGKY hadronisation model to describe the hadronisation process for events with higher invariant mass
Recoil	Refers to either the total outgoing hadronic system in an interaction, or more specifically to its energy
RES	**RES**onant pion production interaction channel in which the (anti)neutrino is energetic enough to excite a nucleon into a baryon resonance which then decays, most often to pions

RFG	**R**elativistic **F**ermi **G**as model for initial state of the nucleons inside the nucleus, treating nucleons as a collection of non-interacting fermions in a constant nuclear potential
RHC	**R**everse **H**orn **C**urrent configuration of the magnetic horns in the beamline, resulting in antineutrino-dominated beam
RPA	**R**andom **P**hase **A**pproximation accounting for long-range correlations in (anti)neutrino-nucleus scattering, arising from the polarisation of the nuclear medium by the electroweak propagator
SF	**S**pectral **F**unction model for the initial state of the nucleons inside the nucleus, taking into account two- and three-body nucleon-nucleon interactions, thereby modifying the available nuclear quantum states
Shadowing	Suppression of the cross-section of bound nucleons due to destructive interference of hadronic fluctuations of the intermediate boson that multiple-scatter off surface nucleons at $x \lesssim 0.1$ compared to a free nucleon
SIS	**S**hallow **I**nelastic **S**cattering referring to the transition region between RES and DIS interaction channels with non-resonant pion production and multi-pion final states, defined by $(m_N + m_\pi) < W < 2$ GeV/c^2 and Q^2 around 1 (GeV/c)^2
SM	**S**tandard **M**odel of particle physics, categorising all elementary particles and describing three out of the four known fundamental forces (excluding gravity)
Smearing	Describes the process that results in a difference between the actual kinematics of the physics that occurred, and the kinematics of the physics measured (reconstructed) in the detector due to finite detector resolution and imperfect reconstruction
SRC	**S**hort-**R**ange **C**orrelations between nucleons arising from brief overlaps of their wavefunctions

Strips	Triangular scintillator bars which make up one scintillator plane, the basic MINERvA tracking unit
SuSA	Super-scaling model based on phenomenon shown by electron-nucleus scattering data, in the context of this work refers to an alternative 2p2h model
TDC	**T**ime-to-**D**igital **C**onverter of the signal timing
Time slice	Time window with a variable length within the gate in which reconstruction steps are performed
true/truth	Direct output of the simulated prediction of the (anti)neutrino event generator (no reconstruction)
Unfolding	Process of reverting the smearing of reconstructed distribution and estimating the true distribution from the measured smeared spectrum in order to report detector-independent cross-section
Upstream	Relative position with respect to the (anti)neutrino beam referring to a position *against* the direction of the beam
Valencia model	Refers to a model used to describe 2p2h and RPA
Warping study	Unfolding study using simulations that have been reweighted to depict alternative physics models, exaggerate features of the underlying distributions, or capture differences in the shapes of distributions between the data and the original underlying simulation to evaluate model dependence in unfolding
WLS	**W**ave**L**ength-**S**hifting; usually refers to a fibre that can change the wavelength of the collected light

Chapter 1

Introduction

Neutrinos and their antimatter counterparts, antineutrinos, are among the most abundant particles in the Universe, yet they barely interact with the matter that comprises it. In many ways, (anti)neutrinos are special—they are extremely light compared to other known particles and can only be observed via the particles they produce upon interaction. Importantly, if neutrinos and antineutrinos travel through space-time differently, as allowed by the phenomenon of neutrino oscillations, they could hold one of the pieces of the puzzle as to why our universe is mostly made of matter rather than antimatter [1]. However, in order to do so, we must precisely understand how (anti)neutrinos interact with matter around us in the first place. This can be done via measuring the probability, parametrised as cross-section, for neutrinos and antineutrinos interacting in various ways with different nuclei.

This thesis presents the first simultaneous measurement of charged-current inclusive muon antineutrino cross-sections on carbon, hydrocarbon, iron, and lead; these measurements are taken at the mean antineutrino energy of $\sim$6 GeV using the MINERvA experiment. Antineutrino scattering is generally a less explored process than neutrino scattering, as antineutrinos typically interact even less often than neutrinos and are also more difficult to produce artificially. Overall, this means that it takes much longer to accumulate enough data to perform precise measurements. Nonetheless, understanding both neutrino and antineutrino interactions is crucial for distinguishing whether they

potentially behave differently when they oscillate. Therefore, the results of this study significantly contribute to expanding the antineutrino datasets used to inform neutrino oscillation experiments. In particular, the measurement spans the antineutrino energy phase space important for the future oscillation experiment called Deep Underground Neutrino Experiment (DUNE).

Moreover, the fact that the antineutrino interacts with bound nucleons, i.e. nucleons in a nuclear environment, rather than free nucleons, has a profound effect on the cross-section and on what is observed in the detector[1]. For example, the particles produced by (anti)neutrinos interacting with a nucleus may re-interact inside the nuclear environment, potentially altering their kinematics or even transforming into different particles before exiting it and being detected. This analysis capitalises on MINERvA's unique capability to measure how antineutrinos interact with different nuclei. Crucially, it explores how these and other effects vary with the increasing complexity of the nuclear environment while using the same detector technology and the same artificially produced beam of antineutrinos. This significantly reduces uncertainties from these sources when comparing measurements across different nuclei. Detailed descriptions of the underlying theory, the MINERvA experiment, and the measurement itself are provided in this work.

The remainder of this chapter outlines various key developments in neutrino physics, spanning from Pauli's initial proposal of the neutrino particle in 1930 to the discovery of the neutrino oscillation phenomenon and the open question of neutrino mass. Additionally, it emphasises the importance of understanding (anti)neutrino interactions in the context of neutrino oscillation experiments, particularly concerning forthcoming ones such as DUNE. This chapter also briefly delves into the measurement of (anti)neutrino cross-section as a means to investigate nuclear effects.

Chapter 2 reviews the theory of (anti)neutrino scattering and how the nuclear environment affects these interactions. The MINERvA experiment and the artificial production of (anti)neutrinos at an accelerator are then detailed in Chapter 3. In Chapter 4, the

[1]One can envision a detector being like a high-speed camera that captures rapid snapshots of these interactions.

focus shifts to a more specific motivation for the measurement described in this thesis, i.e. the measurement of nuclear dependence in inclusive antineutrino scattering, and how it can be performed at MINERvA. Chapter 5 discusses the MINERvA data used in this measurement and the underlying theoretical models employed in the simulation prediction, while Chapter 6 describes the reconstruction steps, i.e. how we go from what we see in the detector to physical quantities essential for the physics interpretation.

The individual steps of the analysis, from defining the antineutrino interactions of interest to the extraction of cross-sections, are thoroughly reviewed in Chapter 7. The discussion of the uncertainties associated with the measurement is then included in Chapter 8. Following that, Chapter 9 presents the results of the cross-section measurements on carbon, hydrocarbon, iron, and lead, along with their comparison and associated discussion. Concluding remarks about the implications of this analysis and the prospects of (anti)neutrino interaction modelling are provided in Chapter 10.

1.1 A brief history of neutrino physics

Neutrinos were first postulated in 1930 by Pauli to explain the observed continuous energy spectrum of electrons and conserve the angular momentum in β decay [2]. This inspired Fermi to present a theory of β decay that incorporated neutrinos and in which particles interacted through a point-like interaction [3], initiating the theory of weak interactions. However, it wasn't until two decades later, in 1956, that neutrinos were experimentally discovered by Reines and Cowan through the observation of inverse β decay $\overline{\nu}_e + p \rightarrow n + e^+$ [4], thus confirming the existence of what is now known as electron antineutrinos.

In the same year, Lee and Yang theorised parity violation in weak interactions [5], which was experimentally confirmed in 1957 by Wu et al. through observations in the beta decay of Co^{60} in a strong magnetic field [6]. This discovery led Sudarshan and Marshak [7, 8] and subsequently Feynman and Gell-Mann [9] to propose and develop the chiral V − A theory of weak interactions. This theory postulated that weak interactions are produced by both vector (V) and axial (A) vector currents, establishing the intrinsic

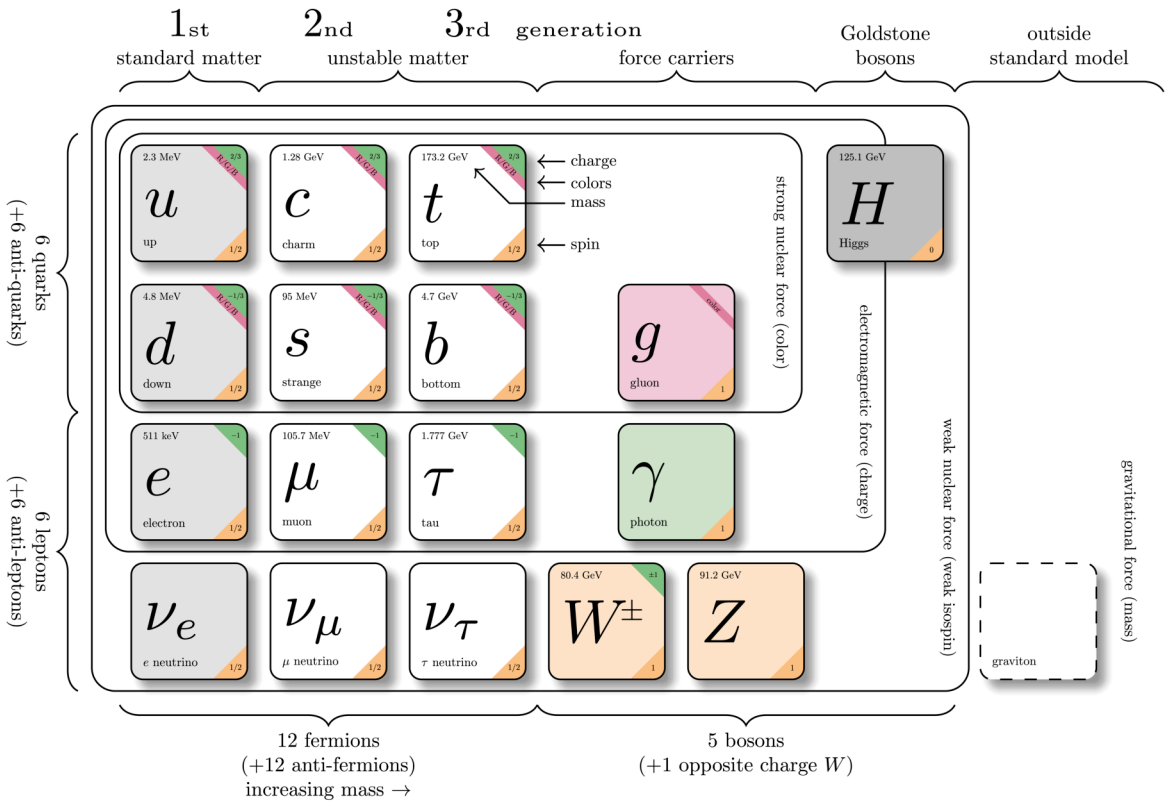

Figure 1.1: The Standard Model diagram. Modified from D. Galbraith and C. Burgard [12].

left-handed chirality of particles and right-handed chirality of antiparticles in weak interactions[2]. Furthermore, it, for example, provided an explanation for the observed differences between the muonic and electronic pion decay modes [11], upholding the universality of lepton interactions.

The existence of the muon neutrino was experimentally confirmed in 1962 [13], and the subsequent discovery of the tau lepton [14] led to theoretical predictions of its corresponding neutrino counterpart, which, however, was not discovered until 2001 by the DONUT experiment [15]. The unification of electromagnetic and weak interactions, i.e. electroweak theory, in the 1960s by Glashow [16], Salam [17], and Weinberg [18], confirmed by the discovery of neutral currents [19,20], and the theory of strong interactions laid the groundwork for the Standard Model (SM), depicted in Figure 1.1. The SM serves as the

[2]In 1958, the neutrino was experimentally confirmed to be left-handed only by Goldhaber et al. [10]

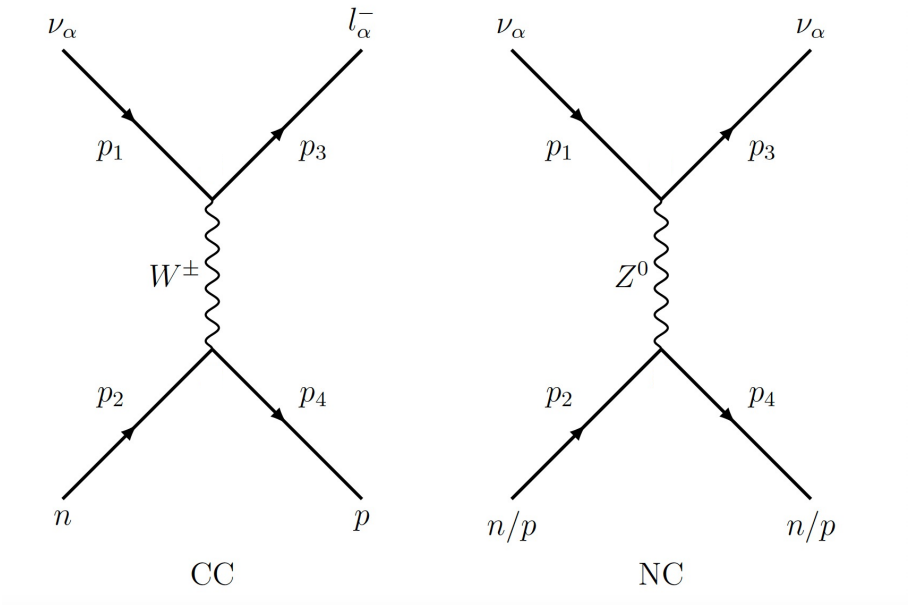

Figure 1.2: Examples of Feynman diagrams of a charged-current (CC) interaction (left) and a neutral-current (NC) interaction (right) on a nucleon.

cornerstone of high-energy physics, categorising all elementary particles and describing three out of the four known fundamental forces (excluding gravity).

In the SM, neutrinos are formulated to be massless leptons (half-integer spin particles) with zero electric charge, interacting only through the weak force. Charged-current interactions are mediated by the $W^\pm$ boson, while the neutral-current interactions involve the Z boson, as demonstrated in Figure 1.2. The specifics of charged-current interactions in the context of (anti)neutrino scattering are reviewed in detail in Chapter 2. Similar to charged leptons, the SM predicts three active flavours of neutrinos, electron neutrino ν_e, muon neutrino ν_μ, and tau neutrino ν_τ. The measurement of the partial width of the Z-boson mass distribution decaying to invisible particles at the Large Electron-Positron Collider (LEP) in 1989 was consistent with this SM prediction and indeed favoured the existence of three light neutrinos [21].

The experimental mystery that would later lead to the discovery of neutrino oscillation and neutrino mass also began to unfold in the 1960s. In 1968, the Homestake experiment detected a large fraction missing from the electron neutrino flux coming from the Sun, contradicting predictions from the well-established model of solar processes [22]. These discrepancies, referred to as 'The Solar Neutrino Problem', were eventually resolved by

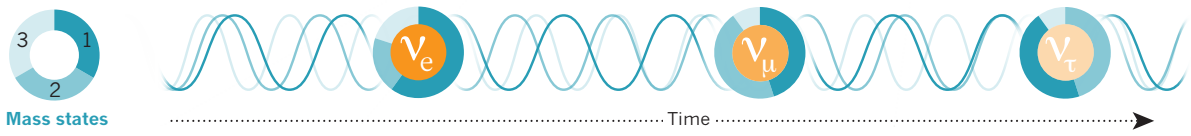

Figure 1.3: Illustration of the evolution of linear superposition of neutrino mass eigenstates over time being detected as neutrino flavour states. Reproduced with permission from Springer Nature [25].

experimental data provided by the Super-Kamiokande (SK) and the Sudbury Neutrino Observatory (SNO) experiments.

In 1998, the SK experiment detected a zenith angle-dependent deficit in atmospheric neutrinos, which was in disagreement with the theoretical predictions. The data was however consistent with the two-flavour ($\nu_\mu \leftrightarrow \nu_\tau$) oscillation hypothesis [23]. The SNO experiment then demonstrated and confirmed neutrino oscillations in solar neutrinos by observing both neutral-current and charged-current interactions in 2001 [24]. Their measurements showed that flavour transformation was taking place, which supplied concrete evidence that neutrinos must have a non-zero mass.

The theoretical framework for neutrino oscillations was first proposed much earlier, in 1957, by Pontecorvo, drawing an analogy to $K^0 - \bar{K}^0$ oscillations [26]. This concept was further developed by Maki, Nakagawa, and Sakata in 1962 [27]. Neutrino oscillation is a quantum mechanical phenomenon whereby neutrinos created in a pure flavour eigenstate, ν_e, ν_μ or ν_τ, can be measured at a later time to be in a different flavour eigenstate. This implies the existence of mass eigenstates, ν_1, ν_2 and ν_3, that are distinct from the flavour eigenstates. The flavour eigenstates can be then interpreted as a coherent linear superposition of these mass eigenstates, propagating as wave packets through space at different frequencies because of their small mass differences, as illustrated in Figure 1.3.

The mass eigenstates and the flavour eigenstates are related via the Pontecorvo-Maki-Nakagawa-Sakata (PMNS) mixing matrix, analogous to the Cabibbo-Kobayashi-Maskawa (CKM) matrix for quarks. The 3×3 PMNS matrix is usually parametrised using three mixing angles, which have been measured by a variety of experiments [28], and a complex phase allowing for possible charge-parity (CP) violation in the leptonic

sector. While CP violation has been detected in the flavour-mixing of quarks [28, 29], its magnitude is not sufficiently large to explain the matter-antimatter asymmetry in the Universe [1, 30, 31]. However, its observation in the neutrino sector could potentially provide an explanation [1]. Specifically, the CP violation can be measured by observing that the oscillations of neutrinos are fundamentally different from the oscillations of antineutrinos[3].

Finally, it is important to note that while the observation of neutrino oscillation showed that neutrinos have mass, their absolute values are still unknown. The neutrino oscillation experiments can only provide information on the difference between the mass values—the mass ordering of the mass eigenstates is one of the outstanding questions in neutrino physics. However, the latest direct neutrino-mass measurements by the Karlsruhe Tritium Neutrino (KATRIN) experiment set the upper mass limit on the effective electron antineutrino mass of $m_\nu \lesssim 0.8\,\mathrm{eV}/c^2$ [32], i.e. orders of magnitude smaller than any other particle.

The origin of the smallness of neutrino mass, much like its absolute value, remains unresolved. Whilst it is conceivable that neutrinos, akin to other fundamental particles, are of Dirac nature (with their right-handed counterparts being 'sterile', i.e. not interacting), the question persists: Why are neutrinos so light? Is the Yukawa coupling of the Higgs field to neutrinos simply minuscule compared to other lepton masses (cf. the mass of an electron, $m_e = 511\ \mathrm{keV}/c^2$)? The neutrino mass is thus often interpreted as a manifestation of Beyond Standard Model (BSM) physics, in particular, that neutrinos could instead be Majorana in nature [33], with the small mass provided by a so-called seesaw mechanism [34]. The interpretation of a Majorana neutrino is that neutrinos and antineutrinos are the same particles, whereby left-handed and right-handed chiral states are related through charge conjugation. Whether neutrinos are indeed Majorana in nature could be answered by the experimental searches for neutrinoless double beta decay.

[3]Current neutrino oscillation experiments measure the unoscillated (anti)neutrinos at the so-called near detector close to their production, and compare them to the measurements at the so-called far detector some distance away after they had likely oscillated.

1.2 Importance of (anti)neutrino cross-sections

One of the current challenges in neutrino physics is to better understand how (anti)neutrinos interact with matter, particularly in the context of neutrino oscillation measurements. This is because neutrino oscillation experiments require accurate measurements of true (anti)neutrino energy, i.e. the energy at the initial (anti)neutrino-nucleus interaction, to infer the oscillation parameters. This is already complicated by the broad spectrum of accelerator-produced beams of mostly muon (anti)neutrinos used to study them. Additionally, to obtain a statistically significant sample of (anti)neutrino interactions for precise measurements, these experiments often employ heavy materials, meaning nuclei with a large number of nucleons, such as water, carbon, hydrocarbon, or argon.

However, as previously mentioned, the nuclear environment can alter particles produced before they exit the nucleus and are detected in the detector. This alteration can lead to what is known as (anti)neutrino energy smearing, where the reconstructed (anti)neutrino energy does not directly correspond to the true (anti)neutrino energy. To mitigate this smearing, experiments rely on simulations that utilise theoretical models of different processes contributing to the (anti)neutrino cross-section at various (anti)neutrino energies as well as account for the effects of the nuclear environment (further discussed in detail in Chapter 2).

Consequently, current long-baseline neutrino oscillation experiments, such as the Tokai-to-Kamioka (T2K) in Japan [35] and the Neutrinos at the main injector Off-axis ν_e Appearance (NOvA) in the USA [36], generally report large uncertainties on their measurements of neutrino oscillation parameters related to modelling of (anti)neutrino-nucleus interactions. For example, in 2020, the results presented by T2K indicated the first measurement of CP violation in leptons [37], in which these uncertainties contributed about 5.9% of the total 6% systematic uncertainty on the predicted relative number of ν_e to $\bar{\nu}_e$ candidates [37].

While the measurements of current oscillation experiments are still limited by the statistical power of the collected samples, the next-generation oscillation experiments,

DUNE [38] and Hyper-Kamiokande (HK) [39], aim to measure neutrino oscillations with unprecedented precision. These experiments will overcome the limitations imposed by the statistics and will become systematics-limited instead. For example, the DUNE near detector is expected to detect about 100 million interactions/year on argon [38]. Therefore, in order to meet their physics goals, i.e. determining mass hierarchy and the extent of CP violation in the neutrino sector, the systematics on their measurements must be constrained within a few percent. For DUNE, this is around 2% uncertainty [38].

Ultimately, our understanding of how (anti)neutrinos scatter off heavy nuclei poses a challenge to these future measurements and needs to be improved. Specifically, we can reduce the uncertainties on the interaction models by constraining them with data from dedicated neutrino-nucleus cross-section measurements such as MINERvA [40]. Furthermore, the cross-section measurements can test various aspects of the current interaction models used in simulations, inform the neutrino interaction community and lead to further developments of the underlying models.

MINERvA's unique contribution lies in extending these models to heavier nuclei, i.e. measuring the nuclear dependence of (anti)neutrino interactions. This provides further insights into interaction models for elements like argon which will be used in DUNE. Importantly, the energy range of (anti)neutrino interactions analysed in this analysis has a large overlap with the future DUNE dataset, especially at higher energies beyond the capabilities of other cross-section experiments which tend to probe the lower-energy regions. As mentioned before, to measure the CP-violating phase by comparing $\nu_\mu \to \nu_e$ and $\bar{\nu}_\mu \to \bar{\nu}_e$, antineutrino cross-sections like the one presented in this work, which have been so far studied less extensively, are necessary.

Finally, cross-section measurements can be used as a probe of nuclear physics itself. In particular, nuclear effects in scattering off heavier nuclei are an active area of research [41]. By examining the cross-section distributions on various nuclei and comparing them to the available nuclear models, we can better understand these effects and extend the existing theory of neutrino-nucleus scattering.

Chapter 2

(Anti)neutrino-nucleus scattering theory

The complex nature of (anti)neutrino-nucleus interaction involves the physics of (anti)neutrinos scattering off nucleons (or quarks and gluons at higher energies), as well as interactions with the nuclear environment, where both initial and final nuclear states need to be considered. The relatively straightforward process of (anti)neutrino-nucleon scattering becomes a nontrivial problem when the interaction occurs not on a free nucleon, but rather on a particle bound within the nucleus. Describing the nuclear environment alone represents a challenging many-body problem, whose solution would require substantial computational resources.

Instead, the majority of (anti)neutrino-nucleus interaction simulations, also known as event generators, implement simpler, more phenomenological models that are informed by and often fitted to the relevant experimental data. Typically, the modelling of (anti)neutrino interaction with nuclei heavily relies on a factorisation into the primary (anti)neutrino interaction on a free nucleon, modifications of the initial state of the nuclear medium (compared to a free nucleon), and the final-state interactions of the resulting particles before they exit the nucleus. This chapter focuses on these individual components and their underlying models important in the context of the presented measurement of inclusive charged-current antineutrino scattering on various nuclei.

Note that the relevant models are discussed with respect to two different (anti)neutrino event generators: GENIE [42,43], which is used as the simulation prediction in the analysis and specifically detailed in Chapter 5, and NEUT [44,45]. The NEUT generator, primarily employed in (anti)neutrino oscillation analyses at the T2K experiment [35], serves as an alternative generator for cross-section result comparisons in Chapter 9.

2.1 Primary (anti)neutrino interaction

In accelerator-based experiments, beams of mostly muon (anti)neutrinos are produced, with a broad spectrum spanning energies between 0.1 and 20 GeV. Therefore, the incoming (anti)neutrino energy must be reconstructed from the final-state particles produced in the interaction. As shown in Figure 1.2, (anti)neutrinos can interact weakly via either charged current (CC) or neutral current (NC) interactions. Since the measurement presented in this work exclusively examines charged-current interactions, the remainder of this section will focus on them. A charged-current (anti)neutrino interaction can be identified by the production of a coupled charged lepton in the final state, which can be detected. In the case of muon antineutrinos specifically, this charged-lepton particle would be an antimuon.

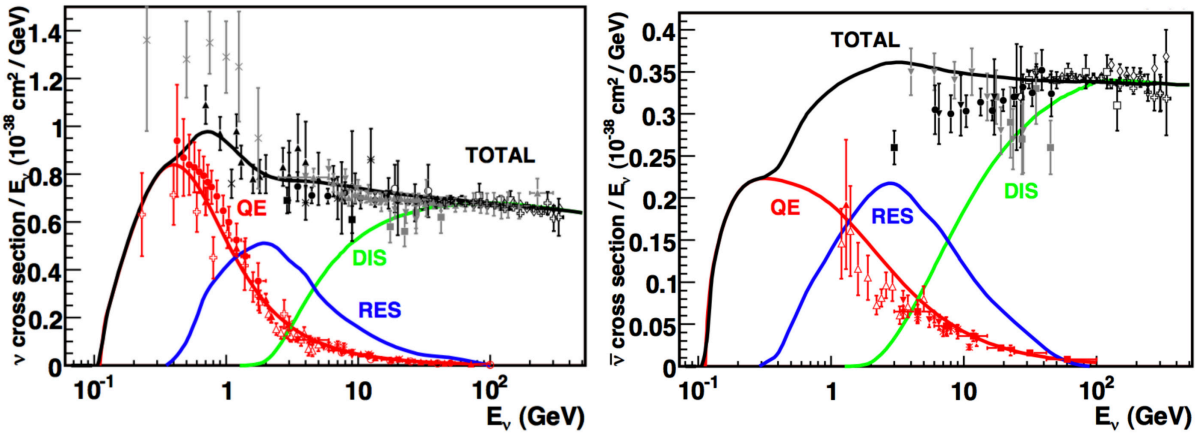

Figure 2.1: Total charged-current neutrino (left) and antineutrino (right) per nucleon cross-sections divided by energy as a function of (anti)neutrino energy, with predictions overlaid with data from experiments up to 2011. As the (anti)neutrino energy increases, so does the energy-momentum transfer, and different interaction channels start to dominate. Reprinted with permission from Ref. [46]. Copyright (2024) by the American Physical Society.

There are several interaction channels through which the charged-current interaction can proceed, often characterised by the energy-momentum transfer squared, Q^2. Note that notation used throughout this section with be further reviewed below. Intuitively, Q^2 is related to the de Broglie wavelength, which suggests the natural length scale of the system it interacts with. For example, $Q^2 = 1$ (GeV/c)^2 corresponds to the size of the nucleon. In contrast, at high Q^2, one can imagine the propagator having a small wavelength and being able to resolve the internal structure of the nucleons, i.e. quarks and gluons.

Figure 2.1 depicts the three dominant interaction channels contributing to the total (anti)neutrino cross-section: quasi-elastic (QE), resonant pion production (RES), and deep inelastic scattering (DIS). Since the available energy transfer is dictated by the initial (anti)neutrino energy, experiments in different energy regimes are sensitive to different types of interactions, and their combinations and transitions. In fact, the total cross-section in Figure 2.1 highlights that QE dominates at antineutrino energies below 1 GeV, RES in the 1–8 GeV region, and DIS above 8 GeV. The Feynman diagrams of these interaction channels in antineutrino scattering are shown in Figure 2.2.

All three interaction channels are pertinent to the analysis presented in this work due to its inclusive nature and are reviewed in this section. However, considering that the mean antineutrino energy in the measurement corresponds to approximately 6 GeV, the

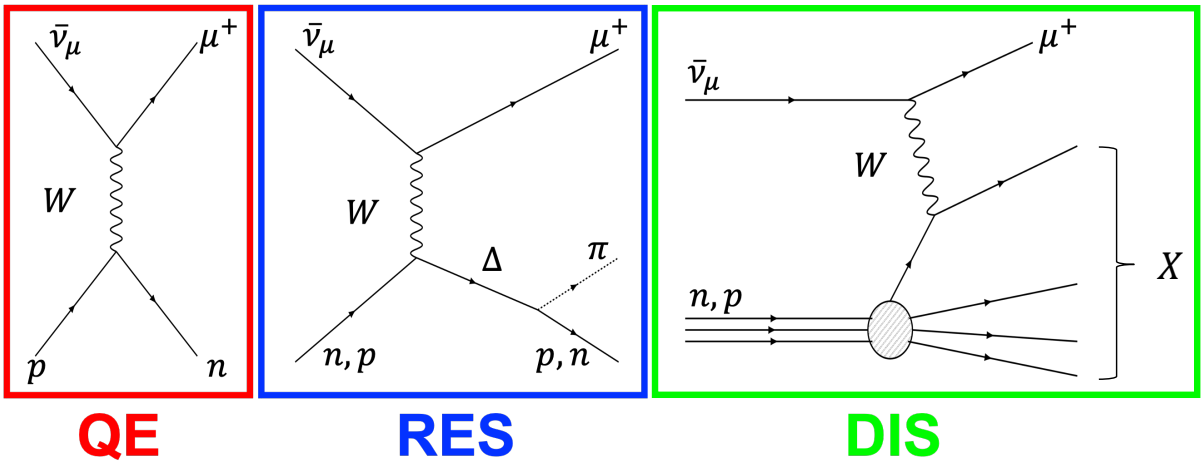

Figure 2.2: Feynman diagrams of the three main interaction channels of the charged-current antineutrino interaction: quasi-elastic scattering (QE), resonant single-pion production (RES), and deep inelastic scattering (DIS).

main contributions are anticipated from the resonant pion production and deep inelastic scattering channels, along with their transition region, referred to as shallow inelastic scattering, which is also discussed.

The notation used in the following subsections is:

$$\bar{\nu}_\mu(p_{\bar{\nu}}) + N(p_N) \rightarrow \mu^+(p_\mu) + X(p_{\text{recoil}}). \tag{2.1}$$

Here, $p_{\bar{\nu}} = (E_{\bar{\nu}}, \boldsymbol{p}_{\bar{\nu}})$ is the antineutrino Lorentz four-vector, $p_N = (E_N, \boldsymbol{p}_N)$ is the initial nucleon four-vector, and $p_\mu = (E_\mu, \boldsymbol{p}_\mu)$ is the outgoing antimuon four-vector. The total four-vector of the outgoing hadronic system X is denoted $p_{\text{recoil}} = (E_{\text{recoil}}, \boldsymbol{p}_{\text{recoil}})$. The four-momentum transfer is calculated as $q = (q_0, \boldsymbol{q}_3) = p_{\bar{\nu}} - p_\mu$, with q_0 and $\boldsymbol{q}_3$ corresponding to the energy and three-momentum transfer, respectively.

The four-momentum transfer squared discussed above and used in the different model descriptions is therefore defined as

$$Q^2 = -q^2 = -(p_{\bar{\nu}} - p_\mu)^2 = 2E_{\bar{\nu}}(E_\mu - |\boldsymbol{p}_\mu| \cos\theta_\mu) - m_\mu^2. \tag{2.2}$$

Additionally, the invariant mass of the final-state hadronic system in the interaction, W, is referred to throughout the discussion of the higher energy inelastic processes. This can be calculated as

$$W^2 = (p_{\text{recoil}})^2 = (p_N + q)^2 = (p_N + p_{\bar{\nu}} - p_\mu)^2 = -Q^2 + 2E_{\text{recoil}} m_N + m_N^2. \tag{2.3}$$

In the equations above, θ_μ is the scattering angle of the antimuon with respect to the incoming antineutrino beam, m_μ is the antimuon mass, and m_N is the mass of the nucleon on which the interaction occurs. E_{recoil} denotes the energy of the outgoing hadronic system. For derivations of these quantities from four-vectors to the measurable kinematic quantities, one can refer to various particle physics textbooks such as Refs. [47, 48].

2.1.1 Quasi-elastic scattering

At low momentum transfers, the dominant process is the quasi-elastic interaction, which primarily contributes to the total (anti)neutrino cross-section below 1 GeV. The (anti)neutrino interacts with a nucleon by exchanging a $W^{\pm}$ boson, resulting in the production of a charged lepton and a nucleon in the final state, with a different electric charge than the initial nucleon. Specifically, in antineutrino scattering, the incoming antineutrino scatters off a target proton, producing a neutron and an antimuon as shown in Figure 2.2. This process is also sometimes referred to as 1p1h—one particle, one hole—and typically leaves the nucleus mostly intact.

The (anti)neutrino quasi-elastic scattering is commonly described using the Llewellyn Smith model [49], expressing the differential cross-section as a function of the four-momentum transfer squared, Q^2. The finite size and the distributed nature of the nucleon are described by the vector $F_1(Q^2)$, $F_2(Q^2)$, pseudoscalar $F_P(Q^2)$, and axial $F_A(Q^2)$ form factors[1]. The vector form factors, F_1 and F_2, are usually related to the neutron and proton electromagnetic form factors from polynomial fits to electron scattering data, e.g. the BBBA05 parametrisation [50].

The pseudoscalar form factor, F_P, is scaled by $\sim m_l^2/m_N^2$, where m_l represents the lepton mass and m_N denotes the nucleon mass. For an (anti)muon, this ratio is about $m_\mu^2/m_N^2 \approx 1.3\times10^{-7}$, making the F_P dependence of the cross-section very small. Additionally, F_P can be linked to F_A through the partial conservation of axial current (PCAC) [51], which states that the axial current is conserved as the mass of the pion approaches zero. Therefore, the only form factor that remains and must be determined experimentally is the axial form factor, F_A.

The axial form factor, F_A, is often approximated using a dipole form,

$$F_A(Q^2) = \frac{F_A(0)}{(1 + Q^2/M_A^2)^2}, \tag{2.4}$$

assuming that the weak charge distribution has an exponential distribution. Here, $F_A(0)$ represents the axial coupling constant, which has been measured through beta decay [52].

[1] If the (anti)neutrino scattered off a point-like charge, the form factors would be constant in Q^2.

The only remaining free parameter is the axial mass, M_A, which is determined through fits to neutrino-deuterium scattering [53–55], pion electro-production [56, 57], or, more recently, antineutrino-proton scattering at MINERvA [58]. Typically, these fits yield values around 1 GeV/c^2 for the nucleon.

The quasi-elastic interaction is one of the most studied channels in (anti)neutrino scattering, with a multitude of cross-section measurements on various nuclei from experiments such as MINERvA [59–61], T2K [62, 63], and MicroBooNE [64]. However, due to the energy phase space of the measurement presented in this work, it is predicted to contribute less than 20% to the inclusive cross-section.

2.1.2 Resonant pion production

At higher (anti)neutrino energies, enough energy can be imparted to the nucleon to raise it to an excited state, creating a baryon resonance. Typically, either nucleon or delta resonances are accessible in the corresponding energy range. Subsequently, the resonance states decay back to the ground state, producing extra particles, mostly pions. An example of a Feynman diagram for the resonant single-pion production, which is the primary focus of this section, was shown in Figure 2.2. The resonant pion production usually dominates the total cross-section in the 1–8 GeV (anti)neutrino energy range as shown in Figure 2.1. Notably, it is predicted to represent the dominant contribution to the inclusive cross-section measurement in this work.

Most (anti)neutrino interaction simulations use the Rein-Sehgal model [65], derived in the limit of zero lepton mass in the rest frame of the individual resonances, to predict the resonant pion production. The Rein-Sehgal model describes the resonance region up to the invariant mass of $W = 2$ GeV, including a total of 18 possible resonances. The double-differential cross-section for an antineutrino-induced resonance with an invariant mass W is given by,

$$\frac{d^2\sigma}{dQ^2dW^2} = \frac{G_F^2\cos^2\theta_C}{8\pi^2 m_N}\kappa\frac{Q^2}{|\boldsymbol{q_3}|^2}(u^2\sigma_R + v^2\sigma_L + 2uv\sigma_S)\delta(W - M), \tag{2.5}$$

where the kinematical factors u and v depend on the initial and final momenta, while the κ factor relates the nucleon mass m_N and the invariant mass W. Their definitions are given in Ref. [65]. G_F is the Fermi constant, θ_C represents the Cabbibo angle, and $\boldsymbol{q_3}$ is the 3-momentum transfer in the lab frame. M is the centre of the mass peak of one of the resonances.

The partial cross-sections $\sigma_{R/L/S}$ for the absorption of the intermediate vector boson $W^{\pm}$ account for its different polarisation/helicity contributions, i.e. positive, negative or zero, to the differential cross-section. The partial cross-sections are proportional to their corresponding helicity amplitudes, which are calculated in terms of the nucleon vector and axial form factors using the relativistic harmonic oscillator quark model [66]. The form factors, similar to Equation 2.4, assume a dipole form, but with values for resonant axial and vector mass instead. The only datasets available for pion production on a nucleon to fit the axial mass parameter are from the Argonne National Laboratory (ANL) [67], Brookhaven National Laboratory (BNL) data [68], and the Big European Bubble Chamber (BEBC) [69]. The vector parameters can be obtained from electron-scattering data.

Importantly, while the Dirac-delta function in Equation 2.5 assumes that the resonance has a mass M and negligible width, it can be replaced by the conventional Breit-Wigner factor taking into account the resonance width Γ instead,

$$\delta(W - M) \rightarrow \frac{\Gamma}{(W - M)^2 + \Gamma^2/4}. \tag{2.6}$$

Therefore, as the invariant mass of the baryonic system, W, approaches the centre of the mass peak, M, of one of the resonances, the probability of producing one of these excited states gets higher.

The Rein-Sehgal model also considers possible interference terms between the resonances, as in reality, the contributions from nearby resonances overlap. However, these terms are not always included in the respective implementations in (anti)neutrino event generators. For example, GENIE does not include the interference terms and instead adjusts the pion production channel to match experimental data. On the other hand, the implementation in NEUT follows the model's prescription [70].

Furthermore, newer versions of GENIE and NEUT often use an improved version of the Rein-Sehgal model which relaxes the zero lepton mass limit and incorporates corrections associated with the non-vanishing lepton mass in the differential cross-section calculation [71–74]. This model is referred to as the Berger-Sehgal model [74]. Alongside advancements in the pion production model, modifications to the expressions for the vector and axial form factors utilised in the calculation of helicity amplitudes have been suggested [75]. These improvements have, for instance, been incorporated into the latest version of GENIE [76] to improve the underlying predictions for observed resonant pion production [77], also improving the vector parameters based on the world's electron scattering data [78].

2.1.3 Shallow inelastic scattering

The resonant single-pion production is not an exclusive channel for producing pions. They can also be produced through a non-resonant interaction, as depicted in Figure 2.3. The non-resonant channel is experimentally indistinguishable from the single-pion production, as it yields the same final-state particles. Furthermore, at even higher energies, the (anti)neutrino may excite higher mass resonances that can decay into multi-pion states. This transition between the resonant pion production and the deep inelastic scattering is referred to as shallow inelastic scattering (SIS). The measurement presented in this work is expected to have a significant contribution from the SIS due to its inclusive nature and the energy phase space it probes.

In the interaction community, the SIS region is defined as a region with inclusive meson production with $(m_N + m_\pi) < W < 2$ GeV/c^2 and $Q^2 < 1$ (GeV/c)^2 [80]. It represents the non-perturbative regime of quantum chromodynamics, and its modelling in (anti)neutrino interaction simulations is thus extremely challenging. However, its description and understanding are crucial for DUNE, where the SIS contribution will be significant [38]. Various (anti)neutrino event generators handle this region in different ways, but the general practice is to extend and scale the model of deep inelastic scattering producing pions to the lower W range. The non-resonant contribution is added incoherently to the

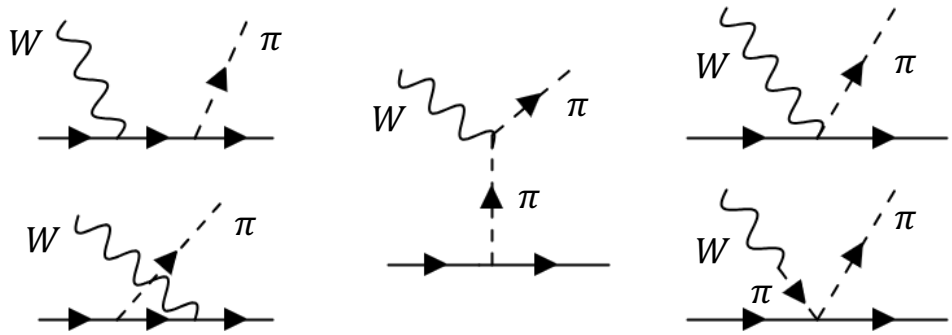

Figure 2.3: Feynman diagrams of the possible non-resonant pion production on the nucleon based on Ref. [79].

resonant pion production, ignoring any interference effects, and its strength is tuned to pion production data[2]. The specific implementation in GENIE, used in the underlying simulation prediction for this work's measurement, is described in Chapter 5.

This extension of the deep inelastic scattering model to lower invariant mass draws on the concept of so-called quark-hadron duality [80], aiming to connect the physics of quarks and gluons from deep inelastic scattering to the physics of nucleons and mesons. In the spirit of duality, the Bodek-Yang model [83, 84], used to describe deep inelastic scattering, extends the parton distribution functions down to the SIS region, implementing corrections to account for non-perturbative effects. Nevertheless, the current lack of high-statistics experimental data in the relevant SIS regime[3] hinders the understanding of how (and whether) quark-hadron duality should be applied to (anti)neutrino scattering and the ability to test current and improved implementations of this transition region in (anti)neutrino event generators.

2.1.4 Deep inelastic scattering

At even higher (anti)neutrino energies corresponding to large energy-momentum transfers, the (anti)neutrino can resolve the quark-parton structure within the nucleon. This process is referred to as deep inelastic scattering. The example Feynman diagram in Figure 2.2

[2]Note that an alternative approach is provided by the MK model for single pion production [79, 81], i.e. for both resonant and non-resonant interactions with included interference effects. Recently, this model extended its pion production model to higher W to provide predictions for the SIS region [82].

[3]At the time of writing this thesis, the first dedicated SIS measurement by MINERvA is being prepared for publication.

demonstrates that the (anti)neutrino interacts with a point-like quark or antiquark inside the nucleon, causing the nucleon to break apart, undergo hadronisation, and form multiple final-state particles. The primary definition of deep inelastic scattering on a free nucleon is given by the phase-space requirement of $Q^2 > 1$ $(\mathrm{GeV}/c)^2$ stemming from the kinematics of the interaction products. In order to further differentiate from the resonance region, the interaction community also often imposes the $W > 2$ GeV/c^2 criterion [85]. As shown in Figure 2.1, deep inelastic scattering starts to dominate the total antineutrino cross-section around 8 GeV, and therefore, it is expected to be the second major contribution to the measurement presented in this thesis (excluding the SIS transition).

Deep inelastic scattering is typically described using two Lorentz-invariant dimensionless quantities: Bjorken x, and the Bjorken inelasticity, y. The Bjorken x can be interpreted as the fraction of the nucleon momentum carried by the struck quark in a frame where the nucleon momentum is very large (and its mass can be therefore neglected), often referred to as the 'infinite momentum frame' or Breit frame. The inelasticity y is the fraction of the (anti)neutrino energy transferred to the hadronic system. They can be defined as

$$x = \frac{Q^2}{2p_N \cdot q} \overset{\text{lab}}{=} \frac{Q^2}{2m_N E_{\text{recoil}}} \tag{2.7}$$

and

$$y = \frac{p_N \cdot q}{p_N \cdot p_{\bar{\nu}}} \overset{\text{lab}}{=} \frac{E_{\text{recoil}}}{E_{\bar{\nu}}}\,, \tag{2.8}$$

where $\overset{\text{lab}}{=}$ denotes the corresponding definitions in the lab frame, where the nucleon is assumed to be stationary. The derivation of these expressions in the lab frame can be found, for example, in Ref [47].

The double-differential cross-section for deep inelastic scattering of antineutrinos in terms of x and y is then given by [47, 86]

$$\frac{d^2\sigma}{dxdy} = \frac{G_F^2 m_N E_{\bar{\nu}}}{\pi(1+Q^2/M_W^2)^2}\left(y^2 x F_1 + (1-y)F_2 - y\left(1-\frac{y}{2}\right)xF_3\right)\,, \tag{2.9}$$

where M_W is the mass of the gauge boson W^-, and $F_i \equiv F_i(x, Q^2)$ for $i = 1, 2, 3$ are the structure functions describing the parton structure of the nucleon. The remaining parameters are as defined in previous subsections. Compared to the charged-lepton scattering, the cross-section expression features the xF_3 structure function, coupling antineutrinos to u and $\bar{d}$ quarks (and similarly in other generations). This arises from the parity-violating terms in the product of leptonic and hadronic tensors. Note, that it would have an opposite sign for neutrinos.

The F_1 and F_2 structure functions can be related via

$$2xF_1 = \frac{F_2(1 + 4M^2x^2/Q^2)}{R_L + 1}, \tag{2.10}$$

where R_L can be interpreted as the ratio of the longitudinal and transverse virtual boson absorption cross-sections, i.e. $R_L \equiv R_L(x, Q^2) = \sigma_L/\sigma_T$ [86]. Importantly, to the leading order, $R_L(x, Q^2) = 0$ for spin-half quarks which are assumed to be massless, and the equation above reduces to the well-known Callan-Gross relationship $2xF_1 = F_2$ [87].

At the leading order, the remaining F_2 and F_3 structure functions can be written in terms of the fractional momentum-weighted parton distribution functions (PDFs) $q_i(x)$ and $\bar{q}_i(x)$. This is assuming the Bjorken scaling limit, i.e. $F_{2,3}(x, Q^2) \to F_{2,3}(x)$, due to the near independence of the structure functions on Q^2 from scattering from point-like particles [47]. For example, for antineutrino scattering from a proton above the charm production treshold, F_2 and F_3 are given by

$$F_2(x) = 2x(u(x) + \bar{d}(x) + c(x) + \bar{s}(x)), \tag{2.11}$$

and

$$xF_3(x) = 2x(u(x) - \bar{d}(x) + c(x) - \bar{s}(x)), \tag{2.12}$$

describing the contributions from valence and sea quarks. At high Bjorken x values, antineutrinos are generally scattering from valence quarks as they carry the majority of the nucleon's momentum, while the sea quarks contribute at low x. Note that only positively charged (anti)quarks participate in antineutrino scattering.

Since PDFs need to be inferred directly from experimental data, lepton deep inelastic scattering, particularly (anti)neutrino deep inelastic scattering, has been intensively stud-

ied at high energies in bubble chambers [88–91] and on heavy targets such as iron [92–94]. However, PDFs on free and bound nucleons differ, and the corresponding modifications to the PDFs in antineutrino-nucleus scattering are reviewed in the next section.

Furthermore, in the deep inelastic scattering regime relevant to accelerator-based experiments, i.e. below 10 GeV, non-perturbative quantum chromodynamics processes, known as higher-twist effects, start to become significant, as discussed for shadow-inelastic scattering. The quarks can no longer be considered massless, and the Callan-Gross relation ceases to be valid as the R_L in Equation 2.10 deviates away from zero [86]. Multi-parton effects also need to be considered, as quarks cannot be seen as non-interacting particles anymore. The Bodek-Yang model used in (anti)neutrino event generators to simulate deep inelastic scattering includes corrections to PDFs based on fits to charged-lepton scattering data to account for these higher-twist effects [83, 84]. To directly explore these effects with (anti)neutrinos and verify model predictions, dedicated measurements from experiments like MINERvA are essential [95].

Finally, modelling the hadronisation process is a crucial step in (anti)neutrino event simulations of deep inelastic scattering in order to predict the outgoing final-state particles and their kinematics for a given value of x and Q^2. For GENIE, this process is detailed in Chapter 5.

2.1.5 Other interactions

Other interaction processes that contribute to the total (anti)neutrino cross-section are subdominant and are predicted to make up less than 1% of the total antineutrino cross-section in the measurement presented in this work. However, interactions such as coherent pion production will be mentioned in the subsequent chapters, particularly in the description of the underlying antineutrino model simulation used in the analysis in Chapter 5.

Coherent pion production is a low four-momentum transfer process in which the (anti)neutrino interacts with the entire nucleus. The charged-current interaction produces very forward-going (anti)muon and pion while leaving the nucleus intact. It can

be interpreted as a fluctuation of the gauge boson to a virtual pion that scatters elastically from the nucleus. The Rein-Sehgal model [96] for coherent pion production predicts that the coherent cross-section scales as $A^{1/3}$ for different nuclei, while the Berger-Sehgal model [72], including mass correction, predicts $A^{2/3}$ scaling. MINERvA has made several measurements of the charged-current neutrino- and antineutrino-induced coherent pion production [97–99].

2.2 Nuclear effects

(Anti)neutrino scattering in most cases does not occur on free nucleons but on nucleons bound inside the nucleus by the strong nuclear force. The effects of the nuclear environment on the interaction channels described above and their outgoing particle kinematics, therefore, must be taken into account. Simulations of (anti)neutrino interactions factorise the interactions to handle the nuclear medium before and after the interaction independently and then combine the individual components incoherently to make predictions. In particular, the modelling process needs to consider the initial nuclear distribution, the impact of the nucleus on the interaction itself—such as the presence of correlated nucleons—and the final state interactions the outgoing particles can undergo before leaving the nucleus. The relevant models for these individual processes are discussed in the following subsections.

2.2.1 Initial state of the nucleons

Nucleons are fermions and must adhere to the Pauli exclusion principle, meaning that no two identical nucleons can occupy the same momentum-spin state within the nuclear potential well. Each nucleon is modelled with an isotropic initial state movement known as Fermi motion, drawn from a momentum distribution, along with the associated binding energy required to free it from the nucleus [100, 101]. The nucleons are therefore distributed among the nuclear quantum states from the bottom of the potential well upwards to the highest filled state. Since the nucleons are localised inside the nucleus with a ra-

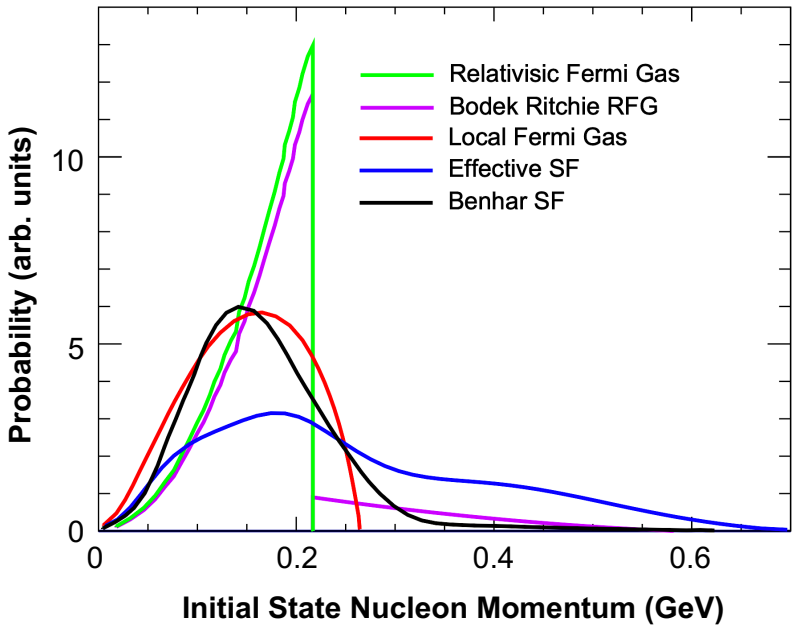

Figure 2.4: Comparison of the different initial state nucleon momentum distributions available in different generators in a ^{12}C nucleus. Modified from Ref. [102].

dius $\mathcal{O}$(1 fm), their typical momentum is $\mathcal{O}$(100 MeV) due to the Heisenberg uncertainty principle.

Overall, determining the precise momentum of the nucleon that the (anti)neutrino interacts with is challenging, particularly for nuclei with many nucleons, i.e. heavy nuclei. Several models implemented in (anti)neutrino interaction simulations attempt to address this, as briefly described below. Note that each of the models implemented in generators uses the impulse approximation, where the incoming (anti)neutrino interacts with a single nucleon.

The Smith-Monitz **Relativistic Fermi Gas (RFG)** [100,101] is the simplest and one of the most common models, treating nucleons as a collection of non-interacting fermions in a constant nuclear potential. The successive quantum nuclear states are filled from the ground state up to the Fermi-momentum level, p_F, which is the highest occupied state—all states above p_F are left empty. As shown in Figure 2.4, this results in a sharp momentum cut-off at p_F. Note that the Pauli exclusion principle also requires that any recoil nucleon from the (anti)neutrino-nucleus interaction has a momentum greater than p_F. This results in so-called Pauli blocking, where interactions with low four-momentum transfer are suppressed.

Ultimately, the RFG does not account for interactions between nucleons, which can result in nucleons with momentum greater than p_F. The **RFG with Bodek-Ritchie tail** [103] extends the base RFG model to higher energies to incorporate correlations between nucleons, based on comparisons of structure functions from deep inelastic scattering for bound versus free nucleons. The extension results in the high-momentum tail observed in Figure 2.4. This nuclear model serves as the base model in the underlying prediction for the measurement presented in this work.

Furthermore, the binding potential experienced by nucleons varies across the nucleus, depending on the local density at the interaction vertex. This variability is considered in the **Local Fermi Gas (LFG)** model [104, 105], which incorporates the radial dependence r of nucleus density $\rho(r)$ observed in electron scattering data [106]. The LFG effectively creates a continuum of RFGs, for which each local p_F varies with radial position following $p_F \propto (\rho(r))^{1/3}$, leading to a more uniform distribution of initial state nucleon momentum. This is also illustrated in Figure 2.4. A newer version of GENIE, against which the results of this measurement are compared in Chapter 9, is based on this model.

Finally, the **Benhar et al. Spectral Function (SF)** [107] is implemented in, for example, NEUT. The SF is specifically calculated for a given nucleus and momentum distribution, taking into account two- and three-body nucleon-nucleon interactions, thereby modifying the available nuclear quantum states. These short-range correlated (SRC) nucleon pairs represent about 20% of the total probability distribution [108] and cause the high-momentum tail beyond p_F, which is more realistic than the RFG with Bodek-Ritchie tail, as visible in Figure 2.4. An **Effective SF** model [109] is also available, even for nuclei where the Benhar et al. SF has not been calculated. It is derived from the empirical observation that the interaction response in electron scattering data can be fitted with a 'super-scaling function' with free parameters tuned to available experimental data across various nuclei and energy-momentum transfers [110]. The SF-based models are referenced in the context of comparing the results with different (anti)neutrino predictions in Chapter 9.

2.2.2 Multi-nucleon correlations

While some initial state models described above consider nucleon-nucleon correlations, their discussion in the context of the impulse approximation means that the primary (anti)neutrino interaction occurs on a single nucleon, with the other nucleon(s) merely spectating. However, at lower Q^2 this approximation breaks down and interactions on a bound state of two or more nucleons, leading to multi-nucleon final states ejected from the interaction vertex, need to be included in the interaction models [111–113].

This was demonstrated by the so-called MiniBooNE puzzle, which refers to a measurement of charged-current quasi-elastic neutrino interaction on carbon by the MiniBooNE experiment [114]. This measurement showed significant disagreement with the predictions of the relativistic Fermi gas model at the time, requiring large values for the axial mass compared to the global bubble chamber fits to describe the data [115]. The result suggested that the scattering between an (anti)neutrino and an independent nucleon strongly underestimates the measured cross-section. Notably, the global axial mass fit was only possible when the interactions from correlated nucleons were included [116].

Nucleons in the nuclear environment are correlated via short-range correlations (SRC) and meson exchange currents (MEC). The typical signature of SRC pairs is their high relative momentum with individual momenta $p > p_F$, populating the high-momentum tail of the initial state nucleon momentum, as discussed in the context of Figure 2.4 [117]. SRC between nucleons (mostly proton-nucleon pairs) arise from brief overlaps of their wavefunctions and represent about 20% of all nucleons [108]. The exchange of virtual mesons, often pions as they are the lightest mesons and thus have the longest range, is another way to consider binding between nucleons. Examples of MEC diagrams are shown in Figure 2.5.

Multi-nucleon correlations were first inferred in electron scattering data [110], but in response to the MiniBooNE measurement, Nieves et al. [113] and Martini et al. [112] proposed models describing the role of multi-nucleon interactions in (anti)neutrino scattering specifically. This process is referred to as the two-particle-two-hole (2p2h) or more generally n-particle-n-hole (npnh) interaction, allowing for two (or more) nucleons in the final

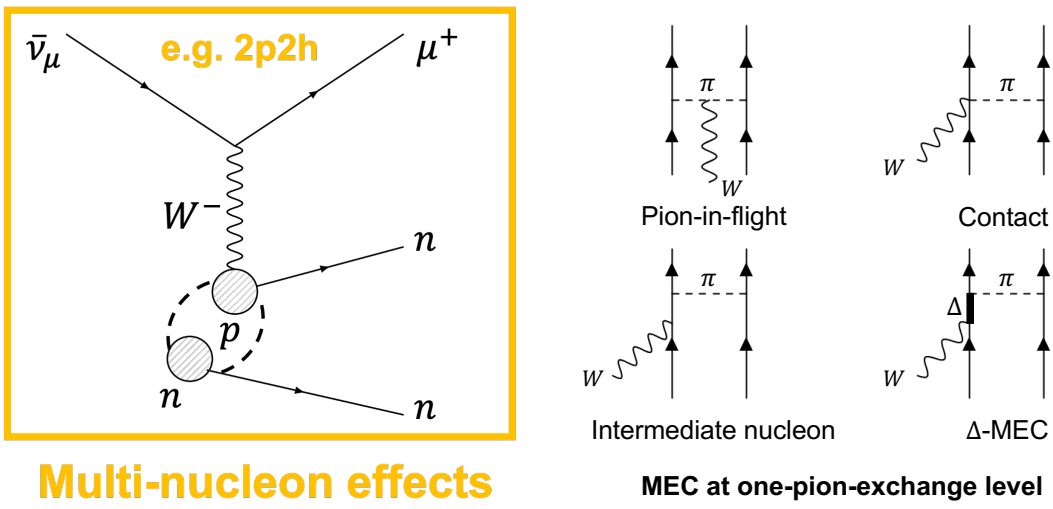

Figure 2.5: Example of antineutrino-induced 2p2h interaction on proton-neutron correlated pair (left) with possible meson exchange currents (MEC) at one-pion exchange level (right). MEC diagrams based on Ref. [118].

state prior to any final state interactions, as demonstrated in Figure 2.5. The 2p2h interaction is often described as sitting in the 'dip-region' between the quasi-elastic scattering and resonant pion production in Figure 2.1.

In addition to the 2p2h interaction, incorporating the random phase approximation (RPA) was found to be crucial for accurately reproducing heavy-target (anti)neutrino scattering data [112,113]. The RPA accounts for long-range correlations in (anti)neutrino-nucleus scattering, arising from the polarisation of the nuclear medium by the electroweak propagator. At low values of Q^2, the RPA suppresses the cross-section, while at large Q^2 its effect vanishes due to the impulse approximation.

An alternative 2p2h model based on the super-scaling phenomenon shown by electron-nucleus scattering data [110,119,120] with improved nuclear dynamics [121–124], SuSAv2-MEC [125], has also been implemented in (anti)neutrino simulations and tested against data in recent years [126,127]. The 2p2h contribution utilises a fully relativistic calculation and differs from the other 2p2h models [112, 113] by, for example, shifting its prediction to lower Q^2 values, extending the prediction to larger three-momentum transfers, and predicting different initial correlated pair distributions [127]. The impact of using this alternative model for 2p2h on the measurement presented in this analysis is considered in Chapter 7.

Finally, it is important to note that while the nucleon correlations in the quasi-elastic region have been studied by various (anti)neutrino experiments and their models exist, the impact of nucleon correlations for pion production and at higher energies is still mostly unknown. Deep inelastic scattering studies of (anti)neutrino scattering can provide some information about the modifications to structure functions due to correlated nucleons at higher energies.

2.2.3 Nuclear modifications to structure functions

The structure functions of nucleons bound in the nucleus differ from those of free nucleons, thus modifying the interaction probabilities of deep inelastic scattering in particular [128], as hinted in Subsection 2.1.4. This was first observed in the measurement of per-nucleon deep inelastic muon scattering cross-section on iron when compared to that of deuterium by the European Muon Collaboration (EMC) [129]. Since then, the nuclear modifications have been studied extensively in charged-lepton scattering measurements [117, 128] and assumed to be the same for (anti)neutrino scattering when implemented in (anti)neutrino simulations [80,83,84]. The nuclear modifications to the cross-section are usually classified in terms of the Bjorken x variable (defined earlier in Equation 2.7) looking at ratios of heavy-to-light nuclei cross-section as shown in Figure 2.6.

The so-called **shadowing** region corresponds to the suppression of the cross-section due to destructive interference of hadronic fluctuations of the intermediate boson that multiple-scatter off surface nucleons at $x \lesssim 0.1$. In other words, this means that the nuclear cross-section is less than the sum of the cross-sections on all bound nucleons [130]. The enhancement of the cross-section due to constructive interference in multiple scattering in the $0.1 \lesssim x \lesssim 0.3$ region is often referred to as **antishadowing**.

The observed depletion in the bound nucleon cross-section ratio in the $0.3 \lesssim x \lesssim 0.7$ is known as the **EMC effect**, named after the European Muon Collaboration that first reported this effect [129]. There is no definitive explanation for the origin of the EMC effect [135], but the possible hypotheses involve either the effect of nuclear mean-field

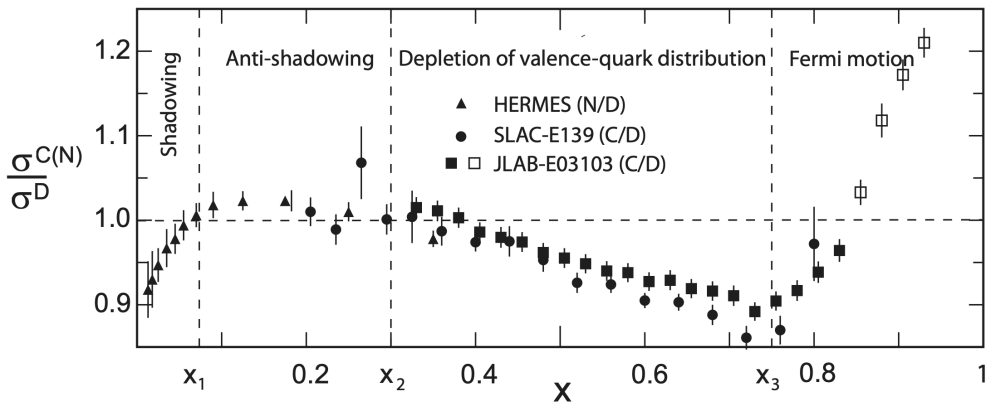

Figure 2.6: Comparisons of charged-lepton scattering cross-section ratios of carbon (C) or nitrogen (N) to deuterium (D) as a function of Bjorken x from HERMES [131], SLAC-E139 [132], and JLAB-E139 [133]. Adapted from Ref. [134].

modifications of the nucleon structure [136] or SRC [137]. Finally, the region of $x \gtrsim 0.7$ is simply known as the **Fermi motion** region, as the valence quarks dominate the structure functions at high x, and the momentum of nucleons bound inside the nucleus becomes the dominant effect [138].

However, since (anti)neutrino scattering involves the axial-vector current, and it is sensitive to specific quark and antiquark flavours, the dependence of F_2 observed in (anti)neutrino scattering is likely different (in addition to including F_3). This has been experimentally suggested by measurements of these nuclear modifications in (anti)neutrino scattering [92–94]. Nevertheless, the observed differences in the structure-function modifications between the charged-lepton data and (anti)neutrino scattering are not yet understood, and additional experimental (anti)neutrino scattering data is needed [130].

Furthermore, while for the free nucleon target, the Bjorken x variable is defined within $0 \leq x \leq 1$ region, for a nuclear target with a nucleon number A, it can theoretically vary between 0 to A [140]. This effectively means that the incoming probe can scatter off two or more correlated nucleons, carrying away a fraction of a momentum larger than 1 and probing the structure of deeply bound nucleons. This has been explored in charged-lepton deep inelastic scattering experiments using different materials. Several experiments observed a plateau in cross-section ratios consistent with the signature of scattering off two-nucleon SRC at $x > 1.5$ [139, 141, 142], as demonstrated in Figure 2.7.

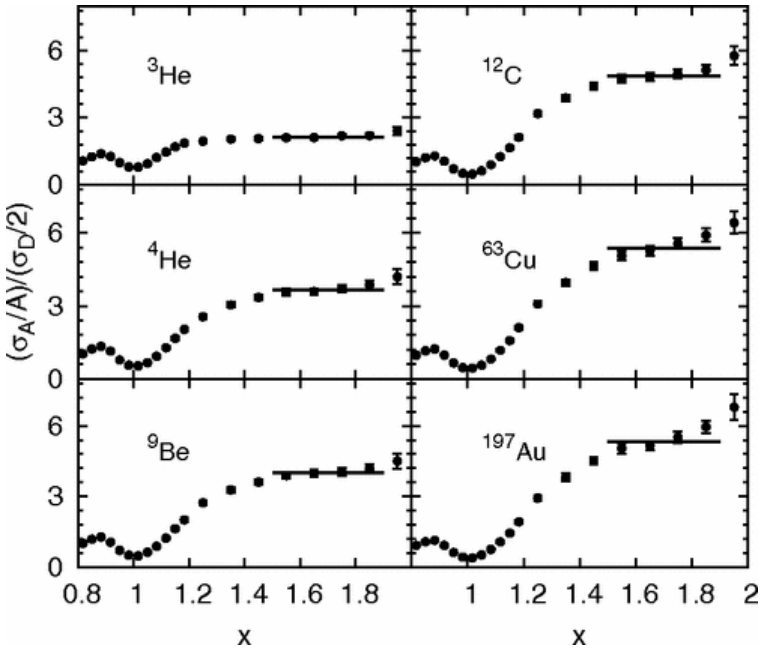

Figure 2.7: Per-nucleon cross-section ratios of electron scattering on different nuclei as a function of Bjorken x from the E02-019 experiment performed at Jefferson Lab (Hall C). Note the two-nucleon SRC plateau at $x > 1.5$. Reprinted with permission from Ref. [139]. Copyright (2024) by the American Physical Society.

2.2.4 Final state interactions

Before any measurements can be made, particles produced inside the nuclear environment by the primary (anti)neutrino interaction must exit the nucleus. However, the outgoing particles can re-interact inside the nuclear environment with the remaining nucleons. These interactions are referred to as the final state interactions (FSI), and they can alter the kinematics of the produced particles, as well as their multiplicities or their types [143]. While the outgoing leptons can undergo multiple Coulomb scattering, the final state interactions primarily refer to the outgoing hadrons.

Figure 2.8 illustrates a concrete example of the impact that FSI have on what is eventually seen in the detector and measured. It depicts both the quasi-elastic interaction and the resonant pion production occurring on a nucleon inside the nucleus. However, in the case of resonant pion production, the nuclear environment can absorb the pion, resulting in outgoing particles that appear identical to those in the quasi-elastic interaction.

The FSI, therefore, renders it impossible to reliably determine the primary interaction channel. Moreover, the impact of FSI increases with the increasing number of nucleons

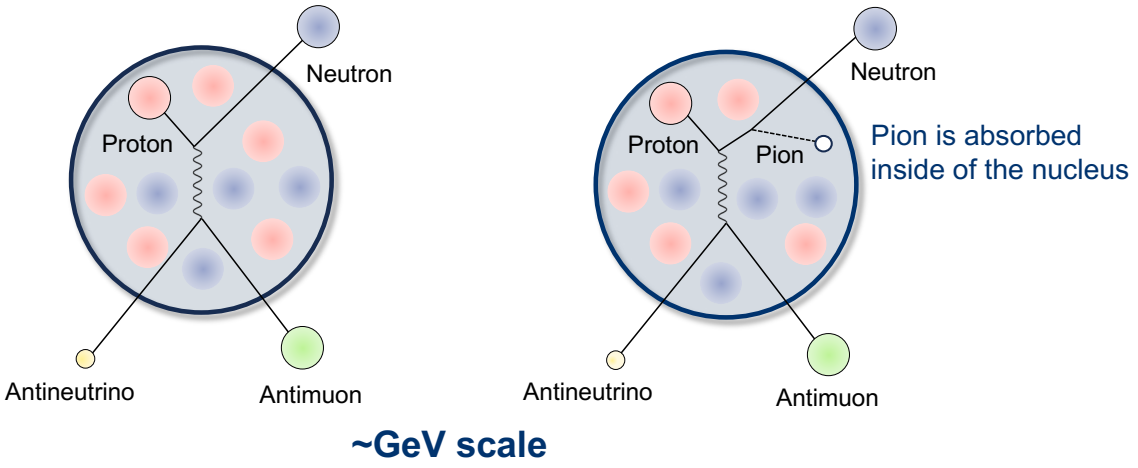

Figure 2.8: An illustration of the final state interactions. Quasi-elastic interaction (left) and resonant pion production (right) on a nucleon bound inside the nucleus result in the same final states, resulting from pion absorption in the latter.

inside the nucleus, as there are more particles for the hadrons to re-interact with. As a result, most experiments publish measurements in terms of final state topologies to minimise the model dependence of the data. For example, interactions with final states such as those shown in Figure 2.8 would be labelled as CC0π or CCQE-like, rather than just pure CCQE [61].

Pions in particular, being the lightest mesons, are a useful probe for studying FSI which can impact the magnitude and direction of the pion momentum. Figure 2.9 shows the most common FSI channels in which the pion (or generally a hadron) can scatter elastically or inelastically, can be absorbed by a pair of nucleons, or undergo a charge exchange. FSI are in general very difficult to model in (anti)neutrino simulations or even constrain with experimental data. Most generators employ an intranuclear cascade model to attempt to do so.

The cascade models simulate the propagation of particles throughout the nucleus by treating the individual hadrons independently and advancing through the nucleus in discrete steps based on the hadron mean free path. At each step, the probability for the various possible FSI is calculated based on the surrounding nuclear density, determining whether the re-interaction takes place [145]. If an interaction is chosen to occur, one of the possible FSI channels is selected at random according to their relative cross-sections,

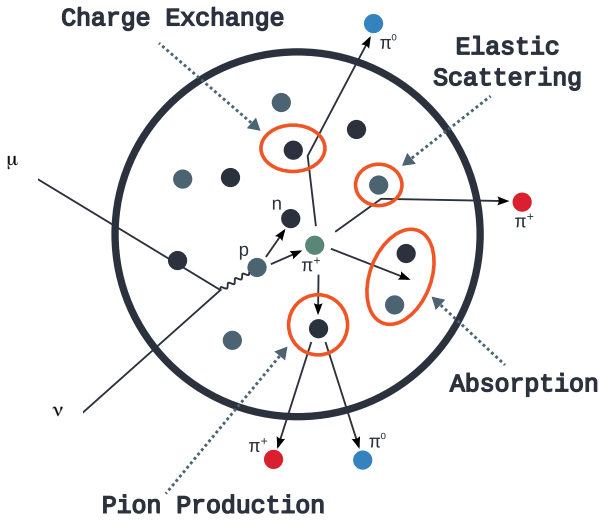

Figure 2.9: Diagram of possible final state interactions of pions while leaving the nucleus. The primary interaction vertex is placed outside the nucleus since the outgoing leptons are not included in the intranuclear cascade. Adapted from Ref. [144], figure by Tomasz Golan.

calculating the kinematics of the outgoing particles. This process continues until the hadron leaves the nucleus. Multiple FSI can occur.

The relative probabilities for different FSI processes are tuned to external data from pion-nucleus and proton-nucleus scattering [42, 43, 146]. Furthermore, suppression of the re-interaction cross-sections at higher energies, as motivated by data [147], is often implemented utilising a so-called formation zone around the vertex, within which recoiling particles cannot interact with the nuclear environment [148]. Hadrons therefore propagate some distance from the (anti)neutrino interaction point, proportional to their momentum, before they can re-interact, making the effect of FSI smaller.

Specific details about the implementation of the intranuclear cascade used in the underlying simulation prediction for this measurement are outlined in Chapter 5.

Chapter 3

MINERvA experiment

MINERvA (Main Injector Neutrino ExpeRiment to study ν–A interactions) was an experiment specifically designed to perform self-contained studies of nuclear dependence in (anti)neutrino scattering. Operational from 2009 until the conclusion of its physics run in 2019, the experiment was situated in the MINOS near detector hall at Fermi National Accelerator Laboratory (Fermilab). At its core was the MINERvA detector, which was exposed to muon (anti)neutrinos from the high-intensity NuMI (Neutrinos at the Main Injection) beam. An integral part of the experiment involved using the data from the MINOS (Main Injector Neutrino Oscillation Search) near detector, utilised as a (anti)muon spectrometer, to constrain the momenta of (anti)muons generated by charged-current (anti)neutrino interactions within the MINERvA detector. This chapter delves into these three components of the experiment enabling the high-precision measurements of (anti)neutrino interactions, with a particular focus on the aspects relevant to the measurement presented in this work.

3.1 NuMI beamline

The NuMI beamline [149, 150] is a conventional accelerator neutrino source originally constructed to supply muon (anti)neutrinos for the long-baseline neutrino oscillation experiment MINOS [151, 152]. It was later upgraded to provide a higher-intensity beam for its successor, NOvA [153]. The (anti)neutrinos are produced via decays of charged pions

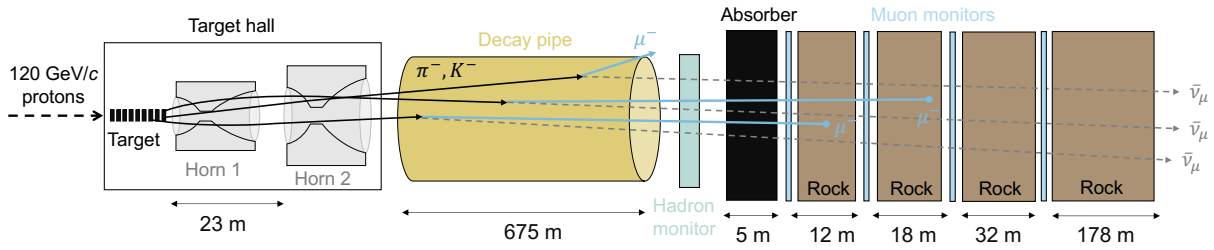

Figure 3.1: Schematic illustrating the components of the NuMI beamline at Fermilab in the medium energy reverse horn current configuration, drawn based on the information provided in Refs. [150, 154].

and kaons, which, in turn, are created from protons striking a graphite target. A schematic of the NuMI beamline starting from the graphite target is depicted in Figure 3.1. The MINERvA experiment spanned both the MINOS and NOvA configuration of the NuMI beamline, with peak (anti)neutrino energies of ∼3 GeV and ∼6 GeV, respectively. These are referred to as the low energy (LE) and medium energy (ME) regimes. The measurement described in this work utilises the ME antineutrino dataset exclusively, which is reflected in the description of the NuMI configuration. Both the instrumentation of the NuMI beamline and the simulation prediction of the NuMI flux are discussed.

3.1.1 Instrumentation

The NuMI beamline hardware and operations are in detail described in Ref. [150]. First, protons from hydrogen ions undergo incremental acceleration in Fermilab's proton accelerator complex [155], including the linear accelerator (Linac) and Booster synchrotron, ultimately reaching the final beam energy of 120 GeV in the Main Injector (MI) synchrotron accelerator. Subsequently, these protons are extracted and directed onto the graphite target in approximately 10 μs long windows, referred to as spills. Upon the extraction from the MI, the proton beam is also bent 3.343° (58.87 mrad) downwards towards the MINOS far detector in Minnesota.

Compared to the LE era, the beam intensity was increased from 400 kW to more than 700 kW in the ME era by placing more protons in the same spill and reducing the spill cycle time to 1.33 seconds from the original 2.2 seconds. The ME configuration

Regime	Mode (POT)	
	Neutrino-dominated	Antineutrino-dominated
Low (LE) ∼3 GeV	4.0×10^{20}	1.7×10^{20}
Medium (ME) ∼6 GeV	10.6×10^{20}	11.2×10^{20}

Table 3.1: The number of protons on target recorded by MINERvA in the low and medium energy regime for both neutrino and antineutrino-dominated beams.

delivered around 4.9×10^{13} protons on target (POT)[1] during each spill, resulting in the ME antineutrino data exposure of 1.12×10^{21} POT recorded by MINERvA and used for this measurement. The total number of POT collected by MINERvA over its physics run both in the LE and ME era is summarised in Table 3.1.

Prior to reaching the graphite target, the proton beam is collimated by passing through a hole in the so-called baffle—a graphite-aluminum tube designed to partially degrade mis-steered beams to protect other components of the beamline. The proton beam size is about ∼1 mm upon impinging onto the 1.2 metres long (about 2.5 proton interaction lengths) graphite target. The target is made out of 50 narrow fins to dissipate heat and reduce the probability of reinteraction of produced hadrons, which are mounted on steel pipes providing water cooling and contained within a helium-filled vessel.

The final state particles produced by the proton beam hitting the target, mostly pions and kaons, are charge-sign selected and focused in a forward direction by two 3 metres long parabolic magnetic horns made of aluminum. The choice of the horn current direction, whether it is forward horn current (FHC) or reverse horn current (RHC), determines the selection of positive or negative charged hadrons, ultimately resulting in a neutrino or antineutrino-dominated beam, respectively. The RHC configuration is shown in Figure 3.2. The horns increase the hadron flux in the desired energy range and provide flexibility in choosing that energy based on their configuration. The ME spectra with the (anti)neutrino energy peak of ∼6 GeV was achieved by increasing the distance between the target and the first horn, and the first horn and the second horn compared to the LE configuration. During the antineutrino-dominated runs used in this measurement, the magnetic field was generated by a -200 kA electric horn current into the horns.

[1]POT is a metric used to characterise the integrated luminosity of the (anti)neutrino beam.

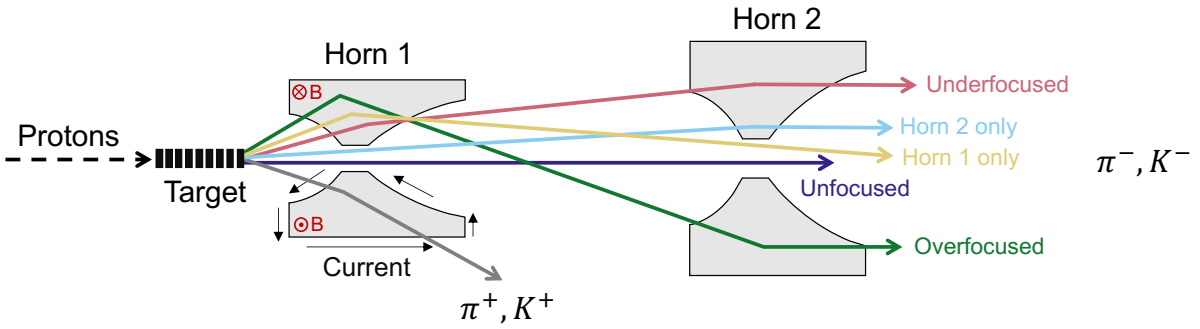

Figure 3.2: Schematic of the working principle of the magnetic horns for the reverse horn current configuration indicating some possible trajectories, drawn based on the information provided in Ref. [156].

The first focusing horn perfectly focuses less than 10% of charged hadrons producing antineutrinos, implying that the majority of hadrons require correction from the second focusing horn [157]. Figure 3.3 illustrates the resulting antineutrino flux in both the ME configuration (used in this work's measurement) and the LE configuration for comparison. Below 20 GeV, most antineutrinos are produced by pion decays, while antineutrinos produced from kaons dominate the high-energy tail. The bump observed at less than 1 GeV arises from low-energy antineutrinos produced by charged hadrons originating from outside the target. The rising part of the flux spectrum primarily originates from antineutrinos produced by charged pions that were initially overfocused by the first horn but subsequently corrected by the second horn. Conversely, the descending part of the flux corresponds to antineutrinos generated by underfocused charged pions, which are corrected by the second horn.

Overall, the first horn predominantly focuses low-momentum charged pions, leading to the production of low-energy antineutrinos in comparison to the second horn. The inclusion of the second focusing horn significantly enhances the focusing, contributing to an increase of almost 50% in the ME configuration [157]. Some high-energy hadrons that are perfectly aligned with the magnetic horns can pass through without being charge-selected. Consequently, some of these hadrons decay into neutrinos, contributing to the contamination of the antineutrino-dominated beam, particularly at higher energies.

Focused negatively charged hadrons enter the 675 metres long decay pipe filled with helium to limit interactions with the hadron beam. As they traverse the decay pipe,

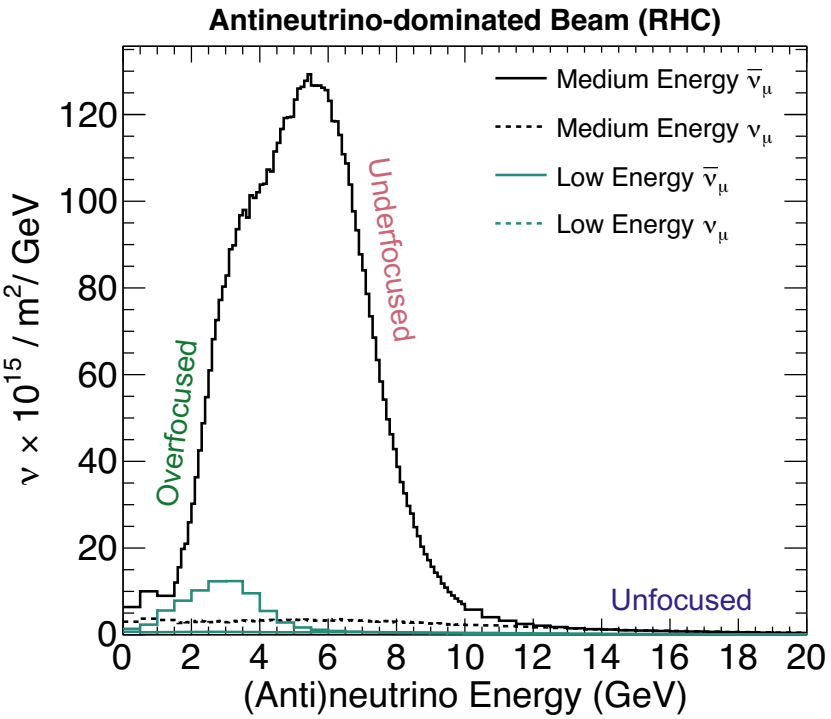

Figure 3.3: Distributions of (anti)neutrino fluxes in the medium and low energy regimes are depicted for the reverse horn current configuration at the MINERvA detector. These distributions represent the energy distributions of (anti)neutrino interactions per unit area. The solid lines represent the primary antineutrino contribution, while the dashed lines indicate neutrino contamination in the antineutrino-dominated beam. The contributions of specific antineutrino parent-focusing components are colour-coded to illustrate their trajectories in Figure 3.2.

the hadrons primarily decay into muon antineutrinos via modes such as $\pi^- \to \mu^- \bar{\nu}_\mu$ with a branching ratio exceeding 99% and $K^- \to \mu^- \bar{\nu}_\mu$ with a branching ratio of 63.5% [28,150]. The muon antineutrino beam is contaminated by ν_μ, ν_e, and $\bar{\nu}_e$ due to other decay modes such as $K^- \to e^- \bar{\nu}_e \pi^0$ or $\pi^- \to \mu^- \bar{\nu}_\mu \to e^- \bar{\nu}_e \nu_\mu \bar{\nu}_\mu$ [28]. Any remaining undecayed hadrons are detected by the hadron monitor and absorbed in the downstream[2] hadron absorber made of aluminium, steel, and concrete. The only particles left in the beam—muons and antineutrinos—travel through 240 metres of dolomite rock interlaid with four muon monitors as depicted in Figure 3.1. The rock acts as a muon shield stopping the residual muons and allowing the antineutrinos to pass downstream to the MINOS near detector hall, which housed the MINERvA detector, located about 1 kilometre from the target. Some antineutrinos interact with the rock, creating additional antimuons referred to as rock muons, which could travel downstream to the MINERvA detector as well.

[2]Downstream and upstream indicate positions relative to the beam direction, where downstream is in the direction of the beam, and upstream is against it.

3.1.2 Simulation and characterisation

Precise knowledge of the (anti)neutrino flux produced by the NuMI beamline is crucial for (anti)neutrino cross-section measurements. In addition to determining the number of (anti)neutrinos that interacted in the detector, understanding how many were initially present in the beam is essential, as indicated in Equation 4.1 in the following chapter. However, understanding the (anti)neutrino beam is challenging, primarily due to the complex processes involved in hadron production and the focusing components of the beamline. MINERvA addresses this challenge by employing a calculated *a priori* flux, i.e. simulated flux adjusted using external hadron production data with varying parameters related to both hadron production and focusing to incorporate relevant systematic uncertainties. Direct flux measurements are also possible [158] but are limited to an accuracy of 15% due to poorly constrained backgrounds and detector uncertainties.

The NuMI beam is simulated using the G4NuMI package, which is based on the GEANT4 (GEometry ANd Tracking) software version 9.4.p02 [159, 160], incorporating detailed geometrical models of the beamline. The G4NuMI package, initially developed for MINOS [158, 161, 162], was subsequently improved by MINERvA [156, 163]. It covers the entire process from the 120 GeV/c protons impinging onto the graphite target to focused charged hadrons decaying into (anti)neutrinos, predicting the number, flavour, and momentum distributions. The underlying phenomenological hadronic models FRITIOF precompound [164, 165] and Bertini cascade [166–169] implemented in the FTFP_BERT package of GEANT4 to predict the hadrons produced by the proton-carbon interactions were, however, shown to disagree with external hadron production data [156]. Therefore, MINERvA developed the Package to Predict the Flux (PPFX) [40,156] to constrain these models using external experimental data.

The PPFX primarily uses the NA49 [170] pion production dataset, which is corrected to the NuMI appropriate energy scale using the FLUKA simulation [171,172]. The NA49 experiment at CERN measured the pion production on a thin, i.e. a few percent of interaction length, carbon target using a 158 GeV/c proton beam [170]. Additional datasets are also employed in the PPFX to constrain kaon and nucleon production, as well as the

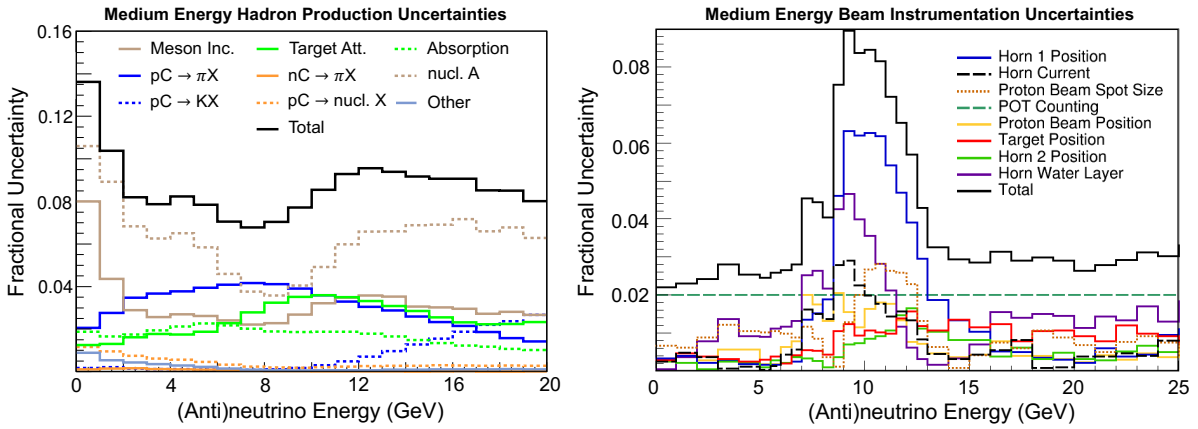

Figure 3.4: PPFX uncertainties on the NuMI medium energy flux. Left: Flux uncertainty from different hadron interaction categories modified from Ref. [156]. Note that 'Meson Inc.' refers to the uncertainty of mesons interacting on any material in the beamline, 'Target Att.' and 'Absorption' are the uncertainties due to the absorption of particles in the target and other materials, respectively, 'nucl. A' represents mainly nucleons interacting in material that is not carbon, and 'Other' includes any other interactions. Right: Beam geometry and focusing uncertainties modified from Ref [173]. 'Baffle Scraping' represents the uncertainty on the tails of the proton beam interacting with the baffle.

absorption of particles in beamline materials as described in detail in Ref. [163]. Uncertainties from each of these datasets are incorporated in the hadron production correction reweight of the base simulation. For interactions with no available data, the uncertainty is evaluated using the spread of various hadronic models in GEANT4.

The hadron production uncertainties are then propagated to the (anti)neutrino energy distribution using a so-called multiverse method [174]. A collection of 100 flux predictions, referred to as universes, is created by randomly sampling from a multidimensional Gaussian distribution centred on the default parameter values of hadron production cross-sections varied within their uncertainties and taking into account correlations between the parameters. The spread of the universes in each bin provides the *a priori* flux uncertainties arising from the hadron production, as depicted in Figure 3.4 for the NuMI beam in medium energy.

Furthermore, PPFX also enables the implementation of uncertainties arising from beamline instrumentation, such as the position of the target relative to the horn, the current applied to the magnetic horns, or the residual water layer on horns due to cooling. These uncertainties can be evaluated similarly to the hadron production uncertainties and are also depicted in Figure 3.4 for the NuMI beam in medium energy. Overall, the

flux uncertainty is dominated by hadron production, except in the falling edge of the (anti)neutrino distribution, where focusing uncertainties dominate. Additionally, MINERvA also improves the flux through *in-situ* measurements of processes with known cross-sections, as discussed in Chapter 5.

3.2 MINERvA detector

The MINERvA detector [40] was located approximately 100 metres underground in the MINOS near detector hall and about 1 kilometre away from the graphite target of the NuMI beamline. As shown in Figure 3.5, MINERvA itself was a hexagonal detector made of an inner detector part in black that is mounted within a metal outer detector frame. On the top of the frame, there was an optical readout system in red and blue. The detector design and methods of operations were fundamental in enabling MINERvA to identify and study (anti)neutrino interactions.

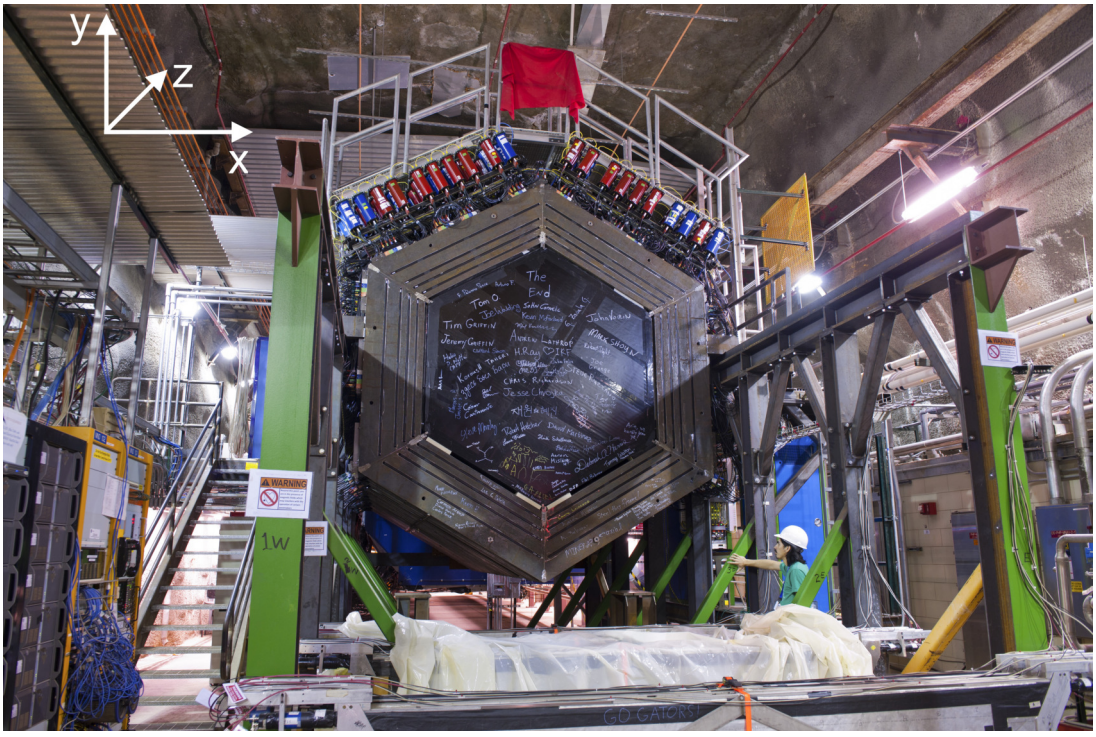

Figure 3.5: Photo of the front view of the MINERvA detector showing the last installed module. The signed black plane is the inner detector, while the metal frame around is the outer detector. The red and blue cylinders on the top of the detector depict the optical readout system. Permission to reuse granted by Fermilab Creative Services. Credit: Reidar Hahn, Fermilab.

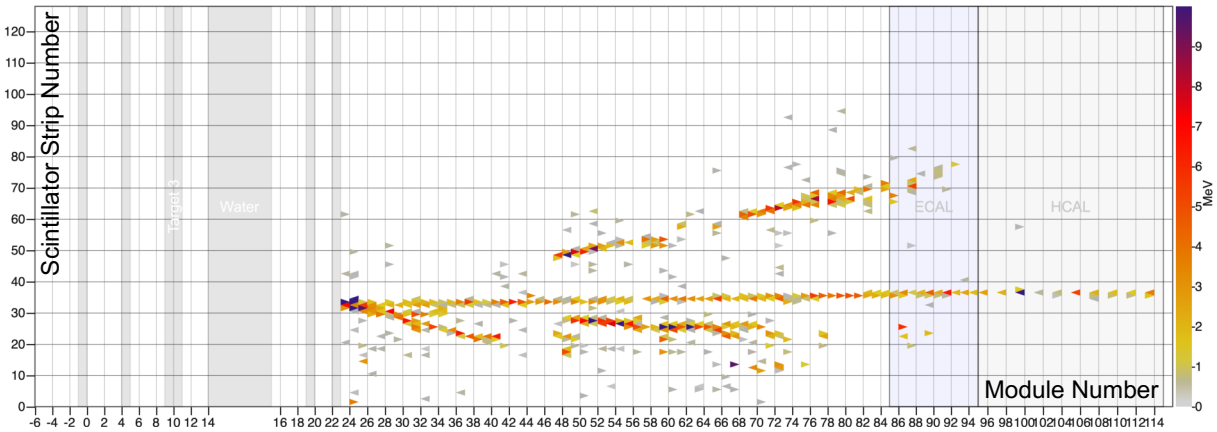

Figure 3.6: Simulated antineutrino deep inelastic scattering (DIS) interaction in the MINERvA detector, producing an antimuon (the longest track) and multiple hadron showers. The individual triangles are the energy deposits, with their colour representing the size of the deposit. The x-axis depicts the detector module number along the general direction of the beam.

Akin to other particle detectors, MINERvA worked like a very fast camera, capturing 'snapshots' in both space and time of the energy deposited in the detector by particles resulting from interactions between (anti)neutrinos and the detector material. An example of such a 'snapshot', referred to as an event, is shown in Figure 3.6. MINERvA's detection capability depended on two key elements: first, the use of finely segmented solid plastic scintillator technology for the active regions, enabling the measurement of energy deposits; and second, fast timing resolution (∼5 ns) to distinguish overlapping events within a single spill, determining how quickly and frequently MINERvA could capture these 'snapshots'.

MINERvA used a right-handed coordinate system with an origin at the centre of the detector, which is superimposed on the front view of the detector in Figure 3.5. In this system, the z-axis pointed downstream along the central axis of the detector, y-axis was pointed upwards, and the x-axis was directed to the left from the perspective of the beam. The (anti)neutrino beam itself, therefore, pointed 3.34° downwards in the y-z plane.

Figure 3.7 shows a schematic of the complete side view of the detector. As depicted, the upstream part of the inner detector consisted of the nuclear target region including carbon, iron, lead and water interleaved between the plastic scintillator planes, enabling the study of nuclear effects in (anti)neutrino interactions. The main fiducial volume comprised the central tracking region, composed purely of finely segmented plastic scintillator planes to resolve and identify multi-particle final states, as well as track low-energy particles with energies greater than about 100 MeV.

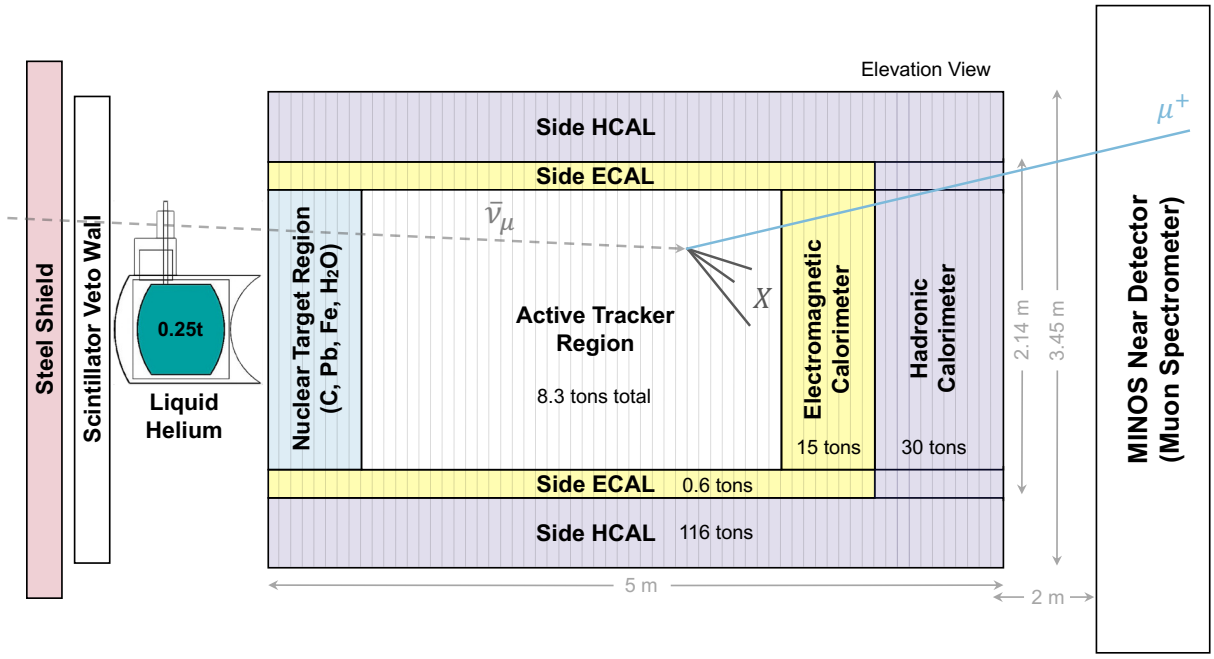

Figure 3.7: Schematic side view of the MINERvA detector. Modified from Ref. [40].

To contain electromagnetic showers and high-energy hadronic final states in the direction of the beam, the tracker was followed by alternating layers of lead–scintillator and steel–scintillator in the sampling electromagnetic (ECAL) and hadronic calorimeter (HCAL), respectively. Additionally, the outermost 15 cm of each ID plane was covered with lead sheets to reduce the amount of energy leaving the ID in the x-y plane, forming the side ECAL. For full containment and also acting as a support structure, the ID was surrounded by the outer detector (OD) steel hadronic calorimeter with four embedded scintillator strips visible in Figure 3.5.

MINERvA was able to tag the highly-energetic rock muons before they entered the detector and reject low-energy hadrons produced in the rock using a veto wall upstream of the main detector, consisting of a steel shield and scintillator. Between the veto wall and the front face of the main body of the detector, there was a liquid helium target in an aluminium cryostat, offering opportunities to measure (anti)neutrino interactions with somewhat less complicated and more easily predicted nuclear effects than heavier targets. The MINOS near detector, located downstream of the main MINERvA detector, functioned as a spectrometer for (anti)muons that were not contained within the MINERvA detector. This is further discussed in Section 3.4.

3.2.1 Scintillator planes

Each hexagonal plane of the ID was made of 127 triangular solid scintillator strips of variable lengths of $\mathcal{O}(1\text{ m})$ stacked in the x-y coordinate plane. Depending on the arrangement of the strips, there were three possible plane orientations, X, U, and V, referred to as views, which are illustrated in Figure 3.8. The X-view consisted of scintillator strips running in parallel to the y-axis, whereas U- and V-view had strip arrangement rotated 60° clockwise and anticlockwise from the X-view, respectively. Figure 3.8 also shows the stacking of different views in the detector, where each X-view is alternately followed by either a U- or V-view. A so-called tracking module is formed by two planes, either XU or XV. Although typically only two orthogonal planes (along with the time dimension) are required for three-dimensional reconstruction, the three different views provided an opportunity to mitigate potential ambiguities in reconstructed hit associations seen when multiple tracks traverse two orthogonal planes.

The individual scintillator strips, primarily made of doped polystyrene, i.e. hydrocarbon (CH), were glued and sealed together with opaque epoxy to prevent light leaks. Additionally, polycarbonate sheets were applied to enhance the overall rigidity of the assembly. Each scintillator strip was also coated by reflective titanium dioxide for optical isolation. Figure 3.8 demonstrates that the triangular strips were overlaid in such a way that a charged particle passing through a plane would deposit energy and hence create

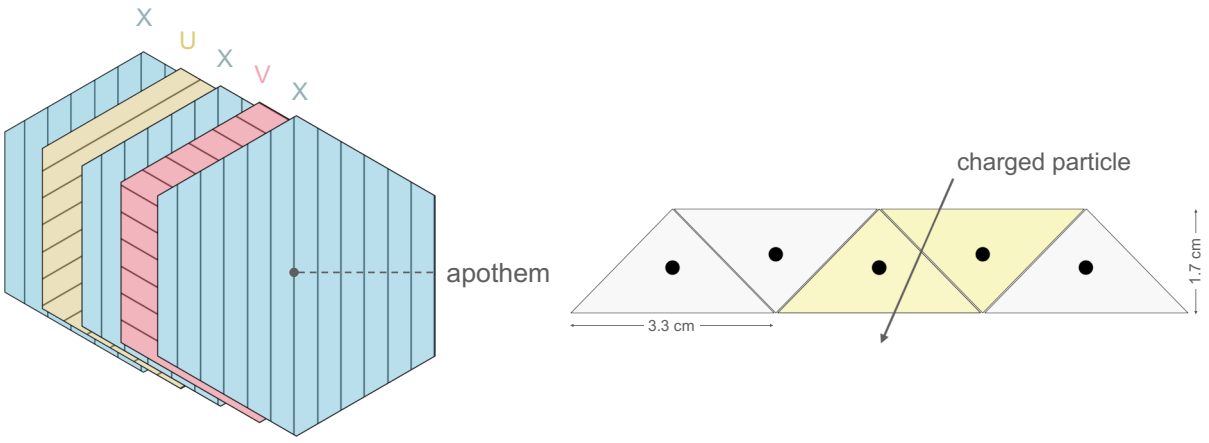

Figure 3.8: Left: Diagram of the three views of scintillator planes and their stacking in the detector. Right: Cross-section of the configuration of triangular scintillator strips, i.e. bars, making up one scintillator plane, showing the impact of a charged particle passing through.

a scintillation signal, i.e. blue light, in at least two scintillator strips. The scintillation light was collected via wavelength-shifting fibres at the centre of each strip, as further discussed in Section 3.2.3.

Note that in contrast to the ID, the scintillator strips embedded in the OD were rectangular with bigger cross-sections.

3.2.2 Nuclear target region

MINERvA's unique capability to perform self-contained measurements of nuclear dependence in (anti)neutrino scattering stems from the nuclear target region. It was composed of five solid passive, i.e. not instrumented, targets made of transverse segments of carbon (C), iron (Fe), and lead (Pb), interlaid with tracking modules (made of two scintillator planes each) as depicted in Figure 3.9. While the geometry of the individual targets may seem complex, it, for example, allowed for the investigation of acceptance differences at various regions of the detector due to the MINOS near detector acceptance constraint discussed later on in Section 3.4. Furthermore, the patterns were chosen so that (anti)neutrinos that did not interact within the nuclear target region would traverse approximately the same amount of material throughout the target region, irrespective of their trajectory in the y-z plane.

Figure 3.9 also shows the geometrical division of the individual target planes into different materials as visible when looking downstream of the detector. Both targets 1 and 2 were composed of roughly 60% iron and 40% lead in terms of fiducial area, with a plane thickness of about 2.6 cm (about one tracking module). However, they contained nearly the same amount of fiducial mass of iron and lead. The orientation of iron and lead in target 2 was flipped horizontally, i.e. reflected around the y-axis, with respect to target 1. As the most upstream target, target 1 was affected by a limited number of upstream tracking planes used to identify particles produced outside the MINERvA detector, particularly the rock muons. This aspect is relevant in the context of this work's measurement discussed later in Section 7.1.

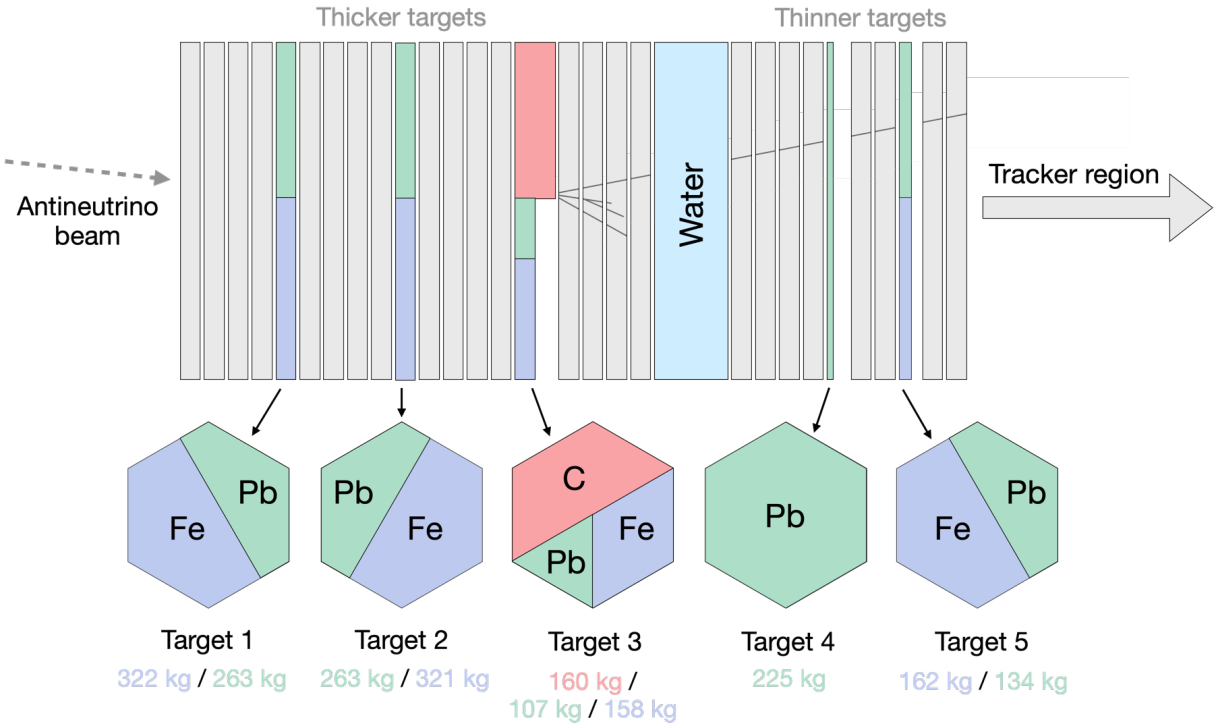

Figure 3.9: Diagram of the nuclear target region in the MINERvA detector. The individual target cross-sections are depicted looking downstream of the detector. The fiducial mass information was taken from Ref. [40].

Target 3 consisted of 50% carbon, approximately 33% iron and 17% lead, i.e. 1/3 iron and 1/6 lead, respectively, allowing for detailed studies of nuclear dependence in (anti)neutrino scattering within one target. The carbon provided valuable cross-validation for the (anti)neutrino interaction cross-sections in plastic scintillator (hydrocarbon) and vice versa, as they are expected to be approximately the same. In general, (hydro)carbon data was crucial for comparison with results from other experiments such as T2K [35]. Target 3 was the thickest of all the solid targets to ensure sufficient fiducial mass for the light carbon. The iron and lead parts had the same thickness as in targets 1 and 2, while the carbon component was about 7.6 cm thick. All materials were aligned at the upstream end, resulting in an air gap downstream of the iron and lead components.

Target 4, the thinnest in the series (comprising less than 1/3 of a tracker module), was constructed using pure lead to ensure the conversion of any produced photons from either upstream or downstream targets. The chosen thickness, approximately 1.5 radiation lengths, allowed photons to initiate a shower but not enough to be fully contained.

This strategy improved event containment in the upstream targets and concurrently reduced noise from photons (or π^0s and neutrons), minimising potential confusion in tracker reconstruction and event selection. Its reduced thickness resulted in an air gap between the target and the first downstream scintillator plane.

Target 5, located directly upstream of the fully active tracking region, had the same shape as target 1 but only half of its thickness (about half of a tracker module). It was designed for the study of lower-energy particles and particle multiplicities, benefiting from enhanced tracking and energy resolution. Similar to targets 3 and 4, there was an air gap between target 5 and the following tracker module, which also allowed for better spatial separation of low-energy final state particles.

Placing thicker targets upstream was done to minimise interference with particles resulting from interactions in downstream targets, thereby optimising the reconstruction of (anti)neutrino interactions and their exclusive final states.

In addition, there was a water target located between the solid targets 3 and 4. It consisted of a circular neoprene balloon filled with (liquid) water suspended on a circular steel frame and held in place with sheets made of polyamide synthetic fibre. The water target thickness varied between 17 cm at the edge of the balloon to 24 cm at the centre of the balloon, with the water volume measured when the target was emptied. The water target is not included in this work's measurement, similar to the helium target described earlier.

In general, each target was separated by four tracking modules, except target 4 and target 5, which were separated by only two tracking modules. Figure 3.9 demonstrates how the active layers between the targets enabled the identification of the location of (anti)neutrino interactions and tracking of final state particles.

3.2.3 Optical readout and data acquisition

A wavelength-shifting (WLS) fibre embedded in the centre of each scintillator strip absorbed the produced blue scintillation light, re-emitting it inside the fibre as green. The WLS fibres then directed the light out of the detector, connecting to clear optical fibres.

The shifted green light was reflected internally within the fibre as it travelled, minimising the signal reduction, while the end of the fibre not pointed towards the readout system was mirrored to reflect the light back.

The clear optical fibres from adjacent scintillator strips were grouped in sets of eight. Eight sets of these optical fibre groups were connected to one photomultiplier tube (PMT) with 64 channels, i.e., an 8×8 array of pixels, which converted the collected light into charge. The fibres were interleaved in such a way that the light signal from adjacent scintillator strips did not go into adjacent pixels of the PMT to prevent signal cross-talk. The PMT converted collected photons into photoelectrons via the photoelectric effect on its photocathode, wherein light incident on a metal surface with energy above the material's binding energy ejected electrons. Subsequently, the electrons were multiplied going through a chain of dynodes with high potential differences between succeeding dynodes. Electrons collided with each anode, producing more electrons, which eventually reached the anode end of the tube, resulting in a sharp current pulse that was easily measurable.

MINERvA had about ∼500 PMTs totalling approximately 32 000 channels. Each PMT was enclosed in a light-tight cylindrical steel enclosure visible on top of the detector in Figure 3.5. Each PMT was read out by one front-end board (FEB), which performed the timing and pulse-height signal digitisation, so-called time-to-digital (TDC) and analog-to-digital (ADC) conversion. MINERvA's readout was synchronised with the NuMI beam spill timing. The readout window, referred to as the gate, was 16 μs long, starting 0.5 μs before the beam spill and adding an extra 5.5 μs after the beam arrived to include delayed activity from (anti)neutrino-produced meson decays. MINERvA also triggered on beam-off data every ∼1500 beam spills to measure the beam-off background and calibrate the detector. Note that channels had a 20 ns long reset time after being fired, rendering them essentially dead to any incoming signals. A full description of the MINERvA data acquisition (DAQ) system can be found in Ref. [175].

3.3 Calibration

A detector calibration allowed retrieving information from the ADC and TDC counts obtained from the DAQ system needed for further physical interpretation. For example, the ADC counts represented energy deposits but were essentially only digits without proper conversion to energy. Calibration also addressed various effects that could introduce biases to these conversions. MINERvA, therefore, calibrated the various detector components both *ex-situ* prior to installation in the detector and *in-situ* during its run, as described in detail in Ref. [40].

In order to be able to convert ADC counts back to charge in reconstruction, all FEBs were bench-tested outside the detector using the same (known) charge injection, producing a response correction factor for each of the FEBs. Furthermore, the attenuation differences of the WLS fibres in different parts of the scintillator strip were measured *ex-situ* using radioactive sources, resulting in attenuation corrections as a function of the position of the energy deposit.

In-situ calibrations were necessary to characterise time-dependent effects. The pedestal ADC count, originating from the inherent background noise levels of the readout electronics and PMTs, as well as background detector activity (such as cosmic rays and radioactivity), was measured during beam-off triggers roughly twice a day. In addition, the photoelectron multiplication strength, known as gain, of the PMTs was measured using a light injection system with a constant light source between each NuMI spill. This calibration process aimed to account for gain variation due to PMT ageing.

During the detector run, numerous MINERvA calibrations also made use of rock muons. Muons, being minimum ionising particles, generally exhibit a consistent and well-understood energy deposition pattern in a detector. For example, rock muon tracks were used to identify dead strips in the detector, or to correct for variations in light yields between different scintillator strips, ensuring a uniform energy response throughout the detector. Rock muons were also instrumental in correcting the absolute energy scale of the detector by comparing muon peak energy deposits in both data and simulation.

This correction factor, derived from the data-to-simulation ratio, evolved over time to compensate for scintillator and WLS fibre ageing.

Finally, timing information was calibrated to account for the finite time it took for light to travel from the detector to the PMT, considering the length of the optical fibre. Additionally, a rock muon sample enabled the correction of time slewing caused by scintillator decay times, which are dependent on energy deposits, and any remaining channel-to-channel offsets between FEBs.

3.4 MINOS near detector

While the design of the MINERvA detector allowed for tracking low-energy charged particles, the majority of GeV-scaled (anti)muons produced in charged-current interactions were not contained within the detector. Therefore, the physics program of the MINERvA experiment relied on the MINOS near detector shown in Figure 3.10 [177], which was positioned 2 metres downstream of the MINERvA detector's hadron calorimeter. Crucially, although somewhat similar in design to the MINERvA HCAL, the MINOS near detector was magnetised, i.e. acting as (anti)muon spectrometer. This

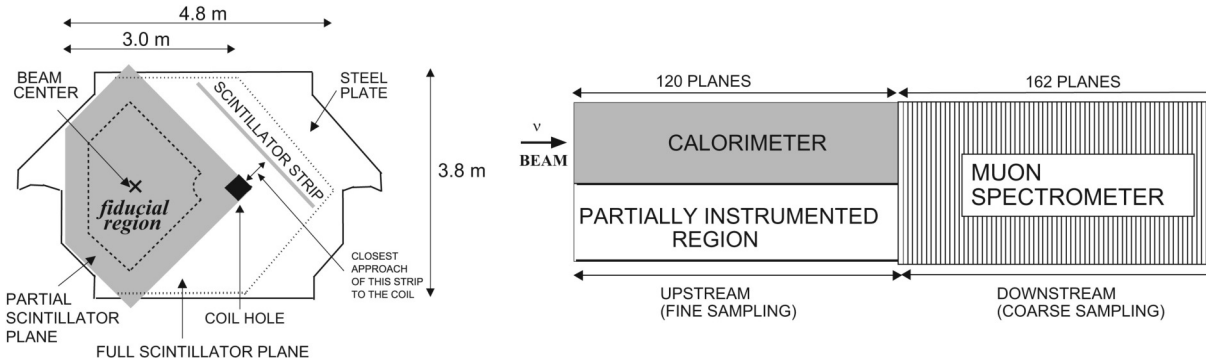

Figure 3.10: Schematic view of the MINOS near detector. Left: Transverse view of the plane configuration looking downstream. The shaded area shows a partially instrumented active scintillator plane while the dotted line shows the outline of a fully instrumented scintillator plane. The black square represents the coil hole. Right: Top view of the MINOS near detector showing the partially instrumented calorimeter region and the muon spectrometer. Note that the partially instrumented region has a full coverage every fifth plane (like the muon spectrometer). Reprinted with permission from the MINOS collaboration [176]. Copyright (2024) by the American Physical Society.

setup enabled precise momentum reconstruction of (anti)muons exiting the MINERvA detector volume in the forward direction.

The MINOS near detector [177] was a sampling calorimeter consisting of alternating planes of magnetised steel and segmented plastic scintillator, oriented in two different views to enable 3D reconstruction. The toroidal magnetic field of approximately 1.3 T was generated by a current-carrying coil spanning the entire length of the detector, as depicted in Figure 3.10. Surrounding the coil, there was also a small region without the scintillator rendering this region effectively dead, which is not shown in the schematic. This aspect motivates part of the selection in this measurement, as discussed later on in Chapter 7. The optical readout system used the same PMTs as MINERvA.

As a charged particle—whether it be an antimuon or a muon, aligning with MINERvA's scope of interest—travelled through MINOS, it was deflected by the magnetic field. The momentum of the (anti)muon was then determined using the range and curvature of the track, while the direction of the curvature was used to specify its charge, i.e. whether it was a muon or an antimuon [178]. In the context of this work, the latter is important for background removal from neutrinos produced in the antineutrino-dominated beam mode. A more detailed discussion about the reconstruction by range and curvature is included in Chapter 6.

Considering the position and transverse dimensions of the MINOS detector relative to the MINERvA detector, the angular coverage of (anti)muons was constrained. Specifically, (anti)muons generated as far upstream as the nuclear target region relevant for this measurement were reconstructed only if they were produced within a maximum angle of 17° relative to the beam. This is later demonstrated in Section 7.4.

Chapter 4

Nuclear dependence of antineutrino cross-section

This thesis presents the first high-statistics simultaneous measurement of charged-current inclusive muon antineutrino differential cross-sections on carbon, hydrocarbon, iron, and lead as a function of antimuon transverse momentum, p_{T}, and Bjorken x. Inclusive analysis, in this case, refers to an analysis considering all final states, i.e. all antineutrino interaction modes. The measurement uses data taken by the MINERvA experiment with peak antineutrino energy of $\sim$6 GeV, and it is kinematically constrained by the detector's acceptance to antimuon angles less than 17 degrees relative to the antineutrino beam, and antimuon energies between 2–20 GeV due to our limited understanding of flux modelling at higher energies. This measurement enables a direct comparison of the impact of nuclear effects in antineutrino scattering since the cross-sections are extracted employing identical techniques within the same detector and with the same antineutrino beam. Additionally, this measurement expands the antineutrino datasets, which are crucial for studying CP violation.

This chapter focuses on the specific motivation for such measurement, as well as the general process of extracting the cross-section in the variables of interest. Subsequent chapters detail the data and simulation sample, their reconstruction, and the analysis procedure itself.

4.1 Motivation for the measurement

In 2014, MINERvA presented its first EMC-like measurement of inclusive charged-current neutrino scattering on carbon, hydrocarbon, iron and lead taken during the low-energy regime with peak neutrino energy of ∼3 GeV [179]. The cross-section ratios of iron-to-hydrocarbon and lead-to-hydrocarbon as a function of reconstructed Bjorken x are shown in Figure 4.1, exhibiting relative depletion at low x and enhancement at large x, neither of which are predicted by the simulation prediction. These discrepancies increase with the size of the nucleus. At low x, the result suggested that the shadowing model based on charged-lepton scattering used in the prediction does not capture the shadowing in neutrino scattering well, and larger suppression may be required. The disagreement at high x was ascribed to the omission of multi-nucleon processes such as 2p2h in the simulation prediction.

At the time, a similar analysis for inclusive antineutrino cross-section on different nuclear targets was impossible due to low statistics of antineutrino interactions in the low-energy sample. However, as a result of the long period of antineutrino operation of the NuMI beam in medium energy, MINERvA collected a high-statistics sample of antineutrino interactions that enables such investigation. Furthermore, the underlying simulation used in the measurement has undergone several improvements such as including

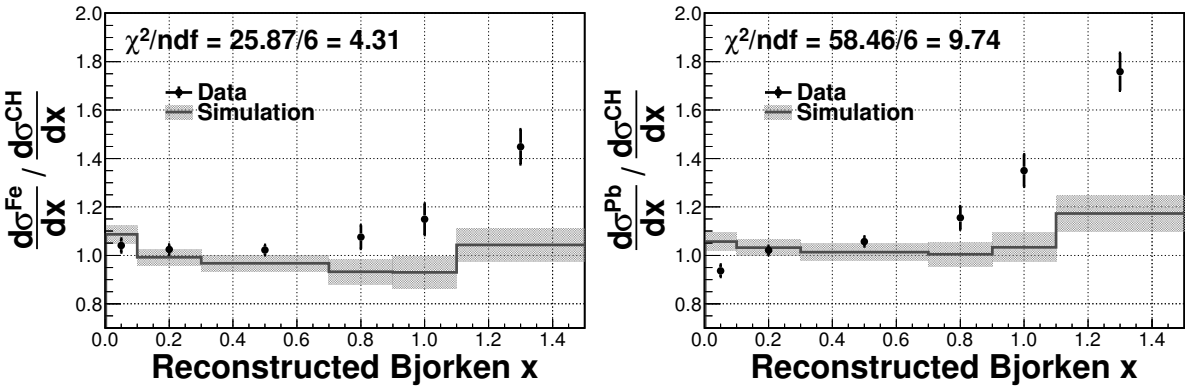

Figure 4.1: MINERvA's measurement of iron-to-hydrocarbon (left) and lead-to-hydrocarbon (right) ratios of inclusive charged-current neutrino cross-sections per nucleon as a function of reconstructed Bjorken x. Reprinted with permission from Ref. [179]. Copyright (2024) by the American Physical Society.

the multi-nucleon scattering, possibly impacting the prediction for the high x region. The full description of the simulation prediction used in the measurement presented in this thesis is included in Chapter 5. In addition, this analysis also benefits from improvements in the reconstruction of the interaction vertex crucial for distinguishing on which nucleus the interaction occurred, which are further elaborated on in Chapter 6.

Notably, the 2014 neutrino analysis was also reported in terms of the reconstructed Bjorken x due to the inability to deconvolute the detector effects from the measurement [154]. Thanks to improvements in interaction modelling, reconstruction techniques, increased statistics in the sample, and rigorous unfolding studies (detailed in Section 7.3), this medium-energy antineutrino analysis can now estimate the cross-section in terms of the true Bjorken x. This allows for reporting a detector-independent cross-section, valuable for interpretation in the context of various theoretical and phenomenological studies, as well as for comparisons with results from other experiments.

Furthermore, motivated by the observation of an SRC plateau at $x > 1$ in electron scattering data in Figure 2.7, this analysis also attempts to make the first such measurement in antineutrino scattering on different nuclei. The expectation is that the antineutrino could scatter from two correlated nucleons, probing the structure of deeply bound nucleons. However, the measurement in this region is limited by the available models of scattering off correlated nucleons in the underlying simulation. The results are also reported in terms of the well-reconstructed antimuon transverse momentum p_{T}, which can be related to the four-momentum transfer in the interaction, as demonstrated in Section 4.3.

Due to the kinematic phase space spanned by the MINERvA medium energy dataset, the measurement presented in this work is predicted to be dominated by the resonant pion production, deep inelastic scattering, and the transition region between these two interaction modes, i.e. the shallow inelastic scattering. Understanding the (anti)neutrino interactions and the nuclear effects in this energy regime is particularly important for the future oscillation experiment DUNE [38]. This is demonstrated in Figure 4.2 showing the expected antineutrino flux seen by the DUNE near detector compared to the MINERvA

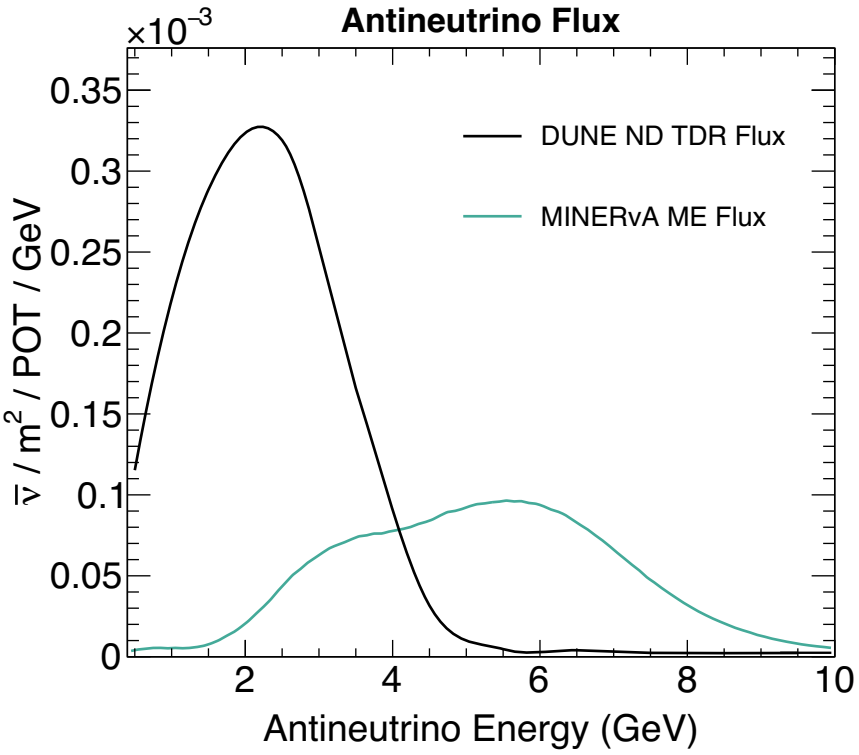

Figure 4.2: Comparison of the expected antineutrino flux at the DUNE near detector (ND) according to ND Technical Design Report (TDR) [38] and the MINERvA medium energy antineutrino flux in the 0–10 GeV range of antineutrino energy. Note the significant overlap at the upper end of DUNE antineutrino energy.

medium energy antineutrino flux utilised in this analysis, with a significant overlap corresponding to the energies where these higher-energy interaction modes are expected (cf. Figure 2.1 in Chapter 2).

Importantly, the (anti)neutrino scattering in DUNE will occur primarily on argon [38]. While experiments measuring (anti)neutrino cross-sections on argon exist, e.g. MicroBooNE [180], they generally probe lower-energy regions dominated by the quasi-elastic scattering. MINERvA is the only experiment that can provide direct high-statistics measurements of nuclear dependence across various nuclei in the kinematic regime dominated by these higher-energy interaction modes. Therefore, MINERvA measurements, including this one, are crucial for refining our understanding and modelling of the impact that nuclear effects have on these interaction modes, enabling the interpolation to interactions on argon. The NOvA experiment [153] is also able to study these interaction channels at slightly lower energies but on a scintillator only.

More generally, this antineutrino measurement also expands the available antineutrino datasets in the energy regime relevant to the oscillation experiments, aiding in the improvements of antineutrino interaction modelling necessary for CP violation searches. Interactions of neutrinos and antineutrinos with nuclei need to be studied separately as they are not identical but differ by the sign of the axial-vector interference term [181], as discussed in Chapter 2. However, large antineutrino datasets are somewhat rare compared to their neutrino counterparts [28], primarily due to the extended time required for collecting antineutrino scattering data. This stems from the production process of the antineutrino beam, where negatively charged pions (that decay to antineutrinos) are less likely to be produced from the protons-carbon interactions [150]. Additionally, antineutrino cross-sections are lower than those for neutrinos, as shown in Figure 2.1.

Most of the available charged-current antineutrino datasets primarily probe the quasi-elastic interaction region, either exclusively or as the dominant channel. These measurements are reported by experiments such as T2K [182–184], MiniBooNE [185], NINJA [186], and MINERvA [60]. The other major group of antineutrino measurements explores the high-energy deep inelastic region, as seen in datasets from IHEP-ITEP [187], IHEP-JINR [188], CDHSW [92], NuTeV [94], and CCFR [93]. An antineutrino cross-section measurement spanning a similar energy regime as this analysis has been reported, for example, for iron by the MINOS collaboration [176]. In comparison, the analysis presented in this work has about 10× more events in its most statistically significant sample on hydrocarbon and approximately the same number of events on iron. Low-statistics measurements on argon at energies dominated by the resonant pion production have also been reported by ArgoNeuT [189, 190]. To date, the analysis presented in this thesis is the largest antineutrino dataset analysed by MINERvA, and it is among the largest antineutrino datasets available in this energy regime.

Finally, due to the dominant contribution from the single-pion production channel, this analysis enables an inclusive investigation of the behaviour observed in MINERvA's measurement of neutrino-induced single-pion production (CC1π^+) across various nuclei [191], as depicted in Figure 4.3, but in the antineutrino mode. The CC1π^+ meas-

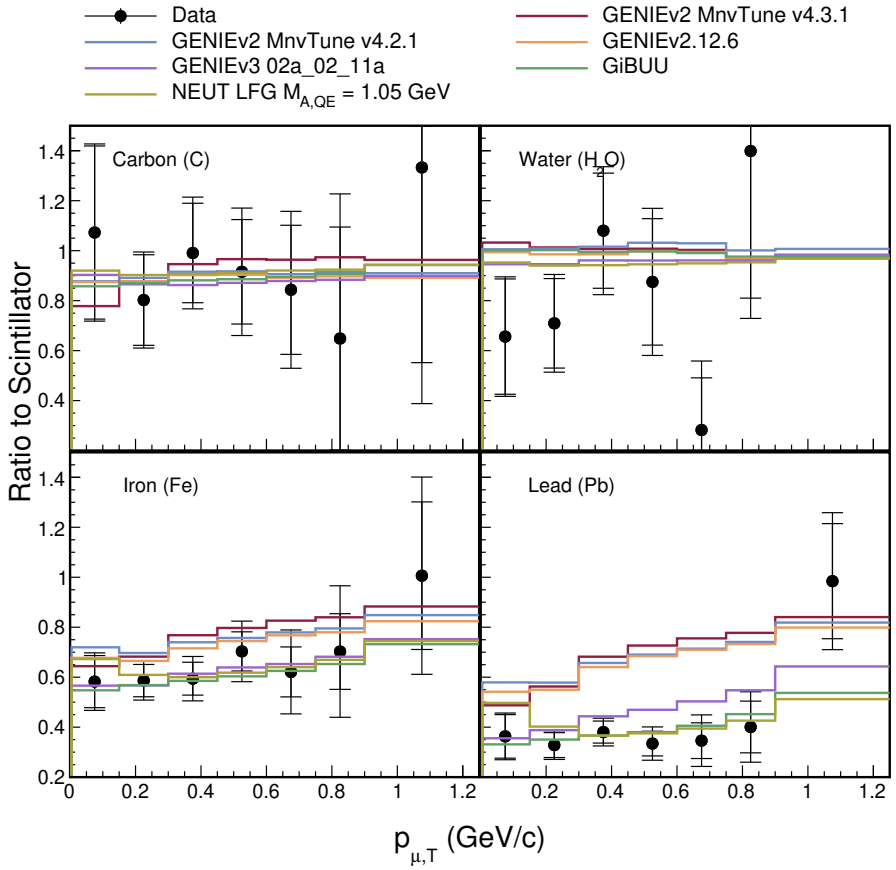

Figure 4.3: MINERvA measurement of cross-section ratios for carbon, water, iron, and lead to the scintillator, i.e. hydrocarbon, for neutrino-induced charged-current single π^+ production in medium energy as a function of muon transverse momentum p_{T} compared to various neutrino simulation predictions. Note that all of them are discrepant for either one or more nuclei with data showing low p_{T} ($\sim Q^2$) suppression increasing with the size of the nucleus compared to the underlying simulation indicated by GENIEv2 MnvTune v4.3.1. Reprinted with permission from Ref. [191]. Copyright (2024) by the American Physical Society.

urement demonstrated a need for strong suppression at low p_{T}, an observable related to the four-momentum transfer squared, Q^2, increasing as the size of the target nucleus increases. This prompted the derivation of weights applied to the underlying MINERvA prediction based on the scintillator measurement, assuming that the suppression originates from interactions within the nucleus, ultimately improving the agreement with the data. The analysis presented in this work tests the applicability of these weights via isospin symmetry for the production of single π^- (consisting of an anti-up quark and a down quark instead of an up quark and an anti-down quark) in final states.

4.2 How to measure the cross-section

The probability that a certain interaction process occurs is parameterised as a cross-section and can be thought of as the effective area subtended by the target particle to an incident beam [192]. This measurement reports flux-integrated differential cross-sections per nucleon on particular nuclei, namely carbon, hydrocarbon, iron, and lead. The cross-section distributions are discretised into a finite number of bins of a quantity of interest, defined in order to obtain a statistically significant sample in each of them, and are extracted as follows,

$$\left(\frac{d\sigma}{dx}\right)_{\alpha} = \frac{\Sigma_j \tilde{U}_{j\alpha}(N_{\text{data},j} - N^{\text{bkg}}_{\text{data},j})}{\epsilon_\alpha T_{\text{nucleons}} \Phi \Delta x_\alpha \text{POT}} \,. \tag{4.1}$$

In the above, the left-hand side corresponds to the cross-section in bin α with respect to a quantity x. In this analysis, this quantity can either be antimuon transverse momentum p_{T} or Bjorken x. To distinguish between the true value of the variable of interest, in which the final detector-independent cross-section is reported, and its reconstructed value, the bin containing the true value is labelled as α, while the bin containing the reconstructed value is represented by j. The difference between the true bin and the reconstructed bin arises from the complex nature of the antineutrino interactions and the imperfect reconstruction, further explained in the following chapters.

$N_{\text{data},j}$ is the number of reconstructed events of interest in bin j and $N^{\text{bkg}}_{\text{data},j}$ is the estimated number of background events. The background-subtracted selected events correspond to the signal. Therefore, in this analysis, it is the number of all charged-current antineutrino interactions that occurred in a specific target material with certain kinematic constraints discussed in Chapter 7. $\tilde{U}_{j\alpha}$ represents the so-called unfolding process which tries to remove the smearing of the reconstructed distribution to report the cross-section in the true quantities. The efficiency correction, ϵ_α, takes into account the signal events that were lost due to detector acceptance and imperfect reconstruction.

Furthermore, the differential cross-section is normalised to the flux prediction integrated over all bins, Φ, the number of nucleons in a given material, T_{nucleons}, the bin width of the corresponding bin, Δx, to make it differential, and the number of protons on the

target, POT, which is the metric used to characterise the integrated luminosity of the antineutrino beam. Note that all these individual steps of the cross-section extraction are described in detail in Chapter 7.

Finally, similar to the MINERvA analysis in Figure 4.1, the cross-section ratios of the nuclear target (A) to scintillator tracker (CH) are reported to minimise the dependence on the underlying antineutrino flux, as well as to cancel out some shared reconstruction and antineutrino interaction modelling effects. While the cross-section ratios are taken directly from the calculated cross-sections according to Equation 4.1, the ratios approximately correspond to

$$\left(\frac{d\sigma^{\mathrm{A}}}{dx}\Big/\frac{d\sigma^{\mathrm{CH}}}{dx}\right)_{\alpha} \approx \frac{\sum_j \tilde{U}^{\mathrm{A}}_{\alpha j}(N^{\mathrm{A}}_{\mathrm{data},j} - N^{\mathrm{bkg,A}}_{\mathrm{data},j})\epsilon^{\mathrm{CH}}_{\alpha} T^{\mathrm{CH}}}{\sum_k \tilde{U}^{\mathrm{CH}}_{\alpha k}(N^{\mathrm{CH}}_{\mathrm{data},k} - N^{\mathrm{bkg,CH}}_{\mathrm{data},k})\epsilon^{\mathrm{A}}_{\alpha} T^{\mathrm{A}}} \,. \tag{4.2}$$

4.3 Variables of interest

The final cross-section and cross-section ratio results are extracted in terms of the antimuon transverse momentum, p_{T}, and Bjorken x. Observables depending solely on antimuon kinematics, such as p_{T}, are well-reconstructed and allow for comparison of results, which are generally almost independent of the underlying interaction models compared to observables involving recoil information. On the other hand, Bjorken x directly considers hadronic final states and describes the nuclear modifications to a bound nucleon cross-section compared to a free nucleon and can be used to inform PDFs.

Importantly, the antimuon transverse momentum can be directly related to the four-momentum transfer squared, Q^2, as follows

$$Q^2 \approx p_{\mathrm{T}}^2 \left(1 + \mathcal{O}\left(\frac{E_{\mathrm{recoil}}}{E_{\mu}}\right)\right) . \tag{4.3}$$

The interpretation of p_{T} distributions is, therefore, intuitive when it comes to the expected interaction mode dominating in a given p_{T} range. Furthermore, p_{T} serves as a direct proxy to the antimuon angle relative to the antineutrino beam. This is especially helpful when discussing the acceptance of the MINERvA detector in the subsequent chapters.

Bjorken x is a dimensionless quantity that can be interpreted as the fraction of the momentum carried by the struck quark in a frame where the nucleon momentum is very large, as described in Chapter 2. Consequently, at low x, the distribution is expected to be dominated by deep inelastic scattering, while quasi-elastic scattering is expected to occur around $x = 1$. The $x > 1$ region should then consist of events in which the antineutrino scattered off two or more correlated nucleons.

In the context of this measurement, Bjorken x is defined as given in Equation 2.7. Its dependence ultimately comes down to the recoil energy reconstructed in the detector, as well as the momentum and angle of the antimuon. The reconstruction details and their limitations, particularly in the context of reconstructed recoil information, are further described in Chapter 6.

Chapter 5

Data and simulation samples

In this measurement, I use MINERvA data collected during antineutrino-dominated medium energy (ME) physics runs with the antineutrino flux peaked near 6 GeV, recorded between June 29th, 2016 and February 26th, 2019. The measurement utilises the minervame5A, minervame6A–6J 'playlists', which are lists of MINERvA runs and subruns that correspond to a specific detector configuration. This amounts to the total data exposure of 1.12×10^{21} protons on target (POT).

The analysis employs Monte Carlo (MC) simulation to try to describe the underlying antineutrino interaction physics, estimate backgrounds, characterise detector inefficiencies, evaluate systematic uncertainties, and perform various other studies. It corresponds to the detector configuration of the data-taking periods described above. The simulated MC POT is equivalent to more than 4× data POT, i.e. 4.96×10^{21} POT, to reduce the statistical fluctuations in the simulation. In order to compare the simulation to data, the simulation distributions are scaled by the ratio of the data POT to the simulated MC POT, so-called POT-normalised.

The MC encapsulates the simulation of the NuMI antineutrino beam, the antineutrino interactions in the nucleus, the environment of the nucleus itself and how it affects particles exiting it, and the propagation of the final-state particles through the MINERvA detector. For further discussion in Chapter 7, it is important to emphasise that antineutrino interactions are only simulated in the nuclear targets and tracker of the MINERvA detector, excluding the electromagnetic and hadronic calorimeter.

5.1 Flux simulation

The simulation begins with the base antineutrino flux simulation constrained by external hadron production data described in Section 3.1. The flux model in this analysis is further improved by *in-situ* measurements of processes with known cross-sections, specifically the (anti)neutrino-electron elastic scattering [193, 194] and inverse muon decay [195].

The (anti)neutrino-electron elastic scattering, $\nu e^- \rightarrow \nu e^-$, is a well understood, purely leptonic process. Therefore, its cross-section can be predicted to a very high precision using the Standard Model electroweak theory. The (anti)neutrino-electron elastic scattering events are relatively rare with cross-section three orders of magnitude smaller than (anti)neutrino-nucleus scattering. However, due to their distinct experimental signature of very forward electromagnetic showers with no other activity, they can be selected with only a few background events. The discrepancies between the data and MC in the electron energy spectrum can be interpreted as mismodelling of the flux distribution, providing a constraint on the normalisation of the flux and thus the peak of the flux. MINERvA

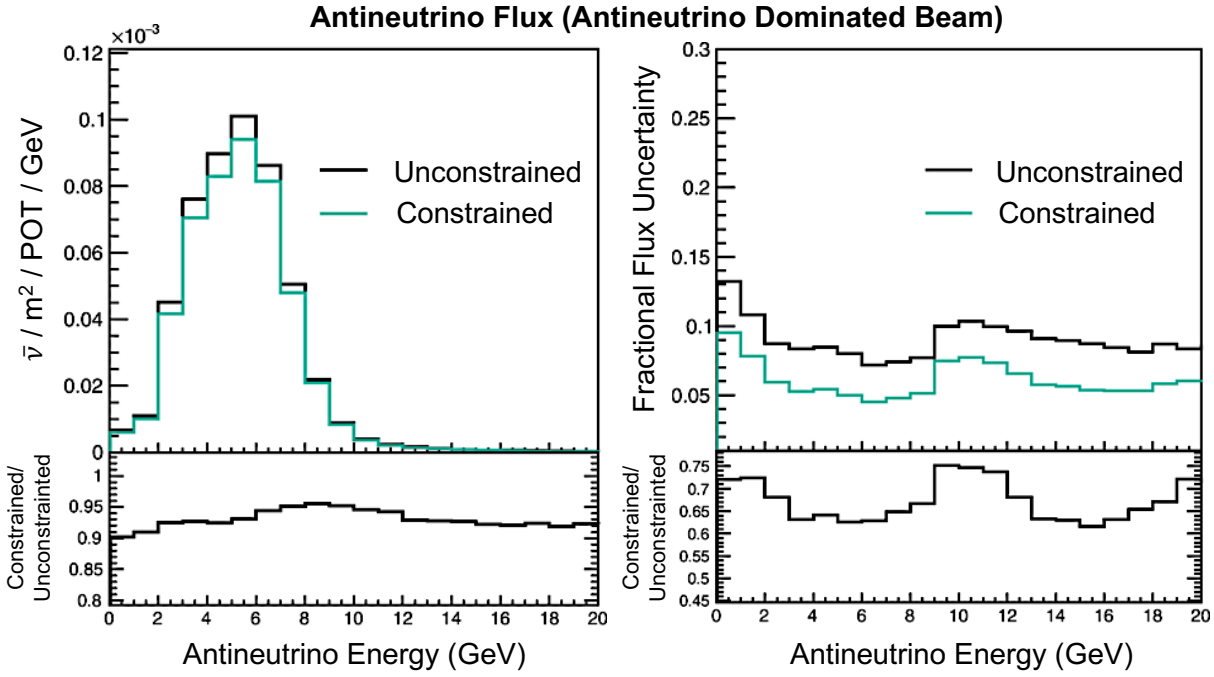

Figure 5.1: Left: Predicted antineutrino flux in bins of antineutrino energy before and after constraining the *a priori* model using the (anti)-neutrino electron scattering and inverse muon decay *in-situ* measurements. Right: Fractional flux uncertainty on the predicted antineutrino flux before and after the constraint. Plots adapted from Ref. [193].

measured the (anti)neutrino-electron elastic scattering electron energy spectra in both ME neutrino and antineutrino dominated beams physics runs [193, 194].

The inverse muon decay (IMD), $\nu_\mu e^- \rightarrow \mu^- \nu_e$, is another leptonic process which was measured by MINERvA in order to constrain the flux [195]. It can be identified by a very forward-going high-energy muon. IMD has (anti)neutrino energy threshold of ≈ 11 GeV. Hence, it provides insight into the high-energy tail of the flux, in which phase space is mostly dominated by (anti)neutrinos produced by underfocused or unfocused K^+ and π^+.

This analysis uses MINERvA's combined flux constraint of (anti)neutrino-electron scattering and IMD [193] whose impact is shown in Figure 5.1. The single normalisation constraint was extracted using Bayes' theorem, where the posterior probability is given by the prior flux prediction multiplied by the likelihood of the electron spectra measurement given the *a priori* model. The *a priori* flux uncertainty is estimated using the multiverse method [174], where an ensemble of flux predictions, so-called universes, is created by varying flux parameters within their uncertainties. The procedure takes into account the correlations between the predictions of the number of events.

The flux simulation is then reweighted by the ratio of the weighted average of post-constraint flux universes to the weighted average of pre-constraint fluxes. The procedure results in predictions from universes with poor data agreement to be weighted down, which reduces the uncertainty (spread of the universes). In antineutrino dominated beam, the antineutrino energy range integrated flux uncertainty is reduced from 7.8% to 4.7% [193] as shown in Figure 5.1 and is further discussed in Chapter 8.

5.1.1 Nuclear target flux

While the antineutrino beam is focused as described in Section 3.1, the transverse distribution of the beam is relatively wide. Additionally, due to the downward pointing of the NuMI beam with respect to MINERvA, this also affects the flux seen by the detector as a function of the longitudinal position. The flux distribution described above provides an accurate representation of the averaged flux in the active tracker region and correctly accounts for these effects. However, the complex geometry of the nuclear target region,

as detailed in Section 3.2, with varying transverse positions of different materials within individual targets, particularly off-centre of the detector and, consequently, off-centre of the beam, is expected to introduce variations in both shape and normalisation of the flux compared to the tracker.

The nuclear target flux differences in the neutrino beam were first taken into consideration in cross-section calculations in Refs. [61, 196] with applied neutrino-electron elastic scattering flux constraint only. To enable flux-independent comparisons between nuclear targets, i.e. the nuclear target-to-scintillator cross-section ratios as discussed in Chapter 4, the procedure in Refs. [61, 196] extracts the scintillator tracker cross-section in different transverse regions of the MINERvA fiducial volume. It is then weighted so that the summed scintillator cross-section has the same effective flux as the target flux.

I extended the procedure to the antineutrino flux with MINERvA's combined flux constraint of (anti)neutrino-electron scattering and IMD, and simultaneously reimplemented the neutrino flux with this new flux constraint as well. The antineutrino fluxes for each nuclear target (or combined nuclear targets of the same material) were calculated, as detailed in Appendix A, using the true information from the simulation.

Figure 5.2 depicts the calculated antineutrino fluxes for the combined nuclear targets used in this work and their ratios to the scintillator tracker flux distribution. Generally,

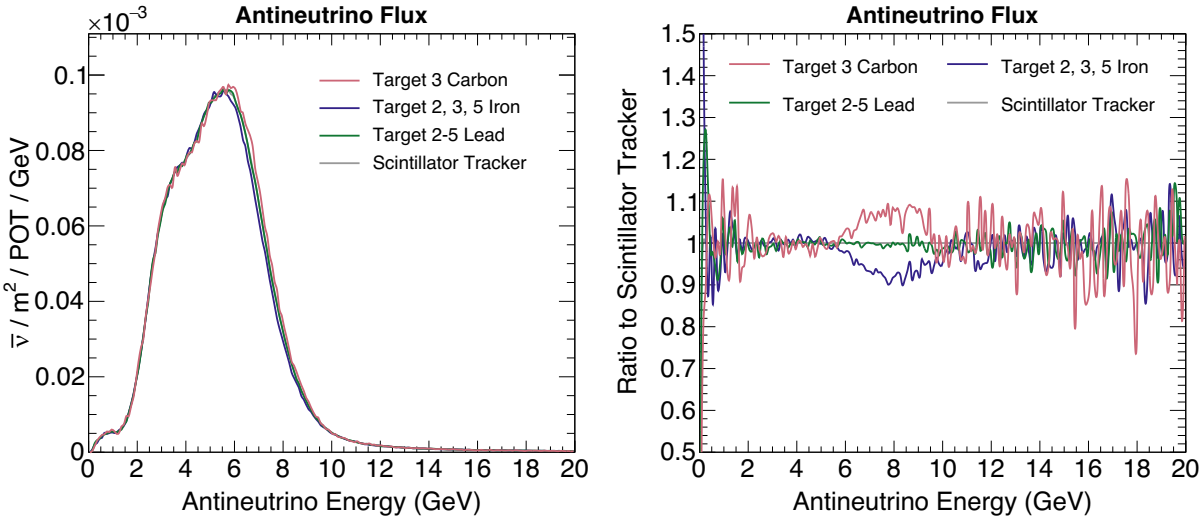

Figure 5.2: Left: Calculated antineutrino flux for carbon, iron, and lead compared to the scintillator tracker flux. Right: Nuclear target-to-scintillator tracker flux ratio illustrating the flux differences in the 6–10 GeV region.

the nuclear target fluxes differ by up to 10% in the 6–10 GeV region (the falling edge of the flux peak). If the average position of the target is above the centre of the beam, as is the case for carbon, the nuclear target flux is higher than that for the scintillator. Conversely, if the average position of the target is below the centre of the beam, as is the case for the combination of iron targets, the nuclear target flux is lower than that for the scintillator. The combination of lead targets has approximately the same centre of mass and shape as the tracker, thus resulting in a flat lead-to-scintillator flux ratio.

Similarly to the nuclear target fluxes, the scintillator tracker flux can be extracted in 12 transverse bins referred to as 'daisy petals', as illustrated in Figure 5.3. A linear combination of these 'daisy petal' fluxes is then taken to create an effective scintillator tracker flux that matches that of the nuclear target combination. The weights for the individual petals are calculated using a regularised χ^2 fit and later applied to the efficiency-corrected 'daisy petal' distributions in the analysis procedure detailed in Chapter 7. Specifics of this so-called 'daisy' reweight technique are also further described in Appendix A.

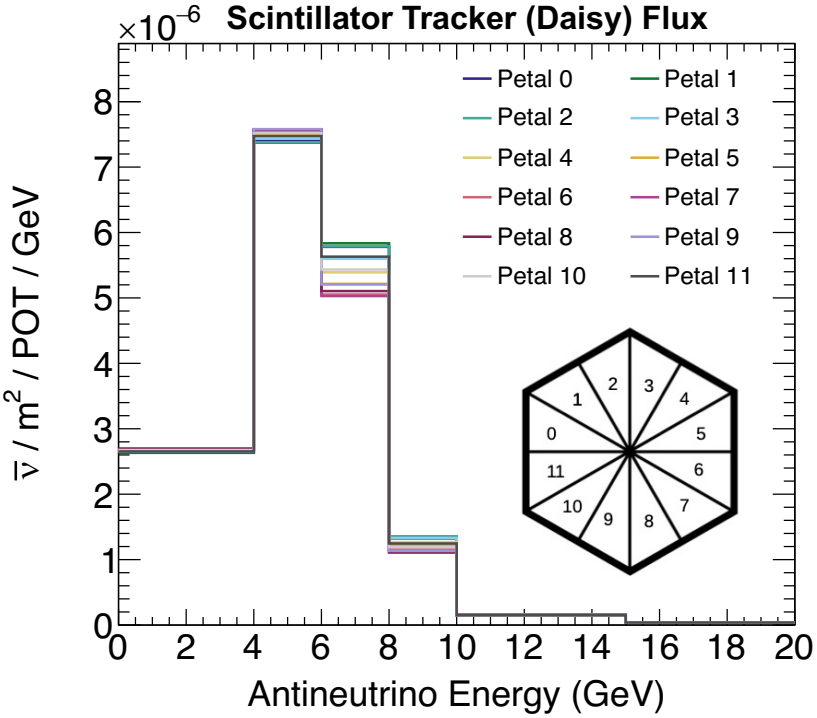

Figure 5.3: Antineutrino scintillator tracker flux for each 'daisy petal' as a function of antineutrino energy. The hexagon insert illustrates petal positions when looking downstream of the detector.

5.2 Antineutrino simulation

MINERvA uses the (anti)neutrino interaction event generator GENIE (Generates Events for Neutrino Interaction Experiments) version 2.12.6 [42,43]. It models how often (anti)neutrinos from NuMI interact with nuclei in MINERvA and what are the underlying interaction physics processes. It also models the nuclear environment of the nucleus and how it affects the initial (anti)neutrino interaction as well as the final-state kinematics, i.e. what particles are produced in the final state. Furthermore, this analysis uses a variety of modifications to the baseline antineutrino simulation to better describe MINERvA data. These are applied as weights to each event, effectively scaling the probability of the event occurring based on the fit to the experimental data.

5.2.1 Nuclear model

As the incoming antineutrino in most cases interacts with the constituents of the nucleus (nucleons or quarks), the simulations need to account for the effects of the nuclear environment. GENIE models the nucleus as a relativistic Fermi gas (RFG) [100], where nucleons are confined to a potential well with walls at the nuclear radius. RFG treats the nucleons within a nucleus as independent particles (so-called impulse approximation). The nucleons inside the nucleus have a nucleus-specific flat momentum distribution between 0 and the Fermi momentum p_{F} in the ground state, determined from inclusive electron scattering, and binding energy E_{B}. The E_{B} refers to the energy needed to separate a bound nucleon from the nucleus.

Because nucleons are fermions, they must obey the Pauli exclusion principle resulting in Pauli blocking. In quasi-elastic interactions, the final-state nucleon has to have momentum above p_{F}, which significantly suppresses the cross-section at low Q^2. To account for short-range correlations between the nucleons, i.e. interactions between the nucleons inside the nucleus, which can lead to a momentum greater than p_{F}, the simulation contains Bodek-Ritchie high-momentum tail [103].

Other nuclear models are relevant in the context of certain antineutrino interaction processes and are discussed below.

5.2.2 Interaction model

As described in Chapter 2, different types of antineutrino interactions occur at different antineutrino energies. Due to the inclusive nature of this analysis, all antineutrino interaction modes contribute to the final cross-section. However, the higher-energy inelastic components such as resonant pion production and deep inelastic scattering will be dominant in the ME sample. The antineutrino interaction model described below will be referred to as MINERvA tune v4.3.0.

Quasi-elastic scattering

Quasi-elastic interactions are simulated using the Llewellyn-Smith formalism [49], which factorises the cross-section as a function of the four-momentum transfer squared, Q^2. The quasi-elastic vector form factors are modelled using the BBBA05 parametrization [50] of the electromagnetic form factors from electron scattering experiments. The axial form factor uses the dipole form with an axial mass of $M_A^{\mathrm{QE}} = 0.99$ GeV/c^2. In addition, MINERvA's low energy low recoil neutrino analysis shown in Figure 5.4 demonstrated suppression of data in the low Q^2 region possibly due to long-range correlations in the nucleus [197]. To address this, MINERvA modifies the baseline simulation as a function of energy and three-momentum transfer based on the random phase approximation (RPA) part of the Valencia model [104, 198].

Multi-nucleon scattering

Multi-nucleon scattering, specifically the 2p2h interaction, is simulated using the Valencia 2p2h model [111,113,200]. However, based on MINERvA's low energy recoil neutrino analysis [197], the cross-section is increased in specific regions of energy and three-momentum transfer as shown in Figure 5.4. This results in 2p2h rate enhancement by 50% over the nominal prediction when integrated over all phase space. Figure 5.4 also shows the equi-

valent analysis in the antineutrino mode [199] and how the 2p2h tune (fit to neutrino data only) naturally improves the simulation prediction for the data.

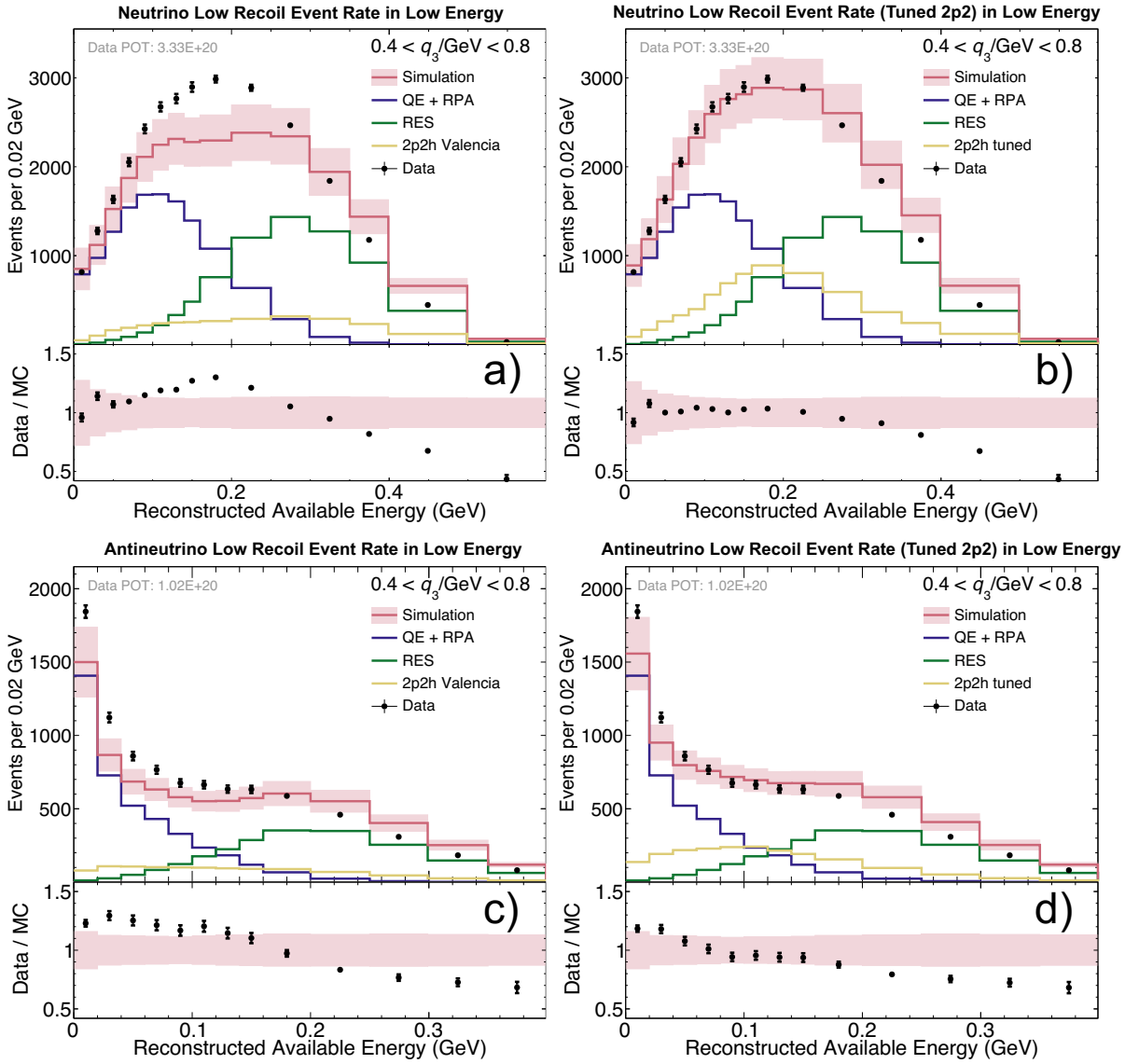

Figure 5.4: MINERvA measurements of neutrino [197] and antineutrino [199] low-recoil scattering in low energy as a function of reconstructed available energy, motivating the addition of RPA and 2p2h modification. Note that the available energy corresponds to the visible recoil energy in the detector. a) Low energy low recoil neutrino comparison of simulated and measured event rate with visible data and simulation discrepancy. b) Improved simulation with enhanced 2p2h events shows better agreement with data. c) Equivalent analysis in antineutrino mode compared to the base simulation. d) Improved simulation in the antineutrino mode using the fit of the 2p2h enhancement from the neutrino mode, i.e. b), also shows better agreement with data. Furthermore, the distributions demonstrate the need for the random phase approximation (RPA) suppression in the quasi-elastic process (QE).

Pion production

GENIE simulates the charged and neutral single pion production via baryon resonances using the Rein-Seghal (RS) model [65] up to the hadronic invariant mass cut of $W = 1.7$ GeV/c^2 [42, 43]. Out of the 18 resonances in the RS model, only 16 are included in GENIE due to $\Delta(1600)$ and $N(1990)$ having ambiguous experimental signatures at the time of implementation [42, 43]. It also does not include interference terms between the resonances and the lepton masses in the cross-section calculation. However, the effect of the latter is taken into account in calculating the phase space limits.

MINERvA reweights its resonant single pion production cross-section based on a reanalysis of the deuterium bubble chamber measurements of single pion production taken by Argonne and Brookhaven National Laboratories (ANL, BNL) [67, 68]. The reanalysis constrained the resonant axial mass to $M_A^{\mathrm{RES}} = 0.94$ GeV/c^2 (from its nominal value of 1.12 GeV/c^2 [42, 43]), and set the resonant normalisation parameter to 1.15 [201].

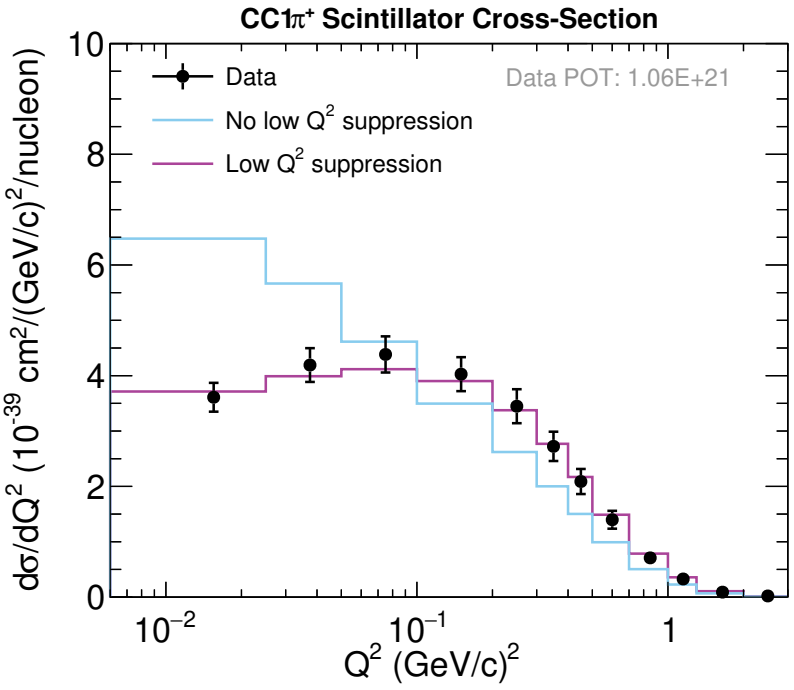

Figure 5.5: Charged-current single pion cross-section measurement on the scintillator (data points) as a function of the four-momentum transfer squared, Q^2, compared to the simulation without and with the low Q^2 suppression. The simulated cross-section with the low Q^2 suppression shows better agreement with the data. Plot uses the medium energy CC1π^+ result [191].

The subdominant process of coherent pion production is simulated in GENIE using the coherent pion RS model [96] including lepton mass terms [72]. It is further reweighted in both energy and the angle of a pion with the highest kinetic energy to agree with MINERvA's recent measurement of coherent pion production [202].

The non-resonant pion production represents part of the transition region between the resonance (RES) and deep inelastic scattering (DIS) depicted in Figure 5.6. In GENIE, it is modelled by the scaled Bodek-Yang model [83, 84] for DIS described later in this section. It is added incoherently to the resonant pion production in the region restricted by the mass of $\Delta^{++}(1232)$ resonance and $W < 1.7$ GeV/c^2 [42, 43]. DIS interactions with resonance-like final states such as 1π and 2π are suppressed to avoid double counting. Additionally, MINERvA reduces the contribution of non-resonant pion production to 43% of its nominal value based on the ANL/BNL data reanalysis [201].

Furthermore, this analysis reweights its single pion production, both resonant and non-resonant, with π^- in final states in the $W < 1.4$ GeV/c^2 region. It applies low Q^2 suppression based on the medium energy charged-current $1\pi^+$ analysis result [191] as shown in Figure 5.5 to events on all nuclei except hydrogen, assuming the suppression comes from interactions in the nucleus.

Deep inelastic scattering

In contrast to the community definition of the DIS kinematic region of $W > 2$ GeV/c^2 and $Q^2 > 1$ (GeV/c)^2, GENIE treats any non-resonant inelastic events as DIS. The antineutrino initially interacts with a single quark which then proceeds to hadronise, resulting in multiple hadrons in the final state.

GENIE's DIS cross-section is calculated at the fully partonic level, accounting for the Bodek-Yang non-perturbative corrections to parton distribution functions (PDFs) as Q^2 decreases [83, 84], such as in the non-resonant pion production transition region described above. The Bodek-Yang model [83, 84] also modifies the nuclear structure functions to incorporate nuclear effects as a function of Bjorken x, reflecting differences between nuclear and free nucleon structure functions, such as shadowing. Specifically,

it utilises the parameterisations of charged lepton DIS measurements of $F_2^{\mathrm{d}}/F_2^{\mathrm{free}}$ and $F_2^{\mathrm{Fe}}/F_2^{\mathrm{d}}$, treating the axial and vector modifications equivalently. The same correction is applied to all nuclei.

The Andreopoulous-Gallagher-Kehayias-Yang (AGKY) model describes the hadronisation process in GENIE [203]. In the AGKY model, the Koba-Nielsen-Olesen (KNO) model [204] is used for the $W_{\mathrm{min}} \leq 2.3$ GeV/c^2 invariant mass, whereas the PYTHIA/JETSET [205] program is utilised in the $W_{\mathrm{max}} > 3.0$ GeV/c^2 region. The transition region $W_{\mathrm{min}} < W \leq W_{\mathrm{max}}$ is smooth as the fraction of PYTHIA hadronised events increases from 0% to 100% (and vice versa for KNO).

The KNO phenomenological model [204] uses an empirical expression tuned to the Fermilab 15-foot bubble chamber neutrino-nucleon data to determine the hadron multiplicity [203]. It selects particle content up to the multiplicity, generally a nucleon and any

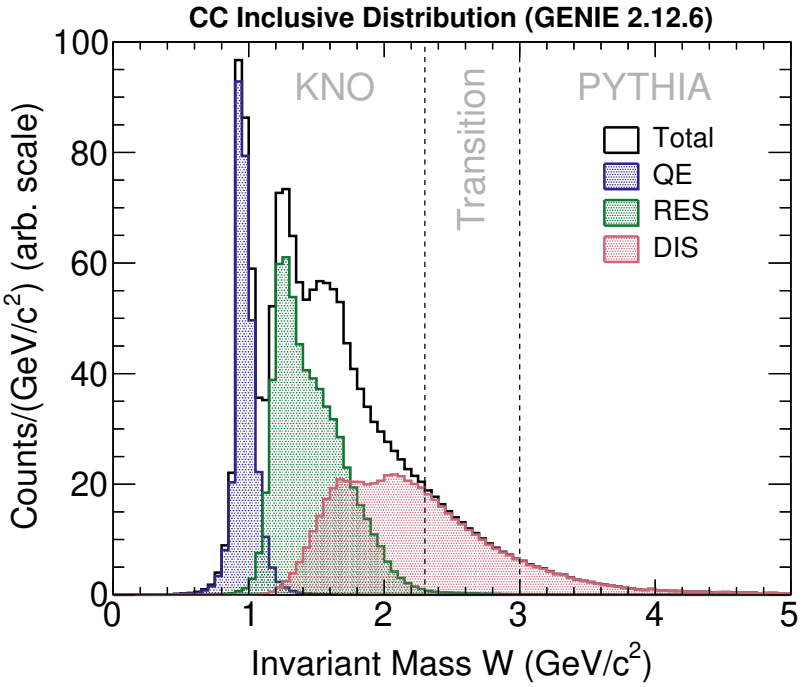

Figure 5.6: Invariant mass distribution W of the charged-current antineutrino inclusive interactions on scintillator in GENIE 2.12.6, using the MINERvA antineutrino flux. The left blue region shows quasi-elastic scattering (QE), the middle green region represents resonance interactions (RES), and the right red region is deep inelastic scattering (DIS). The overlap between RES and DIS represents the transition region. The dashed lines split the W distribution into the KNO-only region on the left, the PYTHIA-only region on the right, and the transition region in the middle.

number of kinematically available low-mass mesons, e.g. π and K. Finally, it partitions the available invariant mass W among the generated hadrons to assign momenta.

PYTHIA/JETSET [205] is a standard tool for the generation of high-energy collisions tuned to the BEBC data, spanning models for few-body hard processes to complex multihadronic final states. In the AGKY model, the PYTHIA region is not accessed until neutrino energy of approximately 3 GeV, and its contribution is equal to the one of KNO at around 9 GeV [203].

5.2.3 Final-state interactions

Final-state interactions (FSI) occur as particles produced via the initial interaction traverse the nucleus to exit it. These interactions can change the final-state particle kinematics as well as the number of particles seen in the final state. GENIE models the FSI of nucleons and pions using intranuclear cascade simulation called INTRANUKE [206, 207]. This analysis uses the effective data-driven model hA [42, 43].

The hA implementation simulates the full cascade from a single effective interaction. It relies on the mean free path of the hadron to determine the probability that the FSI occurs. The interaction type, such as absorption, charge-exchange, elastic or inelastic scattering, relies on the external data, specifically cross-sections of π^+ and p on ^{56}Fe [42, 43]. Cross-sections are scaled by $A^{2/3}$ to predict FSI for other nuclei, and the isospin symmetry can be utilised to allow for predictions for n, π^0, and π^-. Furthermore, GENIE applies the FSI to the hadronic products of the interactions only, therefore the final-state muons are not affected.

5.3 Detector simulation

Detector simulation models the propagation and the energy loss of the final-state particles through the MINERvA detector. Furthermore, it also accounts for the incidental activity in the detector via data overlay and employs the readout simulation to convert the energy deposits to simulated hits which can then be reconstructed.

5.3.1 Particle propagation

Particle propagation through the MINERvA detector uses the GEANT4 (GEometry ANd Tracking) software version 9.4.p02 [159, 160]. The GEANT4 simulation proceeds in steps to determine if and how the final-state particles interact with a detailed description of MINERvA's geometry. The steps within a material are proposed by randomly sampling from the interaction length distributions implied by the interaction cross-sections for each process that applies to the particle. Based on the shortest step length, the particle either interacts or moves into a new material. Similarly, if an interaction produces secondary particles, their propagation is also simulated by GEANT4.

The majority of interactions producing visible particles in the MINERvA detector come from the inelastic interactions. The inelastic hadron interactions in the detector use the QGSP_BERT physics list, which employs the Bertini cascade (BERT) [166–169] for

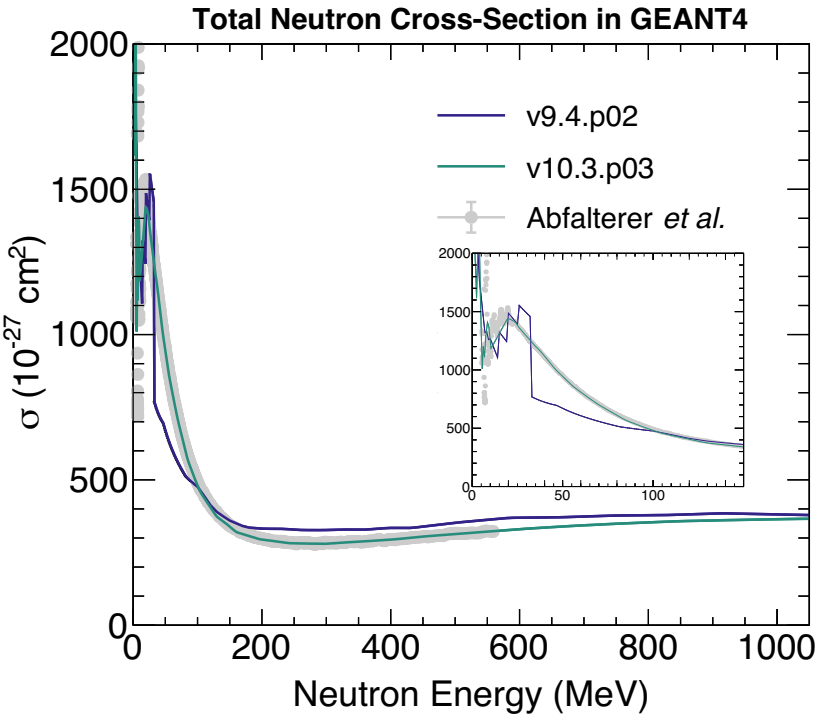

Figure 5.7: Total neutron cross-section simulated by two different versions of GEANT4, v9.4.p02 and v10.3.p03, with overlayed Abfalterer *et al.* data [208]. The older version of GEANT4 v9.4.p02 simulation shows significant disagreement with the Abfalterer *et al.* data, whereas the newer version v10.3.p03 agrees with the data well. The insert shows the low neutron energy (0–200 MeV) behaviour of the two simulations versus data.

particles with momentum less than 10 GeV/c [209]. For hadrons with momentum larger than 10 GeV/c, GEANT4 uses the quark-gluon string precompound (QGSP) [210]. Other processes such as electromagnetic interactions or particle decays use the default modules of GEANT4. The particle propagation simulation ends with energy deposits and their associated timings along the track and at the end of the interaction step.

Furthermore, MINERvA reweights the events to modify the total neutron cross-section to match the Abfalterer *et al.* [208] high-precision neutron scattering data which the newer versions of GEANT4 such as 10.3.p03 agree with [211]. The two GEANT4 total neutron cross-section simulations are compared to the Abfalterer *et al.* data in Figure 5.7. The neutron interaction cross-section is increased via weighting up events with shorter tracks and weighting down events with longer tracks (and vice versa) while keeping the total number of (anti)neutrino events constant. A similar technique is used to evaluate the systematic uncertainties of the proton, pion and neutron interaction cross-sections and is further discussed in Chapter 8.

5.3.2 Data overlay

Additional effects such as particles produced in the rock between the NuMI beam and the detector, and overlapping (anti)neutrino interactions are not directly simulated. Instead, the MC hits are overlaid with data corresponding to random beam spills appropriate to the time periods in the simulation [154, 212]. The inserted data is flagged, ensuring it is not considered a signal candidate in the analysis.

5.3.3 Readout simulation

Both the true deposits and timing need to be decalibrated to reconstruct the MC using the same methods as the data. First, all dead channels coming from the data overlay detector readout window are masked from the readout to account for the detector dead time and dead channels [213].

The energy deposited in the scintillator is converted into light yield using Birks' law [214]. The number of photoelectrons incident on the photomultiplier tube (PMT), which takes into account the attenuation of light in the fibres and additional smearing, is amplified using the gain of the PMT. The simulation also includes electronic noise and cross-talk. Finally, the photoelectrons are translated into raw ADC counts using the known analog-to-digital response [215].

The simulated hit time is decalibrated by rounding to the nearest resolution width of the front-end-board (FEB) clock time. The known FEB offset and the travel time of photons to the PMT given the location of the hit along the scintillator strip is also added to the hit time and further smeared [213].

Chapter 6

Reconstruction

Reconstruction involves converting energy deposits, or hits, along with their positions and timings—calibrated as described in Section 3.3—into physical quantities essential for the physics interpretation. Since the completion of its physics run, part of MINERvA's data preservation efforts [216], in which I have been actively involved, was to integrate reconstruction tools across various analyses and produce unified files containing both low- and high-level reconstructed objects used in all current and future analyses. Recently, the first iteration of these files, passing validation studies, has been produced and is used in this measurement.

This chapter focuses on the individual components of the common MINERvA reconstruction tool relevant for measuring nuclear dependence in antineutrino scattering. Therefore, in addition to the low-level grouping of hits in time and space, the reconstruction of the antimuon—specifically its track, direction, and momentum—is discussed. Furthermore, the reconstruction of the hadronic recoil system, i.e. energy in the detector not associated with the antimuon, needed for calculating Bjorken x as defined in the previous chapter, is also described. Finally, as the accurate placement of the interaction vertex is crucial for studying how antineutrinos interact with different materials, MINERvA's machine-learning technique for doing so is briefly reviewed. Note that both the data and the simulation sample are reconstructed this way.

6.1 Hit clustering by time and position

Multiple antineutrino and other particle interactions could occur during one data-taking period, i.e. a 16 μs gate, of the MINERvA detector. To distinguish each interaction, i.e. event, in time, hits within each gate are initially clustered in 24 ns time windows, referred to as slices, if their total energy deposition surpasses the threshold of 10 photoelectrons. This threshold corresponds to 2/3 of the signal over a plane for a normally incident minimum ionising particle (MIP), such as a rock muon [40]. The time slice is then extended forward to incorporate additional hits until the threshold requirement is no longer met, resulting in variable-length time slice windows. All subsequent reconstruction steps are performed within these time slices.

Thereafter, hits in adjacent strips within a plane are grouped into clusters of various sizes based on total energy deposits, categorized as low activity (less than 1 MeV in total), trackable (consistent with MIP energy deposits), heavy-ionising (similar to trackable, but higher energy), or superclusters (spanning several strips with many high-energy clusters consistent with an electromagnetic or hadronic shower) [40]. There are also low-energy clusters identified as cross-stalk candidates if their corresponding PMT pixels are adjacent to pixels associated with particle interaction. All clusters except the cross-talk candidates are then subjected to further reconstruction processes, involving track finding for the antimuon and summing all other hits for the recoil system. Each cluster is used only once.

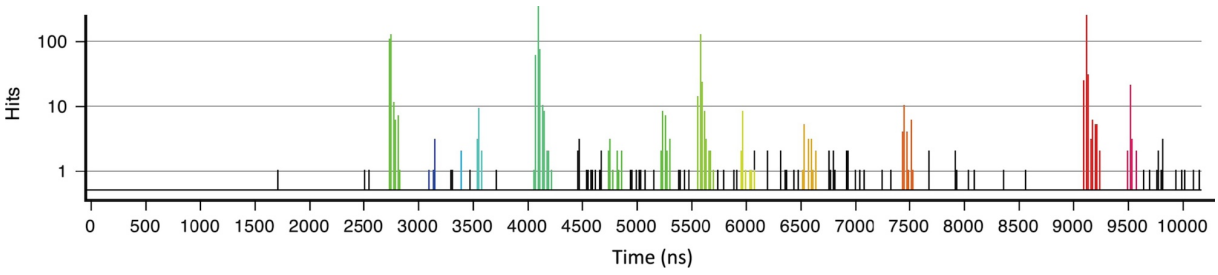

Figure 6.1: Time profile of energy deposits in the MINERvA detector corresponding to the 10 μs beam spill reproduced from Ref. [40]. Coloured groups of hits represent different time slices. The remaining black entries do not meet the time slice requirement.

6.2 Antimuon information

Any antineutrino interactions in the MINERvA detector can be identified by the produced antimuon. An (anti)muon, being a MIP, leaves a distinctive signature of a long straight track in the detector. As described in Ref. [40], the reconstruction starts with finding trackable and heavy-ionising clusters forming a straight track in a minimum of three planes in each of the three views. Any additional clusters with slope and intercept consistent with this straight-track topology are added in each view.

The two-dimensional (2D) candidate tracks from each view are combined into a three-dimensional (3D) track if they are compatible with forming a straight line. Due to the aforementioned three-plane requirement for the 2D candidates and the plane configuration of the MINERvA detector discussed in Section 3.2, the 3D track must span at least eleven planes in total as shown in Figure 6.2. Subsequently, the track is fitted using a Kalman filter [217], considering the potential multiple scattering of the (anti)muon track. Any super-cluster included in this way is subdivided into smaller clusters, ensuring the cluster energy aligns with that of a MIP—otherwise, they are removed and accounted for as a part of the recoil system. The fitted (anti)muon track has a resolution of 3 mm [40].

For the antineutrino interaction to be considered in this work's measurement, the antimuon must have its charge (positive to be identified as antimuon) and its momentum measured by the MINOS spectrometer—various details and constraints of the MINERvA–

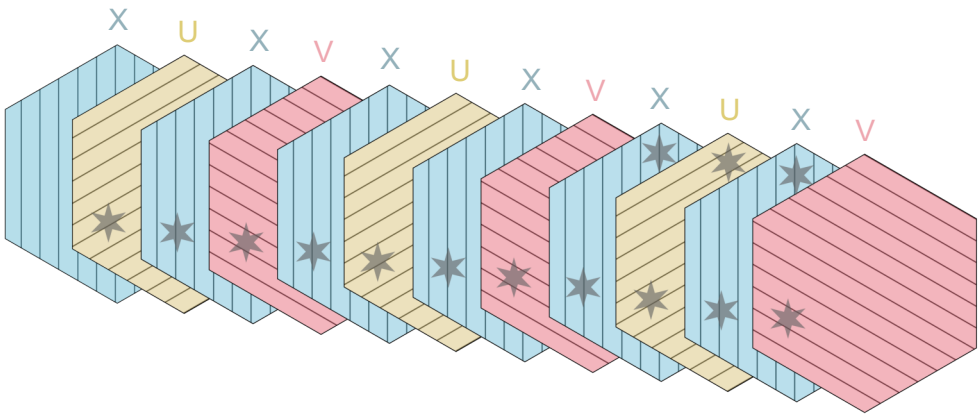

Figure 6.2: Illustration of the MINERvA 3D (anti)muon track reconstruction requirement of 11 planes minimum due to the XUXV plane configuration on the bottom. Grey stars represent the relevant clusters in each plane. In contrast, the top grey stars do not meet the (anti)muon track requirement.

MINOS combination are discussed in Section 3.4. Therefore, the antimuon track found in the MINERvA detector must be matched to the one found in the MINOS spectrometer within a 200 ns time window [40]. The tracks are matched if the difference between the end-point of MINERvA track projected upstream and the start of the MINOS spectrometer track (and vice versa) is less than 40 cm [40].

The (anti)muon track reconstruction in the MINOS near detector has similar steps to the MINERvA reconstruction. An example of a reconstructed antimuon track in the MINERvA detector that was matched to MINOS is shown in Figure 6.3. Note that the matching part of the reconstruction differs for the data and the simulation due to potential mismodelling in the MINOS data overlay. Thus, a correction dependent on the antimuon energy and beam intensity is applied to the simulation to mitigate this difference.

The antimuon momentum in the MINOS spectrometer is reconstructed either by its track range or curvature, utilising the magnetic field. Typically, (anti)muons with momenta up to 6 GeV/c were contained within MINOS and were thus reconstructed by range, i.e. total energy loss through interactions, with momentum resolution of 5% [40, 176]. In order to reconstruct (anti)muons originating from interactions in the MINERvA detector, they had to enter MINOS and penetrate at least 25.4 cm into it, requiring a minimum (anti)muon momentum of about 2 GeV/c [40]. (Anti)muons with higher momenta were reconstructed by curvature with 10% momentum resolution [176]. Specifically, the antimuon

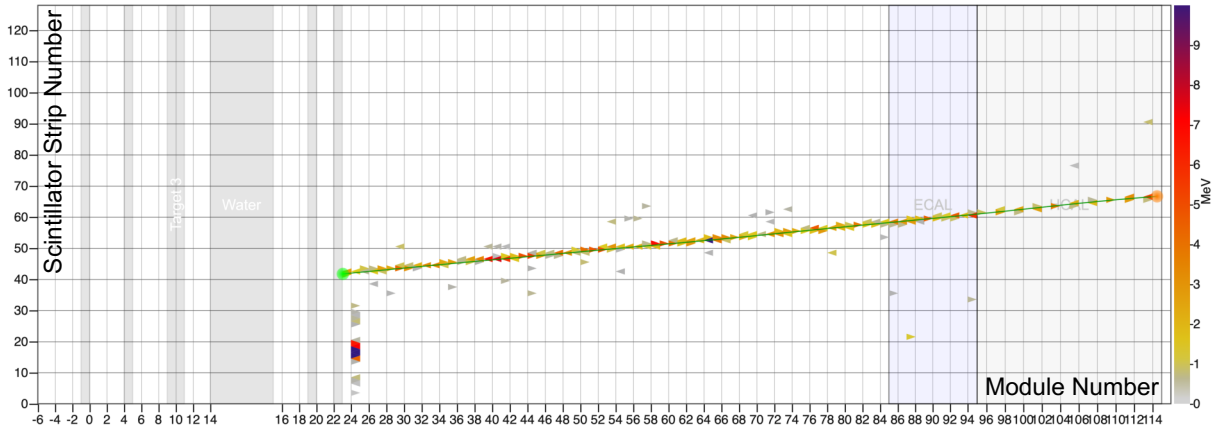

Figure 6.3: Event display showing the reconstructed antimuon track (green line) originating in target 5 lead on top of the antimuon energy deposits, i.e. individual triangles with their colour representing the size of the deposit, in the detector. The x-axis depicts the individual module numbers of the detector along the general direction of the antineutrino beam.

momentum p_{MINOS} measured in the MINOS spectrometer by curvature is proportional to the magnetic field B over the measured radius R of the curvature,

$$p_{\text{MINOS}}\ [\text{MeV}/c] = \frac{0.3B\ [\text{kGauss}]}{R\ [\text{cm}]}\ . \tag{6.1}$$

Here, kGauss corresponds to 0.1 T. In addition to the antimuon momentum measured by MINOS, the total antimuon momentum also accounts for the energy loss while traversing the MINERvA detector, i.e. $p_{\text{total}} = p_{\text{MINOS}} + p_{\text{MINERvA}}$.

The antimuon track reconstruction, i.e. determining the direction and momentum of the antimuon, is performed in the detector coordinates, which differ from the antineutrino beam coordinates as defined in Chapter 3. To express quantities with respect to the incoming antineutrino beam, the antimuon momentum vector in the detector coordinates is rotated 3.34° downwards in the y-z plane to align with the beam coordinates. Subsequently, the transverse antimuon momentum p_{T} is calculated using the rotated antimuon momentum vector, and it is, therefore, perpendicular to the beam direction, as illustrated in Figure 6.4. Furthermore, as noted in Section 3.4, the angular efficiency due to the MINOS matching is constrained to 17° relative to the beam, directly impacting p_{T}. This is further discussed in Section 7.4.

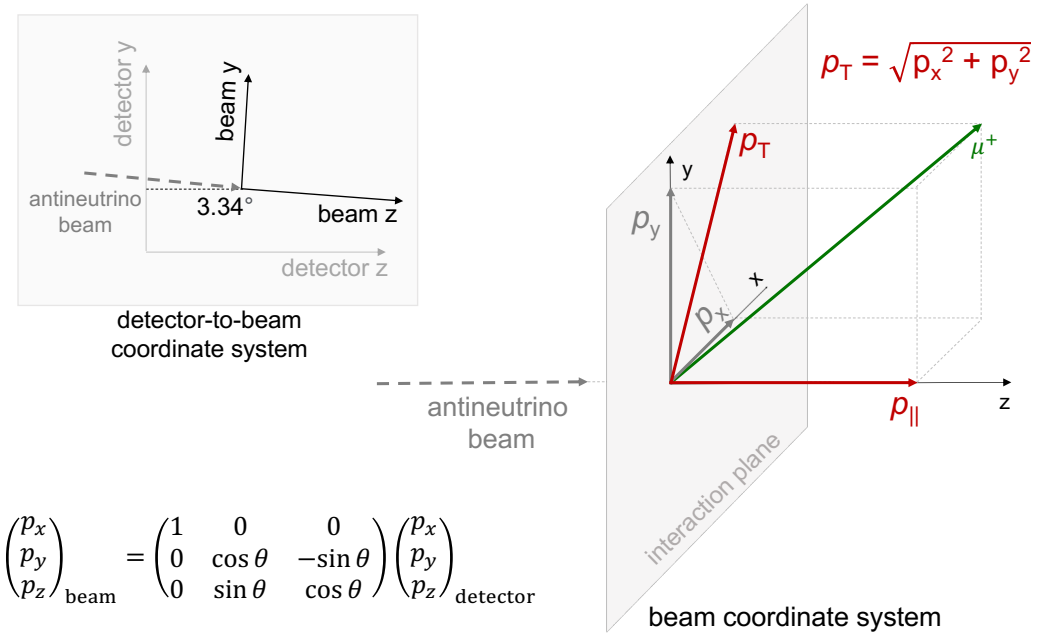

Figure 6.4: Illustration of the rotation from the detector to the beam coordinate system to calculate antimuon transverse momentum, p_{T}.

6.3 Recoil energy

Any remaining clusters in the detector not associated with the antimuon track contribute to the hadronic recoil system, which is relevant for the calculation of Bjorken x (excluding low-activity clusters identified as cross-talk). However, the recoil energy deposited by these clusters must be corrected to account for energy loss in the passive material of the detector. This process of estimating the energy of the hadronic recoil system is known as calorimetry. A detailed description of MINERvA's calorimetry can be found in Refs. [40, 218, 219].

Specifically, the total energy of the non-antimuon clusters per subdetector is corrected by the sampling frequency[1] of the given subdetector, also taking into account that the active scintillator planes are not fully active, as described in Chapter 3. The calorimetrically reconstructed recoil energy corrected for passive material overall is then the sum of these corrected subdetector energies. In the nuclear target region, the calorimetric correction is done cluster by cluster to account for the amount of passive material through which the resulting particles travel; for example, particles produced in target 1 traverse more passive material than those produced in target 5. In addition, if clusters are located only on one side of the target, the sampling frequency is calculated using half of the width of the passive target.

[1]Sampling frequency is defined as the ratio of the energy deposited by an incident MIP in the active part of the detector divided by the sum of energies deposited by an incident MIP in the active and passive part.

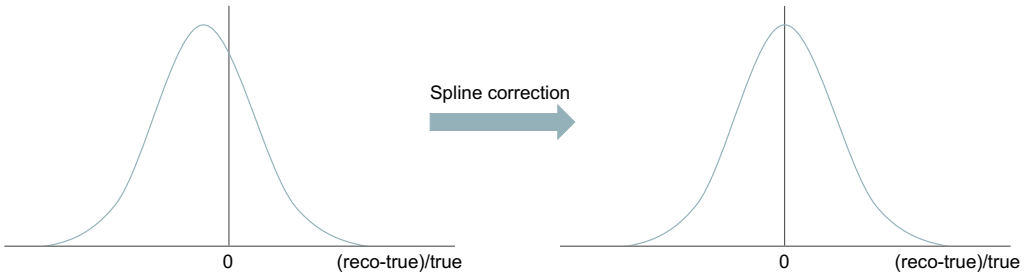

Figure 6.5: Illustration of a Gaussian fit to the energy resolution distribution in a specified energy range (left). The spline correction for the given energy range is determined in such a way that it centres the Gaussian fit to the energy resolution at zero (right).

Moreover, MINERvA also applies an additional calorimetric correction considering any differences between the above-corrected reconstructed recoil energy and the true recoil energy based on the true information available in the simulation, defined as the difference between the true antineutrino and true antimuon energy. This correction accounts for the loss of visible energy due to final-state interactions (FSI), neutral particles, and other effects. Since these effects cannot be disentangled in an inclusive analysis, the correction is somewhat dependent on the underlying understanding of their behaviour encoded in the simulation. In this measurement, this is particularly relevant as antineutrino scattering produces final-state neutrons, whose kinetic energy cannot be reconstructed.

First, the overall scale of the passive material corrected recoil energy for each sub-detector is matched to the true recoil energy, and second, a bin-by-bin correction, i.e. spline correction, is applied to account for energy-dependent effects. For example, higher energy processes can have more significant FSI, produce more neutral particles in final states, etc. Historically, this correction process was carried out at the reconstruction level for each analysis separately, as different analyses choose to account for missing energy differently. However, to support the new data preservation analysis files enabling all current and future analyses, I implemented this process on the post-reconstruction level within the high-level MINERvA Analysis Toolkit (MAT) [174]. This also allows for future improvements of these corrections using simulations with improved interaction models if necessary.

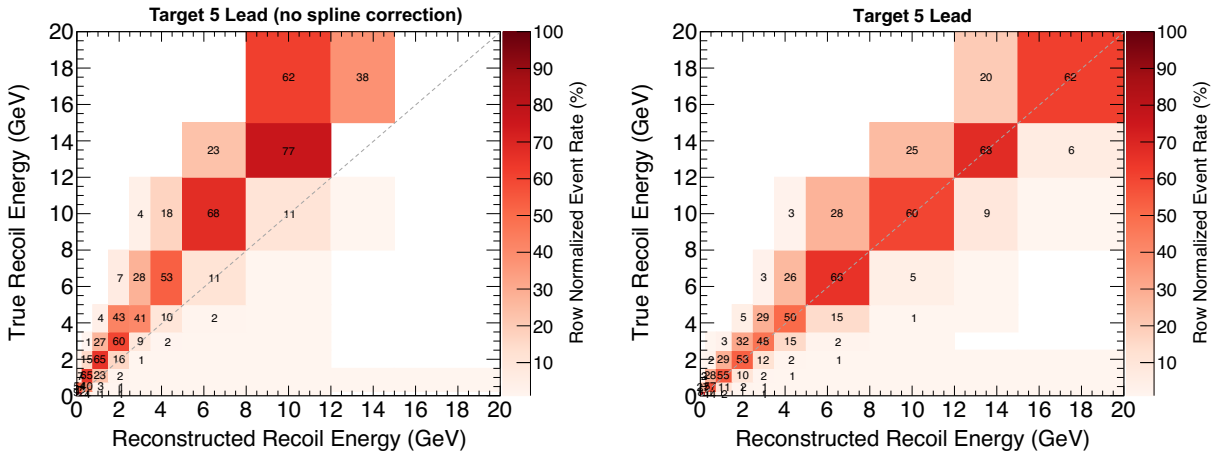

Figure 6.6: Relationship between the reconstructed and true recoil energy without the spline correction (left) and with the spline correction (right). Note the impact of the spline correction on the diagonal, i.e. mapping of the corresponding bins in the reconstructed and truth space (denoted by the grey dashed line). Each row is normalised to one.

In particular, the spline correction part is calculated by fitting a Gaussian to the recoil energy resolution, i.e. the fractional difference between the calorimetric and true recoil energy $\Delta E/E_{\text{recoil}} = (E^{\text{reco}}_{\text{recoil}} - E^{\text{true}}_{\text{recoil}})/E^{\text{true}}_{\text{recoil}}$, in each bin of true recoil energy for the inclusive antineutrino sample for each target and material combination. The spline point for each bin of the recoil energy is such that it will center the resolution at zero, as illustrated in Figure 6.5. Figure 6.6 also shows the relationship between the reconstructed and true recoil energy before and after applying the spline correction.

6.4 Interaction vertex

Precise reconstruction of the interaction vertex in this analysis is crucial for determining in which material the interaction has taken place, especially given the complex geometry of the nuclear target region. Therefore, in analyses involving nuclear targets, MINERvA enhances its vertex reconstruction capabilities by employing machine learning (ML) instead of the conventional technique of track-based vertexing, which involves calculating the intersection of various tracks seen in the detector to identify the vertex. The reconstruction of the interaction vertex is reframed as a multiclass image classification problem solved by MINERvA's deep convolutional neural network (DCNN), described in Refs. [220, 221].

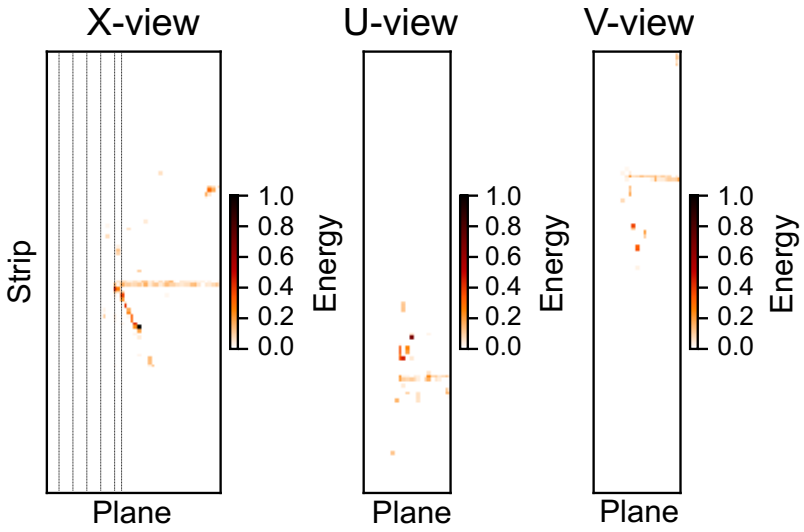

Figure 6.7: Example of an image containing energy deposit information of an event in target 4 used in machine-learning-based vertex reconstruction. An image containing the timing information would look similar. Modified from [176]. Copyright (2024) IOP Publishing. Reproduced with permission. All rights reserved.

First, the information from the antimuon track reconstruction is used to filter out events that visibly occurred outside of the detector and ones that did not continue into the MINOS spectrometer. All events reconstructed using the ML vertexing technique are thus by default so-called MINOS-matched events. Subsequently, the energy and timing information in each of the detector views is encoded to create images used for classification. The images representing the energy information are shown in Figure 6.7.

The multiclass image classification works by assigning objects, in this case, interaction vertices, into a set of predefined categories. These categories are the individual planes of the MINERvA detector, which are numbered to easily encode the position of the vertex in the detector. The DCNN is trained using a separate set of simulated interaction images, i.e. images where the true vertex plane is known. The trained model is then applied to the data and corresponding simulated events to identify the interaction vertex plane, assigning it a probability associated with the DCNN's confidence that the vertex has been placed correctly. This probability is later used in the event selection process of this measurement described in Section 7.1. It is also important to note that any reconstructed quantities associated with the interaction vertex position are updated accordingly based on the assigned ML vertex plane. For example, shifts from the hadronic recoil system to the antimuon track and vice versa corresponding to changes in the antimuon path length are accounted for.

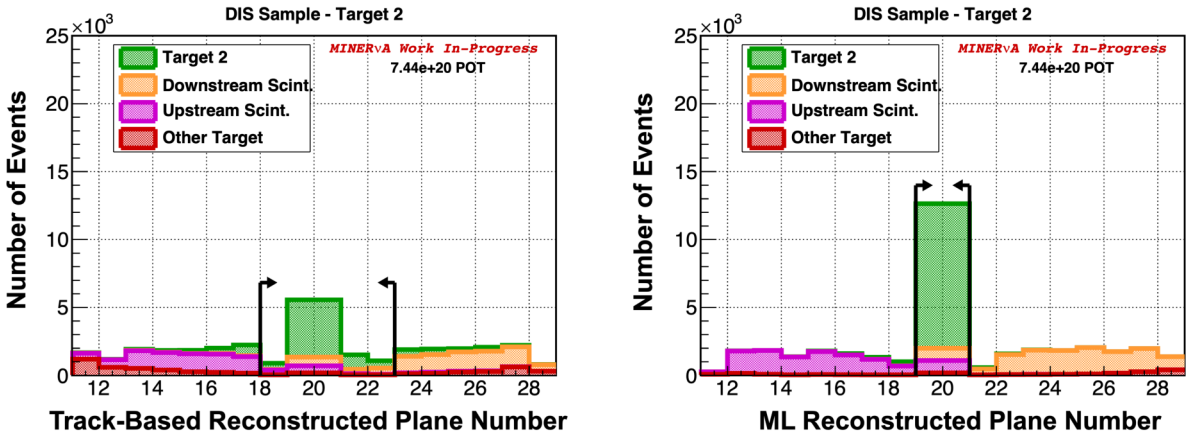

Figure 6.8: Sample of deep inelastic scattering events in target 2 reconstructed using track-based vertex reconstruction (left) and machine-learning-based vertex reconstruction (right). The colours represent the true source material. Modified from [176]. Copyright (2024) IOP Publishing. Reproduced with permission. All rights reserved.

While the performance in the scintillator tracker is somewhat comparable to conventional track-based vertexing, the improvement in the nuclear targets is significant. This is mainly due to the better handling of more complex events with large shower topologies by the DCNN. The number of interaction vertices correctly assigned within a given target relative to all the vertices assigned to the target is improved by 10–15% relative to the track-based vertexing [221]. Furthermore, more interaction vertices are assigned to the individual targets rather than to the surrounding scintillator planes in the first place. This is demonstrated in Figure 6.8.

Chapter 7

Differential cross-section measurement

This chapter delineates the specific steps I performed to extract the cross-section for MINERvA's first measurement of nuclear dependence in inclusive antineutrino scattering in medium energy. The analysis utilises data from an exposure of 1.12×10^{21} protons on target (POT), and the simulation sample detailed in Chapter 5. Both the data and simulation were reconstructed using the techniques described in Chapter 6. The differential cross-sections for carbon, hydrocarbon (scintillator), iron, and lead were determined using Equation 4.1 for antimuon transverse momentum, p_{T}, and Bjorken x. Additionally, the nuclear target to scintillator cross-section ratios were calculated using the matching-flux technique discussed in Subsection 5.1.1. Each step of the analysis is presented for lead and scintillator, with carbon and iron plots included in the appendices. The results are then shown and discussed in Chapter 9, with the systematic uncertainties detailed in Chapter 8.

7.1 Event selection

Event selection refers to a process of counting the number of interactions passing a set of selection cuts according to the analysis signal definition while taking into account the reconstruction capabilities of the detector. In this case, it ensures the cross-section is

extracted for the charged-current interaction type inclusive sample of antineutrino scattering in a specific material. It is the first step of the cross-section extraction represented by $N_{\text{data},j}$ in Equation 4.1 in Chapter 4.

The events considered in this analysis must meet the following signal definition:

- Charged-current antineutrino interaction producing an antimuon μ^+
- Interaction occurring in a specific material, i.e. carbon, hydrocarbon, iron, or lead
- Antimuon energy between 2 and 20 GeV
- Antimuon angle less than 17° with respect to the beam direction

The phase-space cuts included in the signal definition are determined by the detector's ability to reconstruct the antimuon, as discussed later. It is important to note that these selection criteria were also employed to compare the cross-section results with the corresponding samples from different (anti)neutrino event generators in Chapter 9.

Utilising the reconstructed data and the simulation sample from Chapter 6, which comprises all MINERvA reconstructable MINOS-matched events, a set of reconstruction cuts was applied to both samples. These cuts were aimed at identifying events that match the signal definition mentioned above, based on their reconstructed properties. Additionally, the reconstruction cuts serve to reduce background events (i.e. non-signal events) and aid in the selection of events whose kinematics can be reconstructed while minimising systematic uncertainties arising from the detector's reconstruction capabilities, as well as flux and interaction modelling. Most of these reconstruction cuts are shared across all MINERvA analyses as they stem from the MINERvA detector and the MINOS spectrometer designs.

Furthermore, although the final cross-section results are reported for various materials, most of the analysis steps treat individual targets of different materials separately. This separation is necessitated by the distinct efficiencies of the various target and material combinations discussed later on in Section 7.4, which result from their positions in the detector. Therefore, this is also taken into account in the list of reconstruction cuts, which is as follows:

1. The antimuon detected in the MINOS spectrometer must have a positive curvature to ensure an $\bar{\nu}_\mu$ interaction occurred, i.e. $(q/|p|) > 0$, where q is the antimuon's charge and p its momentum.
2. The high-energy antimuon reconstructed by curvature in the MINOS spectrometer must have a curvature significance at least 5σ to reduce the tails of the antimuon energy resolution spread [222], i.e. $(q/|p|)/\sigma_{q/p} \geq 5$, where $\sigma_{q/p}$ is the error on the curvature.
3. The antimuon track must be contained within the fiducial volume of the MINOS spectrometer and cannot cross the MINOS coil hole described in Chapter 3, i.e. the event track must fall within the radial distance of 210 mm $< R_{\text{event}} <$ 2500 mm [151, 222].
4. The interaction vertex must be within the fiducial volume of the MINERvA detector. This is bounded by a hexagon with an 850 mm apothem in the x-y plane, and for mixed targets, the vertex must be located more than 25 mm away from the boundary between the different materials in the x-y plane [40].
5. The event must not contain any dead channels, i.e. channels insensitive to new energy deposits, induced by previous interactions in the path projected upstream of the antimuon track. This is to avoid rock muons whose tracks are partially lost due to the dead time from being confused with fiducial events [40].
6. The event is excluded if the highest machine-learning probability for vertex placement falls below 20%, to eliminate instances where the network may be uncertain. This maintains a consistent and statistically significant contribution with similar pass rates for both data and simulation [223].
7. For hydrocarbon (scintillator), the z position of the machine-learning vertex must be in the tracker region, i.e. 5980 cm $\geq z \geq$ 8422 cm. For carbon, iron, and lead, the z position of the interaction vertex must be located within the passive target 2, 3, 4, or 5 as described in Chapter 6, and in the region of the x-y plane corresponding to the respective material as discussed in Chapter 3. Target 1 is excluded from this analysis due to contamination from rock muons. As the most

upstream target, it has only a small number of upstream tracking planes, making it challenging to distinguish an interaction in this target from a rock muon solely based on the antimuon track.

8. The energy of the antimuon must be within the range of 2 to 20 GeV. The lower limit ensures that the antimuon possesses enough energy to traverse through the MINERvA detector and cross multiple planes in the MINOS spectrometer to form a track. Meanwhile, the upper limit serves to minimise neutrino contamination in the sample, particularly from unfocused high-energy mesons that have not undergone charge selection. Crucially, the 20 GeV cut-off is imposed due to an incomplete understanding of the flux modelling beyond this threshold.
9. The angle of the antimuon with respect to the antineutrino beam must be less than 17°. This requirement is driven by the steep decline in the acceptance of the MINOS spectrometer for larger scattering angles, especially for interactions occurring in the most upstream nuclear targets. This is demonstrated in the p_{T} efficiency plots, where p_{T} serves as a direct proxy for the antimuon angle, later on in Section 7.4.

Included in Appendix B is an illustrative comparison showcasing the impact of each of these cuts on target 5 lead and the scintillator tracker in both data and simulation.

Target	Material	Number of events in data	Predicted purity (%)
2	Iron	75 786	84.4
	Lead	68 559	86.4
3	Carbon	56 760	81.7
	Iron	36 647	84.0
	Lead	22 809	87.0
4	Lead	65 469	75.9
5	Iron	52 247	78.7
	Lead	35 068	81.6
Tracker	Scintillator	1 823 367	98.9

Table 7.1: Number of antineutrino data events reconstructed and selected in all relevant targets of different materials and the scintillator tracker of the MINERvA detector, and the predicted purity of the selection based on the simulation (as defined in Equation 7.1).

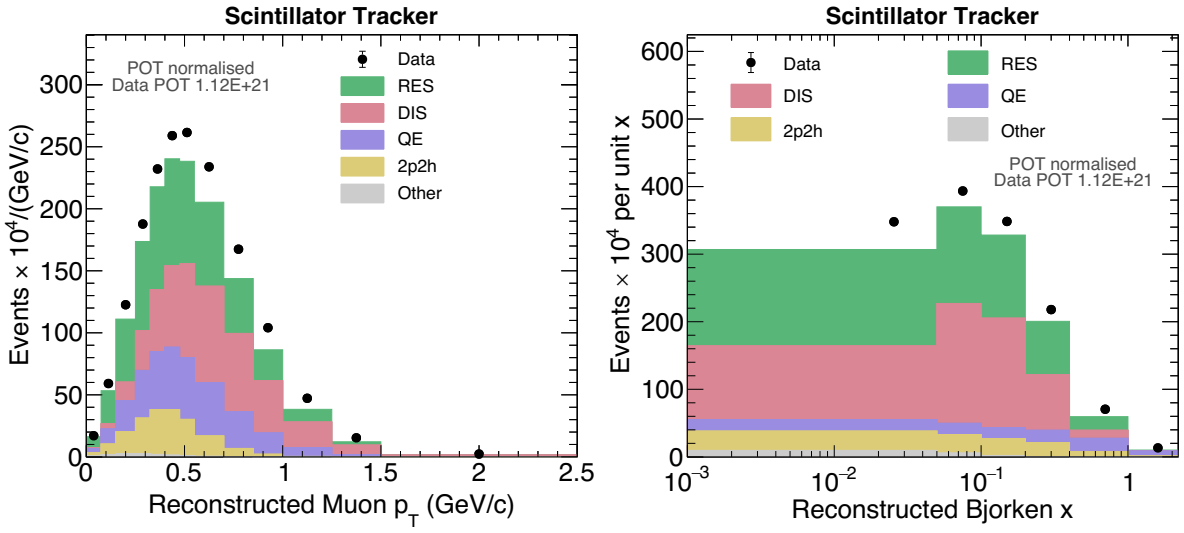

Figure 7.1: Selected event distributions in the scintillator tracker for both antimuon p_{T} (left) and Bjorken x (right). The distributions are bin-width and POT normalised. The black points represent the data with its statistical uncertainty, while the simulation is broken down into the various interaction channels stacked in the descending order of their contribution: resonant pion production (RES), deep inelastic scattering (DIS), quasi-elastic scattering (QE), 2p2h interaction (2p2h), and Other. The simulation visibly underpredicts the data in the scintillator tracker.

The number of antineutrino events reconstructed and selected in all relevant targets of different materials and the scintillator tracker of the MINERvA detector is listed in Table 7.1. In total, this measurement utilises an extensive dataset of antineutrino interactions: 56 760 in carbon, 164 680 in iron, 191 905 in lead, and 1 823 367 in hydrocarbon (scintillator tracker). For comparison, this represents approximately 10× more statistics than those in the MINERvA neutrino analysis in nuclear targets in low energy [179], as mentioned in Chapter 4. Most importantly, it constitutes the largest sample of antineutrino interactions on various materials in the same beam ever analysed to date.

Figure 7.1 displays the bin-width normalised distributions of selected events in the scintillator tracker for both variables of interest: antimuon p_{T} and Bjorken x. Bin-width normalisation in this context means that each bin is divided by its own width. Therefore, the actual content of the bin is the number read off the y-axis (with factor 10^4 included) multiplied by the bin width. The bin edges of antimuon p_{T} and Bjorken x are listed in Table 7.2. The determination of bin edges involved optimising the diagonal of a migration matrix explained in Section 7.3. This optimisation aimed to retain the interesting $x > 1$

Variable	Bin edges													
p_{T} (GeV/c)	0.0	0.075	0.15	0.25	0.325	0.4	0.475	0.55	0.7	0.85	1.0	1.25	1.5	2.5
Bjorken x	0.001		0.05		0.1		0.2		0.4		1.0		2.2	

Table 7.2: Bin edges of the antimuon p_{T} and Bjorken x histograms used in this analysis.

bin in the Bjorken x distribution, as discussed in Chapter 4, while the lower bin boundary was approximately set using the definition of Bjorken x in Chapter 4 and the value of the lowest p_{T} bin. Additionally, the p_{T} distribution was truncated at 2.5 GeV/c due to limitations of the MINOS acceptance, as demonstrated in the p_{T} efficiency plots in Section 7.4.

The simulation prediction for the scintillator tracker in Figure 7.1 is categorised by various interaction types. Given that this inclusive analysis utilises antineutrino data collected during the medium-energy (ME) physics runs of the MINERvA detector, where the antineutrino flux peaks near 6 GeV, the predominant interaction types are resonant pion production and deep inelastic scattering. Across all targets of various materials, resonant pion production contributes, on average, around 38% to the sample, while deep inelastic scattering makes up about 32%. Quasi-elastic scattering and 2p2h interaction constitute approximately 18% and 11% of the sample, respectively. Other interaction types, including coherent pion production and others, contribute less than 1% combined. An example of the nuclear target 5 lead distribution with the simulation broken down into various interaction types is also included in Appendix B.

The aforementioned reconstruction cuts may not exclusively isolate signal events, leading to a contamination of the data sample by background events——interactions that exhibit a similar signature to signal events in the detector and are misidentified as such. To estimate the level of contamination in the reconstructed data sample, the simulation with known true information can be utilised. The metric that does that is called predicted purity, defined as

$$\text{Purity} = \frac{\text{Signal events in the reconstructed sample}}{\text{All events in the reconstructed sample}} \ . \tag{7.1}$$

The analysis predicted purity for all relevant targets of different materials and the scintillator tracker of the MINERvA detector is listed in Table 7.1. The nuclear target purity averages around 82%, while the scintillator tracker purity is almost 99%.

Figure 7.2 illustrates a simulated breakdown of background in the reconstructed distribution for target 5 lead and the scintillator tracker, in both p_{T} and Bjorken x. As depicted, the lower purity in targets, compared to the scintillator tracker, is a result of interactions reconstructed within the target that, in reality, occurred in the surrounding scintillator planes upstream ('Upstream plastic') and downstream ('Downstream plastic') of the relevant target. The 'Other' category for targets combines events from different materials—for instance, in target 5 lead, it could include events from target 5 iron—and neutrino events contaminating the reconstructed charged-current antineutrino events. In the scintillator tracker, it combines the neutrino events with those from outside the tracker region instead. In both cases, it constitutes approximately 1% of the reconstructed sample. The reconstruction cuts effectively eliminate any neutral current events.

It is also crucial to emphasise that there are no background events originating from outside the x–y fiducial volume, the antimuon angle or the antimuon energy range depicted in Figure 7.2. However, these backgrounds are appropriately accounted for in the final cross-section results through efficiency correction, allowing for their migration in and out of the sample during the unfolding procedure explained in Section 7.3. In practice, this involves applying the reconstruction cuts on the fiducial volume, energy, and angle range without utilising the true information of the simulation for these aspects in the background subtraction, migration matrix, and efficiency numerator. The true information requirement is only included in the efficiency denominator.

Furthermore, the data-to-simulation ratio in Figure 7.2 serves as an initial indicator of how well the simulation predicts the data. While the simulation is tuned to encompass the latest measurements of neutrino pion production at MINERvA as described in Chapter 5, both the p_{T} and Bjorken x for target 5 lead and the scintillator tracker data distributions show a disagreement with the prediction, albeit in different ways. All other selected event

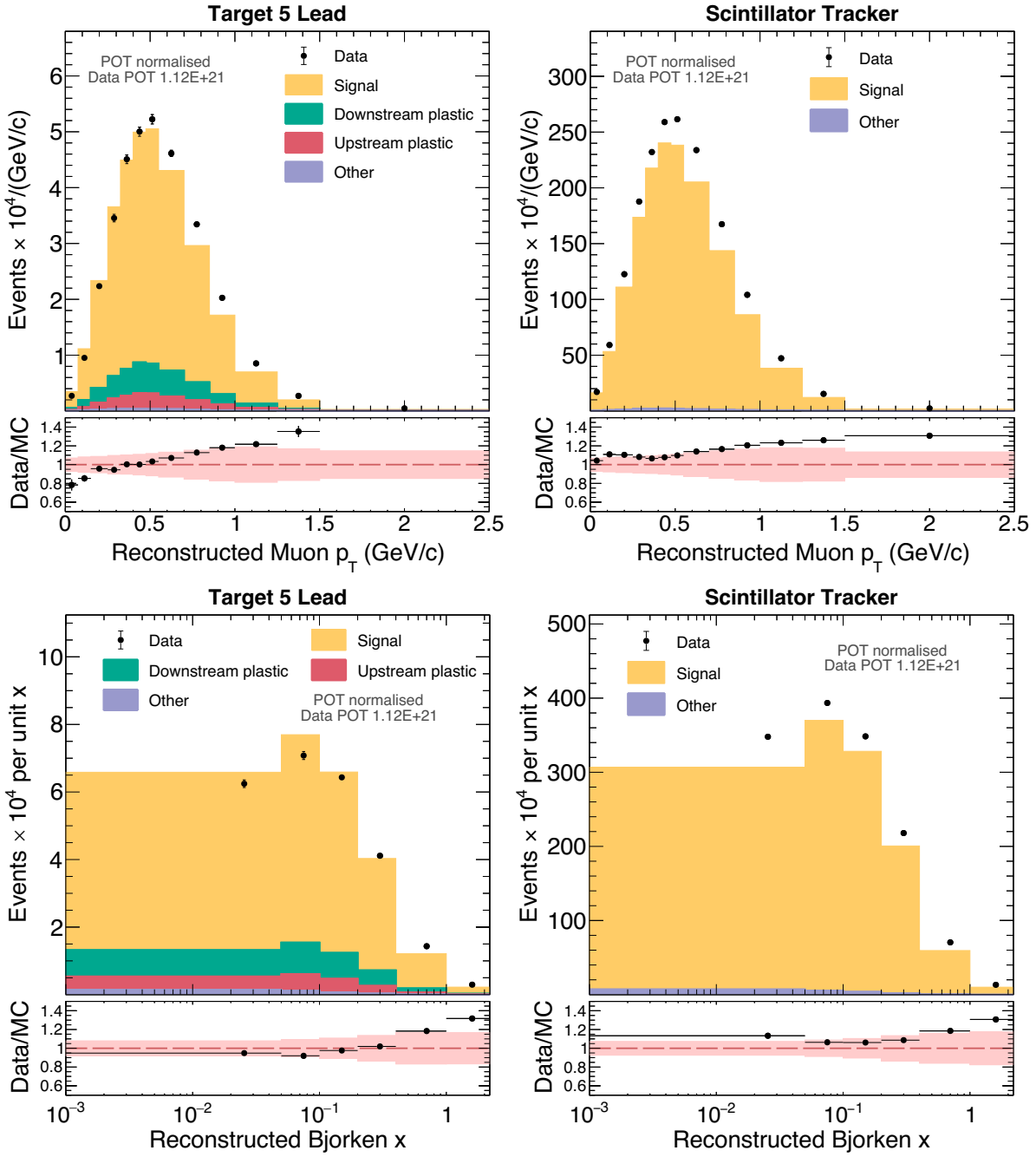

Figure 7.2: Selected event distributions in target 5 lead (left panel) and the scintillator tracker (right panel) for both antimuon p_{T} (top) and Bjorken x (bottom). The distributions are bin-width and POT normalised. In the top panel of each plot, the black points represent the data with its statistical uncertainty, while the simulation is broken down into various sources of signal and background stacked in the descending order of their contribution. The bottom panel shows the data-to-simulation ratio. The solid band around the dashed line at 1 represents the systematic uncertainty on the simulation, while the black points carry the statistical uncertainty of the ratio. The horizontal lines on individual points indicate the bin width.

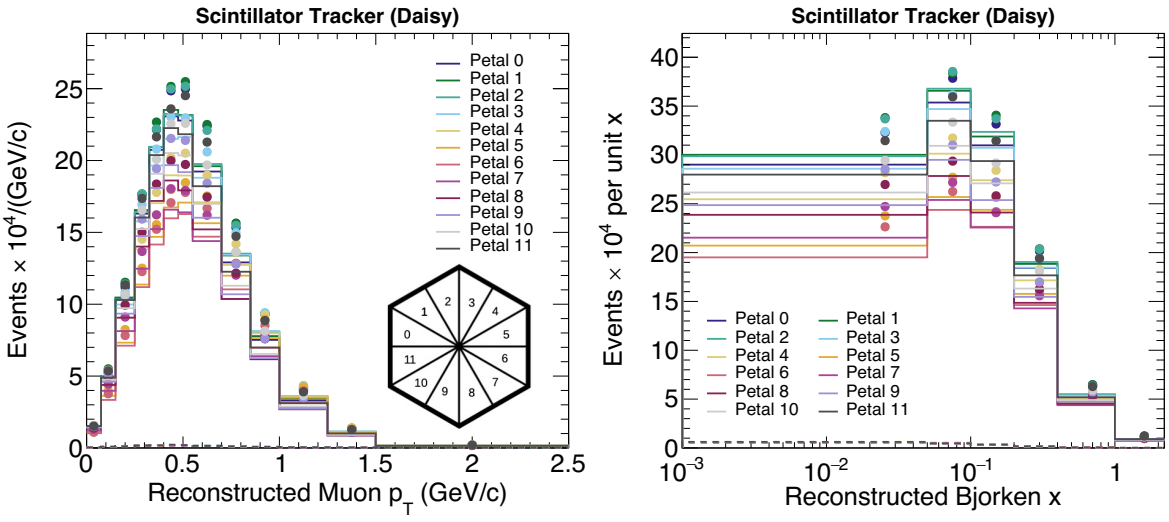

Figure 7.3: Selected event distribution for the scintillator tracker in 'daisy petals' both in antimuon p_{T} (left) and Bjorken x (right). The simulation prediction for individual petals is depicted using coloured solid lines described in the legend, while the dashed lines show the simulated background prediction. For clarity, the uncertainty on the simulation is not shown. The corresponding points represent the data with its statistical uncertainty, which is, however, too small to visualise. The hexagon insert illustrates petal positions looking downstream of the detector.

distributions with the background breakdown and the data-to-simulation ratios for the remaining nuclear targets of different materials are included in Appendix B.

The data distributions for the carbon-heavy scintillator tracker in both p_{T} and Bjorken x are generally higher than predicted by the simulation. Nevertheless, the data mostly falls within the systematic uncertainties of the simulation prediction, except for the high p_{T} and Bjorken x region. The individual sources contributing to the systematic uncertainty band are discussed in Chapter 8. Similarly, the data distributions for target 3 carbon are also higher than the simulation prediction. The heavier iron targets show some agreement with the prediction at low p_{T} and Bjorken x, but they are still underpredicted by the simulation at mid-to-high values of p_{T} and Bjorken x. The data for the heavy lead targets exhibits a significant overprediction at low p_{T} and Bjorken x, while still underpredicting the high p_{T} and Bjorken x region. In summary, the selected event distributions already indicate a significant nuclear dependence in antineutrino scattering which is not modelled by the simulation, especially in the low p_{T} and Bjorken x regions.

Finally, it is important to note that the scintillator tracker event distribution is also selected in 12 geometrical bins, referred to as 'daisy petals', as illustrated in Figure 7.3 for both p_{T} and Bjorken x. This extraction is essential for determining nuclear target-to-scintillator cross-section ratios using the matching-flux technique discussed in Subsection 5.1.1. The number of events selected in each 'daisy petal' reflects the direction of the antineutrino beam traversing the detector. Additionally, 'daisy petals' 5–7 experience a relative reduction in the number of events due to the MINOS coil cut.

7.2 Background subtraction

An inevitable next step in the cross-section analysis is subtracting any background that may have remained in the sample after the selection process to isolate a pure signal sample. Background subtraction, denoted as N^{bkg} in Equation 4.1 in Chapter 4, generally relies on simulation to predict background contamination. However, Figure 7.2 indicates that the background contribution from events originating in the scintillator planes surrounding the nuclear targets, referred to as plastic, to their respective nuclear target samples is relatively large compared to any other background category. Therefore, the background subtraction in passive targets employs data-driven methods to constrain this particular plastic background simulation prediction, aiming to better control its contribution and reduce dependence on the underlying interaction model. Other background contributions in both the nuclear targets and the scintillator tracker are simply subtracted from the data based on their simulation predictions.

The data-driven constraint of the plastic background simulation prediction in targets is referred to as the plastic sideband constraint. A sideband typically denotes a region abundant in the relevant background with minimal signal contamination, essentially representing the reverse of the selected sample in the analysis. Specifically, this

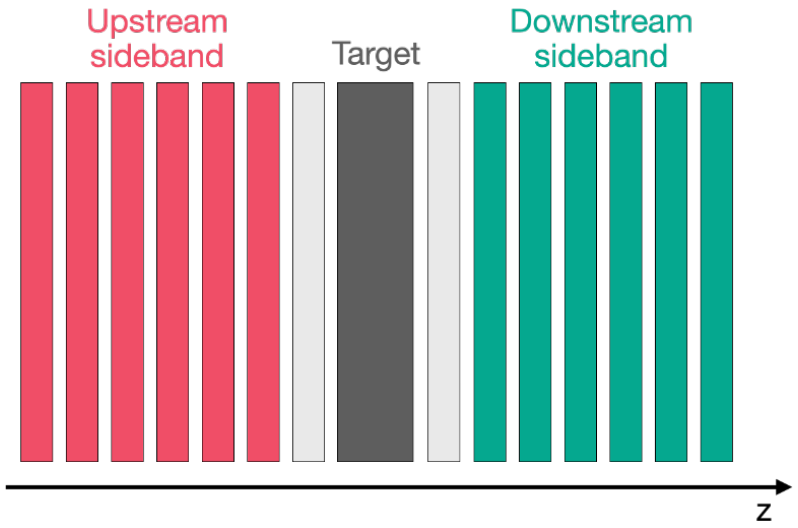

Figure 7.4: Diagram of the upstream (red) and downstream (green) sideband regions for a nuclear target (dark grey), each consisting of 6 scintillator planes. Note that the planes immediately next to the target are not included in the sideband regions.

analysis constructs two plastic sidebands for plastic coming from both the upstream and downstream of the individual targets to constrain the corresponding categories in Figure 7.2. These sidebands are defined as regions spanning six scintillator planes upstream and downstream of the individual targets, shadowing their transverse geometry, i.e. the shape in the x-y plane. This is illustrated in Figure 7.4. It is important to note that the planes immediately neighbouring the target are excluded to ensure that the regions are background-enhanced.

Events in these sideband regions for all targets of a given material are selected based on the criteria outlined in Section 7.1, with relevant adjustments to the z position cuts. Subsequently, they are combined into a single upstream and downstream sideband for one target combination to allow sufficient statistics for the constraint[1]. Similarly to Ref. [224],

[1]Similarly to target 1 itself, the upstream of target 1 is not used due to potential rock muon contamination. Conversely, downstream of target 1 is considered sufficiently downstream to be used in the constraint.

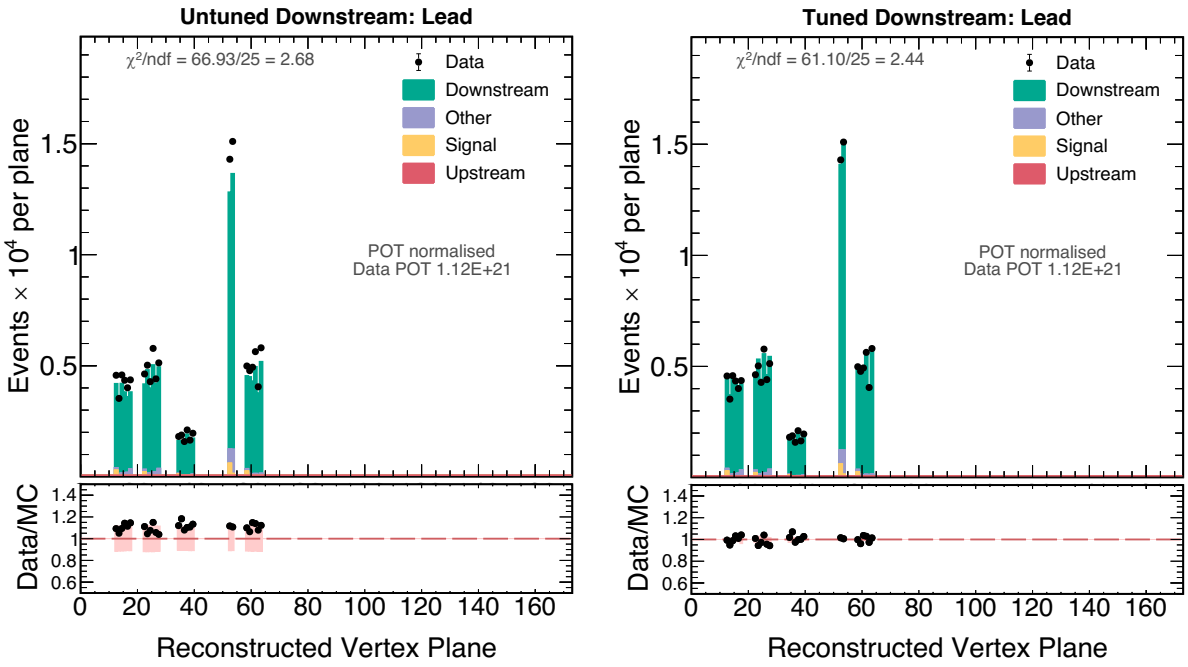

Figure 7.5: Pre-fit (left) and post-fit distribution (right) of the plastic downstream of lead target combination in the fit variable, i.e. the vertex plane. The data points in the top panel carry the statistical uncertainty on the data. The bottom panel displays the data-to-simulation ratio, with the black points including the statistical uncertainty on the ratio and the pink band representing the systematic uncertainty on the simulation (as there are no systematic uncertainties present in the data). Note the constrained systematic uncertainty in the post-fit data-to-simulation ratio.

normalisation factors for both upstream and downstream contributions in the upstream and downstream sideband simulation prediction for each material are fitted by minimising χ^2 with respect to the reconstructed vertex plane. Figure 7.5 illustrates the pre-fit and post-fit distributions in the reconstructed vertex plane for the downstream sideband of lead. Other sideband distributions in the fit variable, i.e. the vertex plane, are included in Appendix C.

Table 7.3 lists the individual scale factors for both upstream and downstream contributions from the upstream and downstream sidebands of carbon, iron, and lead, along with their corresponding statistical and systematic uncertainties. The statistical uncertainty represents the statistical power of the sideband, while the systematic uncertainty is evaluated by performing the sideband fit in each systematic universe (further explained in Chapter 8). As expected, the scale factors for various material sidebands are close to 1 and comparable, considering that all these sidebands constitute scintillator planes. Slight variations can be attributed to differences in the transverse geometries resulting from their shadowing of targets.

Figure 7.6 then illustrates the impact of these scale factors on the p_{T} and Bjorken x kinematic distributions in the downstream sideband of lead. The fitted distribution generally models the data better, but the normalisation scale factor is obviously unable to eliminate the shape differences in the data-to-simulation ratios of these distributions. Notably, the ratio plots highlight the effectiveness of the fit in constraining the systematic uncertainties on the simulation. All other sideband kinematic distributions before and after the fit are included in Appendix C.

Material	Upstream ($\pm$ stat. $\pm$ sys.)	Downstream ($\pm$ stat. $\pm$ sys.)
Carbon	$1.097 \pm 0.005 \pm 0.134$	$1.098 \pm 0.005 \pm 0.126$
Iron	$1.135 \pm 0.004 \pm 0.132$	$1.131 \pm 0.003 \pm 0.131$
Lead	$1.135 \pm 0.003 \pm 0.137$	$1.110 \pm 0.003 \pm 0.132$

Table 7.3: Normalisation scale factors with their statistical and systematic uncertainties for the upstream and downstream contributions from the upstream and downstream sideband fit for carbon, iron, and lead.

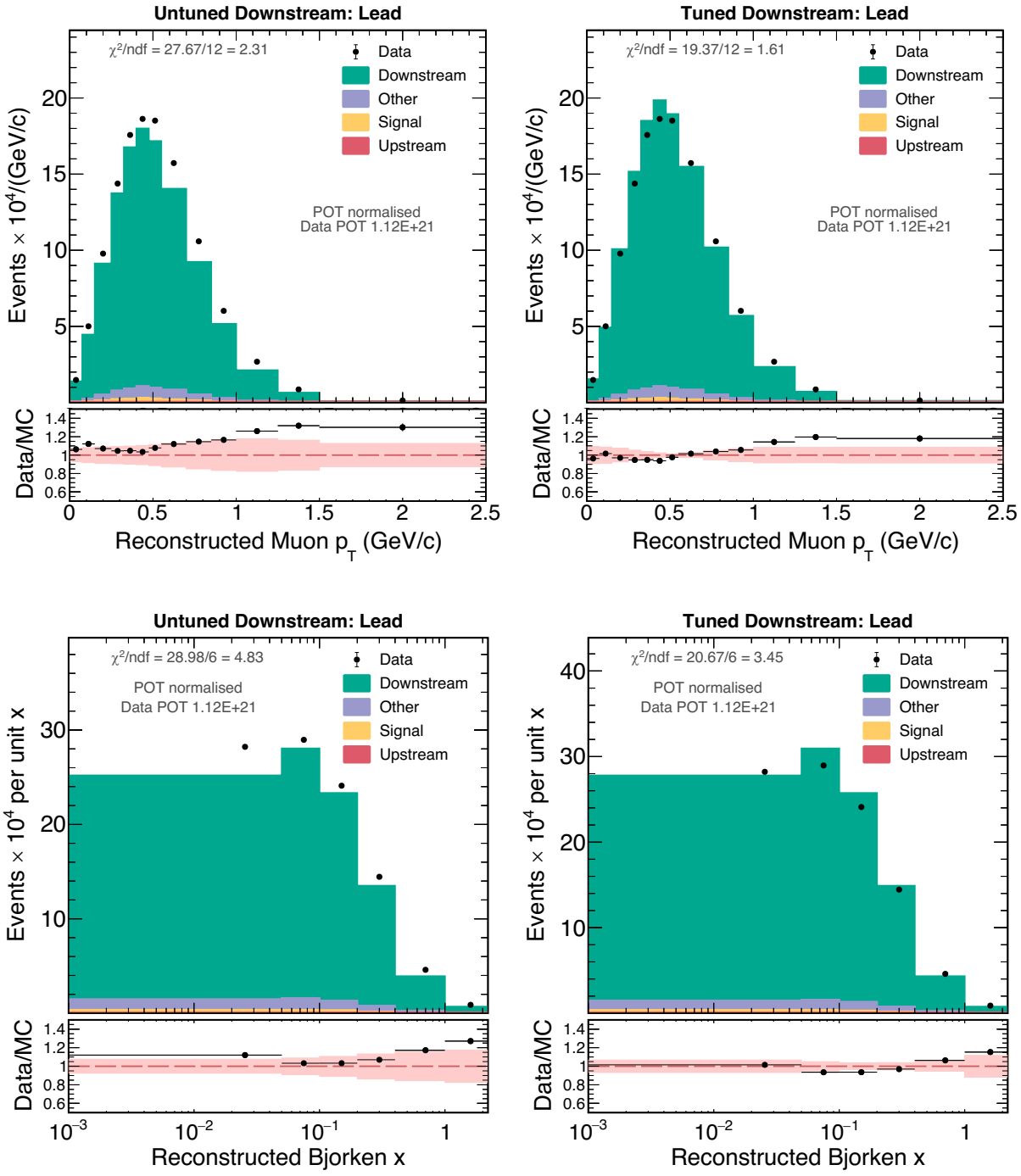

Figure 7.6: Pre-fit distributions (left) of plastic downstream of lead target combination in antimuon p_{T} (top) and Bjorken x (bottom), along with the corresponding post-fit distributions (right) with applied scale factor. The data points in the top panel carry the statistical uncertainty on the data. The bottom panel displays the data-to-simulation ratio, with the black points including the statistical uncertainty on the ratio and the pink band representing the systematic uncertainty on the simulation (as there are no systematic uncertainties present in the data). Note the constrained systematic uncertainty in the post-fit data-to-simulation ratio.

The impact of the scale factors in the signal region is then shown for target 5 lead in both p_{T} and Bjorken x in Figure 7.7. Compared to the corresponding selected event distribution in Figure 7.2, and similarly to the sideband region, there is an improved agreement between the data and the simulation prediction in the signal region.

The scaled upstream and downstream plastic background together with the other background predicted by the simulation is then subtracted from the data distribution in each nuclear target of a given material. Figure 7.8 shows an example of the background-subtracted distribution for target 5 lead both in p_{T} and Bjorken x. The data-to-simulation ratio remains approximately identical to that observed in the selected event distributions in Figure 7.7. All other background-subtracted distributions for all targets of carbon, iron and lead can be found in Appendix D.

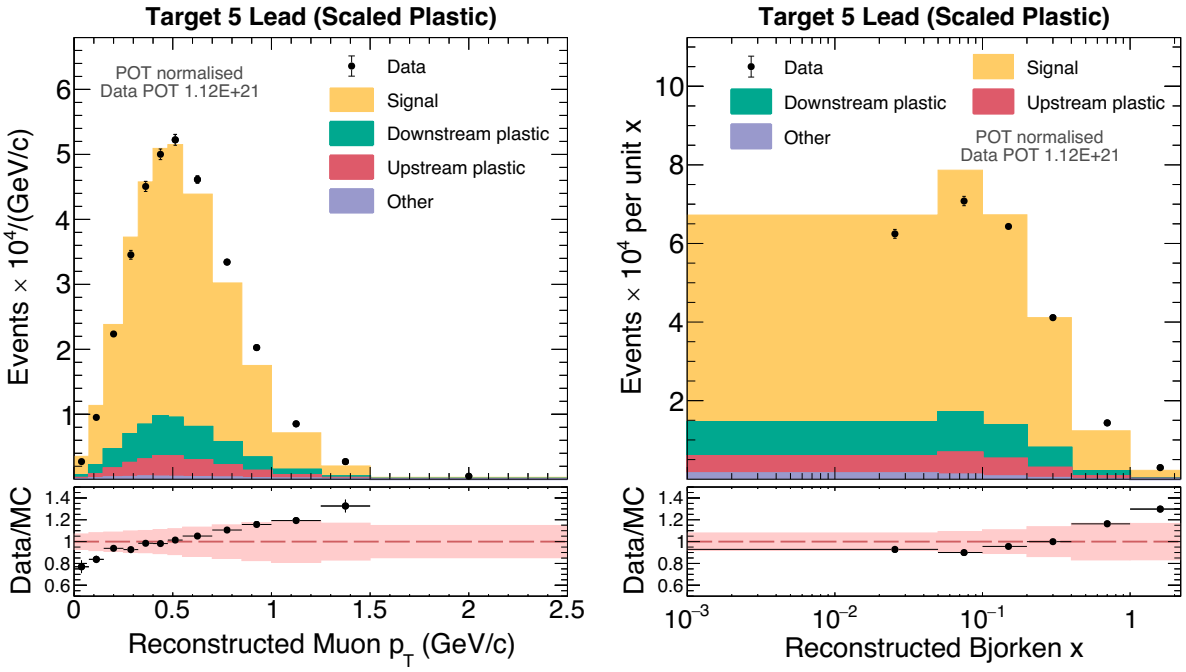

Figure 7.7: Selected event distributions in target 5 lead in both antimuon p_{T} (left) and Bjorken x (right) with the scaled upstream and downstream plastic contribution. In the top panel of each plot, the black points represent the data with its statistical uncertainty, while the simulation is broken down into various sources of signal and background stacked in the descending order of their contribution. The bottom panel shows the data-to-simulation ratio. The solid band around the dashed line at 1 represents the systematic uncertainty on the simulation, while the black points carry the statistical uncertainty of the ratio.

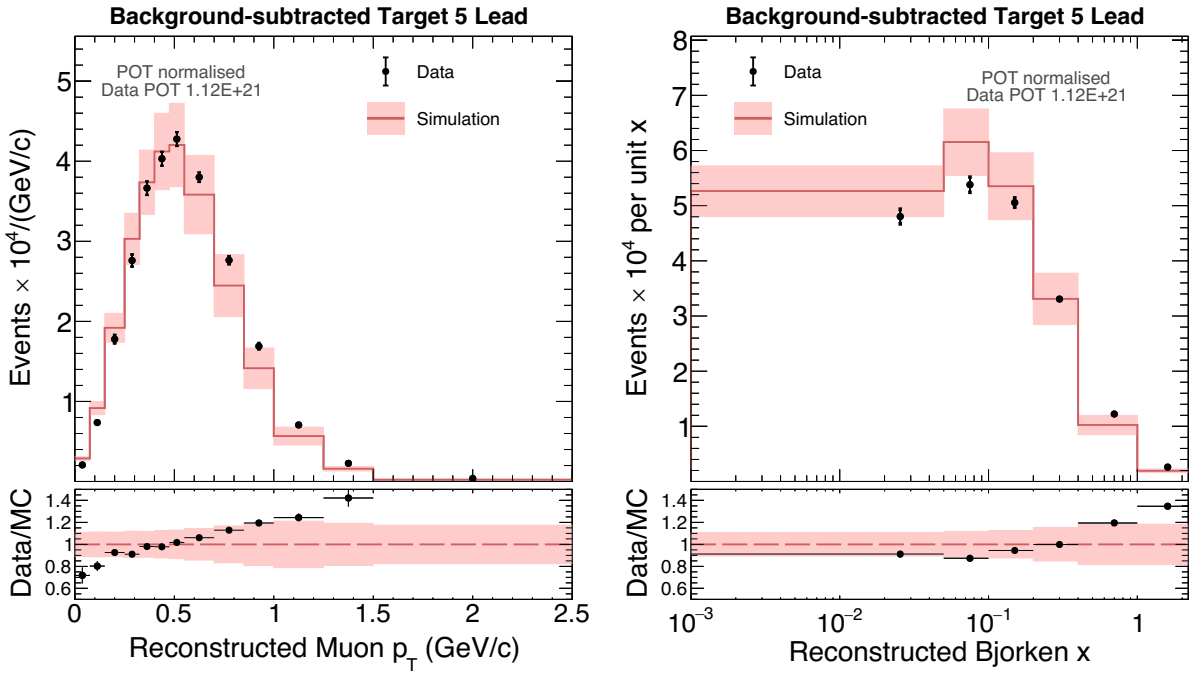

Figure 7.8: Background-subtracted distributions in antimuon p_{T} (left) and Bjorken x (right) for target 5 lead. In the top panel, the pink band on the simulation represents both statistical and systematic uncertainties. The data points also carry both statistical (inner error bar) and systematic (outer error bar, which is the sum of statistical and systematic errors) uncertainties. The bottom panel of each plot displays the data-to-simulation ratio, with the pink band around 1 representing systematic uncertainties on both the data and the simulation, while the black points reflect the statistical uncertainty on the data-to-simulation ratio.

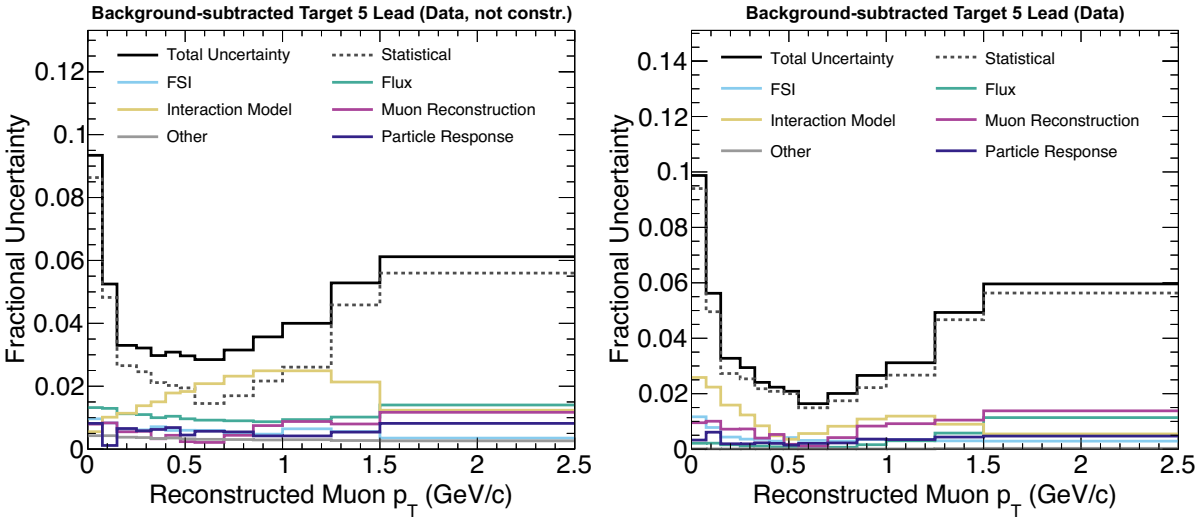

Figure 7.9: Fractional uncertainty breakdown for the background-subtracted data distribution of target 5 lead as a function of p_{T} without (left) and with (right) the plastic sideband constraint. Note the reduction of the uncertainties, particularly the 'Interaction Model' error band, in the bulk of the distribution.

Crucially, background subtraction introduces systematic uncertainties to the data. The fractional uncertainties on the data background-subtracted distributions in p_{T} for target 5 lead are summarised in Figure 7.9. Specifically, Figure 7.9 demonstrates the impact of subtracting background purely based on the simulation prediction compared with subtracting the background with the data-constrained upstream and downstream plastic. The sideband constraint visibly reduces the uncertainties in the main bulk of the distribution while slightly increasing the uncertainty in the tails. This difference is most striking in the 'Interaction Model' error band. Note that a detailed discussion of the systematic uncertainties is included in Chapter 8. The equivalent comparison for Bjorken x distribution is included in Appendix D.

The scintillator tracker background amounting to about 1% is simply subtracted from the data based on its simulation prediction as mentioned earlier. The background-subtracted distributions for the scintillator tracker in both p_{T} and Bjorken x are shown in Figure 7.10 and their corresponding fractional uncertainty breakdowns are displayed

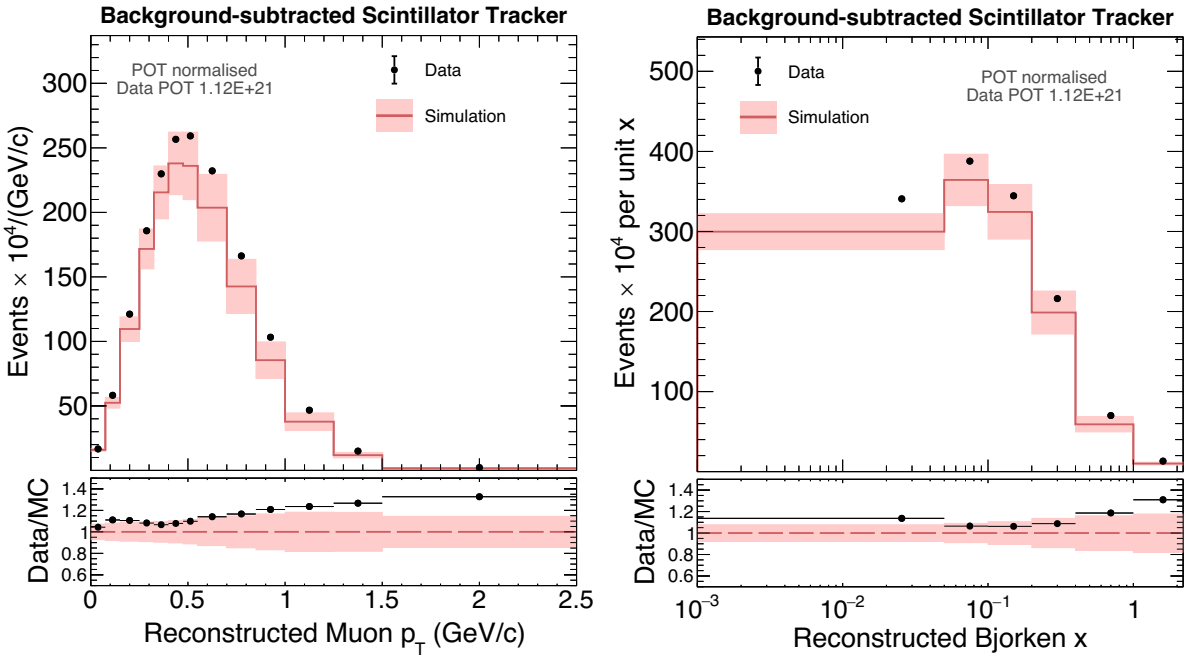

Figure 7.10: Background-subtracted distributions in antimuon p_{T} (left) and Bjorken x (right) for scintillator tracker. In the top panel, the pink band on the simulation represents both statistical and systematic uncertainties. The data points also carry both statistical (inner error bar) and systematic (outer error bar, which is the sum of statistical and systematic errors) uncertainties. The bottom panel of each plot displays the data-to-simulation ratio, with the pink band around 1 representing systematic uncertainties on both the data and the simulation, while the black points reflect the statistical uncertainty on the data-to-simulation ratio.

in Figure 7.11. Furthermore, the background is subtracted in the same manner in each of the 12 'daisy petals' of the scintillator tracker in order to determine the nuclear target-to-scintillator cross-section ratios using the matching-flux technique discussed in Subsection 5.1.1. The background-subtracted 'daisy petal' distributions are shown in both p_{T} and Bjorken x in Figure 7.12.

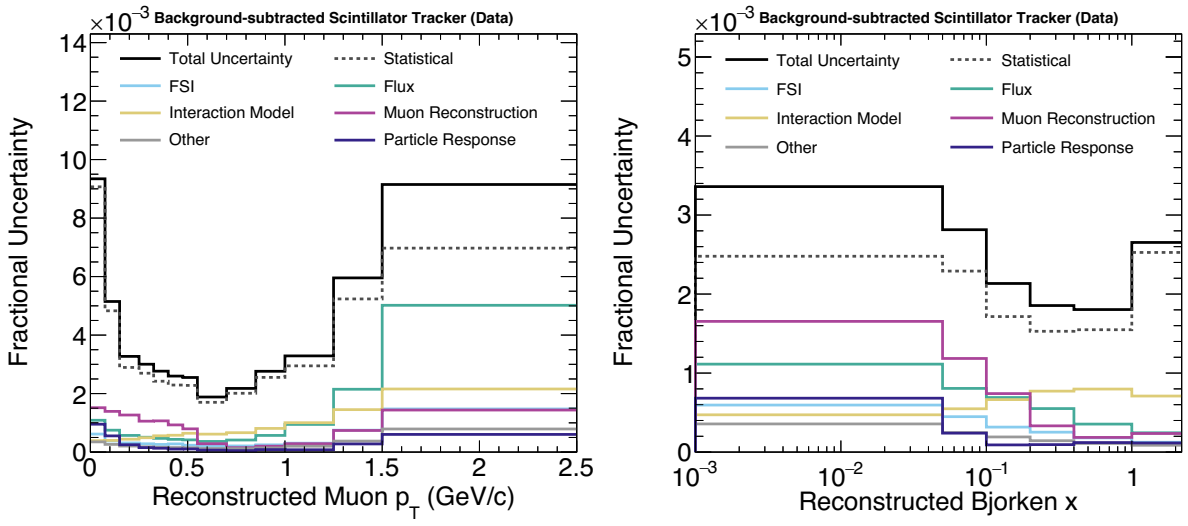

Figure 7.11: Fractional uncertainty breakdown for the background-subtracted data distributions of scintillator tracker as a function of p_{T} (left) and Bjorken x (right).

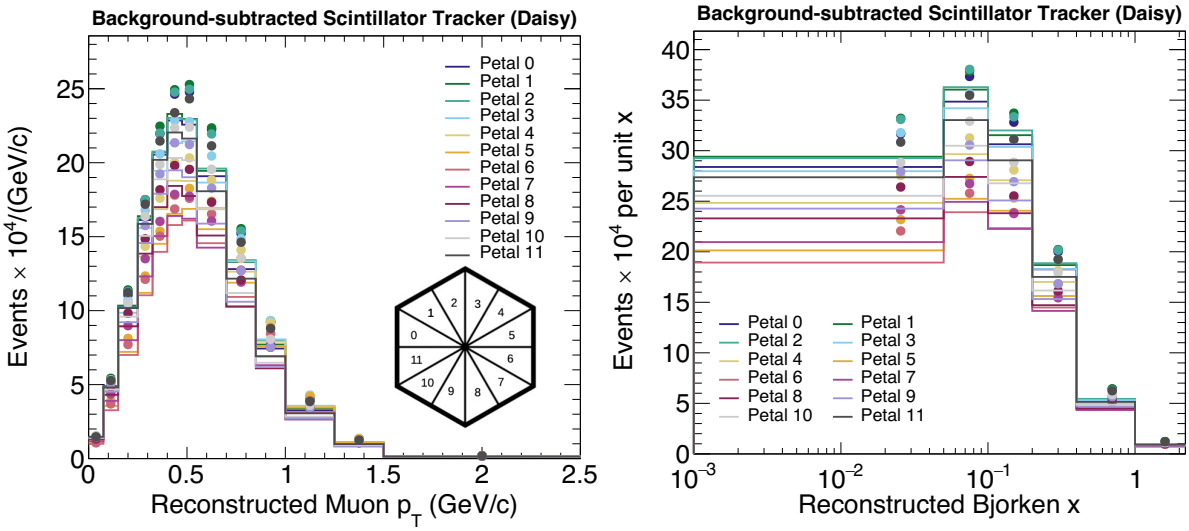

Figure 7.12: Background-subtracted distribution for the scintillator tracker in 'daisy petals' for both antimuon p_{T} (left) and Bjorken x (right). The background-subtracted data and the simulation prediction for individual petals are colour-coded as described in the legend. The statistical and systematic uncertainties on the data are too small to visualise. For clarity, the uncertainty on the simulation is not shown. The hexagon insert illustrates the positions of the petals looking downstream of the detector.

7.3 Migration and unfolding

Background-subtracted distributions offer the most accurate estimates of signal rates in reconstructed quantities. However, finite detector resolution and imperfect reconstruction may lead to deviations in the reconstructed kinematics of an event from its true kinematics, as demonstrated in Figure 7.13. Put simply, there can be a difference between the actual physics that occurred and the physics that was measured. This effect, referred to as smearing, results in some events being reconstructed—or, in other words, migrated—into an adjacent or more distant bin than where they belong, smearing out the fine structure. The extent of this migration depends on how much lower or higher the reconstructed value is compared with the true value. The simulation sample, which contains both the true generated and the reconstructed information about the simulated events, is used to estimate the amount of smearing in data via a so-called migration matrix.

The migration matrix can be represented as a two-dimensional histogram relating bin α of the true generated distribution on the y-axis to bin j of the reconstructed dis-

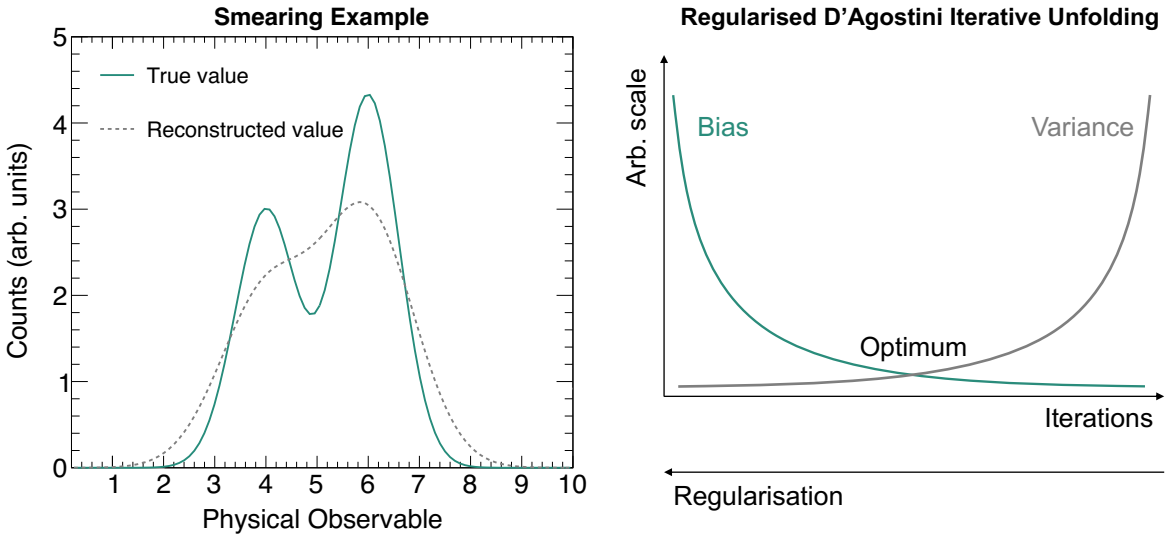

Figure 7.13: Left: Smearing example of a two-component Gaussian model. The true histogram (solid line) shows more prominent peaks than the reconstructed histogram (dashed line) Right: Demonstration of the bias-variance trade-off in regularised D'Agostini iterative unfolding. Increasing the number of iterations leads to a less regularised solution with more variance. In practice, more variance also means that the statistical and systematic uncertainties increase rapidly.

tribution on the x-axis, $U_{j\alpha}$. The more diagonal the matrix is, the less smeared the reconstructed distribution is. Examples of migration matrices for target 5 lead and the scintillator tracker in both p_{T} and Bjorken x are shown in the Figure 7.14. It is important to note that the migration matrices also consider underflow and overflow bins, which include values below or above the lowest and highest bin boundaries. This accounts for smearing in and out of the sample; however, these bins are not explicitly shown in Figure 7.14. All other migration matrices for passive targets and the scintillator tracker divided in the geometrical bins, i.e. 'daisy petals', are included in Appendix E.

The p_{T} distribution is primarily smeared by the finite antimuon momentum resolution of the detector, stemming from the size of the scintillator strips affecting the length of particle tracks. On the other hand, the Bjorken x distribution smearing likely arises from

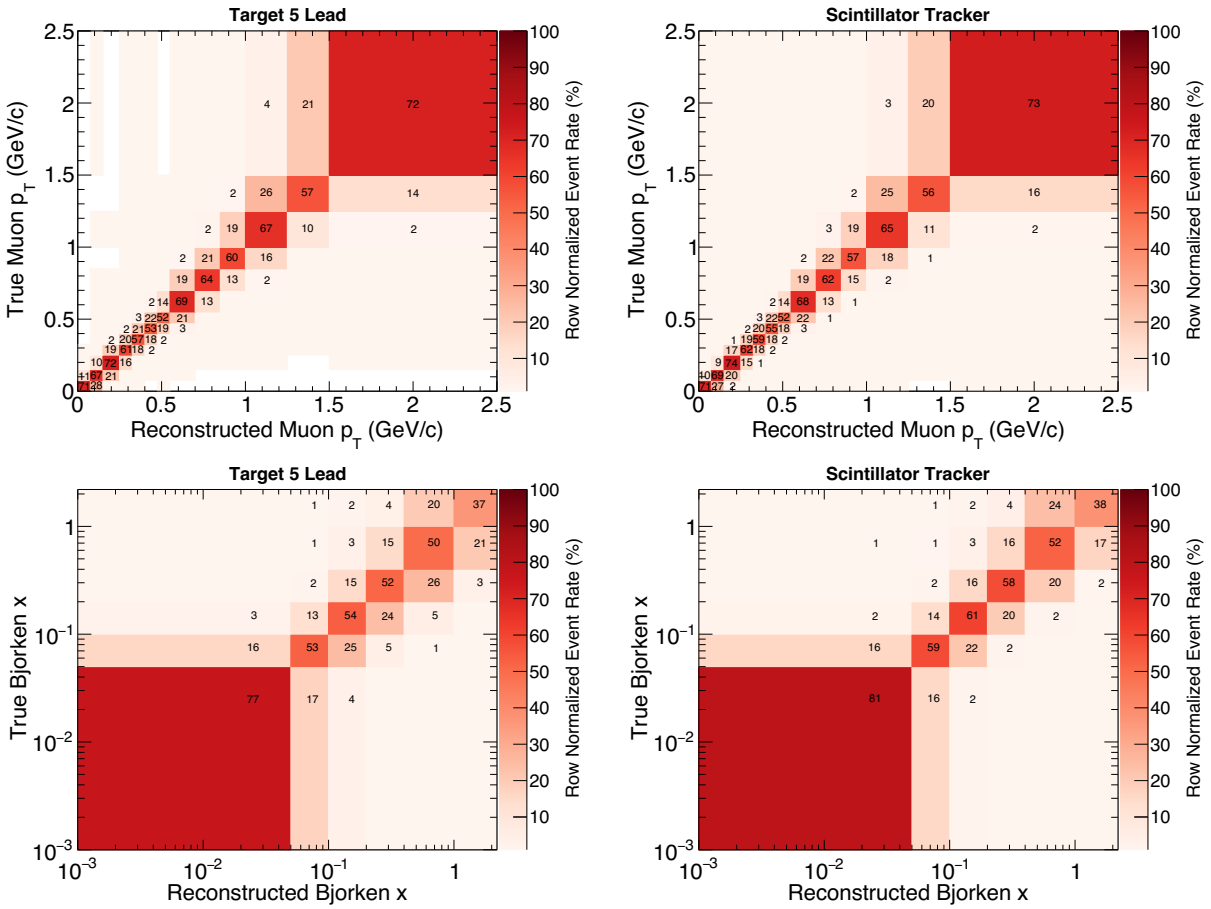

Figure 7.14: Row-normalised migration matrices for target 5 lead (left panel) and scintillator tracker (right panel) both in p_{T} (top) and Bjorken x (bottom). Each row of the migration matrix is normalised to 1 to represent the probability that an event generated in a given bin α will be reconstructed in a bin j.

the calorimetric correction used to estimate the invisible energy from neutrons in the hadronic recoil energy reconstruction, as described in Chapter 6. In addition, the region with $x > 1$, discussed in Chapter 4, is already inherently challenging at the true simulation level. Events in this region predominantly originate from intranuclear scattering, and may not necessarily include other physics contributions such as short-range correlations indicated by electron-scattering data [141, 225]. Therefore, caution is exercised when working with this particular bin, as discussed later on. In general, the migration matrices are more diagonal in the scintillator tracker than in the passive target region due to better tracking (more active material).

In order to report a detector-independent cross-section, the smearing of the reconstructed distribution must be reversed. The process of estimating the true distribution from the measured smeared spectrum is called unfolding. Unfolding the distributions is crucial for future reinterpretations of the result, combinations with other experiments, and aiding the understanding of various physics models. In the cross-section extraction Equation 4.1, the unfolding process is denoted by $\Sigma_j \tilde{U}_{j\alpha}$ acting on bin j of the background subtracted reconstructed distribution.

Unfolding could be achieved by inverting the migration matrix, which is, however, not always invertible. Moreover, unfolding is, by definition, an ill-posed problem as small changes in the measured distribution can lead to significant fluctuations in the true distribution, i.e. large variance [226]. Introducing regularisation in the unfolding process can address this issue by trading off some variance for a controlled amount of bias[2]. Similar to other MINERvA results, this analysis uses the D'Agostini iterative regularisation method [227, 228] implemented in the RooUnfold package [229] in ROOT [230], where the regularisation parameter is the number of iterations, as illustrated in Figure 7.13.

The $(k+1)$th iteration of the D'Agostini method is determined by

$$\lambda_\alpha^{(k+1)} = \frac{\lambda_\alpha^{(k)}}{\sum_j U_{j\alpha}} \sum_j \frac{U_{j\alpha} y_j}{\sum_\beta U_{j\beta} \lambda_\beta^{(k)}}, \tag{7.2}$$

[2]Bias is defined as the difference between the expectation value of the unfolded result and the true expectation value, which in the simulation is the true generated value.

where $U_{j\alpha}$ is the simulation-based migration matrix, $\lambda_{\alpha}^{(k)}$ represents the vector of bins α of the true distribution at iteration k, and y_j is the vector of bins j of the reconstructed distribution. In RooUnfold, the initial prior $\boldsymbol{\lambda}^{(0)}$ is the simulation prediction of the true distribution, i.e. $\boldsymbol{\lambda}^{(0)} = \boldsymbol{\lambda}^{\mathrm{MC}}$ [229]. A more detailed description of the method can be found in the Appendix F.

In practice, the unfolding procedure is independently applied to both the central value histogram and all systematic universes. Since any statistical variation in the reconstructed distribution can be interpreted as a smearing of the fine structure of the true distribution, unfolding the distribution using many iterations results in the statistical and systematic uncertainties increasing rapidly. Therefore, it is crucial to determine the optimal number of iterations demonstrated in Figure 7.13, balancing the aforementioned reduction of bias while keeping variance minimal. MINERvA analyses find this number of iterations via so-called warping studies.

Unfolding the underlying simulation with the migration matrix based on that simulation would result in perfect unfolding in one iteration, leading to maximum modelling bias. Therefore, warping studies involve the unfolding of fake data, referred to as 'warped models'. These warped models are simulations that have been reweighted to depict alternative physics models, exaggerate features of the underlying distributions, or capture differences in the shapes of distributions between the data and the original underlying simulation. The reconstructed distributions of warped models, where the truth is known, are unfolded using a migration matrix based on the original underlying simulation. The number of iterations is then determined by looking at the least number of iterations required for χ^2, defined as

$$\chi^2 = \sum_{\alpha,\beta} \left(\lambda^{(k)} - \lambda\right)_{\beta} V^{-1}_{\beta\alpha} \left(\lambda^{(k)} - \lambda\right)_{\alpha}, \tag{7.3}$$

to stabilise near minimum, i.e. the number of degrees of freedom of the distribution. Here, $\lambda^{(k)}$ is the unfolded distribution after k iterations in bin α or β, λ is the true value of the distribution and V is the unfolding covariance matrix.

Warping studies are performed purely as statistical studies, meaning only the central values of reconstructed distributions are considered. To address statistical fluctuations, central values of warped models are used to generate 100 Poisson-distributed statistical universes with a mean of the number of warped model entries in each bin, and the distributions are unfolded in each of these statistical universes. The list of conducted warping studies can be found in Table 7.4.

Pion production is one of the largest contributions to this medium-energy antineutrino-inclusive sample. Therefore, two warped models affecting the pion production—'Resonant M_A^{RES} nominal' and 'Non-resonant pion production' listed in Table 7.4—were chosen to investigate the potential unfolding instabilities and to assess the model dependence on the underlying simulation. Furthermore, two different models for the 2p2h sample were

Warped Model	Description
Resonant M_A^{RES} nominal	Resonant axial mass M_A^{RES} and CCResNorm in the Rein-Seghal model described in Subsection 5.2.2 are set to their GENIE nominal values, i.e. $M_A^{\mathrm{RES}} = 1.12$ GeV/c^2 and CCResNorm = 1.0
Non-resonant pion production	Non-resonant pion production reduction described in Section 5.2.2 is varied within its 1σ, i.e. reduction to 47% of its nominal value (rather than to 43%)
Valencia 2p2h enhancement off	Nominal Valencia 2p2h model, i.e. the 50% enhancement over the nominal prediction of Valencia 2p2h described in Section 5.2.2 is not used
SuSA 2p2h	Valencia 2p2h is reweighted to the Super-Scaling Approximation (SuSA) 2p2h model [125] according to Refs. [126, 127] (without the 2p2h enhancement)
Bjorken x ratio	Central value is reweighted according to a fitted smooth function to the background subtracted data/MC ratio in the tracker, i.e. 1st-degree polynomial as a function of true Bjorken x with a constant value equal to the ratio value of the centre of the last bin above the centre of the last bin (1.6).
Antineutrino energy ratio	Same as above except using a fitted 3rd-degree polynomial as a function of true antineutrino energy, constant and equal to the ratio value of the centre of the last bin above the centre of the last bin (19 GeV).

Table 7.4: List of warped models used to determine to number of iterations of the D'Agostini unfolding.

tested, specifically the base Valencia 2p2h ('Valencia 2p2h enhancement off') and the alternative 2p2h model based on the Super-Scaling Approximation ('SuSA 2p2h') [125]. The choice of these models was motivated particularly by the impact of neutrons in final states from the 2p2h interaction on the high Bjorken x distribution. Finally, the two last warped models listed in the Table 7.4 are data/MC ratio warps. These warps were implemented to examine potential unfolding issues arising from differences between the underlying simulation and the data, a critical consideration given that data unfolding relies on the simulation.

The warping studies in Table 7.4 were conducted for each kinematic distribution in every target. The same warping studies were also replicated for each of the geometrical bins, referred to as 'daisy petals', of the scintillator tracker distribution used in the nuclear target to scintillator cross-section ratios using the matching-flux technique discussed in Subsection 5.1.1. Generally, the warping studies showed that the passive target region requires one more iteration to unfold than the scintillator tracker. However, to maintain consistency across various materials for each kinematic distribution, the number of iterations was standardised across all warping studies. All antimuon p_{T} distributions were unfolded with 3 iterations of the D'Agostini unfolding, and all Bjorken x distributions were unfolded with 9 iterations as listed in the Table 7.5.

An example of the 'Resonant M_A^{RES} nominal' warping study for target 5 lead and the scintillator tracker petal 7 both in antimuon p_{T} and Bjorken x is shown in Figure 7.15. While the median χ^2 for p_{T} is not very far off from the number of degrees of freedom to begin with and converges almost immediately, the Bjorken x median χ^2 has the typical shape of a warping study—each iteration brings the χ^2 closer to the number of degrees of freedom. Furthermore, the scintillator tracker petal 7 distribution in Bjorken x has a

Variable	Number of iterations
p_{T}	3
Bjorken x	9

Table 7.5: Number of iterations used in the D'Agostini unfolding of antimuon p_{T} and Bjorken x determined by the warping studies to extract final cross-sections.

'check-mark' shape, where the median χ^2 dips to a minimum at the number of degrees of freedom and then slightly diverges to about twice the number of degrees of freedom over several iterations. To investigate the potential model dependence (and given this is not a blind analysis), the data cross-section was extracted with the warped model as an alternative central value employing the standard cross-section extraction procedure

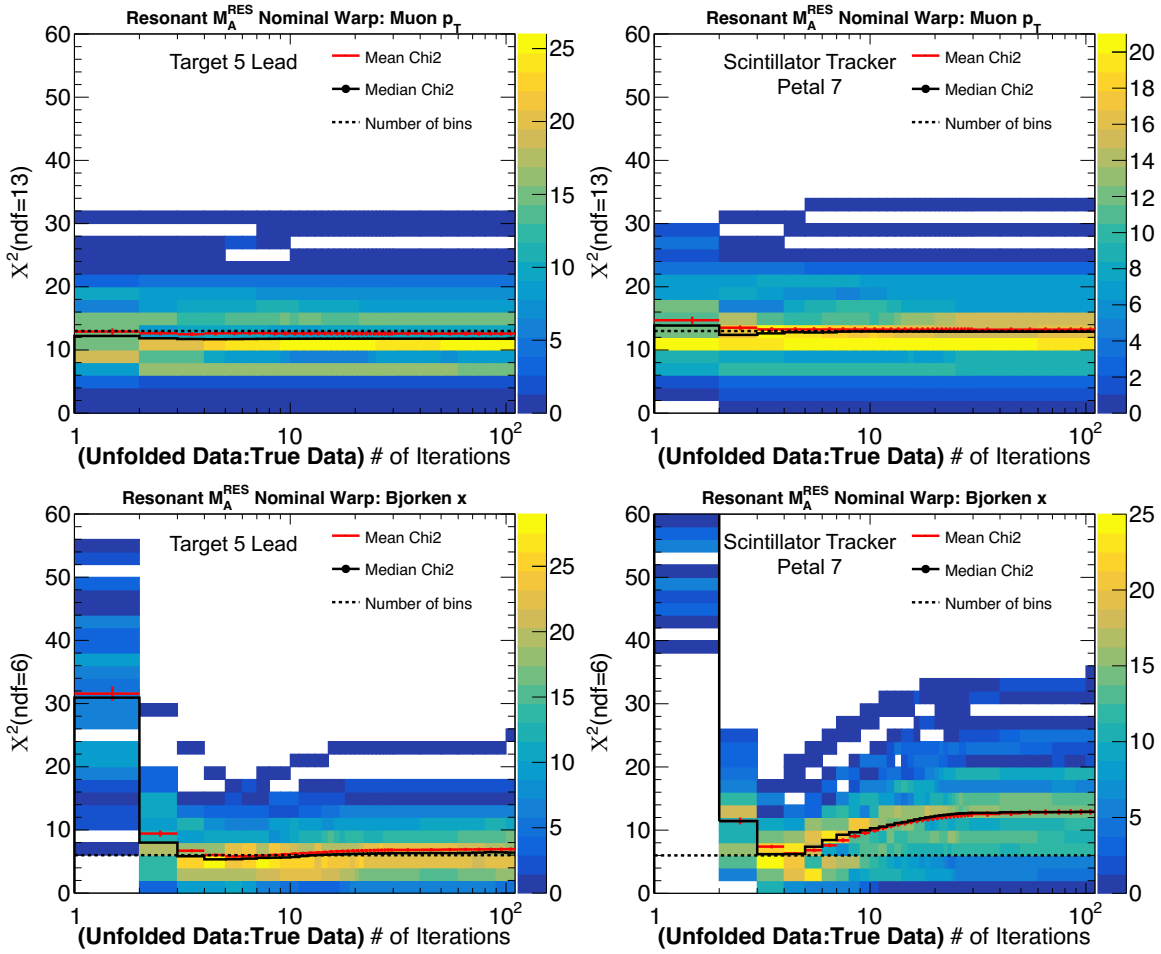

Figure 7.15: The 'Resonant M_A^{RES} nominal' warping study conducted for target 5 lead (left panel) and the scintillator tracker petal 7 (right panel) in both antimuon p_{T} (top) and Bjorken x (bottom). Each heatmap displays the calculated χ^2 between the unfolded and true distribution of the warped model as a function of the number of iterations for each of the 100 Poisson throws. The solid lines represent the median and mean χ^2, while the dashed line indicates the number of bins or degrees of freedom (ndf). In p_{T}, the median χ^2 quickly approaches the ndf, signalling minimal bias. In contrast, the median χ^2 for Bjorken x converges to the ndf more gradually. The bottom right heatmap for the scintillator tracker petal 7 exhibits a 'check-mark' shape, indicating convergence to a minimum and then a slight divergence. This pattern prompted further investigation into potential model dependence.

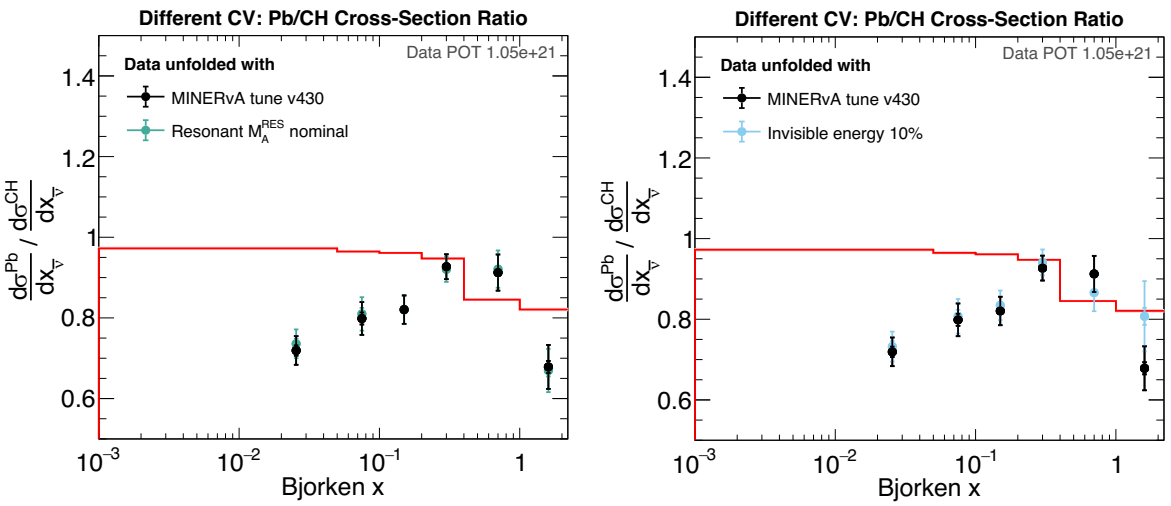

Figure 7.16: Left: Comparison of the lead-to-scintillator data cross-section ratio extracted with the underlying simulation MINERvA tune v4.3.0 and the warped model 'Resonant M_A^{RES} nominal' as a function of Bjorken x. The central values of the data cross-section extracted using the warped model are encompassed by the total uncertainty (including the systematic, represented by the outer error bars) of the data cross-section extracted using the original simulation. This indicates that any potential model dependence is covered by the underlying uncertainty. Right: Comparison of the lead-to-scintillator data cross-section ratio as a function of Bjorken x extracted with the original simulation and 'Invisible energy 10%' central value to investigate model dependence arising from neutron modelling, revealing possible bias in the $x > 1$ bin.

described in this chapter with 9 iterations of unfolding for Bjorken x as listed in the Table 7.5. The data cross-section unfolded with this alternative model was compared with the cross-section extracted with the original simulation to show that the central values of the alternative model are covered by the total (and also just the systematic—outer error bars) uncertainty, and hence any potential model dependence is accounted for by the overall uncertainty. For clarity, this is demonstrated in Figure 7.16 as a lead-to-scintillator cross-section ratio with the individual cross-section comparisons and other cross-section ratio comparisons included in the Appendix G.

The 'SuSA 2p2h' warping study for the same targets (target 5 lead and the scintillator tracker petal 7) in both p_{T} and Bjorken x is also shown in the Figure 7.17 using the calculated mean of the pull distribution in each bin at various numbers of iterations. The pull of a kinematic distribution in each bin i is defined as

$$\mathrm{pull}_i = \frac{(\mathrm{reco} - \mathrm{true})_i}{\sigma_i^{\mathrm{true}}}, \tag{7.4}$$

where 'reco' is the reconstructed value, 'true' is the unfolded value and σ_i^{true} is the uncertainty on the unfolded value in the given bin i. This visualisation of the warping study also illustrates that the 'SuSA 2p2h' warped model can be unfolded using the central value migration matrix for both p_{T} and Bjorken x. The pull distributions nicely represent how with each iteration the unfolding gets less biased, i.e. the mean of the pull distribution in every bin gets closer to zero. The equivalent distribution to Figure 7.15 for the 'SuSA 2p2h' warped model and the pull distribution for the 'Resonant M_A^{RES} nominal' warp are included in the Appendix G.

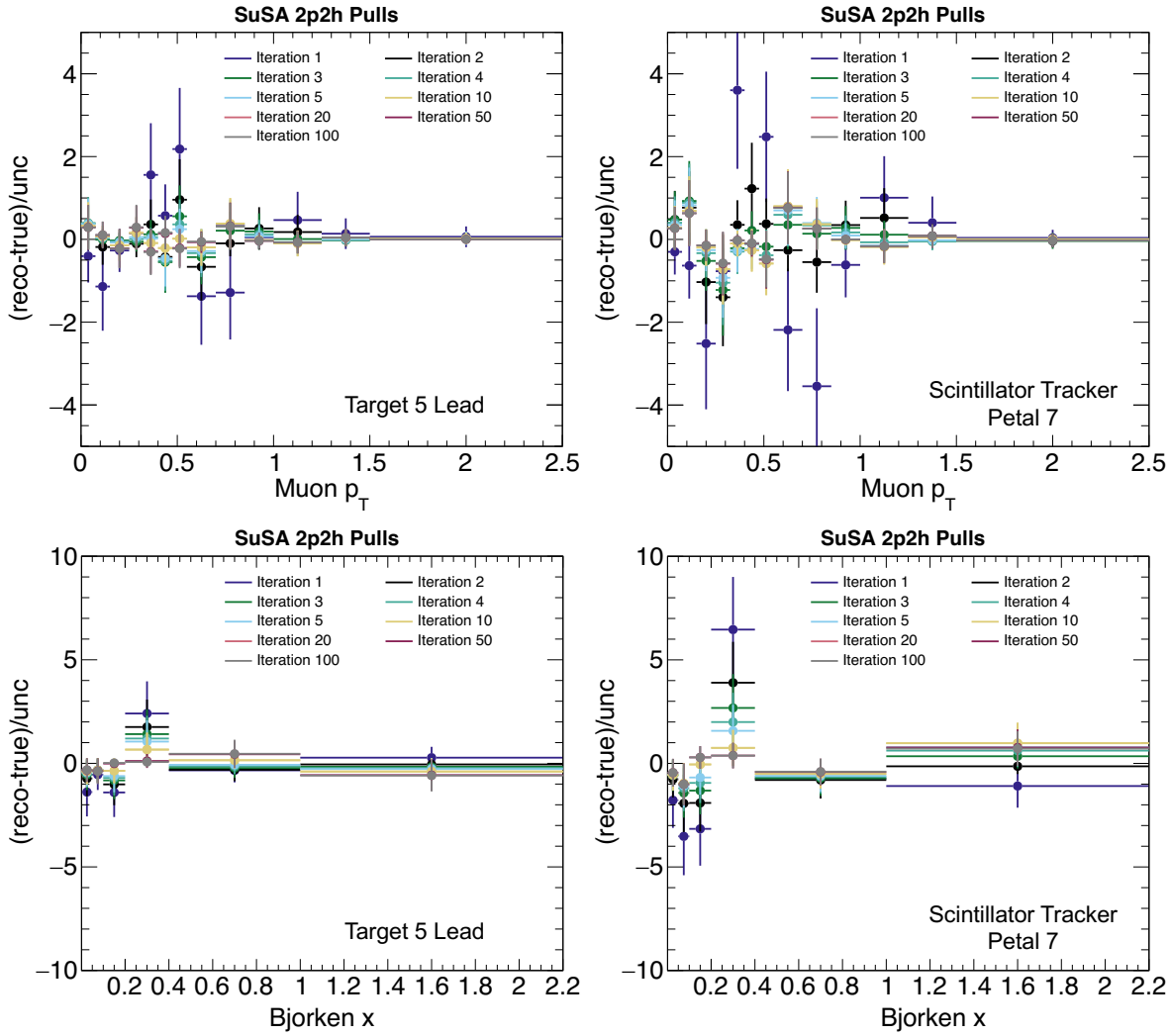

Figure 7.17: Pull distributions for the 'SuSA 2p2h' warping study for target 5 lead (left panel) and the scintillator tracker petal 7 (right panel) in both antimuon p_{T} (top) and Bjorken x (bottom). Each pull distribution illustrates the reduction in bias with each iteration of the unfolding process. In other words, the mean of the pull distribution in each bin converges toward zero.

Apart from the warping studies detailed in Table 7.4, an additional simple study was conducted to evaluate the potential bias introduced by neutron production in antineutrino interactions in this analysis. This is particularly relevant as antineutrino interaction generators are typically employed to correct for these effects, given that most of the energy deposited by neutrons in detectors is invisible. However, a recent MINERvA measurement of multi-neutron cross-sections showed disagreement with predictions from several leading models [231]. Hence, the neutron modelling corrections introduced at the unfolding level could impact the Bjorken x distribution, especially in the high x region, where they are coupled with the already inherently challenging modelling of the $x > 1$ region mentioned earlier in this chapter.

Thus, the strategy was to examine how a change at the true level of the simulation (and not the reconstructed) impacts the analysis. Naïvely, this was accommodated by introducing additional invisible energy into the system, achieved by increasing the true antineutrino energy by 10% of the true invisible energy while keeping the antimuon system intact. Similar to the investigation of the bias in the case of the 'check-mark' shaped warping study discussed above, the data cross-section was extracted with this new model using 9 iterations of unfolding for Bjorken x and compared to the cross-section extracted using the original simulation. The lead-to-scintillator cross-section ratio in Figure 7.16 shows that the central values of the alternative model are covered by the total uncertainty, except for the last $x > 1$ bin. This potential source of model bias requires further action, and the possibility of including an additional source of systematic uncertainty related to neutron modelling is discussed in Chapter 8. The individual cross-section comparisons and the other cross-section ratio comparisons can be found in Appendix G.

Finally, RooUnfold's implementation of the D'Agostini unfolding doesn't take into account uncertainties in the response matrix due to the finite statistics of the simulation sample [229]. This leads to an underestimation of the statistical uncertainty of the unfolded sample and can be particularly significant for large sample analyses such as this one. To address this issue, a correction factor to the statistical uncertainty related to the

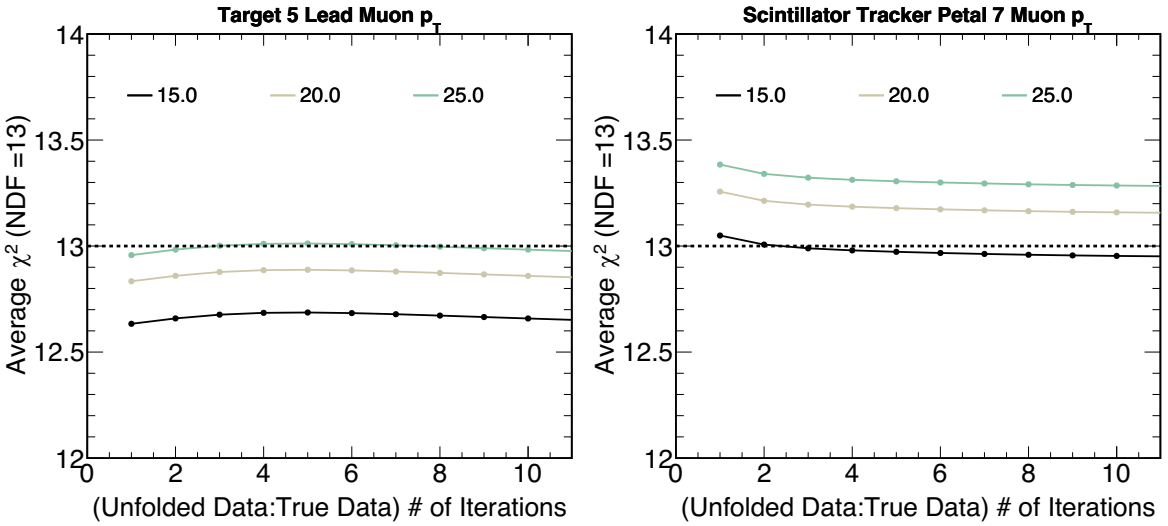

Figure 7.18: Correction factor F to the statistical uncertainty of the unfolded sample due to finite size of the simulation in the migration matrix for target 5 lead and the scintillator tracker petal 7 in antimuon p_{T}. The solid lines illustrate that at the selected number of iterations, i.e. 3 iterations, the calculated χ^2 between the unfolded and true simulation converges to the number of degrees of freedom (dashed line) for the F factor 25 and 15 for the target 5 lead and the scintillator tracker petal 7 respectively.

relative simulation-to-data fraction, i.e. about 4.43 for the antineutrino dataset used in this analysis, was implemented.

In order to do so, a new migration matrix was constructed by Poisson throwing each bin of the original migration matrix as a fraction of data exposure. Then, the new reconstructed simulation coming from the projection of the new migration matrix was unfolded with this new migration matrix and compared to the original true simulation [232, 233]. The statistical covariance of the unfolded sample was multiplied by $\sqrt{(1+1/F)}$, where F is the correction factor.

A search over various F factors for the given fraction of data exposure was performed such as the calculated χ^2 between the unfolded sample with the corrected statistical covariance and the original true distribution corresponded to the number of degrees of freedom at the number of iterations selected. Figure 7.18 illustrates the correction factors F for the antimuon p_{T} distributions in target 5 lead and the scintillator tracker petal 7, which are 25 and 15 respectively. The correction factors for the equivalent Bjorken x distributions are included in Appendix G.

Figure 7.19 displays the unfolded distributions for target 5 lead and the scintillator tracker in both antimuon p_{T} and Bjorken x. Notably, the data-to-simulation ratio remains approximately identical to that observed in the background-subtracted distributions in

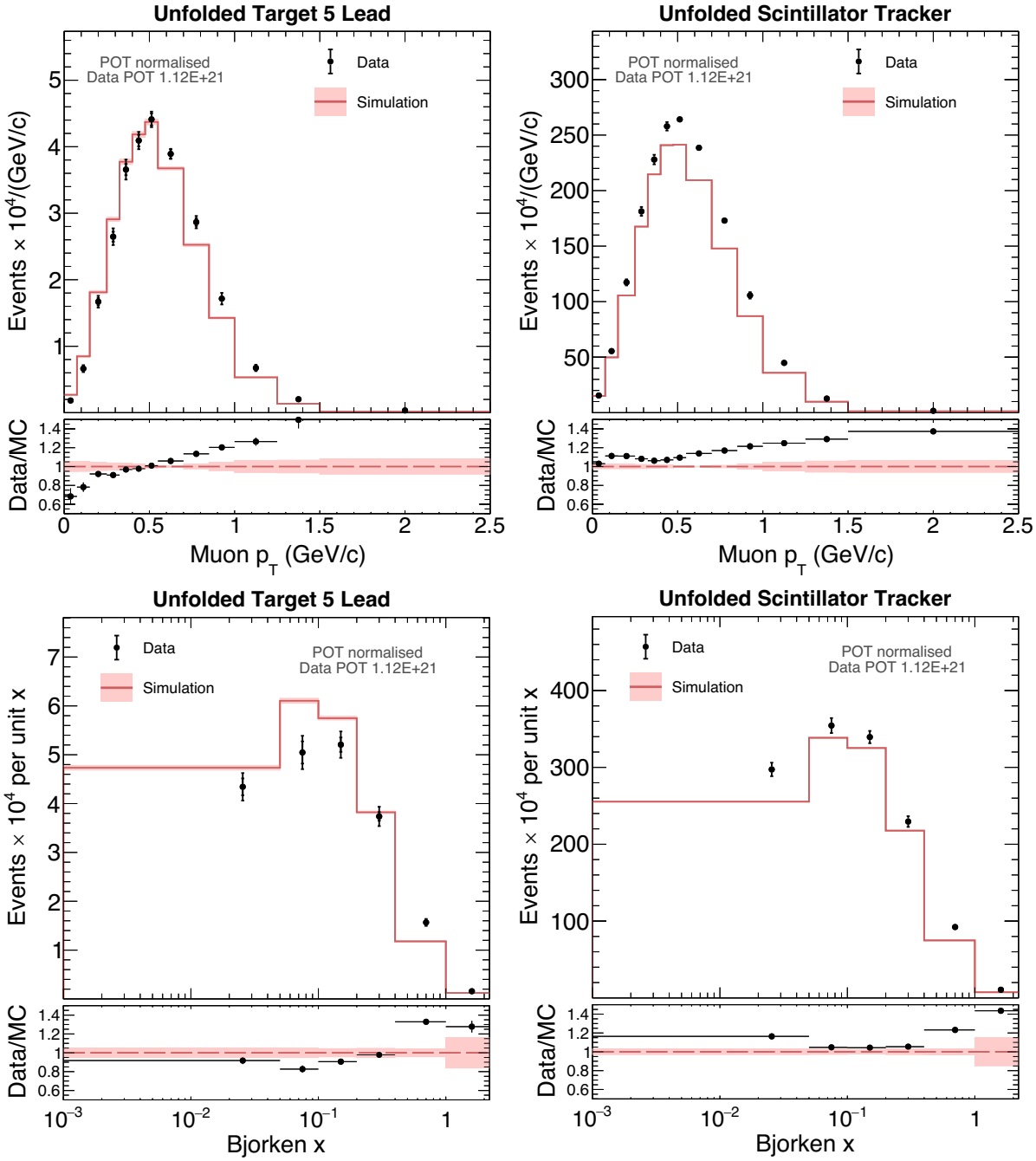

Figure 7.19: Unfolded distributions for target 5 lead (left panel) and scintillator tracker (right panel) as a function of p_{T} (top) and Bjorken x (bottom). In the top panel of each plot, the pink band on the simulation represents the statistical uncertainty of the simulation. The data points carry both statistical (inner error bar) and systematic (outer error bar, which is the sum of statistical and systematic errors) uncertainties. The bottom panel of each plot displays the data-to-simulation ratio, with the pink band around 1 representing systematic uncertainty on the data, while the black points reflect the statistical uncertainty on the data-to-simulation ratio.

Section 7.2. The corresponding fractional uncertainties on the data for these distributions are depicted in Figure 7.20. All other unfolded distributions and their associated fractional uncertainties are included in Appendix H.

Unsurprisingly, the antimuon p_{T} distribution in Figure 7.20 is ultimately dominated by the 'Muon Reconstruction' uncertainty. The $x > 1$ bin of the Bjorken x distribution is visibly governed by the 'Interaction Model' uncertainty, arising from the unsmearing process with a migration matrix in which the simulation does not fully model this region at the nucleon level, as mentioned earlier in this section. In general, the data is unfolded in each of its systematic universes (in addition to its central value), leading to an increase in

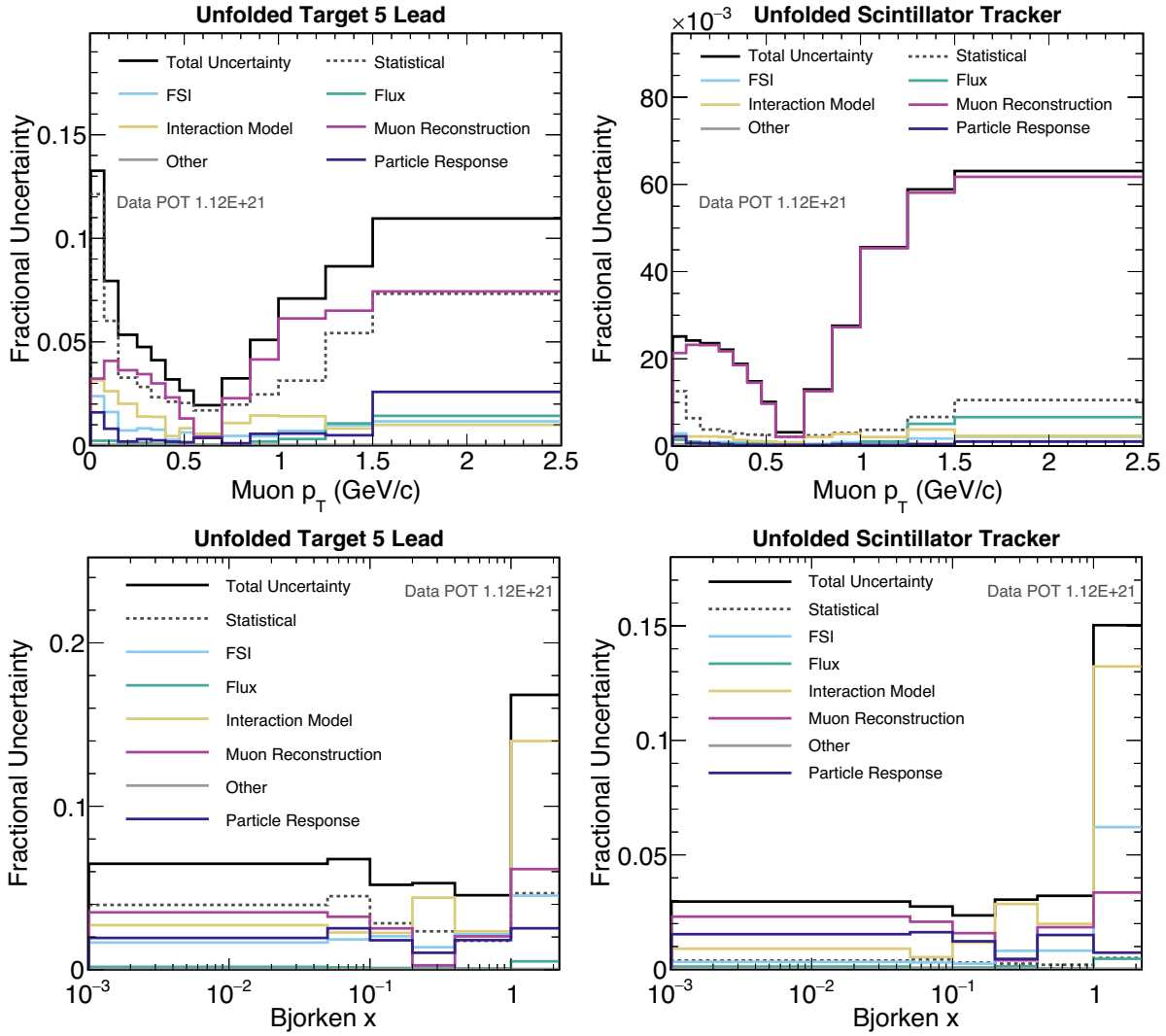

Figure 7.20: Fractional uncertainty breakdown for the unfolded data distributions of target 5 lead (left panel) and scintillator tracker (right panel) as a function of p_{T} (top) and Bjorken x (bottom).

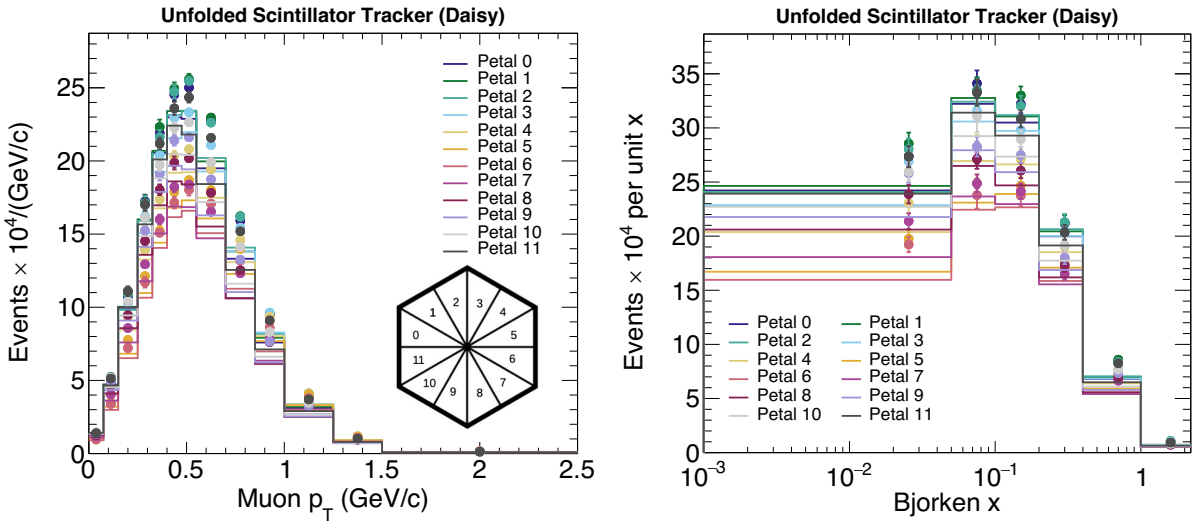

Figure 7.21: Unfolded distribution for the scintillator tracker in 'daisy petals' for both antimuon p_{T} (left) and Bjorken x (right). The unfolded data and the simulation prediction for individual petals are colour-coded as described in the legend. The unfolded data carry both statistical (inner error bar) and systematic (outer error bar, which is the sum of statistical and systematic errors) uncertainties. The hexagon insert illustrates the positions of the petals looking downstream of the detector.

uncertainties compared to the background-subtracted distributions in Section 7.2. Further discussion on the systematic uncertainties is presented in Chapter 8.

Finally, the scintillator tracker distribution is also unfolded in the 12 'daisy petals'. This is illustrated in Figure 7.21 for both p_{T} and Bjorken x. As reviewed in Sections 7.1 and 7.2, this step is essential to determine the nuclear target-to-scintillator cross-section ratios using the matching flux technique explained in Subsection 5.1.1.

7.4 Efficiency correction

Due to the limitations of the detector's acceptance and the imperfect reconstruction, it is impossible to detect and reconstruct every signal event that occurs in the detector. Both of these effects result in reducing the number of signal events in the final sample. As such, they need to be accounted for in the cross-section calculation by applying an efficiency correction derived from the simulation. Specifically, the background-subtracted signal events, which were unfolded to the detector-independent quantities as detailed in the preceding section, are divided by the efficiency correction E_{α} as outlined in Equation 4.1.

The efficiency correction E_α in each bin α for a given analysis variable distribution is defined as

$$E_\alpha = \frac{N_\alpha^{\text{Generated and reconstructed signal events}}}{N_\alpha^{\text{All generated signal events}}}, \tag{7.5}$$

relying on the simulation sample containing both the true generated and the reconstructed information about the simulated events. Due to differences in target geometries and positions, the efficiency has to be calculated separately for each of them. By definition, E_α is always less than one.

In practice, this means filling two histograms representing the numerator and the denominator in Equation 7.5 using the true information of the events and taking their ratio. An example of these two histograms used in the calculation of the scintillator tracker efficiency for both p_T and Bjorken x is shown in Figure 7.22. While the numerator events are selected from the subsample of the reconstructed events and hence carry the systematic uncertainties associated with the detector's acceptance and event reconstruction, the denominator events are independent of them. This is demonstrated in Figure 7.23 showing the systematic uncertainties of both the efficiency numerator and the denominator for the scintillator tracker as a function of p_T.

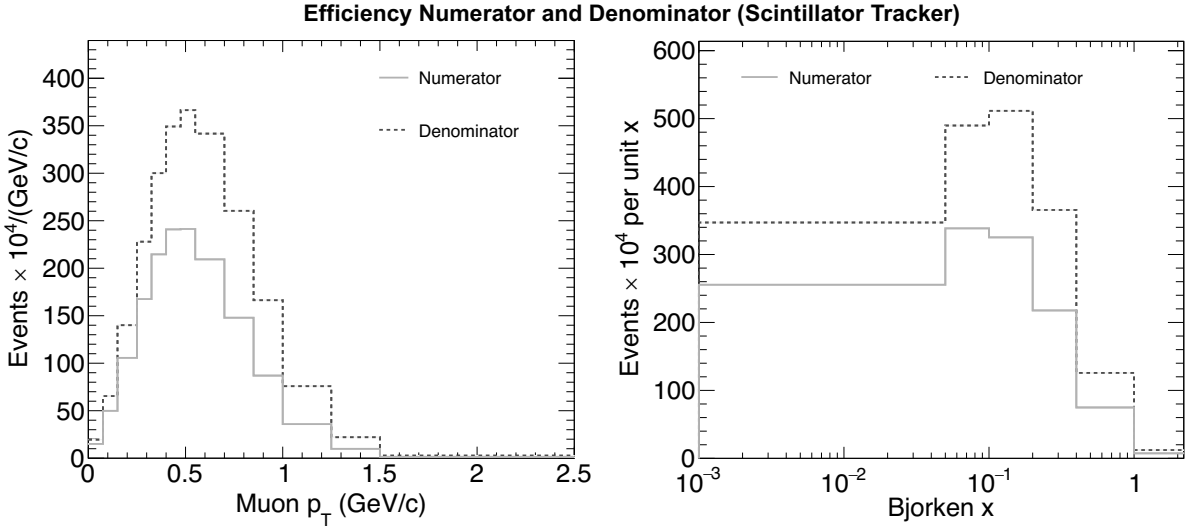

Figure 7.22: Efficiency numerator and denominator distributions for the scintillator tracker in both p_T (left) and Bjorken x (right). The solid line for the numerator represents the generated and reconstructed signal events, while the dashed line for the denominator denotes the superset of all generated signal events.

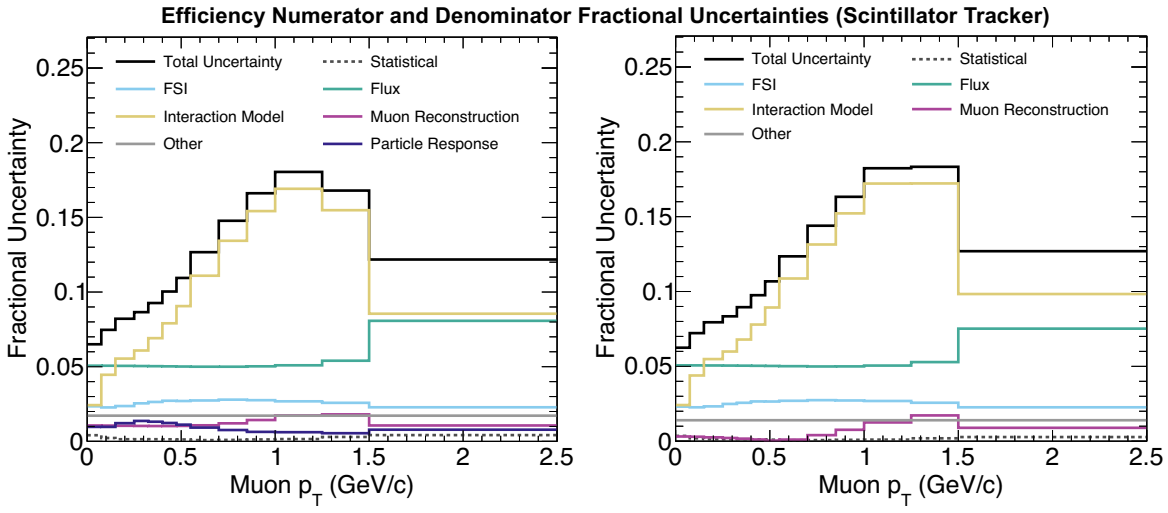

Figure 7.23: Fractional uncertainty breakdown for the efficiency numerator (left) and the denominator (right) distributions of scintillator tracker as a function of p_{T}. Note the omitted 'Particle Response' uncertainty band and the reduced 'Muon Reconstruction' uncertainty band in the denominator uncertainty on the right.

Specifically, Figure 7.23 highlights that the denominator fractional uncertainty does not include the uncertainty linked to the calorimetric energy response of the detector and interaction cross-sections of particles traversing through the detector, represented by the 'Particle Response' uncertainty band. The 'Muon Reconstruction' uncertainty band omits all uncertainty sources except for those related to the MINOS antimuon momentum universes, which are directly correlated with flux. Finally, the 'Other' uncertainty band is reduced by excluding the uncertainty associated with vertex reconstruction. A detailed description of the various systematic uncertainty bands can be found in Chapter 8.

Because the numerator distribution of the selected reconstructed events is a subsample of the denominator distribution of the selected generated events, the two distributions are correlated. Consequently, when calculating the ratio, the correlations between their uncertainties are taken into account using binomial error propagation for the statistical uncertainty. The efficiencies for different lead targets and the scintillator tracker both in p_{T} and Bjorken x are shown in Figure 7.24.

Due to the inclusive nature of the analysis, the efficiency relies on detecting and reconstructing the antimuon both in the MINERvA detector and the MINOS spectrometer. The top panel of Figure 7.24 illustrates the fall-off in the p_{T} efficiency at higher p_{T}. This is attributed to the fact that p_{T} serves as a proxy for the antimuon angle, whose detec-

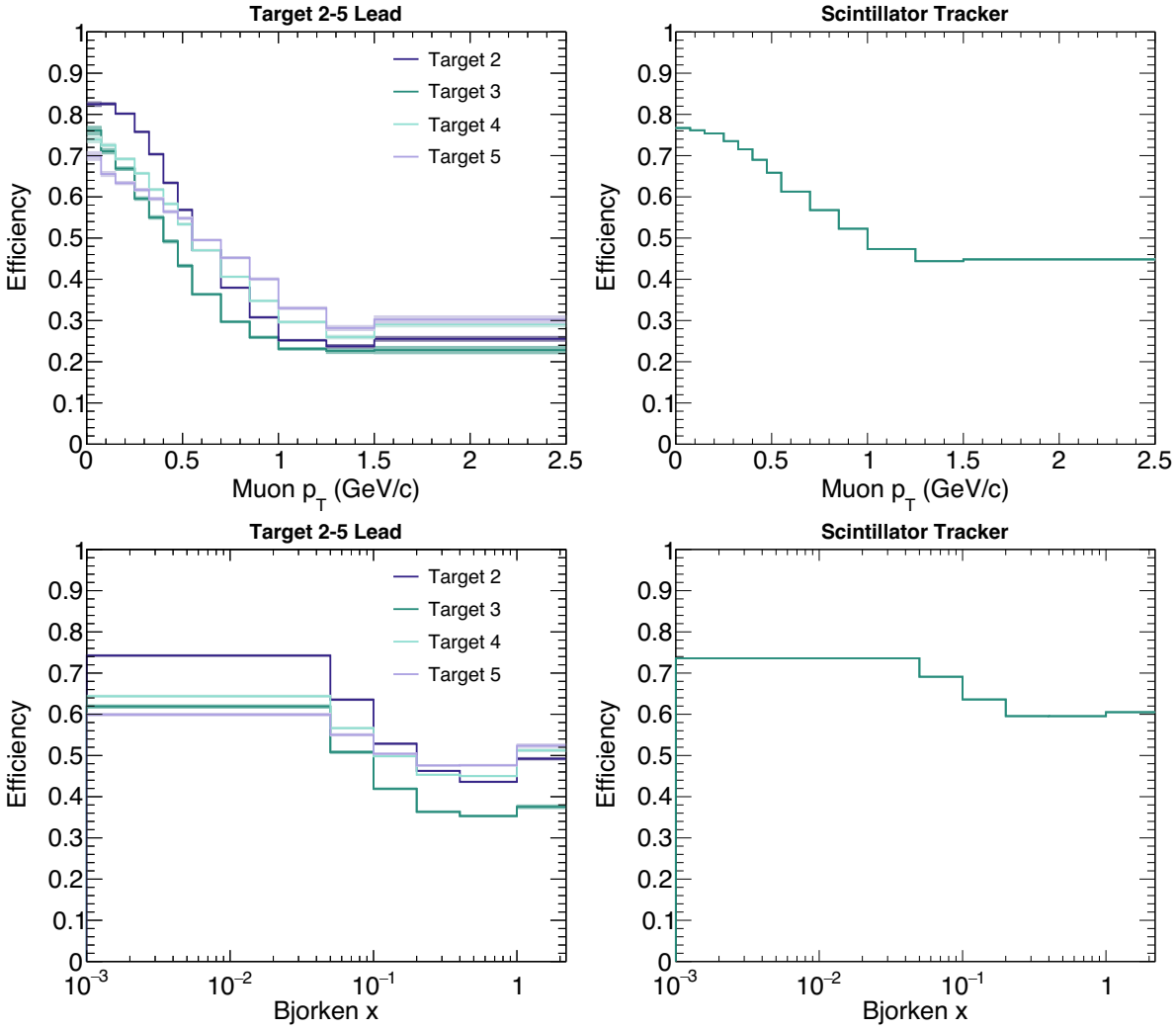

Figure 7.24: Efficiency correction distributions for the various lead targets (left panel) and the scintillator tracker (right panel) as a function of p_{T} (top) and Bjorken x (bottom).

tion is constrained by the limited antimuon acceptance of the MINOS spectrometer at higher angles. Furthermore, the differences between the various lead target efficiencies in Figure 7.24 can be explained due to their positions in the detector with respect to the MINOS spectrometer.

For example, target 2 lead is more upstream than target 5 lead. At lower p_{T} (antimuon angle), the antimuon is likely to be more energetic than at higher p_{T}. This means that a more energetic antimuon produced by an interaction in target 2 lead has to traverse more material before reaching the MINOS spectrometer and loses more energy compared to one produced in target 5 lead. Therefore, the antimuon from target 2 lead is more likely to be able to stop in the MINOS spectrometer and be reconstructed, resulting in

target 2 lead having higher p_{T} efficiency than target 5 lead at lower p_{T}. Conversely, an antimuon produced with a higher angle in a target more downstream and thus closer to the MINOS spectrometer is more likely to be reconstructed. This leads to target 5 lead having a larger efficiency at higher p_{T} compared to target 2 lead.

The Bjorken x efficiency in the bottom panel of Figure 7.24 exhibits similar behaviour as p_{T}. Nevertheless, the decline at higher Bjorken x is less pronounced due to the weaker dependence on the antimuon angle.

The integrated efficiency for all the targets of different materials and the scintillator tracker can be found in Table 7.6. For targets in particular, the efficiency depends on the ability to reconstruct the vertex in the nuclear target, as detailed in Chapter 6. Furthermore, within a given target, the efficiency is lower for materials that shadow the MINOS coil described in Chapter 3, such as iron in the second target or lead in the fifth target.

The fractional uncertainty on the target 5 lead and scintillator tracker efficiency in both p_{T} and Bjorken x is shown in Figure 7.25. The region of low p_{T} and high Bjorken x, mainly associated with quasi-elastic events, is dominated by the 'Particle Response' uncertainty coming from the efficiency numerator. Specifically, this uncertainty is mostly attributed to the uncertainty on the neutron cross-section. Additionally, both high p_{T} and high Bjorken x have prominent 'Interaction Model' uncertainty bands, primarily arising

Target	Material	Efficiency (%)
2	Iron	41.9
	Lead	49.5
3	Carbon	52.4
	Iron	40.3
	Lead	39.7
4	Lead	47.8
5	Iron	50.5
	Lead	48.8
Tracker	Scintillator	63.3

Table 7.6: Integrated efficiency correction for all targets of different materials and the scintillator tracker.

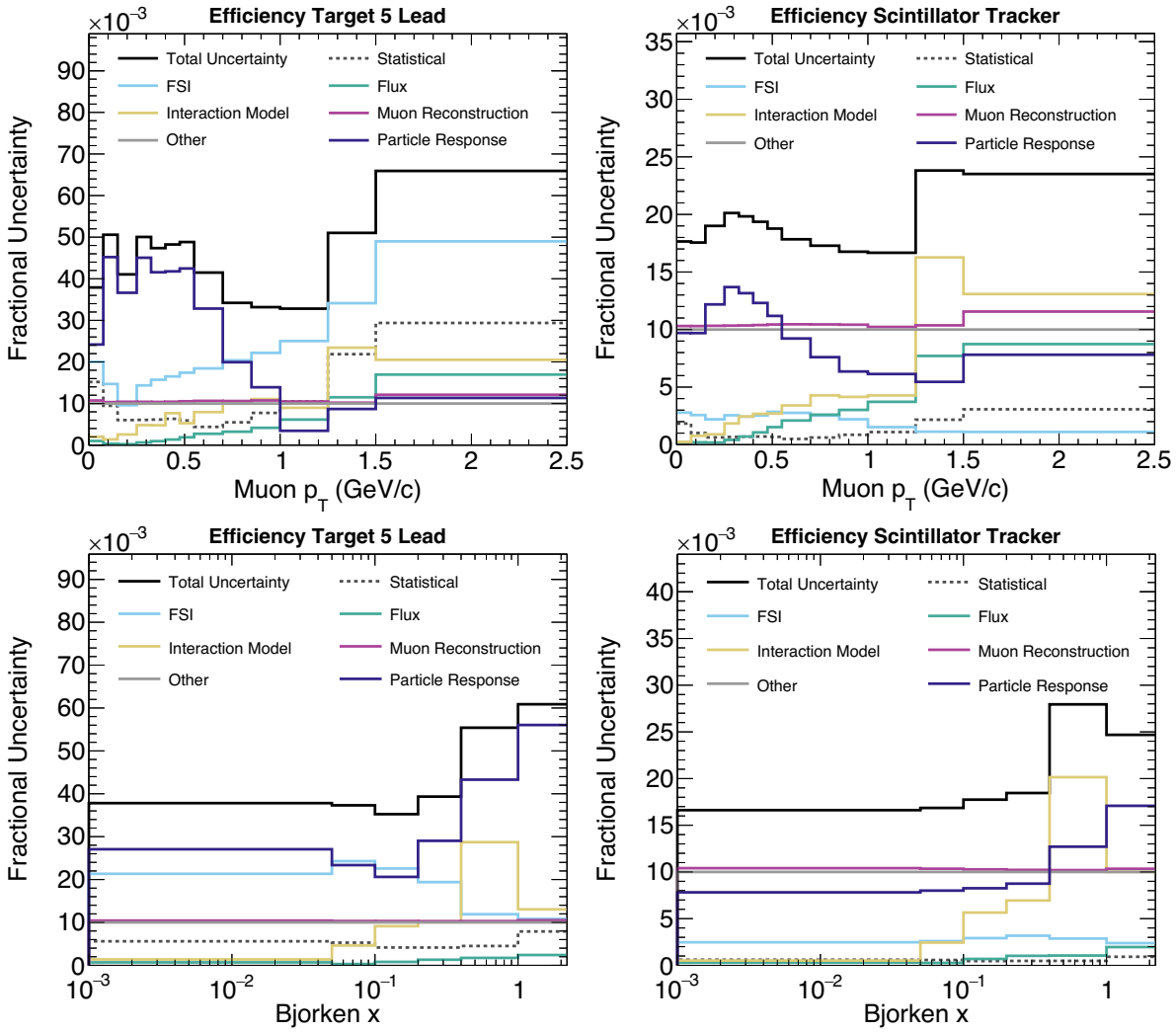

Figure 7.25: Fractional uncertainty breakdown for the efficiency of target 5 lead (left panel) and scintillator tracker (right panel) as a function of p_{T} (top) and Bjorken x (bottom). Note the increase in the 'FSI' uncertainty band for lead compared to the scintillator.

from the resonance production model. Figure 7.25 also illustrates that the 'FSI' uncertainty band is more pronounced the heavier the nucleus is, i.e. heavy lead versus relatively light scintillator in comparison. The 'FSI' band is overall governed by the pion absorption cross-section uncertainty.

Furthermore, the scintillator tracker efficiency is also extracted in the 'daisy petals', as illustrated in Figure 7.26 for p_{T}. This extraction is essential for determining nuclear target-to-scintillator cross-section ratios using the matching-flux technique discussed in Subsection 5.1.1. Similarly to the passive targets, the petals shadowing the MINOS coil

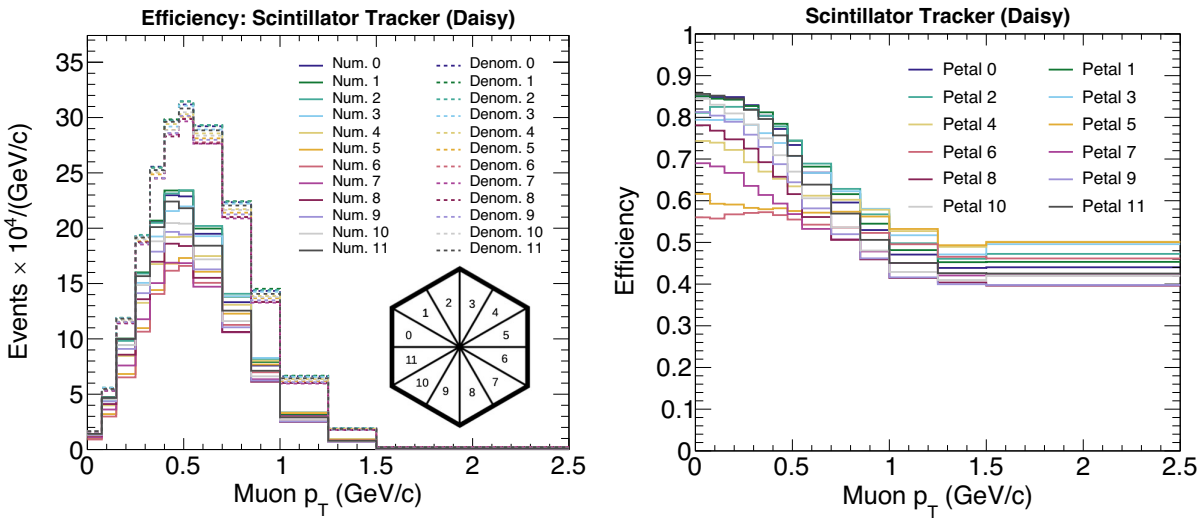

Figure 7.26: Left: Efficiency numerator and denominator for the scintillator tracker in 'daisy petals' in antimuon p_{T}. The hexagon insert illustrates petal positions looking downstream of the detector. Right: Efficiency distribution for the scintillator tracker in 'daisy petals' in antimuon p_{T}.

have reduced efficiency at low p_{T}. All other efficiency correction distributions for passive targets, scintillator tracker, and scintillator tracker divided in the 'daisy petals' and their corresponding fractional uncertainties are included in Appendix I.

Figure 7.27 shows the efficiency-corrected distributions for target 5 lead and scintillator tracker in both antimuon p_{T} and Bjorken x. Importantly, the shape of the data-to-simulation ratio remains consistent with that observed in previous steps of the analysis. The associated fractional uncertainties on the data for these distributions are depicted in Figure 7.28. All other efficiency-corrected distributions and their fractional uncertainties can be found in Appendix J.

Similarly, the efficiency-corrected distribution for the scintillator tracker extracted in the 'daisy petals' is displayed in Figure 7.29 for both antimuon p_{T} and Bjorken x. The spread of the 'daisy petals' distributions is significantly reduced as the efficiency correction aims to eliminate all acceptance-related effects. These individual efficiency-corrected petal distributions are then weighted and combined in Section 7.6 to generate scintillator cross-sections with an effective scintillator tracker flux matching that of carbon, iron, and lead, according to the technique discussed in Subsection 5.1.1.

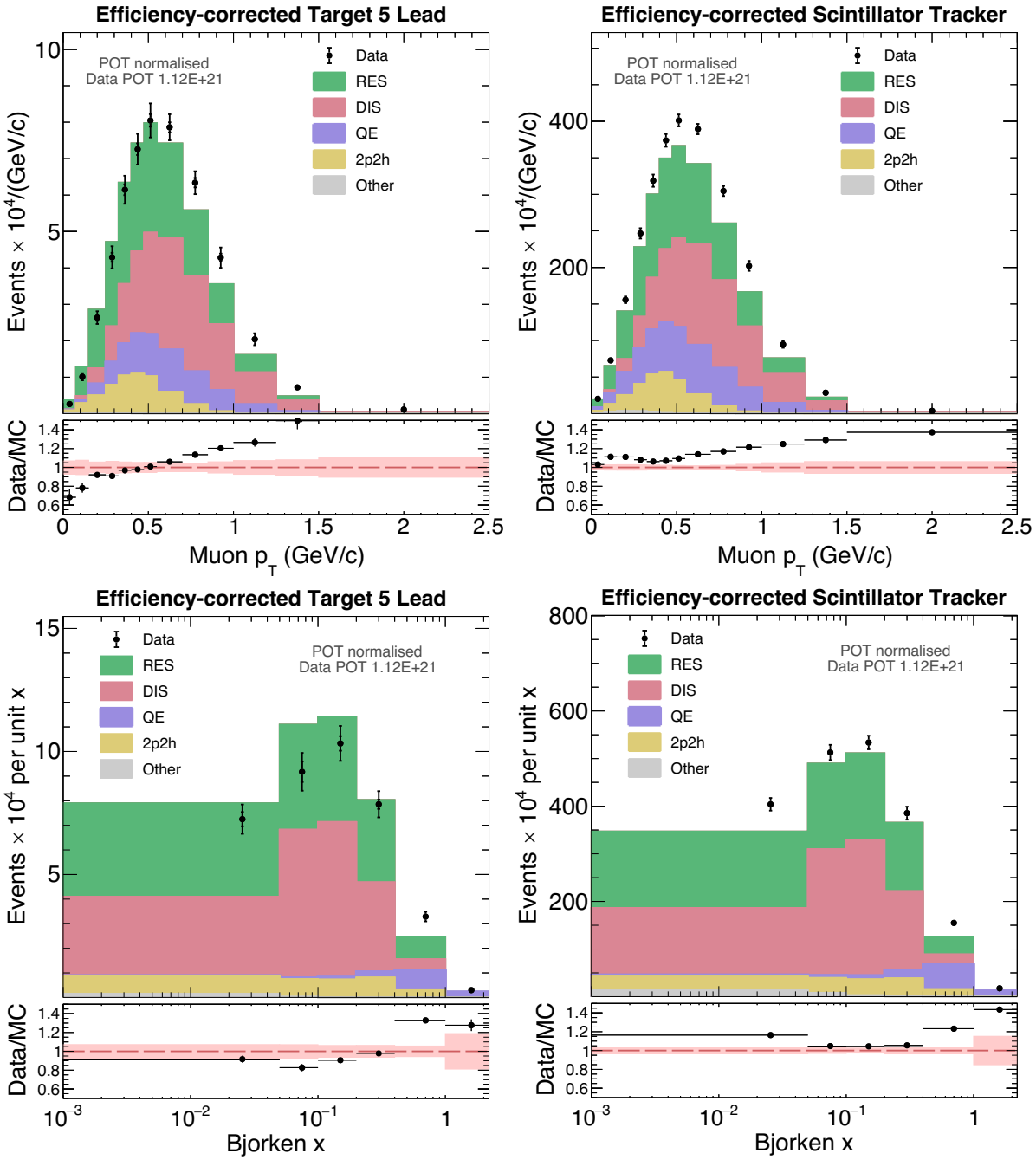

Figure 7.27: Efficiency-corrected distributions for target 5 lead (left panel) and scintillator tracker (right panel) as a function of p_{T} (top) and Bjorken x (bottom) with the simulation broken down into the various interaction channels stacked in the descending order of their contribution. In the top panel of each plot, the data points carry both statistical (inner error bar) and systematic (outer error bar, which is the sum of statistical and systematic errors) uncertainties. The bottom panel of each plot displays the data-to-simulation ratio, with the pink band around 1 representing systematic uncertainty on the data, while the black points reflect the statistical uncertainty on the data-to-simulation ratio.

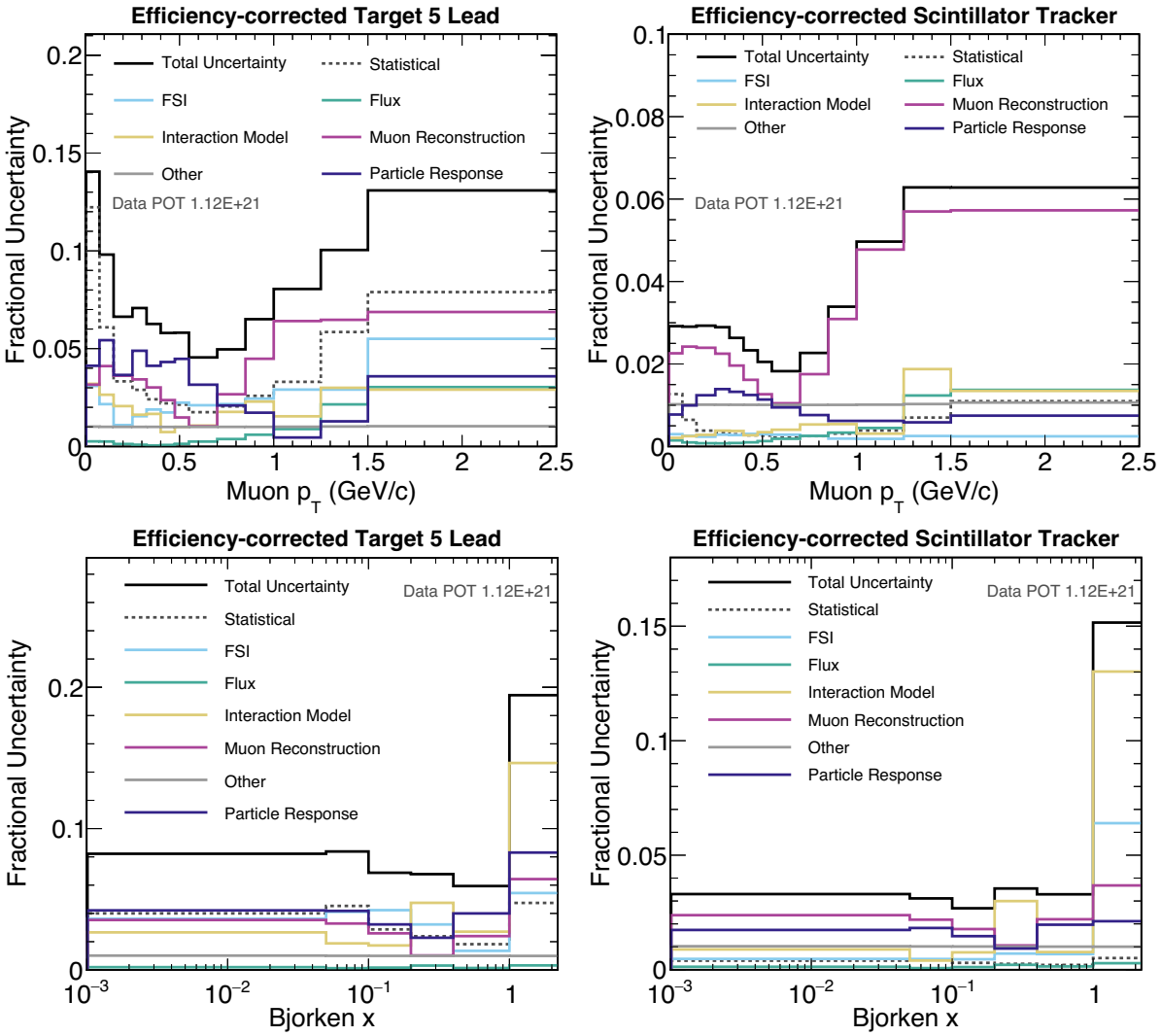

Figure 7.28: Fractional uncertainty breakdown for the efficiency-corrected data distributions of target 5 lead (left panel) and scintillator tracker (right panel) as a function of p_{T} (top) and Bjorken x (bottom).

Furthermore, the efficiency-corrected distributions from the individual targets of the same material can be combined, as the different efficiency-related effects are removed. In practice, this involves adding up the efficiency-corrected histograms for targets 2, 3, and 5 iron and 2–5 lead. An example of the combined lead efficiency-corrected distribution for both antimuon p_{T} and Bjorken x is shown in Figure 7.30, with its associated fractional uncertainty depicted in Figure 7.31. The combined iron efficiency-corrected distribution is included in Appendix J. In comparison to the individual target, the statistical uncertainty for the combined material distribution is significantly reduced.

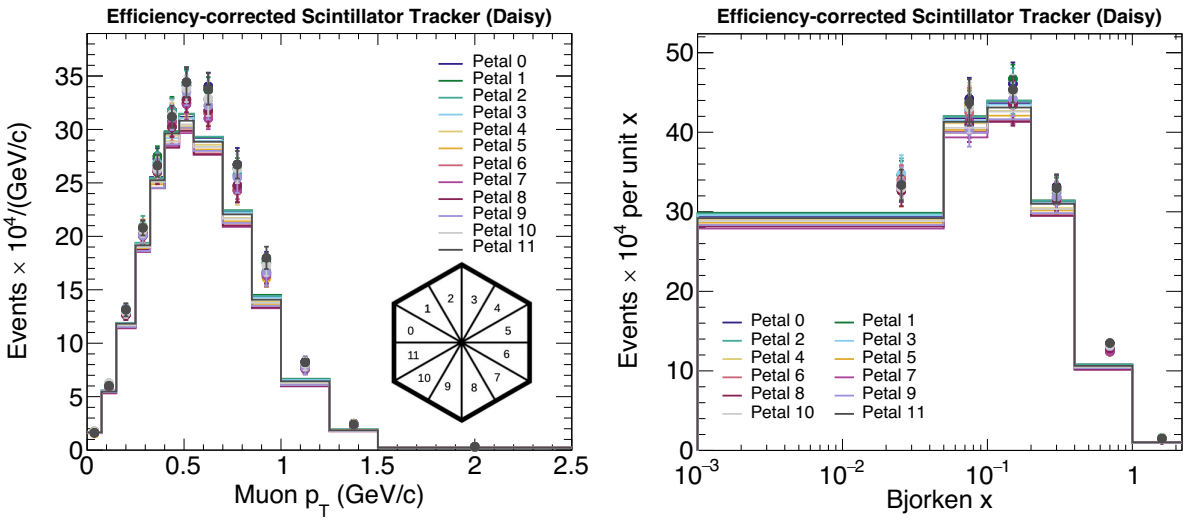

Figure 7.29: Efficiency-corrected distribution for the scintillator tracker in 'daisy petals' for both antimuon p_{T} (left) and Bjorken x (right). The unfolded data and the simulation prediction for individual petals are colour-coded as described in the legend. The unfolded data carry both statistical (inner error bar) and systematic (outer error bar, which is the sum of statistical and systematic errors) uncertainties. The hexagon insert illustrates the positions of the petals looking downstream of the detector.

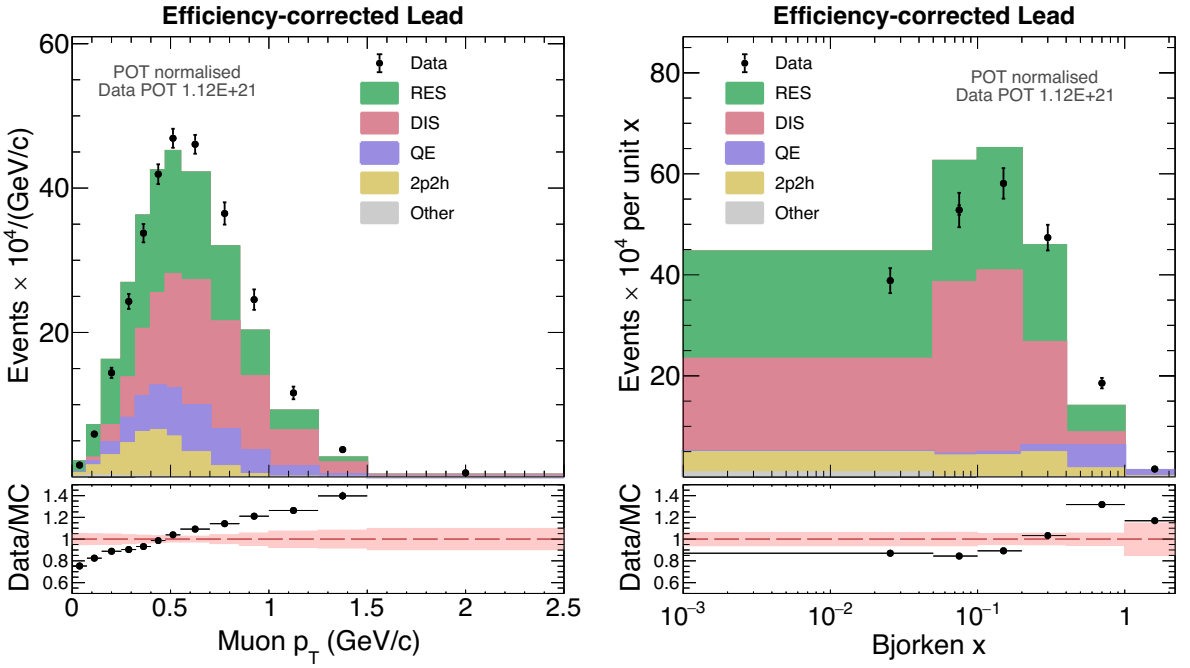

Figure 7.30: Efficiency-corrected distributions for lead, i.e. combined target 2–5 lead, as a function of p_{T} (top) and Bjorken x (bottom) with the simulation broken down into the various interaction channels stacked in the descending order of their contribution. In the top panel of each plot, the data points carry both statistical (inner error bar) and systematic (outer error bar, which is the sum of statistical and systematic errors) uncertainties. The bottom panel of each plot displays the data-to-simulation ratio, with the pink band around 1 representing systematic uncertainty on the data, while the black points reflect the statistical uncertainty on the data-to-simulation ratio.

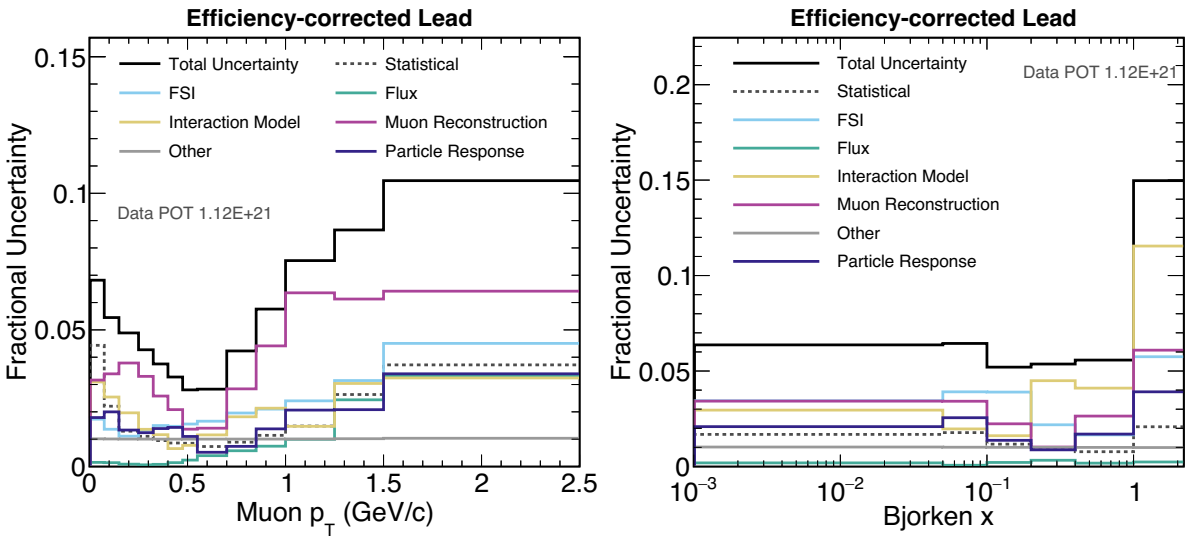

Figure 7.31: Fractional uncertainty breakdown for the combined lead efficiency-corrected data distributions as a function of p_{T} (top) and Bjorken x (bottom).

7.5 Normalisation to cross-section

The final step in the calculation of the differential cross-section involves normalising the efficiency-corrected distributions for carbon, iron, lead, and the scintillator tracker according to Equation 4.1. First, each bin of the efficiency-corrected distribution is divided by the number of scattering centres T_{nucleons}, i.e. the number of nucleons, within the fiducial volume available for an antineutrino to interact with in a given material. Reporting the cross-section per nucleon ensures the result is independent of the detector's mass. The estimates of the number of nucleons in Table 7.7 are derived from MINERvA's material assays [40]. The uncertainty associated with the target masses described in Chapter 8 is also accounted for in the normalisation.

Material	Φ ($\bar{\nu}_\mu \times 10^{-8}/\mathrm{cm}^2/\mathrm{POT}$)	T_{nucleons} ($\times 10^{28}$)
Carbon	4.853	9.598
Iron	4.676	37.841
Lead	4.763	42.768
Scintillator	4.774	323.478

Table 7.7: Cross-section normalisation factors for the passive target region and the scintillator tracker.

Furthermore, to report a differential cross-section, one must divide each bin α of the efficiency-corrected distribution by the integrated antineutrino flux prediction Φ and the corresponding bin width Δx_α. The antineutrino flux integral is calculated as a function of

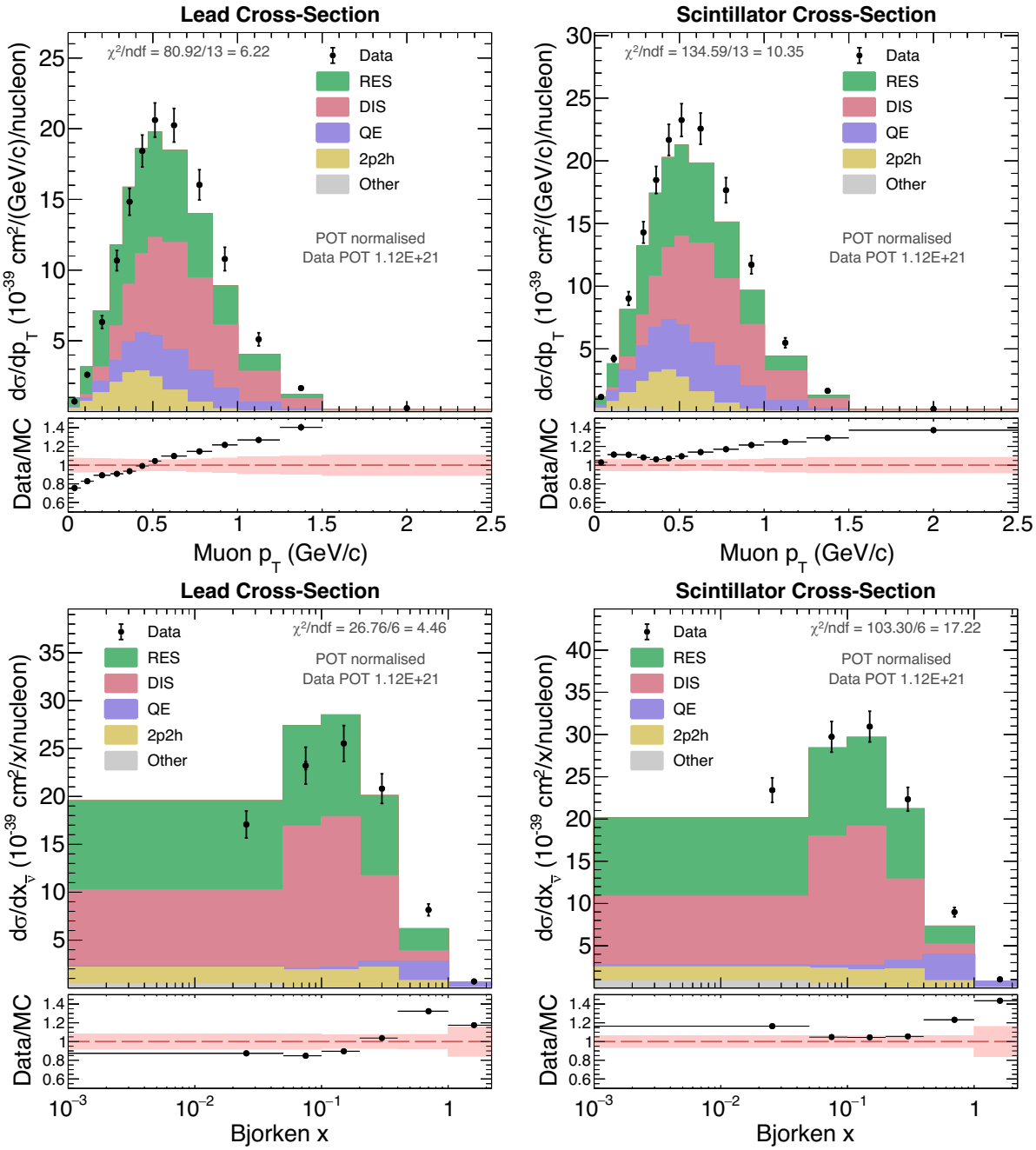

Figure 7.32: Lead (left panel) and scintillator cross-section as a function of p_{T} (top) and Bjorken x (bottom) with the simulation broken down into the various interaction channels stacked in the descending order of their contribution. In the top panel of each plot, the data points carry both statistical (inner error bar) and systematic (outer error bar, which is the sum of statistical and systematic errors) uncertainties. The bottom panel of each plot displays the data-to-simulation ratio, with the pink band around 1 representing systematic uncertainty on the data, while the black points reflect the statistical uncertainty on the data-to-simulation ratio.

true antineutrino energy between 0–120 GeV using the flux simulation prediction outlined in Sections 3.1 and 5.1. The upper limit is determined by the 120 GeV/c protons from which the NuMI antineutrino beam originates. However, the contribution above 20 GeV is negligible due to the antimuon energy cut discussed in Section 7.1.

In line with the discussion in Subsection 5.1.1 and Figure 5.2, it was demonstrated that the antineutrino fluxes across different materials vary. Consequently, the antineutrino flux integrals per protons on target (POT) are also shown to vary for different materials in Table 7.7. It is important to note that the flux normalisation also propagates the uncertainties associated with the flux, which are explained in Chapter 8.

To eliminate the POT dependence, each flux integral in Table 7.7 is multiplied by the total data exposure of 1.12×10^{21} POT in the cross-section extraction. A simple dimensional analysis shows that the differential cross-sections $\mathrm{d}\sigma/\mathrm{d}p_{\mathrm{T}}$ and $\mathrm{d}\sigma/\mathrm{d}x$ can be reported in units of $10^{-39}/\mathrm{cm}^2/\mathrm{unit}/\mathrm{nucleon}$, where 'unit' represents the unit of the kinematic variable for which the differential cross-section was calculated.

Figure 7.32 shows the final lead and scintillator cross-section results both in antimuon p_{T} and Bjorken x. Similarly to the event selection distributions in Section 7.1, the cross-section prediction is categorised by various interaction types and distinctly dominated by the resonant pion production followed by the deep inelastic scatterig. The observed data-to-simulation ratios remain consistent with the previous analysis steps. The fractional uncertainties on these cross-section distributions are shown and discussed in detail in Chapter 8. All cross-section results, i.e. also including iron and carbon cross-sections, are included and discussed in Chapter 9.

7.6 Cross-section ratios

Cross-section ratios offer a convenient and effective way to present comparisons between the nuclear targets and the scintillator, illustrating the nuclear dependence of the anti-neutrino interactions. Crucially, the cross-section ratios are essentially flux-independent,

cancelling out the leading systematic uncertainty coming from the understanding of the incoming antineutrino beam.

In order to do so, the 'daisy reweight' of the scintillator tracker, detailed in Subsection 5.1.1 and Appendix A, is implemented. Ultimately, a linear combination of the efficiency-corrected distributions from the 'daisy petals' in Figure 7.29 is taken to create an effective scintillator tracker flux that matches that of carbon, iron, and lead. This is achieved by applying the corresponding weights shown in Appendix A. The resulting combinations are then normalised to cross-sections, as demonstrated in Figure 7.33. These scintillator cross-sections are used as the denominator in the relevant cross-section ratios.

The top panel of Figure 7.34 shows the lead-to-scintillator cross-section ratio result in both antimuon p_{T} and Bjorken x. The corresponding fractional uncertainties on the data cross-section ratios are displayed in the bottom panel of Figure 7.34. These illustrate that in addition to eliminating most flux effects, other shared detector uncertainties such as the ones related to antimuon reconstruction also partially cancel out in the cross-section ratio. All cross-section ratio results and their respective uncertainties are presented and discussed in Chapter 9.

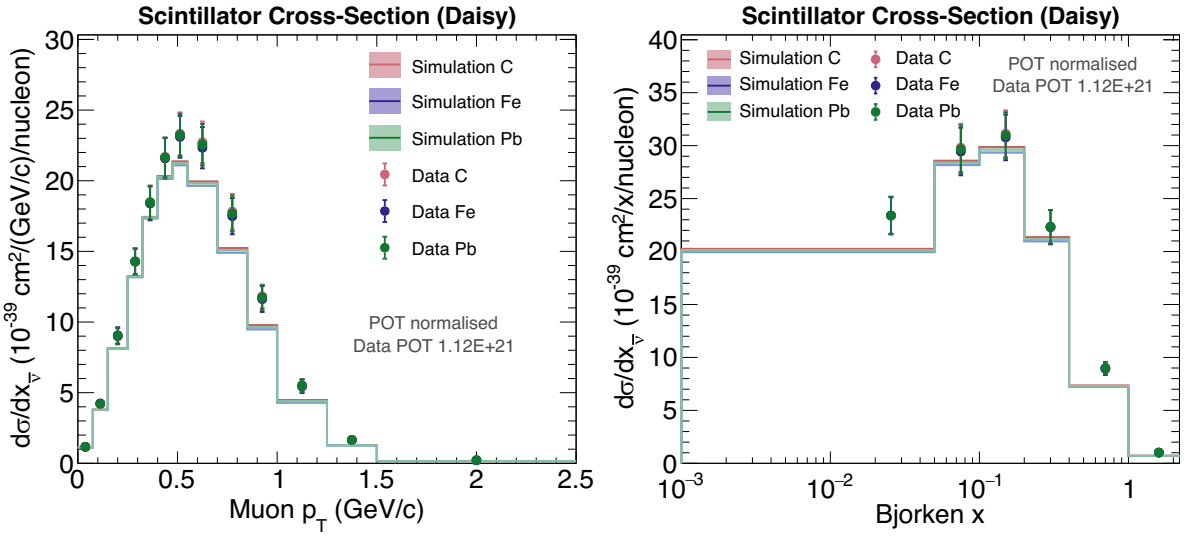

Figure 7.33: Effective scintillator cross-sections with matched flux to carbon, iron, and lead for both antimuon p_{T} (left) and Bjorken x (right). The inner error bars on the data points represent the statistical error, while the outer error bars correspond to the total error (statistical + systematic).

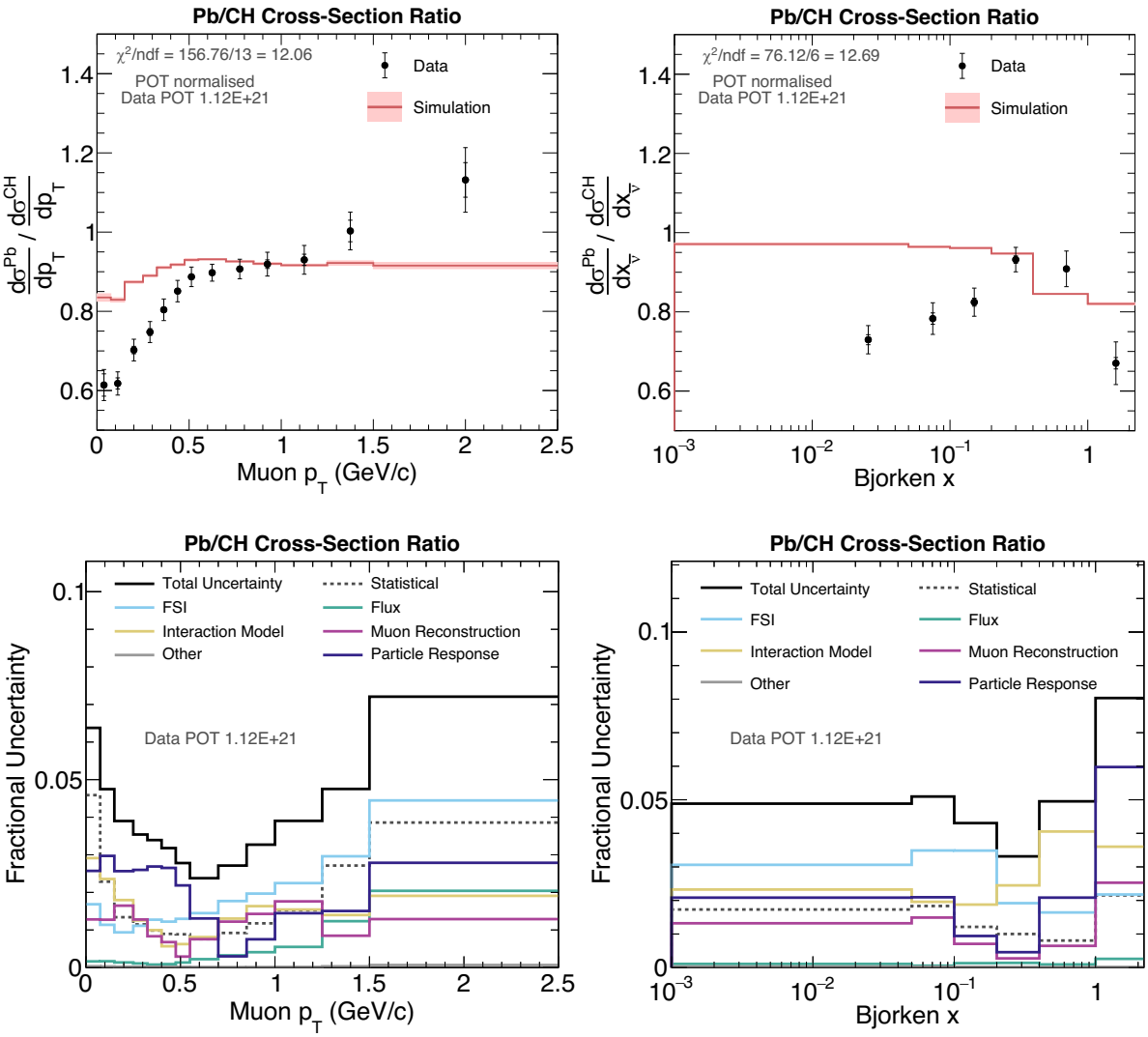

Figure 7.34: Lead-to-scintillator cross-section ratio (top) and the corresponding breakdown of the fractional uncertainties on the data (bottom) in both antimuon p_{T} (left) and Bjorken x (right). The inner error bars on the data points in the cross-section ratio distributions represent the statistical error, while the outer error bars show the total error (statistical + systematic). The pink band on the simulation prediction corresponds to the statistical error on the prediction.

7.7 Note on validation

The cross-section extraction procedure outlined in this chapter was thoroughly examined for consistency across various steps and validated against MINERvA's closure test program, GENIEXSecExtract [234], using simulation. Specifically, by construction, the efficiency numerator and the unfolded simulation should be equal, and the reconstructed

simulated signal and the migration matrix projected onto the reconstructed axis should match. For this analysis, the ratios of these two cases are equal to 1, thereby passing this check.

Additionally, the efficiency denominator was cross-verified against the true event rate from the MINERvA analysis files outside of this analysis's infrastructure using GENIEXSecExtract, resulting in a flat ratio at 1. Similarly, the predicted cross-section underwent a similar validation process using GENIEXSecExtract. Since the same steps are applied to both the simulation prediction and the data, this inherently validates the cross-section extraction procedure for the data as well.

Chapter 8

Systematic uncertainties

Every cross-section measurement, such as the one presented here, inherently carries uncertainties crucial for understanding the reliability and precision of the reported result. These uncertainties can be divided into two categories: statistical and systematic.

The statistical uncertainty essentially accounts for the fact that a cross-section measurement is a counting experiment with a finite number of counts. Specifically, this work involves counting antineutrino interactions in bins of p_{T} and Bjorken x. Each count, i.e. the observed interaction, originates from an underlying Poisson probability distribution. Therefore, the statistical uncertainty of a given bin with N events corresponds to $\sqrt{N}$.

In contrast, systematic uncertainties in this measurement describe the accuracy with which the cross-section can be measured, taking into account the limitations of the MINERvA and MINOS detectors and reconstruction, as well as the understanding of the incident antineutrino beam and its interactions with nuclei. MINERvA uses the underlying simulation to estimate systematic uncertainties in reported cross-section results via the multiverse method [174], which has already been mentioned in Chapters 3 and 5 with respect to flux modelling. The simulation with nominal values for all parameters, as described in Chapter 5, is referred to as the central value (CV). A systematic universe is then a simulation sample in which one or more input parameters are varied within their associated uncertainties.

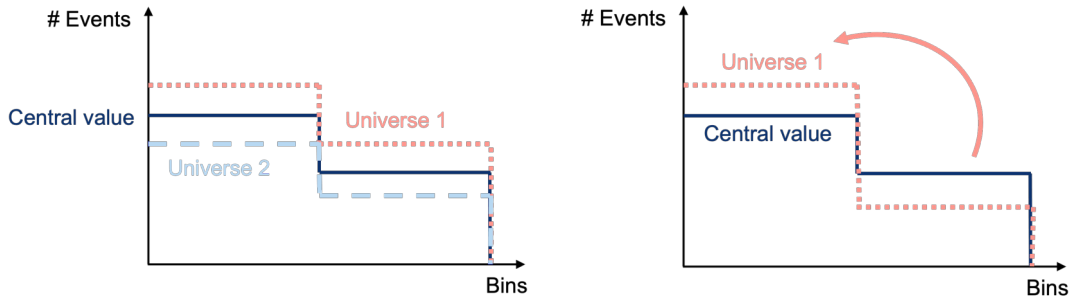

Figure 8.1: Illustration of two different effects a systematic universe can have on an event—a normalisation-like shift (left) and a bin-by-bin shift (right).

As discussed, the antineutrino flux, due to its complex modelling, necessitates the multiverse approach to allow simultaneous variations of multiple parameters. However, most systematic uncertainties have relatively simple underlying models and are typically evaluated by considering two universes where a parameter is shifted by $\pm 1\sigma$, with σ representing the parameter's uncertainty. The magnitude of the uncertainty in each bin is then given by the spread of these two universes, i.e. the average difference between each universe and the CV in that bin. All systematic universes are propagated throughout the analysis.

Conceptually, there are two effects a systematic universe can have on an event: a normalisation-like shift and a bin-by-bin shift, as illustrated in Figure 8.1. Normalisation-like shifts represent uncertainties that affect the weight of an event in a given bin, such as those from interaction models. In contrast, bin-by-bin uncertainties impact the kinematic variables, causing bin-to-bin migration, and represent most detector systematics.

Figure 8.2 shows an example of the fractional uncertainty[1] on the simulation for target 5 lead both in p_{T} and Bjorken x at the event rate level. Appendix K includes the corresponding breakdown of uncertainties for the scintillator tracker. Related sources of uncertainties are grouped together in one error band and will be discussed individually later with respect to the reported cross-section. The individual systematic errors within these groups are constructed by extracting the square root of diagonal entries (variances) of their corresponding covariance matrices.

[1]Fractional uncertainty error band represents the uncertainties relative to the CV, i.e. uncertainty/CV.

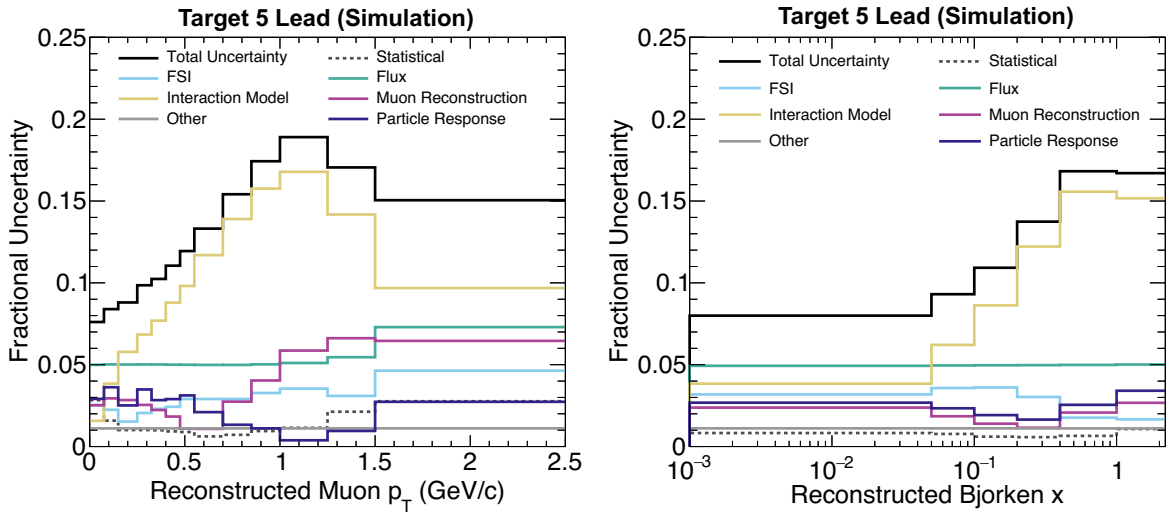

Figure 8.2: Fractional uncertainty breakdown for the simulated event rate in both p_{T} (left) and Bjorken x (right) in target 5 lead.

An element of the covariance matrix relating two bins i and j can be calculated as

$$\mathrm{cov}_{ij} = \frac{1}{N-1}\sum_{n=1}^{N}(x_{n,i} - \bar{x}_i)(x_{n,j} - \bar{x}_j)\ , \tag{8.1}$$

where N represents the total number of universes, x_n is the bin content of a given bin in the universe n, and $\bar{x}$ is the mean of all the universes in that bin. Note that the off-diagonal terms of the covariance matrix are retained and used in comparisons with various other antineutrino generators with different interaction models in Chapter 9 to account for bin-to-bin correlations. The error band grouping related sources of uncertainty in each bin is then calculated as the square root of the sum of the diagonal elements of all relevant individual covariance matrices. The total error band is calculated the same way but also includes the statistical uncertainty.

The multiverse method enables independent cross-section analysis in each universe. While the systematic uncertainty is reported on the simulation at the event rate level, in the final cross-section result, MINERvA reports the systematic uncertainty on the data. This is due to the cross-section extraction steps outlined in Equation 4.1, i.e. background subtraction, unfolding, efficiency correction, and normalisation, where information from the simulation introduces systematic uncertainty to the data.

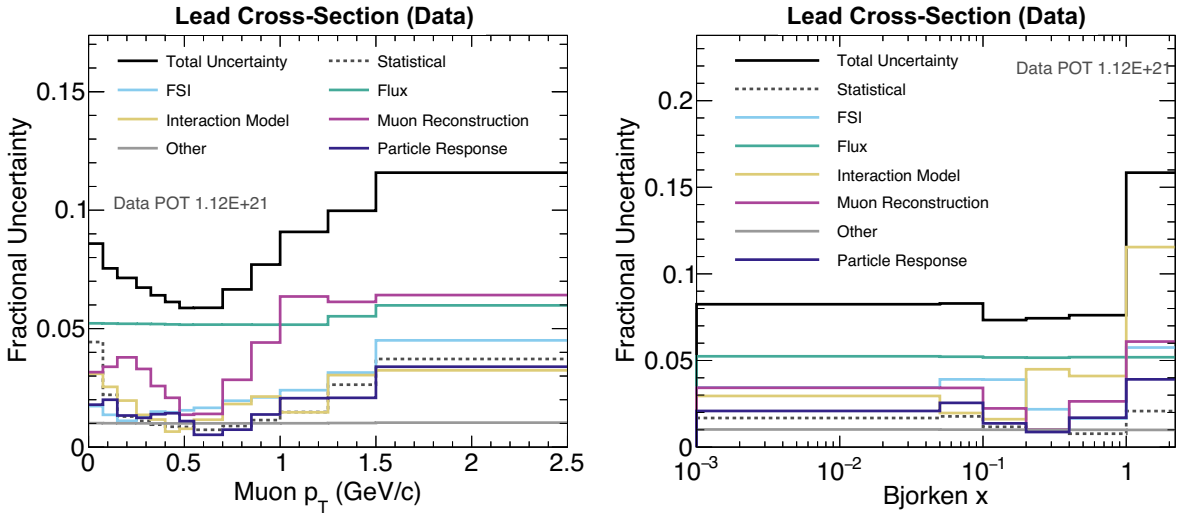

Figure 8.3: Breakdown of the fractional uncertainties propagated to the lead differential cross-section in data in both p_{T} (left) and Bjorken x (right).

The (data) cross-section uncertainty for the differential cross-section on lead in p_{T} and Bjorken x is presented in Figure 8.3. The individual error band categories are discussed in detail in the following sections. However, it is important to note that Figure 8.3 illustrates a general trend observed across various materials for the last p_{T} and Bjorken x bin. Specifically, the last p_{T} bin, extending to the edge of the angular acceptance, leads to statistical fluctuations in the associated systematic uncertainty. On the other hand, the last Bjorken x bin is significantly influenced by interaction model uncertainties since the simulation doesn't directly model this region at the nucleon level, as discussed previously. In the kinematic distributions (as opposed to fractional uncertainty plots), where the data carries the systematic uncertainty, the data points are represented with inner and outer error bars, corresponding to the statistical and total (statistical + systematic) uncertainty, respectively.

8.1 Flux

Similarly to other cross-section analyses, the flux uncertainty represents the leading systematic uncertainty in this measurement as well[2]. The flux modelling and its associated uncertainties have been discussed in detail in Chapters 3 and 5. MINERvA's PPFX

[2]One of the primary reasons for reporting cross-section ratios is to cancel out the dominant flux uncertainty.

package [40, 156] evaluates the flux uncertainty in 1000 systematic universes, where each universe represents an ensemble of systematic variations of underlying beam-focusing and hadron production parameters to account for their non-trivial correlations resulting from the fits described in Subsection 3.1.2.

In addition, MINERvA applies an *in-situ* constraint combining measurements of (anti)neutrino-electron scattering and IMD [193], which significantly reduces the flux uncertainty in the antineutrino-dominated beam to about 5% as evident from Figure 8.3. The *in-situ* constraint assigns weights to the individual flux universes, with some being weighted much more than others, allowing for their ordering in terms of significance. Previous MINERvA studies have shown that, in most cases, the most significant 100 universes adequately sample the range of systematic variations [235]. This allows for a reduction in computational power when evaluating the flux uncertainty at the cross-section measurement level, and is therefore used in this analysis. Note that the flux uncertainty in both p_{T} and Bjorken x, as shown in Figure 8.3, is flat since the cross-sections are differential.

8.2 Antimuon reconstruction

The uncertainty related to antimuon reconstruction is the second-largest (third-largest) uncertainty in the p_{T} (Bjorken x) differential cross-section. Figure 8.4 shows the error band broken down into the various sources of uncertainties for both lead and scintillator

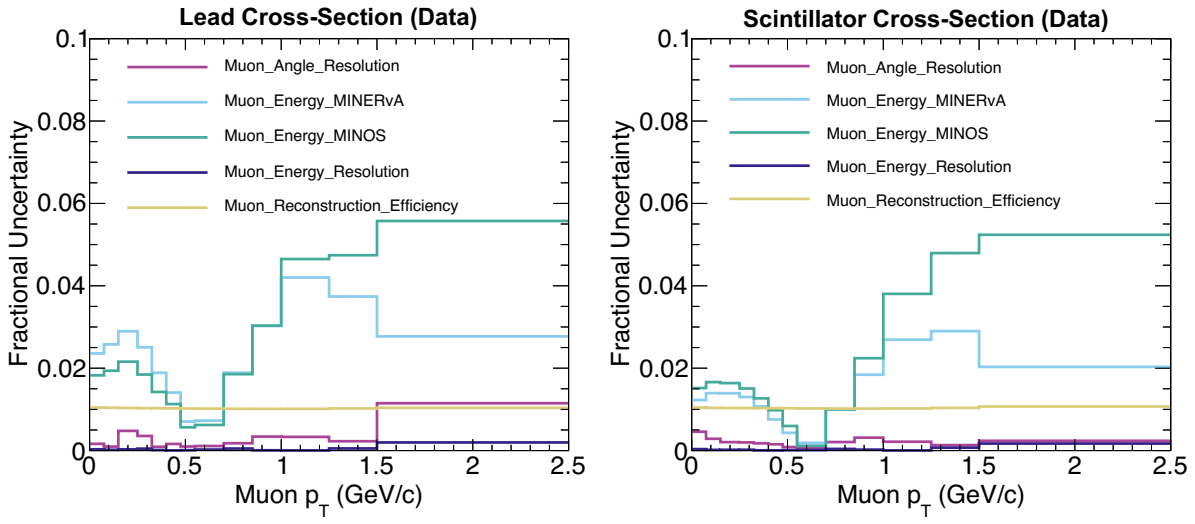

Figure 8.4: Breakdown of various sources of uncertainty in the 'Muon Reconstruction' error band in the lead (left) and scintillator (right) differential cross-section in data in p_{T}.

cross-sections in p_{T}, while the corresponding breakdown for Bjorken x is provided in Appendix K. The p_{T} breakdown is dominated by the uncertainty on the antimuon energy reconstruction in the MINERvA detector and MINOS spectrometer. The MINERvA uncertainty combines the 40 MeV (30 MeV) uncertainty on the energy deposits per unit length and the 17 MeV (11 MeV) material assay uncertainty for the passive target region (active tracker region) [179]. The MINOS uncertainty comes from the 0.98% uncertainty on antimuons reconstructed by range, and the 2.1% (3.2%) uncertainty on antimuons with momenta above (below) 1 GeV reconstructed by curvature [40], as described in Chapter 6.

The flat reconstruction efficiency uncertainty band represents the uncertainty on the tracking efficiency of the MINOS spectrometer stemming from the antimuon energy- and beam intensity-dependent correction applied to the simulation to match the data, also discussed in Chapter 6. The antimuon angle uncertainty encompasses the 2% uncertainty on the reconstructed antimuon angle [236], and the 1 mrad antimuon angle bias coming from the uncertainty on the incoming antineutrino beam angle [237]. Finally, the uncertainty in antimuon energy resolution corresponds to 0.4% [157] and quantifies any remaining antimuon energy resolution differences between the data and the simulation.

8.3 Interaction model

The initial state and initial interaction models used in the simulation, described in detail in Chapter 5, have several parameters that adjust the probability of an interaction process occurring. The underlying uncertainties associated with these parameters in GENIE [42,43], derived from previous experimental measurements, enable the construction of alternative universes to evaluate corresponding systematic uncertainties in the measurement. Some of these default uncertainties are constrained using MINERvA's measurements and reanalyses of other data. There are also additional uncertainties related to the previously discussed RPA and 2p2h implementations. All these uncertainties are combined in the 'Interaction Model' error band, as shown in Figures 8.2 and 8.3.

Figure 8.5 shows the uncertainties that contribute more than 0.5% to the 'Interaction Model' uncertainty band in the p_{T} and Bjorken x differential cross-section in both lead

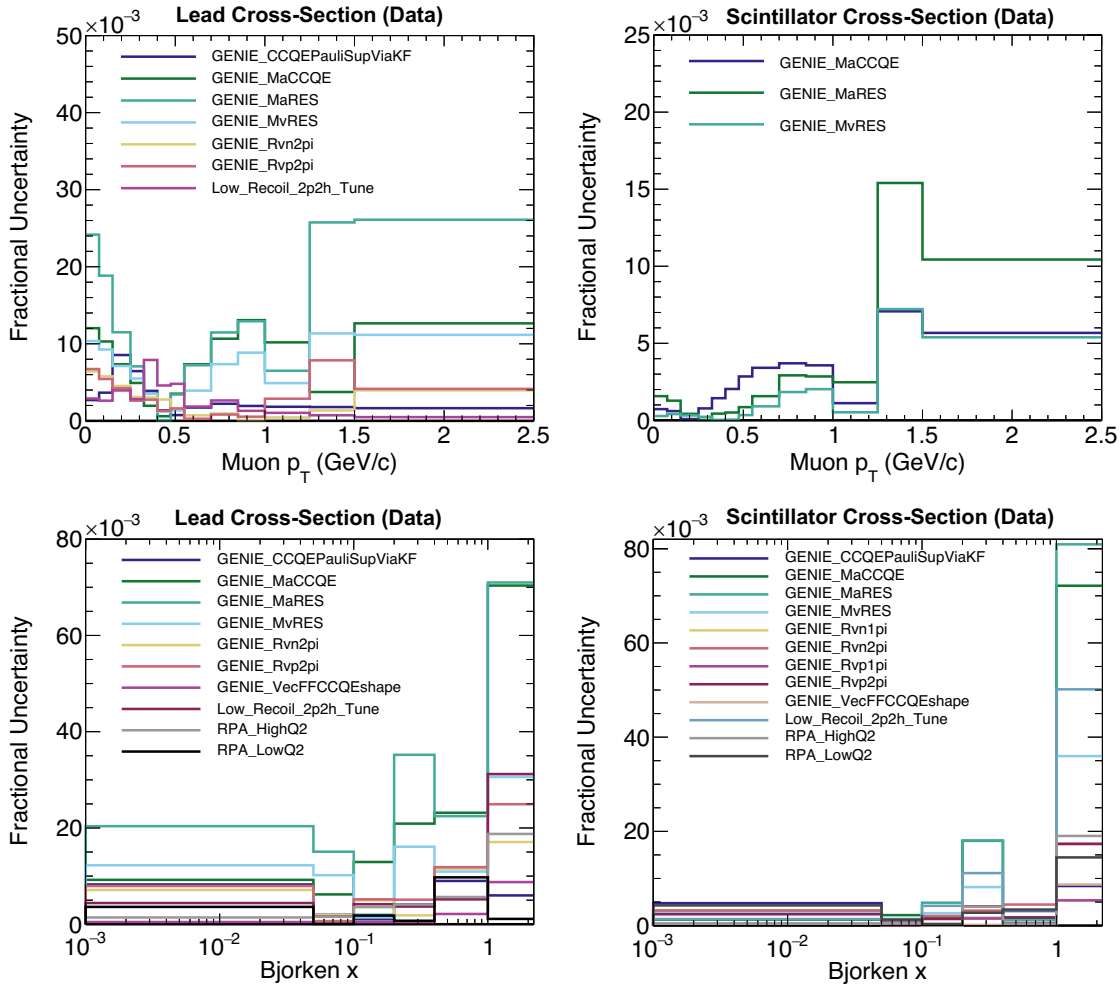

Figure 8.5: Breakdown of various sources of uncertainty in the 'Interaction Model' error band of the differential cross-section in data, both in p_{T} (top) and Bjorken x (bottom) for lead (left panel) and scintillator (right panel), with contributions exceeding 0.5%. Note the dominant contribution from the uncertainty on the resonant pion production axial mass.

and scintillator. A close-up of the scintillator breakdown in Bjorken x for the $x < 1$ region is provided in Appendix K. Overall, the error band is dominated by the resonant pion production axial mass uncertainty, which is expected given that resonant pion production is the dominant interaction channel in this analysis. Additional notable contributions come from the uncertainty on the vector mass in resonant pion production and the axial mass in quasi-elastic scattering. All of these govern the cross-section shape and normalisation of their respective processes. Table 8.1 lists and describes all GENIE parameter uncertainties contributing more than 0.5%. Note that in comparison to the nominal uncertainties in GENIE, the uncertainty on M_A^{RES} is constrained from the nominal 20% to about 5% by

Error band	1σ	Description
CCQEPauliSupViaKF	±30%	Modifies Pauli blocking at low Q^2 by adjusting momentum cutoff
MaCCQE	+25%/-15%	CCQE axial mass (0.99 GeV/c^2) in the Llewellyn-Smith cross-section (shape and normalisation)
MaRES	±0.05 GeV/c^2	RES axial mass (0.94 GeV/c^2) in the Rein-Sehgal cross-section (shape and normalisation)
MvRES	±3%	RES vector mass (0.84 GeV/c^2) in Rein-Sehgal cross-section (shape and normalisation)
Rvn1pi	±4%	Strength of CC and NC 1π production from non-resonant (Bodek-Yang) $\nu n/\bar{\nu}p$ interactions
Rvn2pi	±50%	Strength of CC and NC 2π production from non-resonant (Bodek-Yang) $\nu n/\bar{\nu}p$ interactions
Rvp1pi	±4%	Strength of CC and NC 1π production from non-resonant (Bodek-Yang) $\nu p/\bar{\nu}n$ interactions
Rvp2pi	±50%	Strength of CC and NC 2π production from non-resonant (Bodek-Yang) $\nu p/\bar{\nu}n$ interactions
VecFFCCQEshape	BBBA → dipole	CCQE vector form factor model change from BBBA to dipole (shape)

Table 8.1: Description of various sources of uncertainty in the 'Interaction Model' error band from Figure 8.5 with their corresponding 1σ shifts.

the reanalysis of the ANL/BNL deuterium bubble chamber measurements of single pion production [201], mentioned in Chapter 5. In addition, the uncertainties on the single-pion non-resonant production parameters are constrained from 50% to 4% using the same reanalysis. Fits [78] to pion production in electron-nucleon scattering [238] are also used to reduce the uncertainty on M_V^{RES} from 10% to 3%.

Furthermore, the uncertainty associated with the 2p2h model used in the MINERvA simulation, as described in Section 5.2.2, is assessed by varying the composition of correlated pairs of nucleons. This variation extends to the extremes of either exclusively proton-proton (neutron-neutron) pairs or exclusively neutron-proton pairs involved in the 2p2h process to construct the alternative universes [199]. The RPA uncertainty is evaluated similarly by varying its implementation in the universes separately for the low-momentum and high-momentum transfer regions. The former comes from the comparisons against data for muon capture at low-momentum transfer, while the latter stems from the differences between the relativistic (implemented in the simulation CV) and the non-relativistic RPA calculation at high-momentum transfer [198].

8.4 FSI

The uncertainty on the final-state interactions (FSI) refers to the combination of uncertainties in GENIE parameters governing all interactions following the initial interaction. In this context, in addition to the uncertainties on the intranuclear cascade parameters, the 'FSI' error band also includes uncertainties on hadronisation and delta resonance decay (which are technically not FSI). The uncertainties in these parameters implemented in GENIE were originally determined by the MINOS collaboration [239].

Figure 8.6 displays uncertainties in the p_{T} and Bjorken x differential cross-sections on lead and scintillator that contribute more than 0.5% and more than 0.05%, respectively,

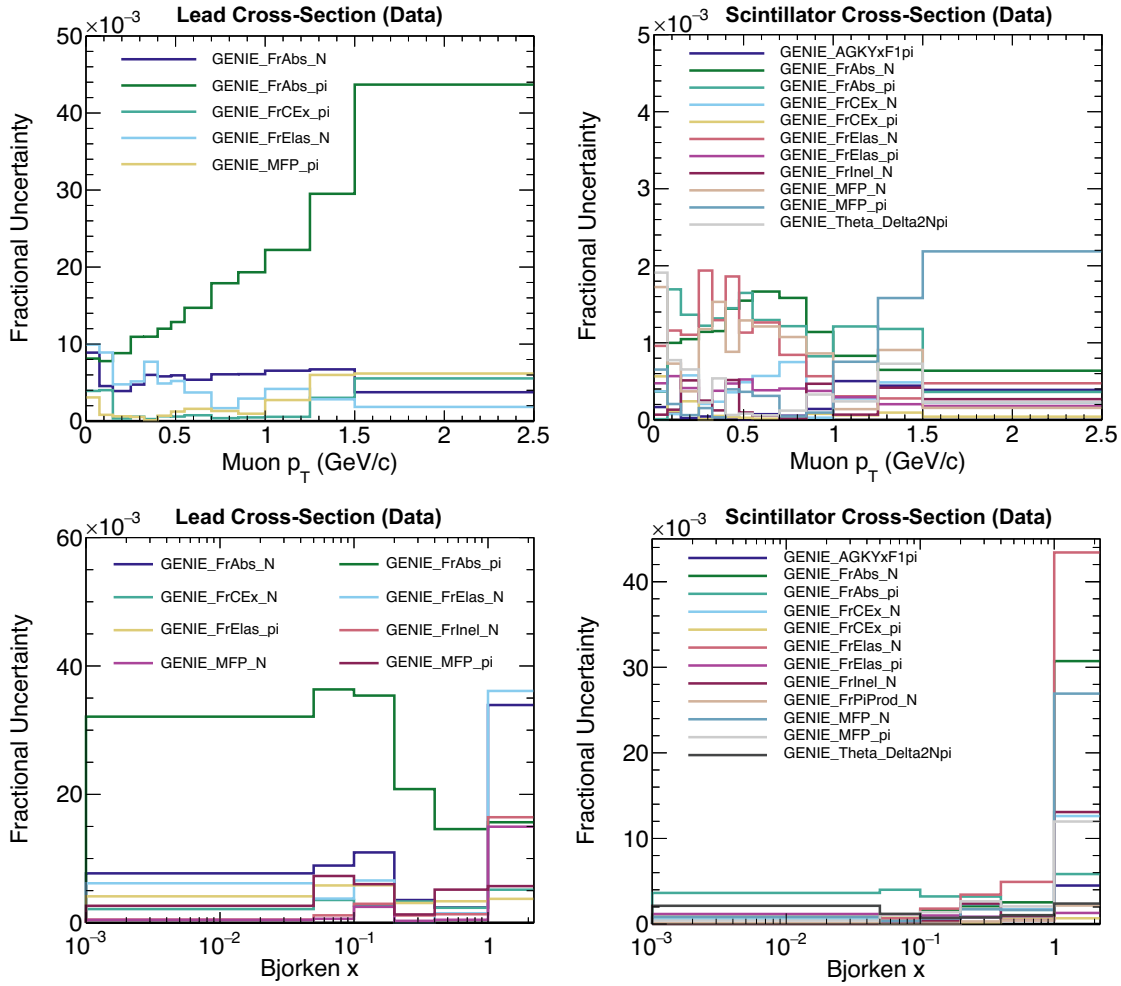

Figure 8.6: Breakdown of various sources of uncertainty in the 'FSI' error band of the differential cross-section in data, both in p_{T} (top) and Bjorken x (bottom) for lead (left panel) and scintillator (right panel). Note that only uncertainties that contribute more than 0.5% for lead and more than 0.05% for scintillator are shown, illustrating the striking difference in the FSI uncertainty in heavier nuclei.

to the 'FSI' uncertainty band. A close-up of the scintillator breakdown in Bjorken x in the $x < 1$ region is included in Appendix K. The comparison between the heavy lead and the light scintillator highlights the major difference in their respective 'FSI' contributions. The larger 'FSI' uncertainty in lead is associated with its complex nuclear environment, characterised by a significantly higher number of nucleons compared to the scintillator, which is primarily composed of carbon. In particular, the primary source of uncertainty contributing significantly to the 'FSI' error band in lead is related to the uncertainty regarding the probability of a pion produced in the initial interaction being absorbed by the nuclear environment, resulting in it not exiting the nucleus. This is not unexpected as the pion production represents the dominant channel in this analysis. Table 8.2 provides a list and description of all parameters associated with the uncertainties presented in Figure 8.6.

Error band	1σ	Description
AGKYxF1pi	±20%	Modifies DIS hadronisation model for low multiplicity production of nucleons and pions
FrAbs_N	±20%	Absorption probability for nucleons (for given total rescattering probability)
FrAbs_pi	±30%	Absorption probability for pions (for given total rescattering probability)
FrCEx_N	±50%	Charge exchange probability for nucleons (for given total rescattering probability)
FrCEx_pi	±50%	Charge exchange probability for pions (for given total rescattering probability)
FrElas_N	±30%	Elastic scattering probability for nucleons (for given total rescattering probability)
FrElas_N	±10%	Elastic scattering probability for pions (for given total rescattering probability)
FrInel_N	±40%	Inelastic scattering probability for nucleons (for given total rescattering probability)
FrPiProd_N	±20%	Pion production probability for nucleons (for given total rescattering probability)
MFP_N	±20%	Modifies the mean free path for nucleons
MFP_pi	±20%	Modifies the mean free path for pions
Theta_Delta2Npi	±100%	Uncertainty on the anisotropy of the delta decay angular distribution

Table 8.2: Description of various sources of uncertainty in the 'FSI' error band from Figure 8.6 with their corresponding 1σ shifts.

8.5 Particle response

The 'Particle Response' error band in Figures 8.2 and 8.3 includes uncertainties concerning both the interaction cross-sections used by GEANT4 [159, 160] for simulating final-state particles as they traverse the MINERvA detector (discussed in Chapter 5) and the calorimetric detector response relevant to recoil reconstruction (described in Chapter 6). Figure 8.7 breaks down the sources of uncertainties contributing to this error band in the p_{T} and Bjorken x differential cross-sections on lead and scintillator.

To evaluate the uncertainty associated with the GEANT4 simulation, MINERvA varies the hadronic inelastic cross-section of the final-state protons and pions based on

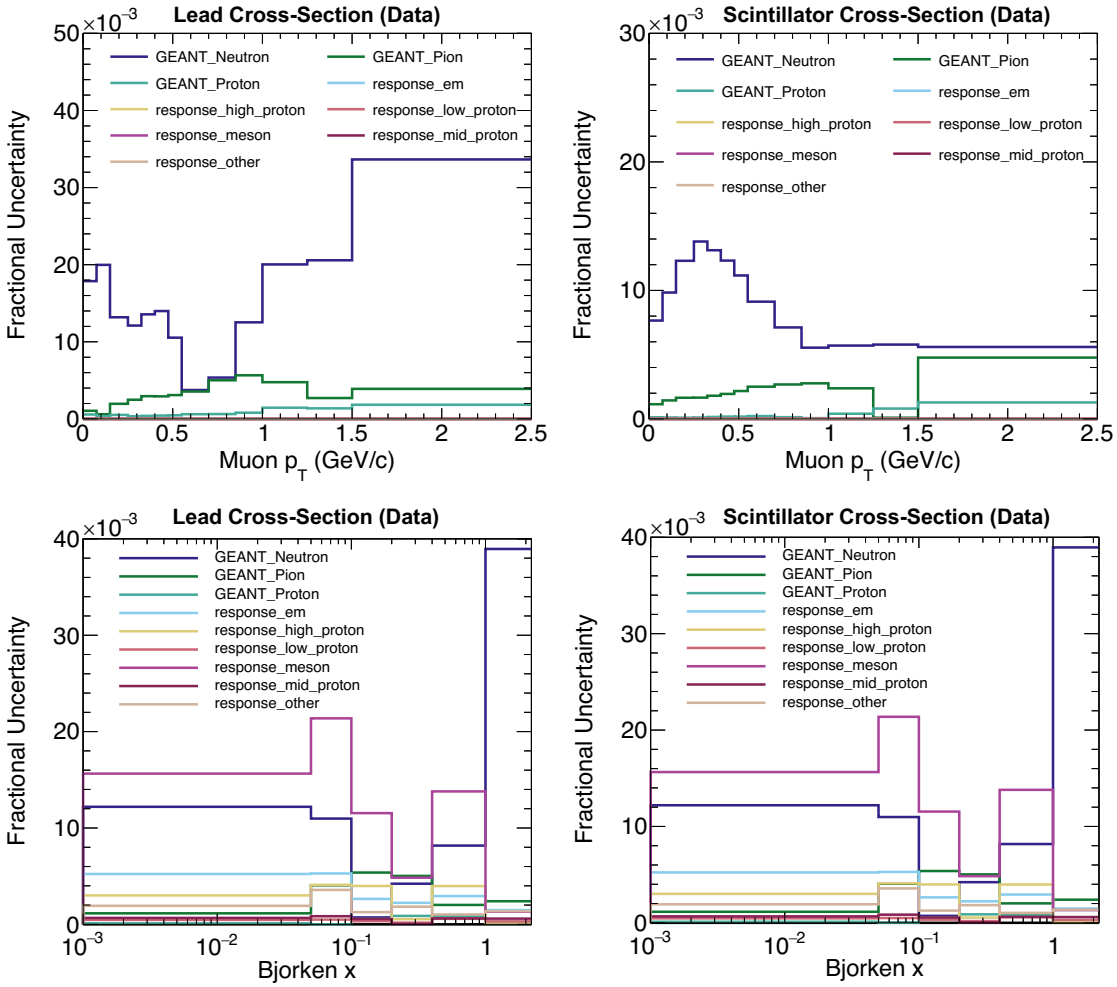

Figure 8.7: Breakdown of various sources of uncertainty in the 'Particle Response' error band of the differential cross-section in data, both in p_{T} (top) and Bjorken x (bottom) for lead (left panel) and scintillator (right panel). Note the additional contribution from uncertainties related to the calorimetric detector response relevant to recoil reconstruction in Bjorken x.

the MINERvA test beam data [240] according to the procedure described in Subsection 5.3.1. The uncertainty on the neutron inelastic cross-section reflects the reweight to the Abfalterer *et al.* data [208] also outlined in Subsection 5.3.1. The GEANT4 neutron uncertainty also accounts for the uncertainty on neutron energy deposits, as the neutron energy deposition is dependent on the neutron inelastic cross-section.

The uncertainties on how the MINERvA detector responds to various calorimetric recoil energy deposits from protons [241] and pions [242] are also constrained by the test beam studies [240]. The electromagnetic response uncertainty is derived from differences between data and simulation when observing Michel electrons (electrons from muon decay) [40]. Other unconstrained contributions are assigned conservative uncertainties. All these uncertainties for various particle energy deposits are summarised in Table 8.3.

The comparison between lead and scintillator in Figure 8.7 highlights that uncertainties in the modelling of inelastic cross-sections are more pronounced for heavier targets. Overall, the uncertainty on neutron modelling is the largest, contributing significantly to both p_{T} and Bjorken x distribution. In p_{T} in particular, the effect is attributed to correlations between the outgoing particle kinematics, with p_{T} serving as a proxy for the momentum transfer. Furthermore, as expected, uncertainties in the calorimetric response of the detector have a significant impact on the Bjorken x distribution, in contrast to the p_{T} distribution, which, by definition, does not depend on recoil reconstruction. Note that in Bjorken x, the dominant source of uncertainty corresponds to the detector's response to pions (mesons), consistent with pion production constituting the primary channel in this analysis.

Error band	1σ	Description
response_low_proton	±4.0%	Proton kinetic energy < 50 MeV
response_mid_proton	±3.5%	Proton kinetic energy between 50 MeV and 100 MeV
response_high_proton	±3.0%	Proton kinetic energy > 100 MeV
response_meson	±5.0%	Pion kinetic energy between 400 MeV and 1.9 GeV
response_em	±3.0%	Electromagnetic shower
response_other	±20.0%	Other

Table 8.3: Description of various sources of uncertainty related to the calorimetric detector response relevant to recoil reconstruction in the 'Particle Response' error band from Figure 8.7 with their corresponding 1σ shifts.

8.6 Other

Other uncertainties considered in this analysis are related to the material mass and the machine-learning-based vertex reconstruction. Specifically, the estimated uncertainties on the fiducial masses due to density and thickness variations are represented by ±0.5% shifts for the carbon and lead mass, ±1.0% for the iron mass, and ±1.4% for the scintillator mass [40]. The uncertainty associated with the ability to correctly resolve the vertex position using machine learning is set conservatively by ±1.0% shifts relative to the central value based on my studies of the differences between the data and the simulation in the plane prediction distributions for antineutrino interaction vertices [223]. The 'Other' error band in Figures 8.2 and 8.3 represents the combination of these two uncertainties above and contributes slightly over 1% to the total uncertainty in the differential cross-section.

8.7 Additional sources of uncertainties

Two additional systematic uncertainties arising from two aspects of the analysis procedure described in Chapter 7 are under consideration for implementation. Specifically, an uncertainty is proposed to account for the disagreement between the data and simulation after the data-driven plastic sideband fit procedure, outlined in Section 7.2. This proposed uncertainty is aimed at addressing discrepancies that are not, in some bins, fully covered by the current list of systematic uncertainties. Alternatively, the shape differences could be mitigated by introducing a bin-by-bin scale factor, potentially eliminating the need for this additional systematic uncertainty, which is further discussed in Chapter 9.

Additionally, another uncertainty could account for potential model bias in the Bjorken x cross-section introduced by the neutron modelling corrections at the unfolding level suggested by the exploratory study in Section 7.3. This proposed uncertainty would address the differences observed in the $x > 1$ region when unfolding data using simulations with modified true invisible energy distributions, as shown in Figure 7.16 in the relevant section. However, in order to do so, it is essential to examine and understand the magnitude of the variations in invisible energy first.

Chapter 9

Results and discussion

This chapter presents the results and the related discussion of the nuclear dependence measurement in antineutrino scattering using MINERvA, the analysis that I conducted and detailed in this work. Specifically, the cross-section results include differential cross-sections in antimuon p_{T} and Bjorken x for carbon, hydrocarbon (scintillator), iron, and lead, along with their associated uncertainty breakdowns.

Additionally, the chapter features ratios of carbon-, iron-, and lead-to-hydrocarbon in both variables of interest, each with corresponding uncertainty breakdowns. These comparisons effectively highlight (mostly) flux-independent differences between the different nuclei. While the chapter includes all cross-section and cross-section ratio results, the discussion focuses on and summarises observed general trends. The discussion also considers potential future improvements to the analysis.

Furthermore, the cross-section and cross-section ratio results are reviewed in the context of other (anti)neutrino event generators. In particular, the results are compared with a newer version of GENIE and with NEUT, which employ different interaction models than the underlying simulation.

9.1 Antimuon p_{T} results

Figure 9.1 shows the extracted differential cross-sections in antimuon transverse momentum p_{T} for inclusive antineutrino scattering on carbon, hydrocarbon (scintillator), iron, and lead, while Figure 9.2 illustrates the corresponding nuclear target-to-scintillator ratios. As explained in Chapter 4, p_{T} serves as a convenient recoil energy independent proxy to the square of the four-momentum transferred, Q^2, in the course of the scattering process. Therefore, the peaks of the individual interaction type contribution in the simulation prediction breakdown in Figure 9.1 can be visibly seen to follow the low-transfer to high-transfer ordering from low-p_{T} to high-p_{T} region, indicating that quasi-elastic scattering and 2p2h mainly contribute at low p_{T}, whereas the deep inelastic scattering tends to dominate at high p_{T}. However, overall, the cross-section is predicted to be dominated by the resonant pion production (even at lowest p_{T}) followed by the deep inelastic scattering as this analysis utilises MINERvA's medium energy dataset with antineutrino flux peak near 6 GeV.

Importantly, the data-to-simulation ratios in Figure 9.1 reflect the trend observed throughout the analysis process. The region from the falling edge of the p_{T} distribution to large p_{T} is systematically underpredicted by the simulation for all nuclei. The data excess grows as p_{T} increases. Interestingly, a similar excess was reported in MINERvA's measurement of antineutrino quasi-elastic-like scattering only [60]. This indicates that either quasi-elastic scattering or resonant pion production, or a combination thereof, is being mismodelled, i.e. underpredicted, by the underlying simulation.

Furthermore, the low p_{T} region presents an interesting insight into the nuclear dependence of the inclusive antineutrino scattering, which is mostly ascribed to the resonant pion production in the simulation. The simulation prediction ranges from underprediction of the data for relatively light nuclei, i.e. low-A carbon and hydrocarbon, to significant overprediction of the data for high-A lead. In other words, the discrepancy changes and grows as a function of the mass number A. Notably, this has been seen in MINERvA's medium-energy neutrino charged-current single π^+ production on various nuclear tar-

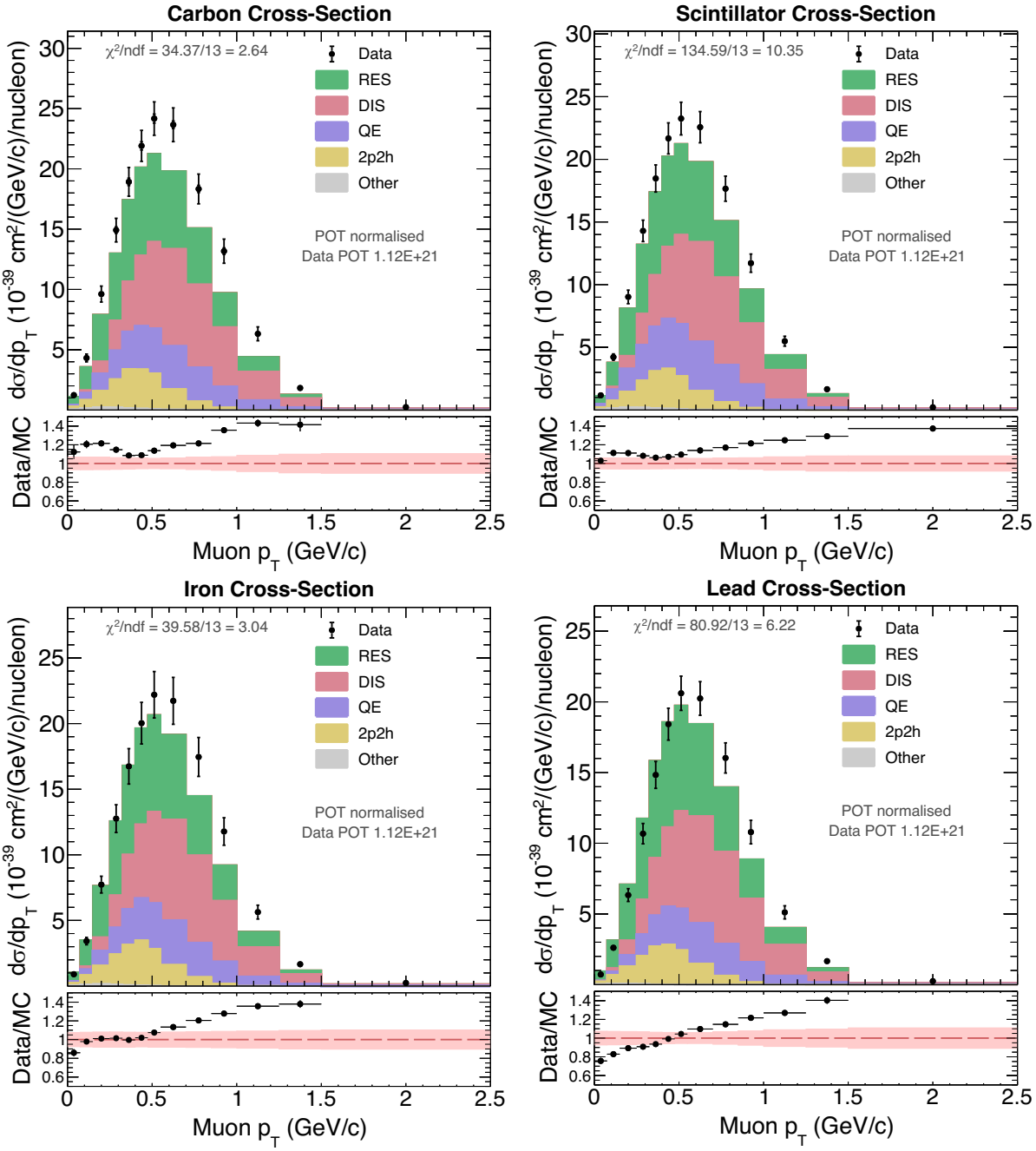

Figure 9.1: Carbon, scintillator, iron, and lead (from left to right, top to bottom) cross-section as a function of p_{T} with the simulation broken down into the various interaction channels stacked in the descending order of their contribution. In the top panel of each plot, the data points carry both statistical (inner error bar) and systematic (outer error bar, which is the sum of statistical and systematic errors) uncertainties. The bottom panel of each plot displays the data-to-simulation ratio, with the pink band around 1 representing the systematic uncertainty on the data, while the black points reflect the statistical uncertainty on the data-to-simulation ratio.

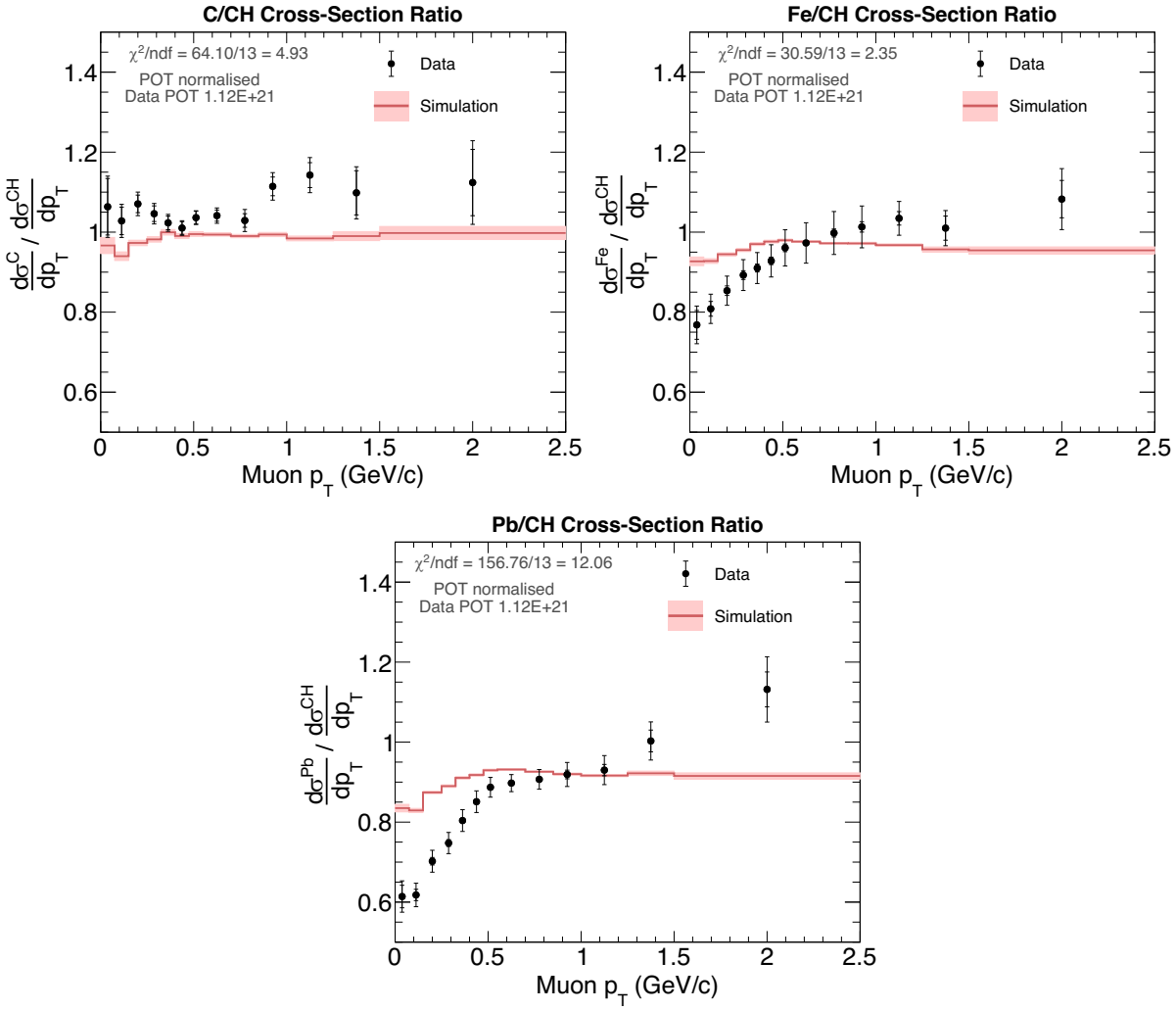

Figure 9.2: Carbon-to-scintillator (top left), iron-to-scintillator (top right), and lead-to-scintillator (bottom) cross-section ratios in antimuon p_{T}. The data points carry both statistical (inner error bar) and systematic (outer error bar, which is the sum of statistical and systematic errors) uncertainties. The error band around the simulation predictions represents its statistical error. Note the significant A-dependence across the measured ratios, particularly in the low-p_{T} region.

gets [191]. The low Q^2 suppression was also featured in several other datasets including MINOS neutrino measurement on iron [243], and MINERvA low-energy measurements of neutrino pion production on the scintillator [244–247] and one low-energy antineutrino pion-induced production also on the scintillator [245]. This analysis result is the first such observation in an antineutrino dataset in medium energy across various nuclei.

As described in Chapter 5, this analysis tried to partially remedy the suppression by reweighting its single pion production, both resonant and non-resonant, with π^- in final states, to match the low Q^2 (low p_{T}) suppression observed in the medium-energy single

π^+ production on scintillator [191]. While the interpolation from neutrino to antineutrino mode was not necessarily expected to work, the suppression improved the simulation agreement with the data which is demonstrated in Appendix L. The results show that this suppression seems to partially capture antineutrino interactions on iron, but it is not strong enough for lead.

These observed trends are further amplified by looking at the carbon-, iron-, and lead-to-scintillator ratios in Figure 9.2. While the carbon-to-scintillator ratio in antimuon p_{T} is relatively flat as expected, the iron-to-scintillator and lead-to-scintillator ratios demonstrate dramatic A-scaling changes as a function of p_{T}, specifically at low and high p_{T} as mentioned above. Overall these results suggest that both the total cross-section scaling versus A and the low Q^2 suppression are larger than modelled and that the effect increases with increasing p_{T} (square of the four-momentum transfer). Crucially, while the low Q^2 suppression is based on the pion production measurements, the inclusive antineutrino analysis spans other interaction channels that may contribute to the suppression observed in this region.

An interesting observation is the flat carbon-to-scintillator ratio in Figure 9.2, which does not completely agree with the simulation prediction at unity, contrary to expectations. However, it is important to note that the systematic uncertainties on the data are missing the uncertainty accounting for the discrepancy in the plastic sidebands after the normalisation tune discussed in Section 7.2 and Chapter 8. Given that the shape of the ratio somewhat mirrors the shape of the data-to-simulation ratio in the sideband, this is expected to account for the discrepancy between the data and the simulation prediction in the carbon-to-scintillator cross-section ratio. Alternatively, this discrepancy is also expected to be mitigated if the plastic sideband procedure is improved, for example, by fitting in the three distinct regions of p_{T} (low, peak, and high p_{T}) to remove the shape differences in the sideband rather than using a simple normalisation fit.

Finally, the breakdowns of fractional uncertainties for both the cross-sections and cross-section ratios in p_{T} are presented in Figures 9.3 and 9.4, respectively. The individual cross-sections are primarily influenced by systematic uncertainty rather than stat-

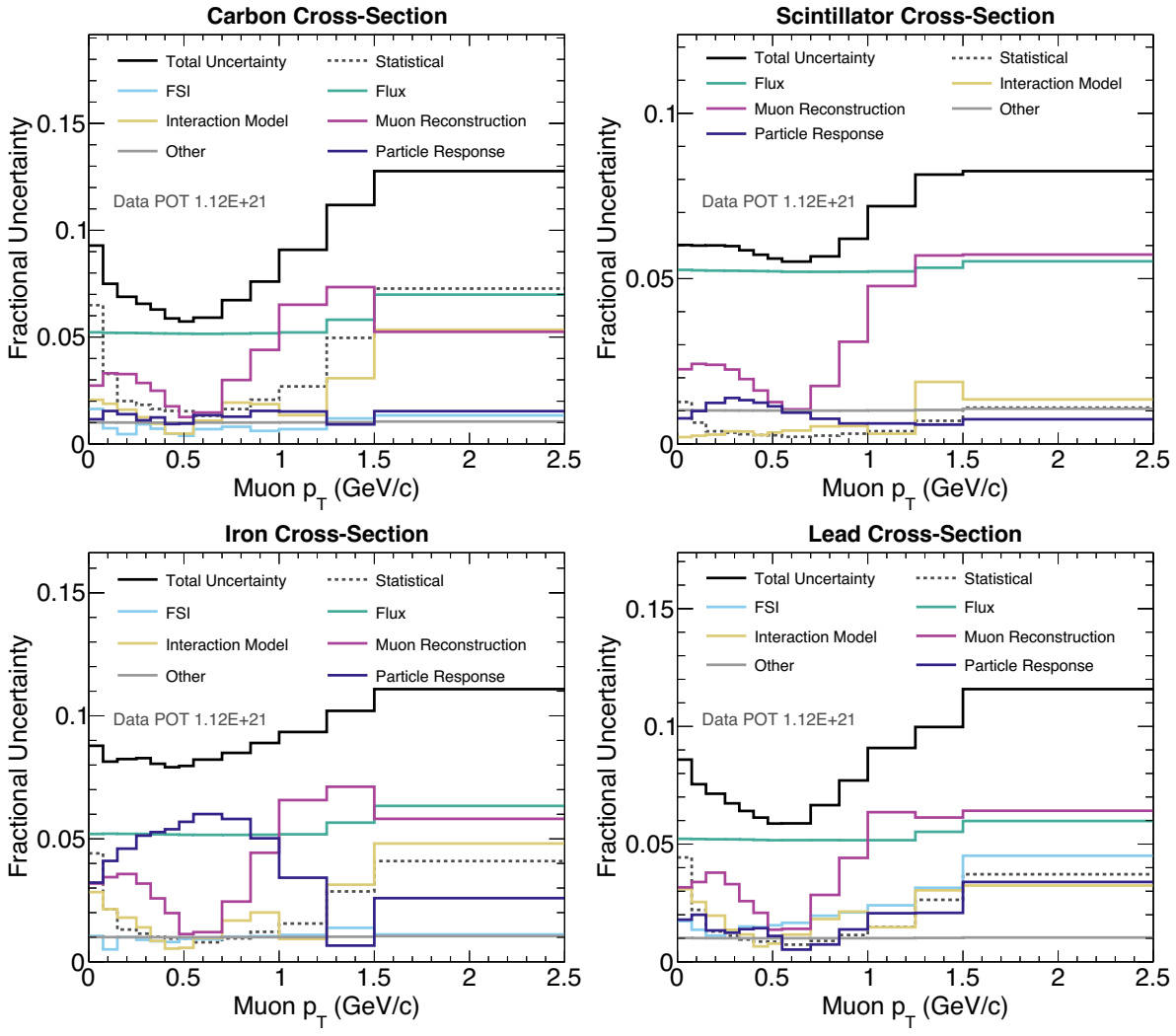

Figure 9.3: Breakdown of the fractional uncertainties on the data cross-section in p_T for carbon, hydrocarbon, iron, and lead (from left to right, top to bottom). Note that the cross-sections are dominated by the uncertainties on flux and antimuon reconstruction.

istical uncertainty, specifically stemming from the flux and the antimuon reconstruction uncertainties. These two sources of uncertainty tend to cancel out to a large extent in the cross-section ratios, as evident in Figure 9.4. Consequently, the cross-section ratios become predominantly limited by statistical uncertainties.

When comparing C/CH, Fe/CH, and Pb/CH, a noticeable increase in the uncertainty on the final-state interaction ('FSI') is observed as FSI becomes more significant and complex for heavier nuclei. It is important to note that the 'Particle Response' uncertainty band is mainly driven by uncertainties in GEANT4 neutron interaction modelling, impacting the analysis due to correlations between outgoing particle kinematics (as p_T

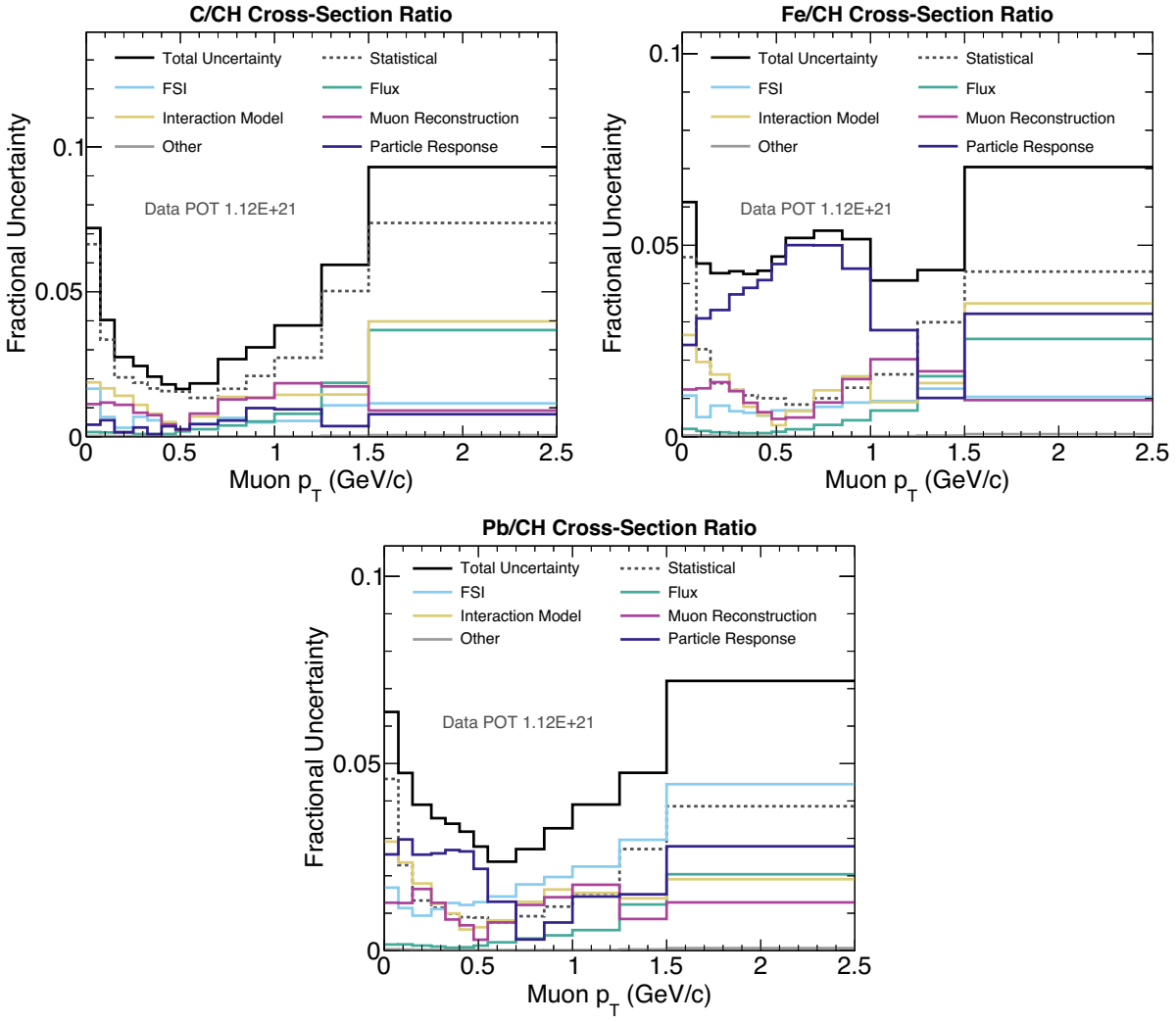

Figure 9.4: Breakdown of the fractional uncertainties on the data cross-section ratios to scintillator for carbon (top left), iron (top right), and lead (bottom) in antimuon p_{T}. Note that the flux and detector-related uncertainties are mostly cancelled out. A significant feature is the increase of the 'FSI' error band going from light carbon to heavy lead.

serves as a proxy for the momentum transfer). A similar impact of the GEANT4 neutron modelling uncertainty in iron has been observed in other MINERvA analyses [191] and is currently under investigation, potentially arising from large weights in the neutron reweight described in Subsection 5.3.1.

9.2 Bjorken x results

Figures 9.5 and 9.6 show the results of the differential cross-sections and cross-section ratios for various nuclei as functions of the dimensionless scaling variable Bjorken x. As discussed in Chapter 4, Bjorken x is used to describe nuclear modifications to a bound nucleon cross-section compared to a free nucleon. While this effect is primarily associated with deep inelastic scattering (DIS), the substantial DIS contribution in this analysis sample makes the investigation interesting. By definition, the DIS contribution is expected to be large at low x (corresponding to large recoil energy), while the quasi-elastic contribution should dominate the high x region. This is illustrated in the interaction breakdown of the simulation prediction cross-section in Figure 9.5.

The cross-section ratios for iron and lead in Bjorken x in Figure 9.6 exhibit significant disagreement with the underlying simulation in the low x region. These ratios particularly demonstrate a notable suppression of the iron and lead cross-section in this region compared to the scintillator, and the suppression grows with the size of the nucleus. This is in agreement with MINERvA's first investigation of such effects in the low-energy inclusive neutrino scattering [179]. Note that the results of this analysis represent the first comprehensive and statistically significant investigation of such effects across various nuclei in the medium-energy inclusive antineutrino sample. The low-energy equivalent was not possible due to limited statistics. Compared to the neutrino results in low energy [179], this analysis was performed using roughly $10\times$ more interactions in each nucleus.

The depletion in the cross-sections for heavy targets at low x, referred to as shadowing-like region, mainly due to the DIS contribution is generally expected, and it is attributed to the destructive interference of hadronic fluctuations of the intermediate boson that multiple-scatter off surface nucleons [179, 248, 249], as explained in Chapter 4. There are several reasons why the depletion may be larger in the data than predicted by the simulation. First, the shadowing corrections included in the simulation prediction are based on charged lepton data, which, unlike antineutrinos, do not have axial-vector contributions. Additionally, the same shadowing corrections based on iron data are also applied to car-

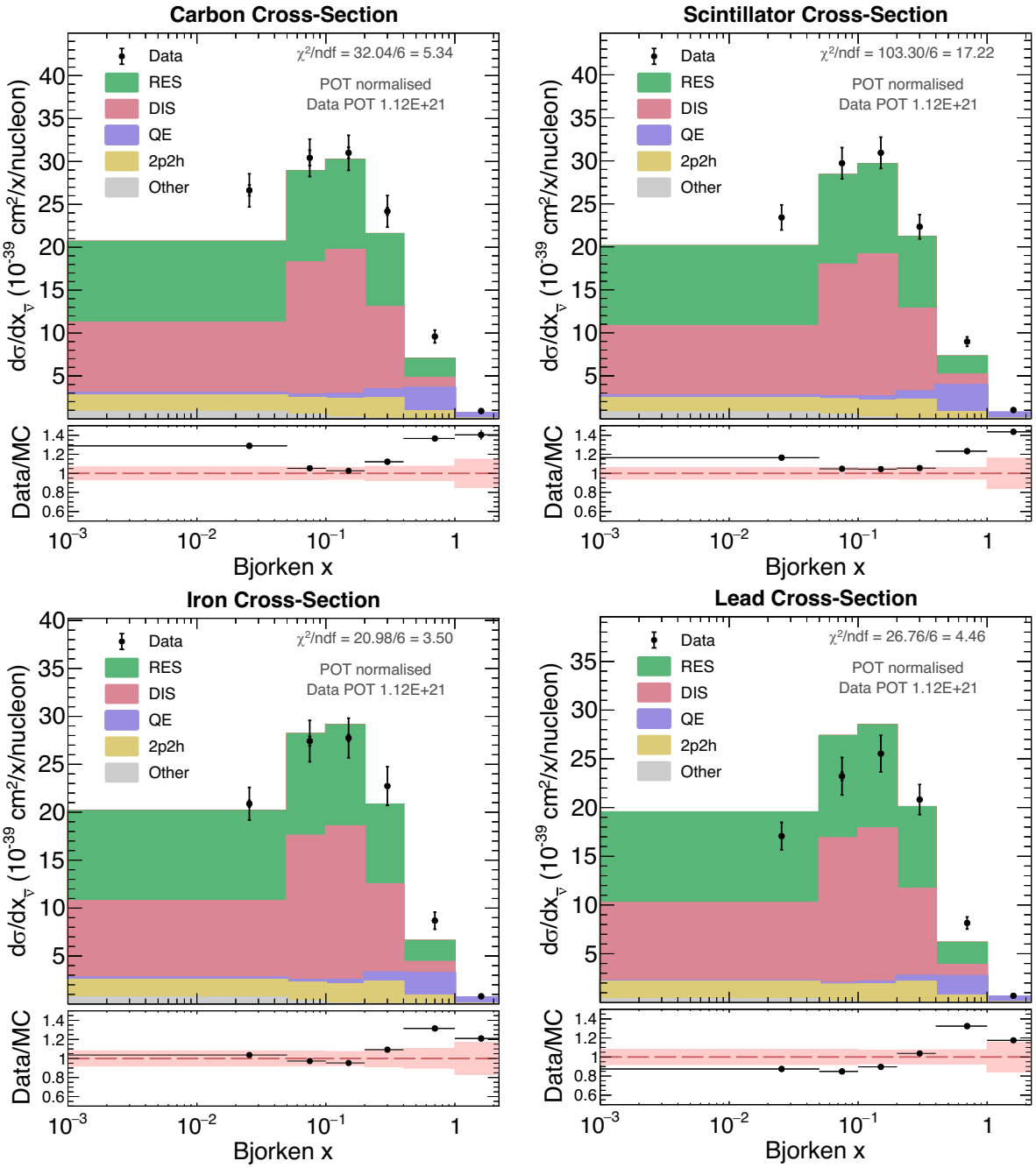

Figure 9.5: Carbon, scintillator, iron, and lead (from left to right, top to bottom) cross-section as a function of Bjorken x with the simulation broken down into the various interaction channels stacked in the descending order of their contribution. In the top panel of each plot, the data points carry both statistical (inner error bar) and systematic (outer error bar, which is the sum of statistical and systematic errors) uncertainties. The bottom panel of each plot displays the data-to-simulation ratio, with the pink band around 1 representing the systematic uncertainty on the data, while the black points reflect the statistical uncertainty on the data-to-simulation ratio.

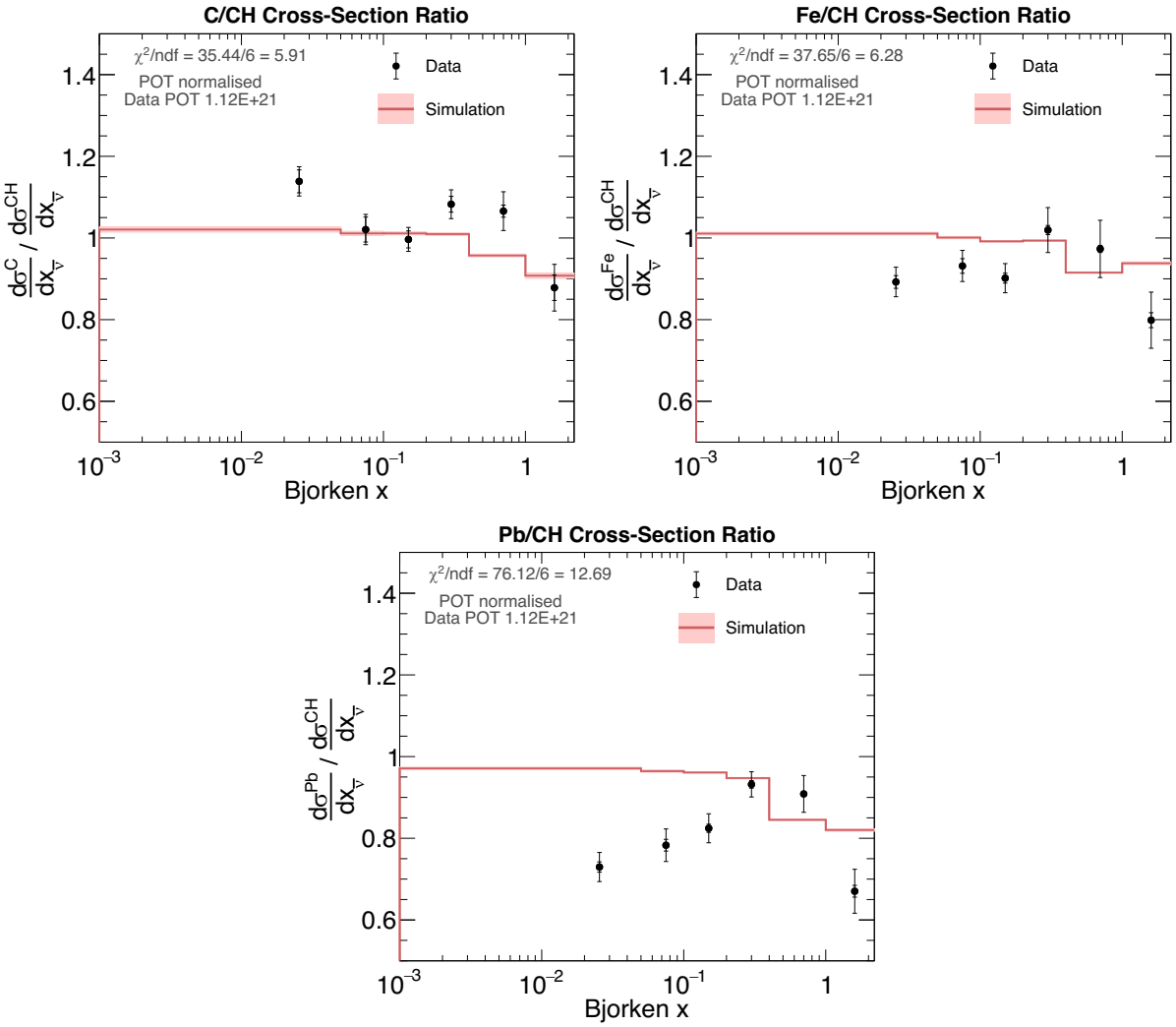

Figure 9.6: Carbon-to-scintillator (top left), iron-to-scintillator (top right), and lead-to-scintillator (bottom) cross-section ratios in Bjorken x. The data points carry both statistical (inner error bar) and systematic (outer error bar, which is the sum of statistical and systematic errors) uncertainties. The error band around the simulation predictions represents its statistical error. Note the A-dependent difference across the measured ratios, particularly in the low-Bjorken x region.

bon and lead [84], as mentioned in Chapter 5. Furthermore, more than 85% of the data has $Q^2 < 1$ (GeV/c)^2, whereas the underlying simulation is tuned to the perturbative region of higher Q^2 data.

Importantly, interpreting the observed suppression of heavy target cross-sections at low x is challenging, as it is impossible to disentangle FSI and nuclear effects due to the inclusive nature of the analysis. FSI effects may distort the observed Bjorken x distribution by increasing or decreasing the observed recoil energy, with such effects possibly more

pronounced in heavier nuclei, introducing strong nuclear dependence effects. Additional complexity also arises due to the interplay between pion production and deep inelastic scattering in the low x region, which may be resolved with MINERvA's upcoming deep and shallow inelastic scattering results.

The high-x region, dominated by quasi-elastic scattering across various nuclei, is also overpredicted in the cross-section ratios for iron and lead. However, its interpretation is also somewhat complex. The corresponding migration matrices in Section 7.3 showed large smearing in this region, and while the model dependence in unfolding was studied, the quasi-elastic scattering in antineutrino interactions results in neutrons, which are often invisible to the calorimetric recoil reconstruction. The correction to the recoil energy accounting for this is inherently model-dependent as described in Chapter 6.

Furthermore, the $x > 1$ region simulated by GENIE comes mostly from smearing from final-state interactions and does not include predictions of interactions from short-range correlated nucleons. These are expected to occur in this region based on electron-scattering data [141,225]. Also, the exploratory study of the potential bias due to neutron modelling corrections in Section 7.3 suggested a need for additional uncertainty in this region, as discussed in Chapter 8. Nevertheless, this analysis presents the first attempt to measure this region in antineutrino scattering and the data seems to indicate the need for a larger suppression at high x compared to carbon. However, the challenges described above preclude the analysis from making any definitive conclusions.

Similarly to p_{T}, the carbon-to-scintillator ratio is most consistent with the simulation and with unity. The sideband effects discussed above for p_{T} could potentially explain the differences from the underlying prediction of the ratio. Moreover, the low-x region is also sensitive to the recoil energy scale, prompting a potential investigation into whether the recoil scale differs between the nuclear target region and the scintillator tracker.

Figures 9.7 and 9.8 summarise the breakdowns of the fractional uncertainties on the Bjorken x cross-sections and the cross-section ratios for various nuclei. Similar to the p_{T} cross-section, the Bjorken x cross-section is dominated by flux uncertainty. The $x > 1$ region is governed by the understanding of the underlying interactions, i.e. 'Interaction

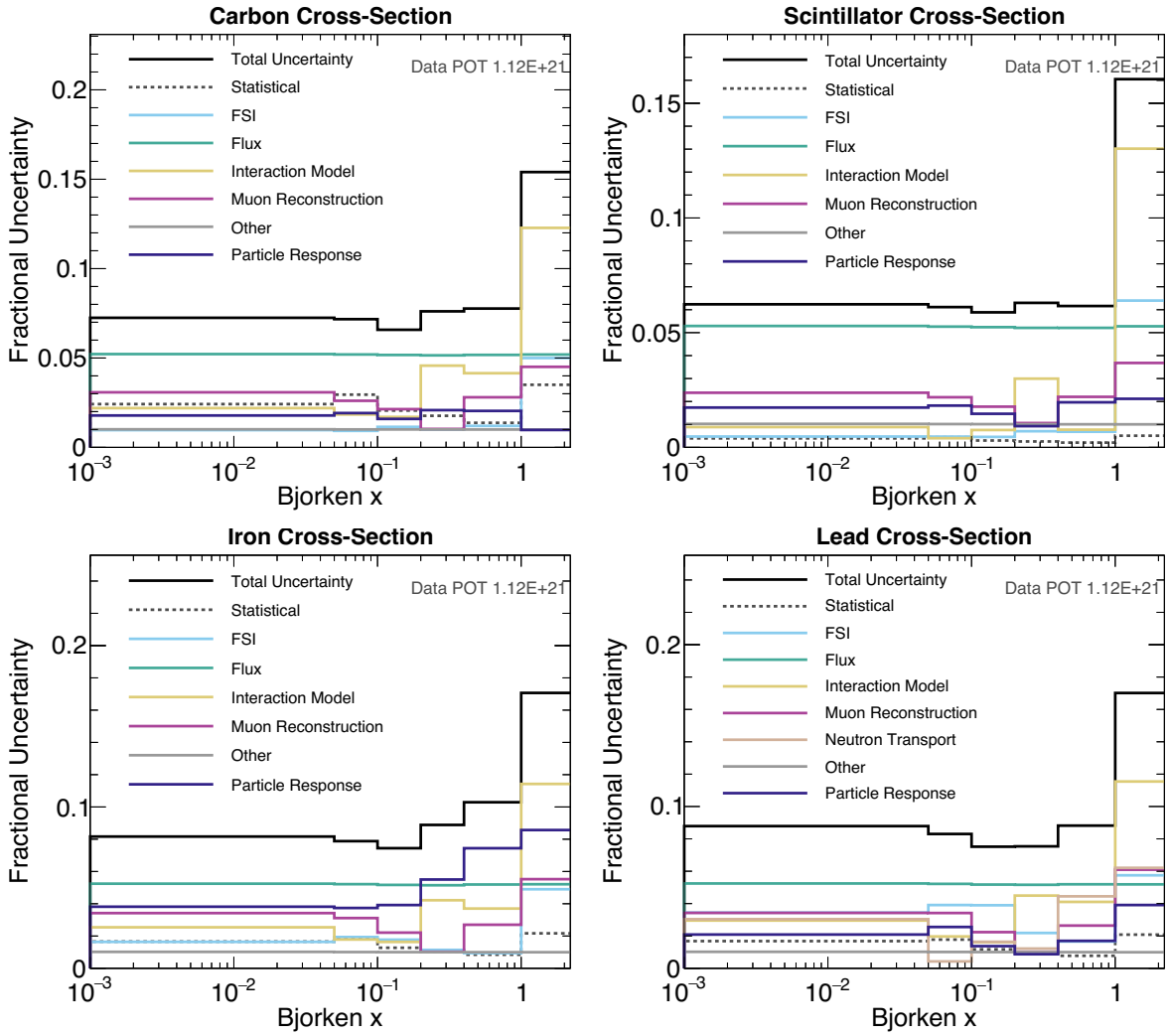

Figure 9.7: Breakdown of the fractional uncertainties on the data cross-section in Bjorken x for carbon, hydrocarbon, iron, and lead (from left to right, top to bottom). Note that, in general, the cross-sections are dominated by uncertainties on flux, with the exception of the high-x region, which is dominated by uncertainties on the underlying interaction model.

Model' error band, for the reasons described above. The C/CH ratio is mostly limited by the underlying statistics (except at large x).

Overall, in all ratios, the 'Interaction Model' error band represents the leading source of systematic uncertainty. Akin to the p_{T} results, the contribution in iron from the 'Particle Response' uncertainty band, i.e. GEANT4 neutron modelling, is being investigated. However, the 'Particle Response' in this case also includes the calorimetric detector response, as Bjorken x depends on recoil reconstruction, making its contribution overall

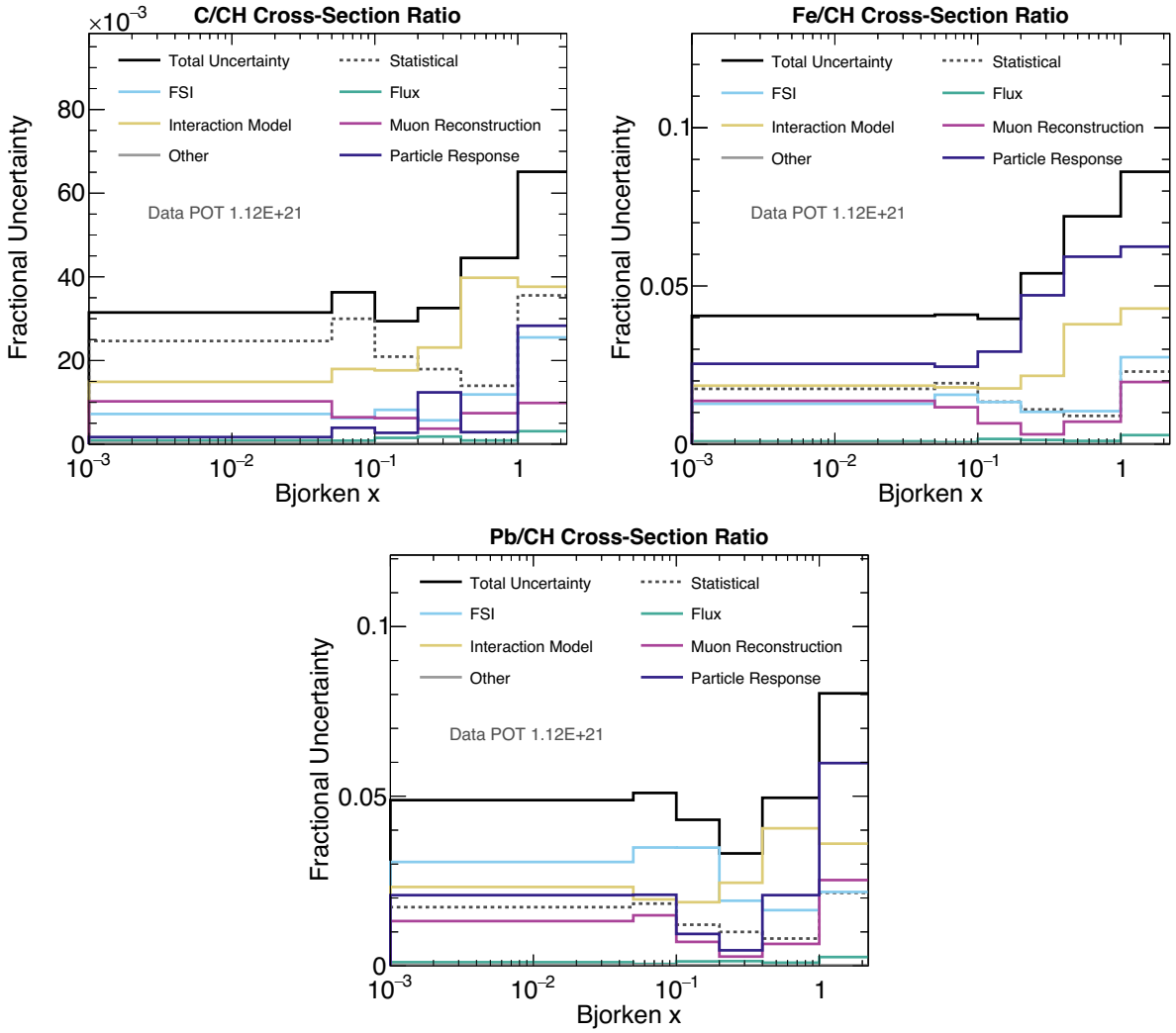

Figure 9.8: Breakdown of the fractional uncertainties on the data cross-section ratios to scintillator for carbon (top left), iron (top right), and lead (bottom) in Bjorken x. Note that the flux and detector-related uncertainties are mostly cancelled out.

larger than in p_{T}. Finally, the 'FSI' uncertainty becomes more prominent in the ratio as the nucleus in the numerator gets heavier.

9.3 Model comparisons

It is important to review the measured results in the context of other (anti)neutrino event generators that implement different interaction models than the underlying simulation used in the analysis. The different generator-to-data comparisons might give some insight into various aspects of the models, especially when extended to larger A, inform the neutrino interaction community, and potentially lead to further developments.

Both the cross-sections and cross-section ratios are compared with a newer version of GENIE [42, 43], and a different event generator called NEUT [44, 45], which is primarily used in (anti)neutrino oscillation analyses at the T2K experiment [35].

Various aspects of the different generators that are relevant to the analysis and in which they differ from the underlying simulation (outlined in Chapter 5) are briefly described below.

GENIE version 3.0.6 [76]: The resonant pion production is simulated by the Berger-Sehgal model [74] instead of the Rein-Sehgal [65]. The Berger-Sehgal update includes effects due to the muon mass in the cross-section calculation [71–73], and new implementation [77] of different axial and vector form factors [75]. The parameters of the vector form factor are determined from electron scattering data [78]. Furthermore, the FSI model is improved by emphasising medium correlations between nucleons which suppress multiple scattering and have a strong A-dependence [76, 148]. There are two FSI models available, effective cascade hA and full intranuclear cascade model hN. In addition, the differences between the individual labels in the model comparisons are:

- GENIE3 G18_02a/b uses the empirical 2p2h model [42, 250]. The 'a/b' tag represents the hA and hN FSI model, respectively. The label is a shorthand for the official GENIE 3 release G18_02a/b_02_11a.
- GENIE3 G18_10a/b employs the local Fermi gas nuclear model [104] instead of the relativistic Fermi gas [100,101], and the quasi-elastic and 2p2h interactions are based on the Valencia model [113]. Again 'a' refers to hA and 'b' to hN FSI model. The label is a shorthand for the official GENIE 3 release G18_10a/b_02_11a.

NEUT version 5.4.1 [44,45]: The resonant pion production is simulated by the Berger-Sehgal model [74]. A custom multi-pion-production model is used for $W < 2$ GeV/c^2, while deep inelastic scattering with $W > 2$ GeV/c^2 is simulated using PYTHIA/JETSET [205]. Both are based on the Bodek-Yang model [83,84] parton distribution functions. The 2p2h interaction is simulated using the Valencia model [113]. FSI uses a custom intranuclear cascade model. The two different labels have further distinguishing features:

- NEUT LFG ma105 uses the local Fermi gas nuclear model [104] and the quasi-elastic scattering is based on the Valencia model [113, 251] with $M_A = 1.05$ GeV/c^2.
- NEUT SF ma103 utilises the spectral function for the nuclear ground state with the associated quasi-elastic scattering [107, 252, 253] with $M_A = 1.03$ GeV/c^2.

Note that the general differences between the various theoretical models were addressed in Chapter 2, and that there is no NEUT SF prediction currently available for lead.

In addition to the visual comparison, the agreement between the measured data and the various models is calculated using χ^2, which takes into account bin-to-bin correlations,

$$\chi^2 = \sum_{ij}(x_i - \mu_i)\mathrm{cov}_{ij}^{-1}(x_j - \mu_j)\,. \tag{9.1}$$

The cov_{ij} represents the element of the covariance matrix defined in Chapter 8, x_i is the data in bin i, and μ_i is the corresponding model prediction. Note that the χ^2 differences in the inclusive sample are often small as some model changes do not have a large impact on the inclusive cross-section.

Figures 9.9 and 9.10 show the p_T cross-section and cross-section ratio model comparisons, respectively, across the different nuclei. The corresponding fully-correlated χ^2s per degree of freedom (the number of bins) are summarised in Tables 9.1 and 9.2. The Bjorken x results are compared to other models in Figures 9.11 and 9.12 with the corresponding χ^2s presented in Tables 9.3 and 9.4, respectively.

The p_T cross-section data generally indicates a preference for the new version of GENIE 3, with a slight inclination towards G18_02a/b. G18_10a/b, on the other hand, tends to provide a slightly better prediction for the carbon data based on the calculated χ^2. The improvements over the underlying simulation are likely to stem mainly from better modelling of the low p_T regions using updated axial and vector mass form factors. The NEUT model using the spectral function nuclear ground state performs similarly well for carbon, scintillator, and iron. Overall, the models tend to underpredict the data, except in the low p_T region for heavier nuclei where the models overpredict. All models fail to reproduce the high p_T behaviour.

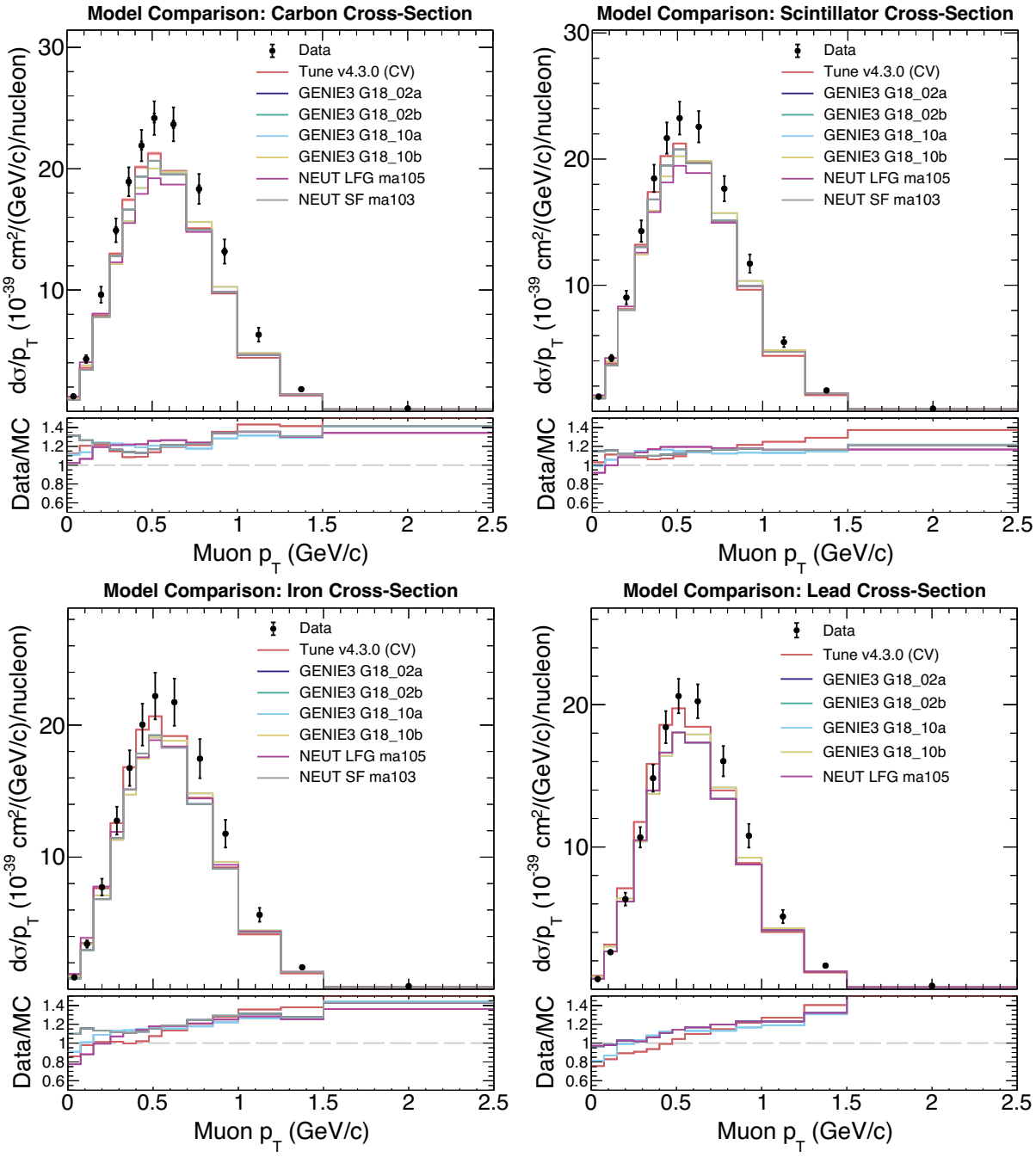

Figure 9.9: Measured carbon, scintillator, iron, and lead (from left to right, top to bottom) cross-section as a function of antimuon p_{T} compared to various antineutrino generator predictions. The inner error bar on the data indicates the statistical error while the outer error bar corresponds to the total, i.e. statistical + systematic, error. The statistical errors on the various model predictions are not shown for clarity (but they are also negligible). The bottom panel indicates the agreement between the data and various models through their respective data-to-model prediction ratios.

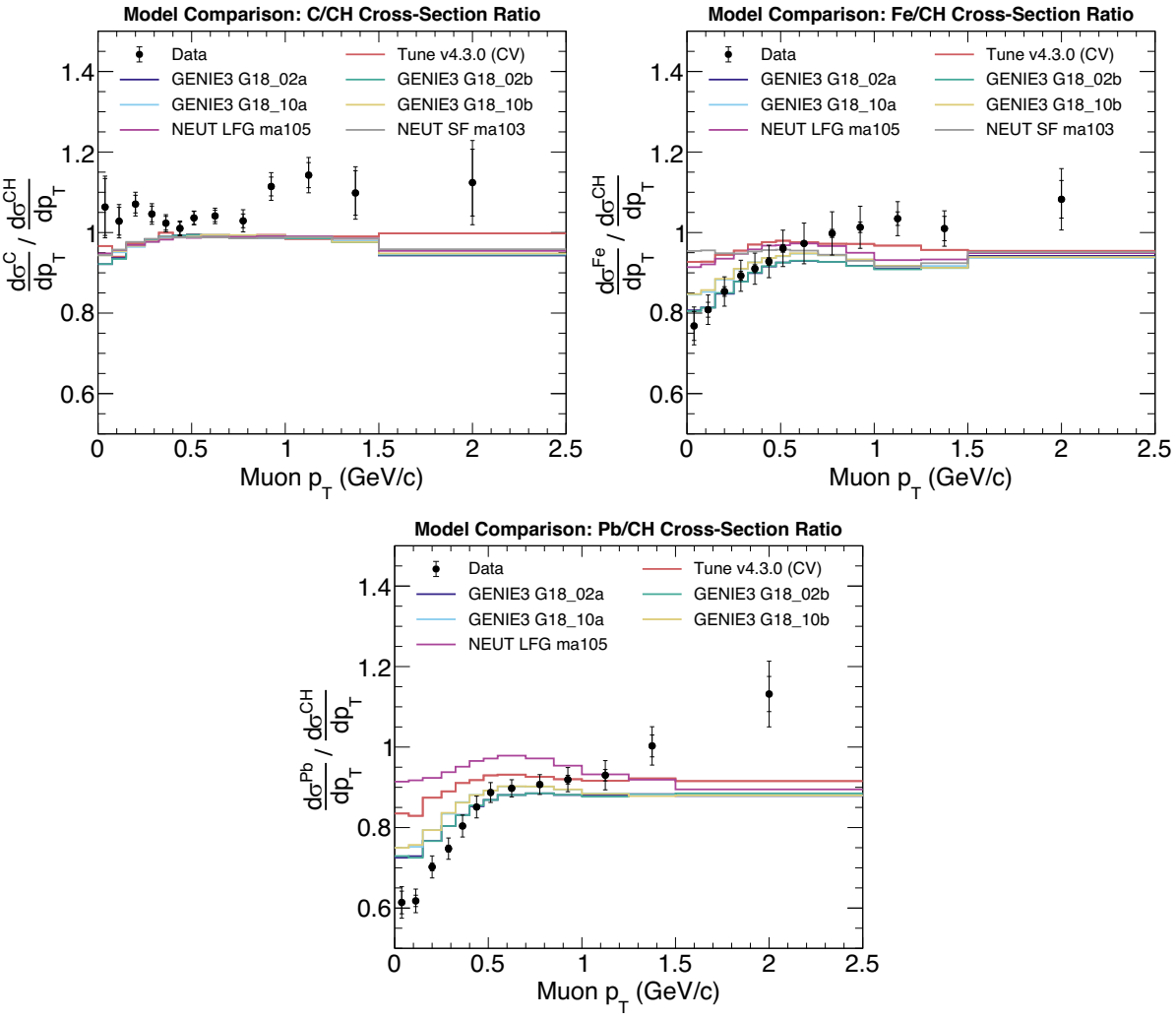

Figure 9.10: Measured carbon-to-scintillator (top left), iron-to-scintillator (top right), and lead-to-scintillator (bottom) cross-section ratios in antimuon p_{T} compared to various antineutrino generator predictions. The data is displayed with both the statistical (inner error bars) and the total (outer error bars) uncertainty. Note that the suppression predicted by the GENIE 3 models at low p_{T} mostly follows the shape of the data.

The comparisons of cross-section ratios in p_{T} demonstrate the improved A-dependent features of GENIE 3 in the low p_{T} region. Specifically, the shape of the measured iron-to-scintillator ratio is well-captured by G18_02a/b. However, the lead-to-scintillator cross-section ratio suggests that additional suppression strength in G18_02a/b may be necessary. The Pb/CH also indicates a slight preference for the full intranuclear cascade rather than the effective FSI model (which is very slightly preferred by iron).

The Bjorken x cross-section results across the various nuclei prefer both NEUT implementations over GENIE 3. Specifically, the local Fermi gas model appears to perform

Cross-section	Model χ^2/ndf for p_T (ndf = 13)						
	CV	G18_02a	G18_02b	G18_10a	G18_10b	LFG_ ma105	SF_ma103
Carbon	2.64	2.15	2.15	1.67	1.67	2.26	2.15
Scintillator	10.35	4.37	4.47	12.77	12.22	40.75	4.37
Iron	3.04	1.63	1.67	3.12	3.13	8.34	1.63
Lead	6.22	3.20	3.11	9.07	9.24	3.20	-

Table 9.1: Fully correlated χ^2/ndf calculated according to Equation 9.1 to assess the agreement between the measured data and the various models for carbon, scintillator, iron, and lead cross-section in antimuon p_T. Note that the relatively large χ^2/ndf for the scintillator is attributed to the large statistics of the sample. The first numerical column indicates the agreement with the underlying simulation prediction.

Cross-section ratio	Model χ^2/ndf for p_T (ndf = 13)						
	CV	G18_02a	G18_02b	G18_10a	G18_10b	LFG_ ma105	SF_ma103
C/CH	4.93	5.72	5.75	5.80	5.74	5.90	5.59
Fe/CH	2.35	1.63	1.68	1.71	1.73	2.52	3.90
Pb/CH	12.06	5.06	4.80	6.11	6.41	22.00	-

Table 9.2: Fully correlated χ^2/ndf calculated according to Equation 9.1 to assess the agreement between the measured data and the various models in the cross-section ratios to scintillator for carbon, iron, and lead in antimuon p_T. The first numerical column indicates the agreement with the underlying simulation prediction.

quite well. This preference could potentially be attributed to differences in the treatment of the resonant pion production to deep inelastic scattering transition region compared to GENIE 3, or the distinct intranuclear cascade. However, further investigation would be required for a more detailed understanding.

In contrast, many of the differences between the data and the models cancel out in the Bjorken x cross-section ratios to the scintillator. Consequently, GENIE 3 shows its strength in modelling the A-dependence of the overall cross-section again. Both G18_02a/b and G18_10a/b predict the suppression in the low-x region relatively well, with the Pb/CH ratio requiring additional strength, similar to the p_T ratios.

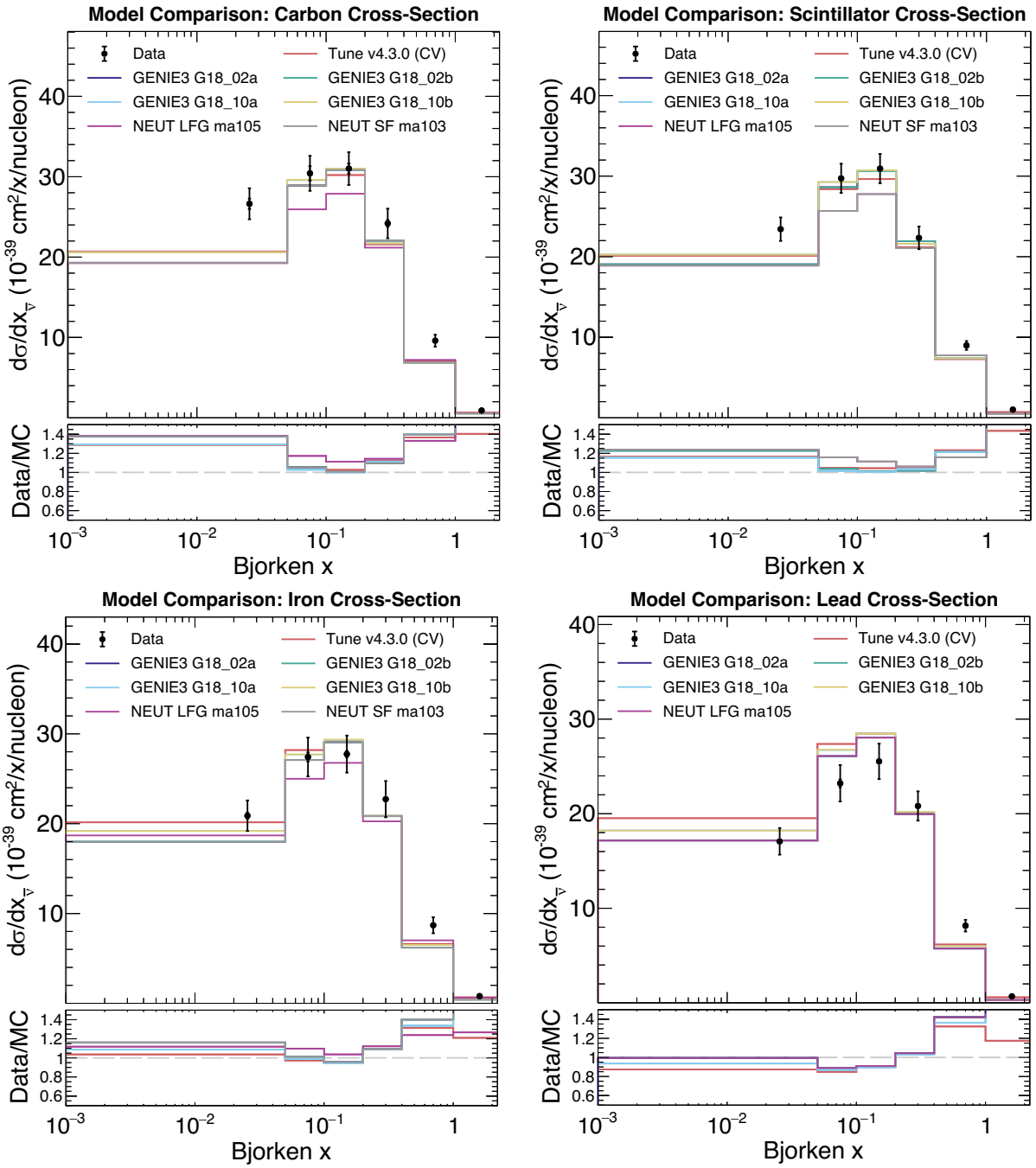

Figure 9.11: Measured carbon, scintillator, iron, and lead (from left to right, top to bottom) cross-section as a function of Bjorken x compared to various antineutrino generator predictions. The inner error bar on the data indicates the statistical error while the outer error bar corresponds to the total, i.e. statistical + systematic, error. The statistical errors on the various model predictions are not shown for clarity (but they are also negligible). The bottom panel indicates the agreement between the data and various models through their respective data-to-model prediction ratios.

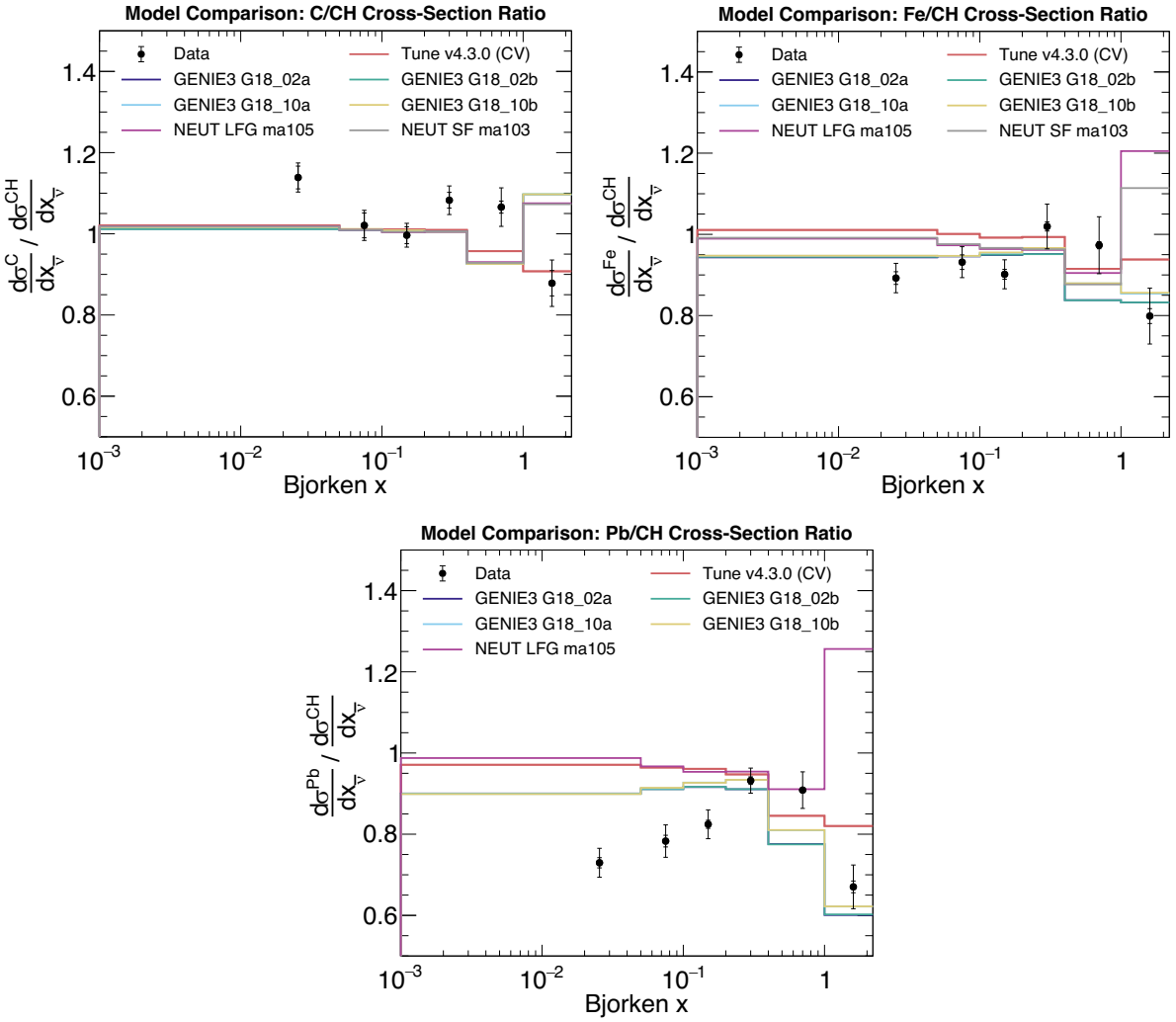

Figure 9.12: Measured carbon-to-scintillator (top left), iron-to-scintillator (top right), and lead-to-scintillator (bottom) cross-section ratios in Bjorken x are compared to various antineutrino generator predictions. The data is displayed with both the statistical (inner error bars) and the total (outer error bars) uncertainty. The suppression predicted by the GENIE 3 models at low Bjorken x attempts to follow the shape of the data.

Cross-section	Model χ^2/ndf for Bjorken x cross-section (ndf = 6)						
	CV	G18_02a	G18_02b	G18_10a	G18_10b	LFG_ ma105	SF_ma103
Carbon	5.34	8.44	8.47	7.02	7.07	4.45	8.44
Scintillator	17.22	44.61	44.30	29.79	30.12	10.49	10.49
Iron	3.50	7.64	7.64	5.98	6.10	1.65	7.64
Lead	4.46	5.94	5.92	5.19	5.23	5.94	-

Table 9.3: Fully correlated χ^2/ndf calculated according to Equation 9.1 to evaluate the agreement between the measured data and the various models for carbon, scintillator, iron, and lead cross-section in Bjorken x. Note that the relatively large χ^2/ndf for the scintillator is attributed to the large statistics of the sample. The first numerical column indicates the agreement with the underlying simulation prediction.

Cross-section ratio	Model χ^2/ndf for Bjorken x (ndf = 6)						
	CV	G18_02a	G18_02b	G18_10a	G18_10b	LFG_ ma105	SF_ma103
C/CH	5.91	5.80	5.85	5.73	5.71	5.56	5.59
Fe/CH	6.28	3.39	3.47	3.01	3.08	17.44	13.12
Pb/CH	12.69	11.14	11.13	7.74	7.69	31.95	-

Table 9.4: Fully correlated χ^2/ndf calculated according to Equation 9.1 to assess the agreement between the measured data and the various models in the cross-section ratios to scintillator for carbon, iron, and lead in Bjorken x. The first numerical column indicates the agreement with the underlying simulation prediction.

Finally, various MINERvA results are also reported with different MINERvA tunes applied to the base GENIE 2.12.6, i.e. tunes different from the underlying v4.3.0 used in this analysis. To enable further review of the results of this analysis in the context of other MINERvA results, the comparisons of the measured cross-sections and cross-section ratios are included in Appendix L.

Chapter 10

Conclusions and outlook

This thesis focused on the first simultaneous measurement of charged-current inclusive muon antineutrino cross-sections on carbon, hydrocarbon, iron, and lead as a function of antimuon transverse momentum, p_{T}, and Bjorken x. Additionally, cross-section ratios of carbon, iron, and lead to hydrocarbon were determined to directly compare the nuclear dependence in antineutrino scattering. These measurements were taken at a mean antineutrino energy of approximately $\sim$6 GeV using the MINERvA experiment, with restricted kinematic phase space of antimuon angle less than 17° relative to the antineutrino beam and an antimuon energy of 2–20 GeV. Due to the energy regime spanned by this analysis, the dominant contributions to the cross-section come from the single-pion production, deep inelastic scattering, and the transition region between these two interaction modes.

While carbon and hydrocarbon cross-sections and their ratio were found to be most consistent with the underlying simulation prediction, the results for iron and lead indicated strong suppression at low p_{T} and Bjorken x, along with an enhancement of the cross-section at high p_{T}. These effects were observed to be more pronounced with the increasing size of the target nucleus, and they were not reproduced by the underlying simulation prediction. Comparisons with alternative models in existing (anti)neutrino interaction generators were presented and showed some improvements in the modelling over the base prediction model, in particular in the case of the Berger-Sehgal model

for single-pion production with updated axial and vector form factors and updated FSI modelling utilised in GENIE 3. Nevertheless, the alternative models were still unable to fully reproduce the observed nuclear dependence in this analysis. Furthermore, while an attempt to extend the analysis to the $x > 1$ region was made to measure antineutrino scattering from deeply bound nucleons, its dependence on the interaction model rendered its interpretation difficult. The per-nucleon differential cross-sections were reported with a precision of 7–9%, while the cross-section ratios which effectively mitigate shared detector and interaction modelling effects resulted in uncertainties of approximately 5% or less.

Potential improvements to the analysis and additional studies relevant to the interpretation of the results were also discussed. In particular, the shape and slight deviation from unity in the carbon-to-hydrocarbon ratio in both p_{T} and Bjorken x are expected to be accounted for by a systematic uncertainty covering the shape of the data-to-simulation ratio in the tuned sidebands, which has not been included in the analysis so far. Alternatively, a more complex fit could be performed instead of fitting a singular scaling factor. In addition, a study testing invisible energy changes in the underlying simulation suggested that additional systematic uncertainty may be required for the $x > 1$ bin. The measurement also showed that further investigation into the neutron modelling uncertainty should be also considered.

It is important to note that while this thesis presents a one-dimensional analysis of inclusive antineutrino scattering on different nuclei, I have been simultaneously working on its two-dimensional equivalent in the antimuon transverse and longitudinal momentum. Currently, this measurement is undergoing rigorous warping studies to determine the optimal number of iterations for unfolding to the true distribution. The two-dimensional analysis will provide an even more detailed understanding of the nuclear dependence presented in this work.

Finally, this measurement represents one of the largest antineutrino datasets in this energy regime analysed to date and significantly contributes to our understanding of antineutrino scattering and the associated nuclear effects. This is relevant for the future

high-statistics oscillation experiments such as DUNE which need to refine their underlying interaction models in order to achieve their physics goals, i.e. search for CP violation. Crucially, this measurement probes the interaction channels dominant in DUNE, which are generally less well understood than, for example, quasi-elastic scattering, and their observed nuclear dependence can be interpolated to argon, the primary target in DUNE.

Bibliography

[1] A. D. Sakharov. Violation of CP invariance, C asymmetry, and baryon asymmetry of the universe. *Sov. Phys. Uspekhi*, 34(5):392, may 1991. DOI:10.1070/PU1991v034n05ABEH002497.

[2] W. Pauli. Open Letter to the Group of Radioactive People at the Gauverein Meeting in Tübingen, 1930.

[3] E. Fermi. Versuch einer Theorie der β-Strahlen. I. *Z. Physik*, 88:161–177, 1934. DOI:10.1007/BF01351864.

[4] C. L. Cowan *et al.* Detection of the Free Neutrino: A Confirmation. *Science*, 124(3212), 1956. DOI:10.1126/science.124.3212.103.

[5] T. D. Lee and C. N. Yang. Question of parity conservation in weak interactions. *Phys. Rev.*, 104:254–258, 1956. DOI:10.1103/PhysRev.104.254.

[6] C. S. Wu *et al.* Experimental Test of Parity Conservation in Beta Decay. *Phys. Rev.*, 105:1413–1415, 1957. DOI:10.1103/PhysRev.105.1413.

[7] E. C. G. Sudarshan and R. E. Marshak. The Nature of the Four-Fermion Interaction. In *Proc. of the Conference on Mesons and Newly-Discovered Particles*, Padua-Venice, Sept. 1957. URL: https://web2.ph.utexas.edu/~gsudama/pub/1958_005.pdf.

[8] E. C. G. Sudarshan and R. E. Marshak. Chirality Invariance and the Universal Fermi Interaction. *Phys. Rev.*, 109:1860–1862, 1958. DOI:10.1103/PhysRev.109.1860.2.

[9] R. P. Feynman and M. Gell-Mann. Theory of the Fermi Interaction. *Phys. Rev.*, 109:193–198, 1958. DOI:10.1103/PhysRev.109.193.

[10] M. Goldhaber *et al.* Helicity of neutrinos. *Phys. Rev.*, 109:1015–1017, 1958. DOI: 10.1103/PhysRev.109.1015.

[11] H. L. Anderson *et al.* Branching ratio of the electronic mode of positive pion decay. *Phys. Rev.*, 119:2050–2067, 1960. DOI:10.1103/PhysRev.119.2050.

[12] D. Galbraith and C. Burgard. Standard model of physics, 2012. Accessed on March 16th, 2024. URL: https://texample.net/tikz/examples/model-physics/.

[13] G. Danby *et al.* Observation of High-Energy Neutrino Reactions and the Existence of Two Kinds of Neutrinos. *Phys. Rev. Lett.*, 9:36–44, 1962. DOI:10.1103/PhysRevLett.9.36.

[14] M. L. Perl *et al.* Evidence for anomalous lepton production in $e^+ - e^-$ annihilation. *Phys. Rev. Lett.*, 35:1489–1492, 1975. DOI:10.1103/PhysRevLett.35.1489.

[15] K. Kodama *et al.* Observation of tau neutrino interactions. *Phys. Lett. B*, 504(3):218–224, 2001. DOI:10.1016/S0370-2693(01)00307-0.

[16] S. L. Glashow. Partial-symmetries of weak interactions. *Nuclear Physics*, 22(4):579–588, 1961. DOI:10.1016/0029-5582(61)90469-2.

[17] A. Salam and J. Ward. Electromagnetic and weak interactions. *Phys. Lett.*, 13(2):168–171, 1964. DOI:10.1016/0031-9163(64)90711-5.

[18] S. Weinberg. A model of leptons. *Phys. Rev. Lett.*, 19:1264–1266, 1967. DOI: 10.1103/PhysRevLett.19.1264.

[19] F. Hasert *et al.* Search for elastic muon-neutrino electron scattering. *Phys. Lett. B*, 46(1):121–124, 1973. DOI:10.1016/0370-2693(73)90494-2.

[20] F. Hasert *et al.* Observation of neutrino-like interactions without muon or electron in the gargamelle neutrino experiment. *Phys. Lett. B*, 46(1):138–140, 1973. DOI: 10.1016/0370-2693(73)90499-1.

[21] D. Decamp *et al.* A Precise Determination of the Number of Families with Light Neutrinos and of the Z Boson Partial Widths. *Phys. Lett. B*, 235(3), 1990. DOI: 10.1016/0370-2693(90)91984-J.

[22] B. T. Cleveland *et al.* Measurement of the Solar Electron Neutrino Flux with the Homestake Chlorine Detector. *Astrophys. J.*, 496(1), 1998. DOI:10.1086/305343.

[23] Y. Fukuda *et al.* Evidence for Oscillation of Atmospheric Neutrinos. *Phys. Rev. Lett.*, 81(8), 1998. DOI:10.1103/PhysRevLett.81.1562.

[24] Q. R. Ahmad *et al.* Measurement of the Rate of $\nu_e + d \rightarrow p + p + e^-$ Interactions Produced by ^8B Solar Neutrinos at the Sudbury Neutrino Observatory. *Phys. Rev. Lett.*, 87:071301, 2001. DOI:10.1103/PhysRevLett.87.071301.

[25] E. Gibney. Age of the neutrino: Plans to decipher mysterious particle take shape (Graphics by N. Hawtin). *Nature*, 524:148–149, 2015. DOI:10.1038/524148a.

[26] B. Pontecorvo. Mesonium and anti-mesonium. *Sov. Phys. JETP*, 6:429, 1957.

[27] Z. Maki *et al.* Remarks on the unified model of elementary particles. *Prog. Theor. Phys.*, 28:870–880, 1962. DOI:10.1143/PTP.28.870.

[28] R. L. Workman and Others. Review of Particle Physics. *PTEP*, 2022:083C01, 2022. DOI:10.1093/ptep/ptac097.

[29] J. H. Christenson *et al.* Evidence for the 2π Decay of the K_2^0 Meson. *Phys. Rev. Lett.*, 13:138–140, 1964. DOI:10.1103/PhysRevLett.13.138.

[30] A. Riotto. Theories of Baryogenesis. In *Summer School in High Energy Physics and Cosmology*, Trieste, Italy, 29 June–17 July 1998. arXiv:hep-ph/9807454[hep-ph].

[31] C. Hagedorn *et al.* CP violation in the lepton sector and implications for leptogenesis. *Int. J. Mod. Phys. A*, 33(05n06):1842006, 2018. DOI:10.1142/S0217751X1842006X.

[32] M. Aker *et al.* Direct neutrino-mass measurement with sub-electronvolt sensitivity. *Nat. Phys.*, 188:160–166, 2022. DOI:10.1038/s41567-021-01463-1.

[33] E. Majorana. Teoria simmetrica dell'elettrone e del positrone. *Nuovo Cim*, 14:171—-184, 1937. DOI:10.1007/BF02961314.

[34] R. Mohaptra. Seesaw Mechanism and Its Implications. In *SEESAW 25*, Paris, France, June 2004. arXiv:hep-ph/9807454[hep-ph], DOI:10.1142/9789812702210_0003.

[35] K. Abe *et al.* The T2K experiment. *Nucl. Instrum. Meth. A*, 659(1):106–135, 2011. DOI:10.1016/j.nima.2011.06.067.

[36] D. S. Ayres *et al.* The NOvA Technical Design Report. 10 2007. DOI:10.2172/935497.

[37] K. Abe *et al.* Constraint on the matter–antimatter symmetry-violating phase in neutrino oscillations. *Nature*, 580(7803):339–344, 2020. DOI:10.1038/s41586-020-2177-0.

[38] B. Abi *et al.* Deep Underground Neutrino Experiment (DUNE), Far Detector Technical Design Report, Volume I: Introduction to DUNE, 2020. arXiv:2002.02967[physics.ins-det].

[39] K. Abe *et al.* Hyper-Kamiokande Design Report, 2018. arXiv:1805.04163[physics.ins-det].

[40] L. Aliaga *et al.* Design, calibration, and performance of the MINERvA detector. *Nucl. Instrum. Meth. A.*, 743:130–159, 2014. DOI:10.1016/j.nima.2013.12.053.

[41] U. Mosel. Neutrino Interactions with Nucleons and Nuclei: Importance for Long-Baseline Experiments. *Annu. Rev. Nucl. Part. Sci.*, 66(1):171–195, 2016. DOI:10.1146/annurev-nucl-102115-044720.

[42] C. Andreopoulos *et al.* The GENIE neutrino Monte Carlo generator. *Nucl. Instrum. Meth. A*, 614(1):87–104, 2010. DOI:10.1016/j.nima.2009.12.009.

[43] C. Andreopoulos *et al.* The GENIE Neutrino Monte Carlo Generator: Physics and User Manual, 2015. arXiv:1510.05494[hep-ph].

[44] Y. Hayato. A neutrino interaction simulation program library NEUT. *Acta Phys. Polon. B*, 40:2477–2489, 2009. URL: https://www.actaphys.uj.edu.pl/R/40/9/2477/pdf.

[45] Y. Hayato and L. Pickering. The NEUT neutrino interaction simulation program library. *Eur. Phys. J. Spec. Top.*, 230:4469–4481, 2021. DOI:10.1140/epjs/s11734-021-00287-7.

[46] J. A. Formaggio and G. P. Zeller. From eV to EeV: Neutrino cross sections across energy scales. *Rev. Mod. Phys.*, 84:1307–1341, 2012. DOI:10.1103/RevModPhys.84.1307.

[47] M. Thomson. *Modern Particle Physics*. New York: Cambridge University Press, 2013.

[48] D. J. Griffiths. *Introduction to Elementary Particles*. New York: Wiley-VCH, 2008.

[49] C. Llewellyn Smith. Neutrino reactions at accelerator energies. *Physics Reports*, 3(5):261–379, 1972. DOI:10.1016/0370-1573(72)90010-5.

[50] R. Bradford *et al.* A New Parameterization of the Nucleon Elastic Form Factors. *Nucl. Phys. Proc. Suppl.*, 159:127–132, 2006. DOI:10.1016/j.nuclphysbps.2006.08.028.

[51] S. L. Adler. Tests of the Conserved Vector Current and Partially Conserved Axial-Vector Current Hypotheses in High-Energy Neutrino Reactions. *Phys. Rev.*, 135:B963–B966, 1964. DOI:10.1103/PhysRev.135.B963.

[52] D. H. Wilkinson. Analysis of Neutron Beta Decay. *Nucl. Phys. A*, 377:474–504, 1982. DOI:10.1016/0375-9474(82)90051-3.

[53] S. J. Barish *et al.* Study of neutrino interactions in hydrogen and deuterium: Description of the experiment and study of the reaction $\nu + d \rightarrow \mu^- + p + p_s$. *Phys. Rev. D*, 16:3103–3121, 1977. DOI:10.1103/PhysRevD.16.3103.

[54] L. A. Ahrens *et al.* A Study of the Axial Vector Form-factor and Second Class Currents in Anti-neutrino Quasielastic Scattering. *Phys. Lett. B*, 202:284–288, 1988. DOI:10.1016/0370-2693(88)90026-3.

[55] A. Bodek *et al.* Extraction of the axial nucleon form factor from neutrino experiments on deuterium. *JPCS*, 110(8), 2008. DOI:10.1088/1742-6596/110/8/082004.

[56] S. Choi *et al.* Axial and pseudoscalar nucleon form factors from low energy pion electroproduction. *Phys. Rev. Lett.*, 71:3927–3930, 1993. DOI:10.1103/PhysRevLett.71.3927.

[57] V. Bernard *et al.* Axial structure of the nucleon. *J. Phys. G Nucl. Part. Phys.*, 28(1):R1–R35, 2001. DOI:10.1088/0954-3899/28/1/201.

[58] T. Cai *et al.* Measurement of the axial vector form factor from antineutrino–proton scattering. *Nature*, 614:48–53, 2023. DOI:10.1038/s41586-022-05478-3.

[59] M. F. Carneiro *et al.* High-Statistics Measurement of Neutrino Quasielasticlike Scattering at 6 GeV on a Hydrocarbon Target. *Phys. Rev. Lett.*, 124:121801, 2020. DOI:10.1103/PhysRevLett.124.121801.

[60] A. Bashyal *et al.* High-statistics measurement of antineutrino quasielastic-like scattering at $E_{\overline{\nu}}$ 6 GeV on a hydrocarbon target. *Phys. Rev. D*, 108:032018, 2023. DOI:10.1103/PhysRevD.108.032018.

[61] J. Kleykamp *et al.* Simultaneous Measurement of ν_μ Quasielastic-like Cross Sections on CH, C, H_2O, Fe, and Pb as a Function of Muon Kinematics at MINERvA. *Phys. Rev. Lett.*, 130:161801, 2023. DOI:10.1103/PhysRevLett.130.161801.

[62] K. Abe *et al.* Measurement of the ν_μ charged current quasielastic cross section on carbon with the T2K on-axis neutrino beam. *Phys. Rev. D*, 91:112002, 2015. DOI:10.1103/PhysRevD.91.112002.

[63] K. Abe *et al.* First measurement of muon neutrino charged-current interactions on hydrocarbon without pions in the final state using multiple detectors with correlated energy spectra at T2K. *Phys. Rev. D*, 108:112009, 2023. DOI:10.1103/PhysRevD.108.112009.

[64] P. Abratenko *et al.* First Measurement of Differential Charged Current Quasielastiklike ν_μ-Argon Scattering Cross Sections with the MicroBooNE Detector. *Phys. Rev. Lett.*, 125:201803, 2020. DOI:10.1103/PhysRevLett.125.201803.

[65] D. Rein and L. M. Sehgal. Neutrino-excitation of baryon resonances and single pion production. *Ann. Phys.*, 133(1):79–153, 1981. DOI:10.1016/0003-4916(81)90242-6.

[66] R. P. Feynman *et al.* Current Matrix Elements from a Relativistic Quark Model. *Phys. Rev. D*, 3:2706–2732, 1971. DOI:10.1103/PhysRevD.3.2706.

[67] G. M. Radecky *et al.* Study of single-pion production by weak charged currents in low-energy νd interactions. *Phys. Rev. D*, 25:1161–1173, 1982. DOI:10.1103/PhysRevD.25.1161.

[68] T. Kitagaki *et al.* Charged-current exclusive pion production in neutrino-deuterium interactions. *Phys. Rev. D*, 34:2554–2565, 1986. DOI:10.1103/PhysRevD.34.2554.

[69] D. Allasia *et al.* Investigation of exclusive channels in neutrino/antineutrino deuteron charged current interactions. *Nucl. Phys. B*, 343:285–309, 1990. DOI:10.1016/0550-3213(90)90472-P.

[70] S. Boyd *et al.* Comparison of models of neutrino-nucleus interactions. *AIP Conf. Proc.*, 1189(1):60–73, 2009. DOI:10.1063/1.3274191.

[71] K. S. Kuzmin *et al.* Lepton polarisation in neutrino-nucleon interactions. *MPLA*, 19:2815–2829, 2004. DOI:10.1142/S0217732304016172.

[72] D. Rein and L. Sehgal. PCAC and the deficit of forward muons in π^+ production by neutrinos. *Phys. Lett. B*, 657(4):207–209, 2007. DOI:10.1016/j.physletb.2007.10.025.

[73] S. L. Adler. *Adventures in Theoretical Physics: Selected Papers with Commentaries.* World Scientific, 2006. DOI:10.1142/5856.

[74] C. Berger and L. M. Sehgal. Lepton mass effects in single pion production by neutrinos. *Phys. Rev. D*, 76:113004, 2007. DOI:10.1103/PhysRevD.76.113004.

[75] K. M. Graczyk and J. T. Sobczyk. Form factors in the quark resonance model. *Phys. Rev. D*, 77:053001, 2008. DOI:10.1103/PhysRevD.77.053001.

[76] L. Alvarez-Ruso *et al.* Recent highlights from GENIE v3. *Eur. Phys. J. Spec. Top.*, 230:4449–4467, 2021. DOI:10.1140/epjs/s11734-021-00295-7.

[77] J. A. Nowak *et al.* Four Momentum Transfer Discrepancy in the Charged Current π^+ Production in the MiniBooNE: Data vs. Theory. In *AIP Conference Proceedings.* AIP, 2009. DOI:10.1063/1.3274164.

[78] O. Lalakulich *et al.* Resonance production by neutrinos: The second resonance region. *Phys. Rev. D*, 74:014009, 2006. DOI:10.1103/PhysRevD.74.014009.

[79] M. Kabirnezhad. Single pion production in neutrino-nucleon interactions. *Phys. Rev. D*, 97:013002, 2018. DOI:10.1103/PhysRevD.97.013002.

[80] M. S. Athar and J. G. Morfin. Neutrino (Antineutrino)-Nucleus Interactions in the Shallow- and Deep-Inelastic Scattering Regions. *J. Phys. G: Nucl. Part. Phys.*, 48:034001, 2021. DOI:10.1088/1361-6471/abbb11.

[81] M. Kabirnezhad. Single pion production in electron-nucleon interactions. *Phys. Rev. D*, 102:053009, 2020. DOI:10.1103/PhysRevD.102.053009.

[82] M. Kabirnezhad. Single-pion production in electron-proton interactions. *Phys. Rev. C*, 107:025502, 2023. DOI:10.1103/PhysRevC.107.025502.

[83] A. Bodek and U. K. Yang. Higher twist, ξ_w scaling, and effective LO PDFs for lepton scattering in the few GeV region. *J. Phys. G*, 29(8):1899, 2003. DOI:10.1088/0954-3899/29/8/369.

[84] A. Bodek *et al.* Improved low Q2 model for neutrino and electron nucleon cross sections in few GeV region. *Nucl. Phys. Proc. Suppl.*, 139:113–118, 2005. DOI:10.1016/j.nuclphysbps.2004.11.208.

[85] J. G. Morfin. Shallow-and-Deep Inelastic Scattering with Neutrinos. In *The 22nd International Workshop on Neutrinos from Accelerators (NuFact2021)*, Cagliari, Italy, 6–11 September 2021. DOI:10.22323/1.402.0010.

[86] J. M. Conrad *et al.* Precision measurements with high-energy neutrino beams. *Rev. Mod. Phys.*, 70:1341–1392, 1998. DOI:10.1103/RevModPhys.70.1341.

[87] C. G. Callan and D. J. Gross. High-Energy Electroproduction and the Constitution of the Electric Current. *Phys. Rev. Lett.*, 22:156–159, 1969. DOI:10.1103/PhysRevLett.22.156.

[88] G. A. Snow *et al.* Preliminary Proposal to Study Neutrino Interactions with Neutrons and Protons Using the 15-Foot Bubble Chamber at NAL Filled with Deuterium. 1971. DOI:10.2172/991307.

[89] P. C. Bosetti *et al.* Analysis of Nucleon Structure Functions in CERN Bubble Chamber Neutrino Experiments. *Nucl. Phys. B*, 142:1–28, 1978. DOI:10.1016/0550-3213(78)90399-1.

[90] D. Allasia *et al.* Proton and Neutron Structure Functions From Anti-neutrinos interactions in deuterium. *Phys. Lett. B*, 117:262–266, 1982. DOI:10.1016/0370-2693(82)90559-7.

[91] D. Allasia *et al.* Measurement of the Neutron and Proton Structure Functions From Neutrino and Anti-neutrinos Scattering in Deuterium. *Phys. Lett. B*, 135:231, 1984. DOI:10.1016/0370-2693(84)90488-X.

[92] P. Berge *et al.* A measurement of differential cross-sections and nucleon structure functions in charged-current neutrino interactions on iron. *Z. Phys. C - Part. Fields*, 49:187–223, 1991. DOI:10.1007/BF01555493.

[93] E. Oltman *et al.* Nucleon structure functions from high energy neutrino interactions. *Z. Phys. C - Part. Fields*, 53:51–71, 1992. DOI:10.1007/BF01483872.

[94] M. Tzanov *et al.* Precise measurement of neutrino and antineutrino differential cross sections. *Phys. Rev. D*, 74:012008, 2006. DOI:10.1103/PhysRevD.74.012008.

[95] J. Mousseau *et al.* Measurement of partonic nuclear effects in deep-inelastic neutrino scattering using minerva. *Phys. Rev. D*, 93:071101, 2016. DOI:10.1103/PhysRevD.93.071101.

[96] D. Rein and L. M. Sehgal. Coherent π^0 production in neutrino reactions. *Nucl. Phys. B*, 223(1):29–44, 1983. DOI:10.1016/0550-3213(83)90090-1.

[97] A. Higuera *et al.* Measurement of Coherent Production of $\pi^{\pm}$ in Neutrino and Anti-neutrino Beams on Carbon from E_{ν} of 1.5 to 20 GeV. *Phys. Rev. Lett.*, 113:261802, 2014. DOI:10.1103/PhysRevLett.113.261802.

[98] A. Mislivec *et al.* Measurement of total and differential cross sections of neutrino and antineutrino coherent $\pi^{\pm}$ production on carbon. *Phys. Rev. D*, 97:032014, 2018. DOI:10.1103/PhysRevD.97.032014.

[99] M. A. Ramírez *et al.* Neutrino-Induced Coherent π^+ Production in C, CH, Fe, and Pb at $<E_\nu> \sim 6$ GeV. *Phys. Rev. Lett.*, 131:051801, 2023. DOI:10.1103/PhysRevLett.131.051801.

[100] R. Smith and E. Moniz. Neutrino reactions on nuclear targets. *Nucl. Phys. B.*, 43:605–622, 1972. DOI:10.1016/0550-3213(72)90040-5.

[101] R. Smith and E. Moniz. Neutrino reactions on nuclear targets. *Nucl. Phys. B*, 101(2):547, 1975. DOI:10.1016/0550-3213(75)90612-4.

[102] J. P. Stowell. *Effects of Nucleon and Nuclear Structure in Neutrino Interactions.* PhD thesis, The University of Sheffield, UK, 2019.

[103] A. Bodek and J. L. Ritchie. Further studies of Fermi-motion effects in lepton scattering from nuclear targets. *Phys. Rev. D*, 24:1400–1402, Sep 1981. DOI:10.1103/PhysRevD.24.1400.

[104] J. Nieves *et al.* Inclusive quasielastic charged-current neutrino-nucleus reactions. *Phys. Rev. C*, 70:055503, 2004. DOI:10.1103/PhysRevC.70.055503.

[105] T. Leitner *et al.* Electron- and neutrino-nucleus scattering from the quasielastic to the resonance region. *Phys. Rev. C*, 79:034601, 2009. DOI:10.1103/PhysRevC.79.034601.

[106] H. De Vries *et al.* Nuclear charge-density-distribution parameters from elastic electron scattering. *At. Data Nucl. Data Tables*, 36(3):495–536, 1987. DOI:10.1016/0092-640X(87)90013-1.

[107] O. Benhar *et al.* Spectral function of finite nuclei and scattering of GeV electrons. *Nucl. Phys. A*, 579:493–517, 1994. DOI:10.1016/0375-9474(94)90920-2.

[108] R. Subedi *et al.* Probing cold dense nuclear matter. *Science*, 320(5882):1476–1478, 2008. DOI:10.1126/science.1156675.

[109] A. Bodek *et al.* Effective Spectral Function for Quasielastic Scattering on Nuclei. *Eur. Phys. J.*, 74(10), 2014. DOI:10.1140/epjc/s10052-014-3091-0.

[110] T. W. Donnelly and I. Sick. Superscaling of inclusive electron scattering from nuclei. *Phys. Rev. C*, 60:065502, 1999. DOI:10.1103/PhysRevC.60.065502.

[111] R. Gran *et al.* Neutrino-nucleus quasi-elastic and 2p2h interactions up to 10 GeV. *Phys. Rev. D*, 88:113007, 2013. DOI:10.1103/PhysRevD.88.113007.

[112] M. Martini *et al.* Unified approach for nucleon knock-out and coherent and incoherent pion production in neutrino interactions with nuclei. *Phys. Rev. C*, 80:065501, 2009. DOI:10.1103/PhysRevC.80.065501.

[113] J. Nieves *et al.* Inclusive charged-current neutrino-nucleus reactions. *Phys. Rev. C*, 83:045501, 2011. DOI:10.1103/PhysRevC.83.045501.

[114] A. A. Aguilar-Arevalo *et al.* First measurement of the muon neutrino charged current quasielastic double differential cross section. *Phys. Rev. D*, 81:092005, 2010. DOI:10.1103/PhysRevD.81.092005.

[115] C. Juszczak *et al.* Extraction of the axial mass parameter from MiniBooNE neutrino quasielastic double differential cross-section data. *Phys. Rev. C*, 82:045502, 2010. DOI:10.1103/PhysRevC.82.045502.

[116] J. Nieves *et al.* The nucleon axial mass and the MiniBooNE quasielastic neutrino–nucleus scattering problem. *Phys. Lett. B*, 707(1):72–75, 2012. DOI:10.1016/j.physletb.2011.11.061.

[117] J. Arrington *et al.* Progress in understanding short-range structure in nuclei: An experimental perspective. *Annu. Rev. Nucl. Part. Sci.*, 72(1):307–337, 2022. DOI:10.1146/annurev-nucl-102020-022253.

[118] J. Van Orden and T. Donnelly. Mesonic processes in deep-inelastic electron scattering from nuclei. *Ann. Phys.*, 131(2):451–493, 1981. DOI:10.1016/0003-4916(81)90038-5.

[119] T. W. Donnelly and I. Sick. Superscaling in inclusive electron-nucleus scattering. *Phys. Rev. Lett.*, 82:3212–3215, 1999. DOI:10.1103/PhysRevLett.82.3212.

[120] C. Maieron *et al.* Extended superscaling of electron scattering from nuclei. *Phys. Rev. C*, 65:025502, 2002. DOI:10.1103/PhysRevC.65.025502.

[121] J. A. Caballero. General study of superscaling in quasielastic (e, e') and (ν, μ) reactions using the relativistic impulse approximation. *Phys. Rev. C*, 74:015502, 2006. DOI:10.1103/PhysRevC.74.015502.

[122] J. E. Amaro *et al.* Using electron scattering superscaling to predict charge-changing neutrino cross sections in nuclei. *Phys. Rev. C*, 71:015501, 2005. DOI:10.1103/PhysRevC.71.015501.

[123] J. E. Amaro *et al.* Superscaling and neutral current quasielastic neutrino-nucleus scattering. *Phys. Rev. C*, 73:035503, 2006. DOI:10.1103/PhysRevC.73.035503.

[124] A. Meucci *et al.* Relativistic descriptions of inclusive quasielastic electron scattering: Application to scaling and superscaling ideas. *Phys. Rev. C*, 80:024605, 2009. DOI:10.1103/PhysRevC.80.024605.

[125] G. D. Megias *et al.* Charged-current neutrino-nucleus reactions within the superscaling meson-exchange current approach. *Phys. Rev. D*, 94:093004, 2016. DOI:10.1103/PhysRevD.94.093004.

[126] S. Dolan *et al.* Implementation of the SuSAv2-meson exchange current 1p1h and 2p2h models in GENIE and analysis of nuclear effects in T2K measurements. *Phys. Rev. D*, 101:033003, 2020. DOI:10.1103/PhysRevD.101.033003.

[127] M. Ascencio *et al.* Implementation of SuSA 2p2h and QE weights for MINERvA. *MINERvA Technical Note*, TN92, 2021. URL: https://minerva-docdb.fnal.gov/cgi-bin/sso/ShowDocument?docid=29414.

[128] M. Arneodo. Nuclear effects in structure functions. *Phys. Rep.*, 240(5):301–393, 1994. DOI:10.1016/0370-1573(94)90048-5.

[129] J. Aubert *et al.* The ratio of the nucleon structure functions F_2^N for iron and deuterium. *Phys. Lett. B*, 123(3):275–278, 1983. DOI:10.1016/0370-2693(83)90437-9.

[130] B. Z. Kopeliovich *et al.* Nuclear shadowing in electro-weak interactions. *Prog. Part. Nucl. Phys.*, 68:314–372, 2013. DOI:10.1016/j.ppnp.2012.09.004.

[131] K. Ackerstaff and et al. Nuclear effects on $r = \sigma_L/\sigma_T$ in deep-inelastic scattering. *Phys. Lett. B*, 475(3-4):386–394, 2000. DOI:10.1016/s0370-2693(99)01493-8.

[132] J. Gomez and et al. Measurement of the a dependence of deep-inelastic electron scattering. *Phys. Rev. D*, 49:4348–4372, 1994. DOI:10.1103/PhysRevD.49.4348.

[133] J. Seely and et al. New Measurements of the European Muon Collaboration Effect in Very Light Nuclei. *Phys. Rev. Lett.*, 103:202301, 2009. DOI:10.1103/PhysRevLett.103.202301.

[134] K. Rith. Present Status of the EMC effect. In *International School of Subnuclear Physics*, Erice, Sicily, 24 June–3 July 2013. arXiv:1402.5000[hep-ex].

[135] X. G. Wang *et al.* Do Short-Range Correlations Cause the Nuclear EMC Effect in the Deuteron? *Phys. Rev. Lett.*, 125:262002, 2020. DOI:10.1103/PhysRevLett.125.262002.

[136] A. W. Thomas. Reflections on the origin of the EMC effect. *Int. J. Mod. Phys. E*, 27(12):1840001, 2018. DOI:10.1142/s0218301318400013.

[137] O. Hen *et al.* Nucleon-nucleon correlations, short-lived excitations, and the quarks within. *Rev. Mod. Phys*, 89(4), 2017. DOI:10.1103/revmodphys.89.045002.

[138] A. Bodek and J. L. Ritchie. Fermi Motion Effects in Deep Inelastic Lepton Scattering from Nuclear Targets. *Phys. Rev. D*, 23:1070, 1981. DOI:10.1103/PhysRevD.23.1070.

[139] N. Fomin *et al.* New measurements of high-momentum nucleons and short-range structures in nuclei. *Phys. Rev. Lett.*, 108:092502, 2012. DOI:10.1103/PhysRevLett.108.092502.

[140] M. S. Athar *et al.* Nuclear medium effects in lepton-nucleus dis in the region of $x \gtrsim 1$. *Phys. Rev. D*, 105:093002, 2022. DOI:10.1103/PhysRevD.105.093002.

[141] J. Arrington *et al.* Progress in Understanding Short-Range Structure in Nuclei: An Experimental Perspective. *Annu. Rev. Nucl. Part. Sci.*, 72(1):307–337, 2022. DOI:10.1146/annurev-nucl-102020-022253.

[142] N. Fomin *et al.* New Results on Short-Range Correlations in Nuclei. *Annu. Rev. Nucl. Part. Sci.*, 67(1):129–159, 2017. DOI:10.1146/annurev-nucl-102115-044939.

[143] T. Golan *et al.* Effects of final-state interactions in neutrino-nucleus interactions. *Phys. Rev. C*, 86:015505, Jul. DOI:10.1103/PhysRevC.86.015505.

[144] L. Alvarez-Ruso *et al.* NuSTEC White Paper: Status and challenges of neutrino-nucleus scattering. *Prog. Part. Nucl.*, 100:1–68, 2018. DOI:10.1016/j.ppnp.2018.01.006.

[145] L. Salcedo *et al.* Computer simulation of inclusive pion nuclear reactions. *Nucl. Phys. A*, 484(3):557–592, 1988. DOI:10.1016/0375-9474(88)90310-7.

[146] W. Y. Ma *et al.* Current status of final-state interaction models and their impact on neutrino-nucleus interactions. *JPCS*, 888(1):012171, 2017. DOI:10.1088/1742-6596/888/1/012171.

[147] S. J. Brodsky and A. Mueller. Using nuclei to probe hadronization in QCD. *Phys. Lett. B*, 206(4):685–690, 1988. DOI:10.1016/0370-2693(88)90719-8.

[148] S. Dytman *et al.* Comparison of validation methods of simulations for final state interactions in hadron production experiments. *Phys. Rev. D*, 104:053006, 2021. DOI:10.1103/PhysRevD.104.053006.

[149] K. Anderson *et al.* The NuMI Facility Technical Design Report. 1998. DOI:10.2172/1156372.

[150] P. Adamson *et al.* The NuMI neutrino beam. *Nucl. Instrum. Meth. A.*, 806:279–306, 2016. DOI:10.1016/j.nima.2015.08.063.

[151] I. Ambats *et al.* The MINOS Detectors Technical Design Report. 10 1998. DOI:10.2172/1861363.

[152] D. G. Michael *et al.* Observation of Muon Neutrino Disappearance with the MINOS Detectors in the NuMI Neutrino Beam. *Phys. Rev. Lett.*, 97:191801, 2006. DOI:10.1103/PhysRevLett.97.191801.

[153] D. Ayres *et al.* NOvA Proposal to Build a 30 Kiloton Off-Axis Detector to Study Neutrino Oscillations in the Fermilab NuMI Beamline, 2005. arXiv:hep-ex/0503053[hep-ex].

[154] B. Tice. *Measurement of nuclear dependence in inclusive charged current neutrino scattering*. PhD thesis, Rutgers, The State University of New Jersey, 2014. DOI:10.7282/T3668B8S.

[155] M. Convery *et al.* Fermilab Accelerator Complex: Status and Improvement Plans. 2018. DOI:10.2172/1556948.

[156] L. Aliaga. *Neutrino Flux Prediction for the NuMI Beamline*. PhD thesis, The College of William and Mary in Virginia, 2016. DOI:http://doi.org/10.21220/S2G59J.

[157] A. Bashyal. *DUNE and MINERvA Flux Studies and a Measurement of the Charged-Current Quasielastic Antineutrino Scattering Cross Section with $< E_\nu > \sim 6$ GeV on a CH Target*. PhD thesis, Oregon State University, 2021. DOI:10.2172/1779472.

[158] L. J. Loiacono. *Measurement of the Muon Neutrino Inclusive Charged Current Cross Section on Iron using the MINOS Detector*. PhD thesis, The University of Texas at Austin, 2010. DOI:10.2172/1151630.

[159] S. Agostinelli *et al.* Geant4—a simulation toolkit. *Nucl. Instrum. Meth. A*, 506(3):250–303, 2003. DOI:10.1016/S0168-9002(03)01368-8.

[160] J. Allison *et al.* Geant4 developments and applications. *IEEE Trans. Nucl. Sci.*, 53(1):270–278, 2006. DOI:10.1109/TNS.2006.869826.

[161] Z. Pavlovic. *Observation of Disappearance of Muon Neutrinos in the NuMI Beam*. PhD thesis, The University of Texas at Austin, 2008. DOI:10.2172/945117.

[162] D. Koskinen. *MINOS Sterile Neutrino search*. PhD thesis, University College London, 2009. DOI:10.2172/969510.

[163] L. Aliaga *et al.* Neutrino flux predictions for the NuMI beam. *Phys. Rev. D*, 94:092005, 2016. DOI:10.1103/PhysRevD.94.092005.

[164] B. Andersson *et al.* A Model for Low p(t) Hadronic Reactions, with Generalizations to Hadron - Nucleus and Nucleus-Nucleus Collisions. *Nucl. Phys. B*, 281:289–309, 1987. DOI:10.1016/0550-3213(87)90257-4.

[165] B. Nilsson-Almqvist and E. Stenlund. Interactions Between Hadrons and Nuclei: The Lund Monte Carlo, Fritiof Version 1.6. *Comput. Phys. Commun.*, 43:387, 1987. DOI:10.1016/0010-4655(87)90056-7.

[166] H. W. Bertini. Low-Energy Intranuclear Cascade Calculation. *Phys. Rev.*, 131:1801–1821, 1963. DOI:10.1103/PhysRev.131.1801.

[167] M. P. Guthrie *et al.* Calculation of the capture of negative pions in light elements and comparison with experiments pertaining to cancer radiotherapy. *Nucl. Instrum. Meth.*, 66:29–36, 1968. DOI:10.1016/0029-554X(68)90054-2.

[168] H. W. Bertini. Intranuclear-Cascade Calculation of the Secondary Nucleon Spectra from Nucleon-Nucleus Interactions in the Energy Range 340 to 2900 MeV and Comparisons with Experiment. *Phys. Rev.*, 188:1711–1730, 1969. DOI:10.1103/PhysRev.188.1711.

[169] H. W. Bertini and M. P. Guthrie. News item results from medium-energy intranuclear-cascade calculation. *Nucl. Phys. A*, 169(3):670–672, 1971. DOI:10.1016/0375-9474(71)90710-X.

[170] C. Alt *et al.* Inclusive production of charged pions in p+c collisions at 158gev/c beam momentum. *EPJ C*, 49(4):897–917, 2007. DOI:10.1140/epjc/s10052-006-0165-7.

[171] A. Ferrari *et al.* FLUKA: A multi-particle transport code (Program version 2005). 10 2005. DOI:10.2172/877507.

[172] T. Böhlen *et al.* The FLUKA Code: Developments and Challenges for High Energy and Medical Applications. *Nucl. Data Sheets*, 120:211–214, 2014. DOI:10.1016/j.nds.2014.07.049.

[173] B. Messerly. *Single Charged Pion Production by Muon Neutrinos in the MINERvA Detector Using the NuMI Beam.* PhD thesis, University of Pittsburgh, 2019. DOI: 10.2172/1599317.

[174] B. Messerly *et al.* An Error Analysis Toolkit for Binned Counting Experiments. *EPJ Web of Conferences*, 251:03046, 2021. DOI:10.1051/epjconf/202125103046.

[175] G. Perdue *et al.* The MINERvA data acquisition system and infrastructure. *Nucl. Instrum. Meth. A*, 694:179–192, 2012. DOI:10.1016/j.nima.2012.08.024.

[176] P. Adamson *et al.* Neutrino and antineutrino inclusive charged-current cross section measurements with the MINOS near detector. *Phys. Rev. D*, 81:072002, 2010. DOI:10.1103/PhysRevD.81.072002.

[177] D. Michael *et al.* The magnetized steel and scintillator calorimeters of the MINOS experiment. *Nucl. Instrum. Meth. A*, 596(2):190–228, 2008. DOI:10.1016/j.nima.2008.08.003.

[178] R. Ospanov. *A measurement of muon neutrino disappearance with the MINOS detectors and NuMI beam.* PhD thesis, The University of Texas at Austin, 2008. DOI:10.2172/1415814.

[179] B. G. Tice *et al.* Measurement of Ratios of ν_μ Charged-Current Cross-Sections on C, Fe, and Pb to CH at Neutrino Energies 2–20 GeV. *Phys. Rev. Lett.*, 112:231801, 2014. DOI:10.1103/PhysRevLett.112.231801.

[180] R. Acciarri *et al.* Design and construction of the MicroBooNE detector. *JINST*, 12(02):P02017, 2017. DOI:10.1088/1748-0221/12/02/P02017.

[181] M. Ericson and M. Martini. Neutrino versus antineutrino cross sections and *CP* violation. *Phys. Rev. C*, 91:035501, 2015. DOI:10.1103/PhysRevC.91.035501.

[182] K. Abe *et al.* Measurements of $\bar{\nu}_\mu$ and $\bar{\nu}_\mu + \nu_\mu$ charged-current cross-sections without detected pions or protons on water and hydrocarbon at a mean anti-neutrino energy of 0.86 GeV. *Prog. Theor. Exp.*, 2021(4), 2021. DOI:10.1093/ptep/ptab014.

[183] K. Abe *et al.* First measurement of the charged current $\bar{\nu}_\mu$ double differential cross section on a water target without pions in the final state. *Phys. Rev. D*, 102(1), 2020. DOI:10.1103/physrevd.102.012007.

[184] K. Abe *et al.* First combined measurement of the muon neutrino and antineutrino charged-current cross section without pions in the final state at T2K. *Phys. Rev. D*, 101(11), 2020. DOI:10.1103/physrevd.101.112001.

[185] A. A. Aguilar-Arevalo *et al.* First measurement of the muon antineutrino double-differential charged-current quasielastic cross section. *Phys. Rev. D*, 88(3), 2013. DOI:10.1103/physrevd.88.032001.

[186] A. Hiramoto *et al.* First measurement of $\overline{\nu}_\mu$ and ν_μ charged-current inclusive interactions on water using a nuclear emulsion detector. *Phys. Rev. D*, 102:072006, 2020. DOI:10.1103/PhysRevD.102.072006.

[187] A. I. Mukhin *et al.* Energy Dependence of Total Cross-sections for Neutrino and Anti-neutrino Interactions at Energies Below 35-GeV. *Sov. J. Nucl. Phys.*, 30:528, 1979.

[188] V. B. Anikeev *et al.* Total cross-section measurements for ν_μ, $\bar{\nu}_\mu$ charged current interactions in 3–30 GeV energy range with IHEP-JINR neutrino detector. *Z. Phys. C*, 70:39–46, 1996. DOI:10.1007/s002880050078.

[189] R. Acciarri *et al.* Measurements of inclusive muon neutrino and antineutrino charged current differential cross sections on argon in the numi antineutrino beam. *Phys. Rev. D*, 89:112003, 2014. DOI:10.1103/PhysRevD.89.112003.

[190] R. Acciarri *et al.* First measurement of the cross section for ν_μ and $\overline{\nu}_\mu$ induced single charged pion production on argon using ArgoNeuT. *Phys. Rev. D*, 98:052002, 2018. DOI:10.1103/PhysRevD.98.052002.

[191] A. Bercellie *et al.* Simultaneous Measurement of Muon Neutrino ν_μ Charged-Current Single π^+ Production in CH, C, H_2O, Fe, and Pb Targets in MINERvA. *Phys. Rev. Lett.*, 131:011801, 2023. DOI:10.1103/PhysRevLett.131.011801.

[192] D. H. Perkins. *Introduction to High Energy Physics*. Cambridge University Press, 4th edition, 2000. DOI:10.1017/CBO9780511809040.

[193] L. Zazueta *et al.* Improved constraint on the MINERνA medium energy neutrino flux using $\overline{\nu}e^- \to \overline{\nu}e^-$ data. *Phys. Rev. D*, 107:012001, 2023. DOI:10.1103/PhysRevD.107.012001.

[194] E. Valencia *et al.* Constraint of the MINERvA medium energy neutrino flux using neutrino-electron elastic scattering. *Phys. Rev. D*, 100:092001, 2019. DOI:10.1103/PhysRevD.100.092001.

[195] D. Ruterbories *et al.* Constraining the NuMI neutrino flux using inverse muon decay reactions in MINERvA. *Phys. Rev. D*, 104:092010, 2021. DOI:10.1103/PhysRevD.104.092010.

[196] J. Kleykamp. *A-scaling of CCQE-like cross sections at MINERvA*. PhD thesis, University of Rochester, NY, 2021. URL: https://www.osti.gov/biblio/1824189.

[197] P. A. Rodrigues *et al.* Identification of Nuclear Effects in Neutrino-Carbon Interactions at Low Three-Momentum Transfer. *Phys. Rev. Lett.*, 116:071802, Feb 2016. DOI:10.1103/PhysRevLett.116.071802.

[198] R. Gran. Model uncertainties for Valencia RPA effect for MINERvA, 2017. arXiv:1705.02932[hep-ex].

[199] R. Gran *et al.* Antineutrino Charged-Current Reactions on Hydrocarbon with Low Momentum Transfer. *Phys. Rev. Lett.*, 120:221805, Jun 2018. DOI:10.1103/PhysRevLett.120.221805.

[200] J. Schwehr *et al.* GENIE implementation of IFIC Valencia model for QE-like 2p2h neutrino-nucleus cross-section, 2017. arXiv:1601.02038[hep-ph].

[201] P. Rodrigues *et al.* Constraining the GENIE model of neutrino-induced single pion production using reanalyzed bubble chamber data. *Eur. Phys. J. C*, 76(8), 2016. DOI:10.1140/epjc/s10052-016-4314-3.

[202] M. A. Ramírez *et al.* Neutrino-Induced Coherent π^+ Production in C, CH, Fe, and Pb at $<E_\nu> \sim 6$ GeV. *Phys. Rev. Lett.*, 131:051801, 2023. DOI:10.1103/PhysRevLett.131.051801.

[203] T. Yang *et al.* A hadronization model for few-GeV neutrino interactions. *Eur. Phys. J. C*, 63(1):1–10, 2009. DOI:10.1140/epjc/s10052-009-1094-z.

[204] Z. Koba *et al.* Scaling of multiplicity distributions in high energy hadron collisions. *Nucl. Phys. B*, 40:317–334, 1972. DOI:10.1016/0550-3213(72)90551-2.

[205] T. Sjöstrand *et al.* High-energy-physics event generation with PYTHIA 6.1. *Comput. Phys. Commun.*, 135(2):238–259, 2001. DOI:10.1016/s0010-4655(00)00236-8.

[206] R. Merenyi *et al.* Determination of pion intranuclear rescattering rates in $\nu_\mu -$ Ne versus $\nu_\mu -$ D interactions for the atmospheric ν flux. *Phys. Rev. D*, 45:743–751, 1992. DOI:10.1103/PhysRevD.45.743.

[207] S. Dytman. Final state interactions in neutrino-nucleus experiments. *Acta Phys. Pol. B*, 40, 2009. URL: https://www.actaphys.uj.edu.pl/R/40/9/2445/pdf.

[208] W. P. Abfalterer *et al.* Measurement of neutron total cross sections up to 560 MeV. *Phys. Rev. C*, 63:044608, 2001. DOI:10.1103/PhysRevC.63.044608.

[209] A. Heikkinen *et al.* Bertini intra-nuclear cascade implementation in Geant4, 2003. arXiv:nucl-th/0306008[nucl-th].

[210] G. Folger and J. P. Wellisch. String Parton Models in Geant4, 2003. arXiv:nucl-th/0306007[nucl-th].

[211] M. Elkins *et al.* Neutron measurements from antineutrino hydrocarbon reactions. *Phys. Rev. D*, 100:052002, 2019. DOI:10.1103/PhysRevD.100.052002.

[212] R. Hatcher. Beyond the Detector: Event Generation in the Rock and Event Overlays, 2011. URL: https://minerva-docdb.fnal.gov/cgi-bin/sso/ShowDocument?docid=6032.

[213] C. Marshall. *Measurement of charged kaon production by neutrinos at MINERvA*. PhD thesis, University of Rochester, NY, 2016. DOI:10.2172/1325973.

[214] J. B. Birks. Scintillations from Organic Crystals: Specific Fluorescence and Relative Response to Different Radiations. *Proc. Phys. Soc. A*, 64:874–877, 1951. DOI: 10.1088/0370-1298/64/10/303.

[215] J. Wolcott. *Measurement of the Charged-Current Quasi-Elastic Cross-Section for Electron Neutrinos on a Hydrocarbon Target*. PhD thesis, University of Rochester, NY, 2015. DOI:10.2172/1226351.

[216] R. Fine *et al.* Data Preservation at MINERvA. *Snowmass 2021 Contributed Paper*, 2020. arXiv:2009.04548[hep-ex].

[217] R. Luchsinger and C. Grab. Vertex reconstruction by means of the method of Kalman filtering. *Comput. Phys. Commun.*, 76(3):263–280, 1993. DOI:10.1016/0010-4655(93)90055-H.

[218] J. Devan. Calorimetry Note. *MINERvA Document*, 7712-v2, 2012. URL: https://minerva-docdb.fnal.gov/cgi-bin/sso/ShowDocument?docid=7712.

[219] A. E. Norrick. *A Measurement of Nuclear Effects in Deep Inelastic Scattering in Neutrino-Nucleus Interactions*. PhD thesis, The College of William and Mary in Virginia, 2018. DOI:10.21220/s2-dxxp-bs17.

[220] A. M. Terwilliger *et al.* Vertex reconstruction of neutrino interactions using deep learning. In *2017 International Joint Conference on Neural Networks (IJCNN)*, pages 2275–2281, 2017. DOI:10.1109/IJCNN.2017.7966131.

[221] G. Perdue *et al.* Reducing model bias in a deep learning classifier using domain adversarial neural networks in the MINERvA experiment. *J. Instrum.*, 13(11):P11020, nov 2018. DOI:10.1088/1748-0221/13/11/P11020.

[222] J. Mousseau. Optimizing High Momentum MINOS Muon Selection. *MINERvA Document*, 10154-v2, 2014. URL: https://minerva-docdb.fnal.gov/cgi-bin/sso/ShowDocument?docid=10154.

[223] A. Klustová. Preparations For The Inclusive Antineutrino Target Analyses. *MINERvA Document*, 29420-v3, 2021. URL: https://minerva-docdb.fnal.gov/cgi-bin/sso/ShowDocument?docid=29420.

[224] M. O. Wospakrik. *Measurement of Neutrino Absolute Deep Inelastic Scattering Cross Section in Iron, Lead, Carbon, and Plastic Using MINERvA Detector at E_ν = 6 GeV*. PhD thesis, The University of Florida, 2018. DOI:10.2172/1484178.

[225] K. S. Egiyan *et al.* Measurement of Two- and Three-Nucleon Short-Range Correlation Probabilities in Nuclei. *Phys. Rev. Lett.*, 96:082501, 2006. DOI:10.1103/PhysRevLett.96.082501.

[226] V. Blobel. An Unfolding Method for High Energy Physics Experiments. In *Conference on Advanced Statistical Techniques in Particle Physics*, Durham, UK, 18–22 March 2002. arXiv:hep-ex/0208022[hep-ex].

[227] G. D'Agostini. A Multidimensional unfolding method based on Bayes' theorem. *Nucl. Instrum. Meth. A*, 362:487–498, 1995. DOI:10.1016/0168-9002(95)00274-X.

[228] G. D'Agostini. Improved iterative Bayesian unfolding. In *Alliance Workshop on Unfolding and Data Correction*, Hamburg, Germany, 27–28 May 2010. arXiv:1010.0632[physics.data-an].

[229] T. Adye. Unfolding algorithms and tests using RooUnfold. In *PHYSTAT 2011*, pages 313–318, Geneva, Switzerland, 17-–20 January 2011. CERN. DOI:10.5170/CERN-2011-006.313.

[230] R. Brun and F. Rademakers. ROOT: An object oriented data analysis framework. In *Proceedings AIHENP'96 Workshop*, Lausanne, Switzerland, 2–6 September 1996. *Nucl. Instrum. Meth. A*, 389:81–86, 1997. DOI:10.1016/S0168-9002(97)00048-X.

[231] A. Olivier *et al.* Measurement of the multineutron $\bar{\nu}_\mu$ charged current differential cross section at low available energy on hydrocarbon. *Phys. Rev. D*, 108(11):112010, 2023. arXiv:2310.17014[hep-ex], DOI:10.1103/PhysRevD.108.112010.

[232] D. Ruterbories. Unfolding – A Matter of Uncertainty. *MINERvA Document*, 28899-v1, 2021. URL: https://minerva-docdb.fnal.gov/cgi-bin/sso/ShowDocument?docid=28899.

[233] D. Ruterbories. Unfolding – A Matter of Uncertainty – Round 2. *MINERvA Document*, 28992-v2, 2021. URL: https://minerva-docdb.fnal.gov/cgi-bin/sso/ShowDocument?docid=28992.

[234] The MINERvA Collaboration. GENIEXSecExtract. *GitHub repository*, 2021. URL: https://github.com/MinervaExpt/GENIEXSecExtract.git.

[235] R. Fine. Updates to the standard flux files. *MINERvA Document*, 24666-v1, 2019. URL: https://minerva-docdb.fnal.gov/cgi-bin/sso/ShowDocument?docid=24666.

[236] B. P. Ziemer. *A Measurement of the Two Track Charged Current Quasi-Elastic Cross Section with the MINERνA Detector*. PhD thesis, The University of California, Irvine, 2012. DOI:10.2172/1209542.

[237] E. Valencia-Rodriguez. *Neutrino - Electron Scattering in MINERνA for Constraint NuMI Flux at Medium*. PhD thesis, The Universidad de Guanajuato, 2016. DOI:10.2172/1341804.

[238] L. Tiator *et al.* Electroproduction of nucleon resonances. *EPJ A*, 19(S1):55–60, 2004. DOI:10.1140/epjad/s2004-03-009-9.

[239] S. Dytman *et al.* Hadronic Shower Energy Scale Uncertainty in the MINOS Experiment. 2008. arXiv:0806.2119[hep-ex].

[240] L. Aliaga *et al.* MINERvA neutrino detector response measured with test beam data. *Nucl. Instrum. Meth. A*, 789:28–42, 2015. DOI:10.1016/j.nima.2015.04.003.

[241] J. Devan. Testbeam Proton Calorimetry Technical Note 51. *MINERvA Document*, 9986-v3, 2014. URL: https://minerva-docdb.fnal.gov/cgi-bin/sso/ShowDocument?docid=9986.

[242] R. Gran. Testbeam Pion Calorimetry Technical Note 45. *MINERvA Document*, 9474-v4, 2013. URL: https://minerva-docdb.fnal.gov/cgi-bin/sso/ShowDocument?docid=9474.

[243] P. Adamson *et al.* Study of quasielastic scattering using charged-current ν_μ-iron interactions in the minos near detector. *Phys. Rev. D*, 91:012005, 2015. DOI: 10.1103/PhysRevD.91.012005.

[244] B. Eberly *et al.* Charged pion production in ν_μ interactions on hydrocarbon at $<E_\nu>$ = 4.0 GeV. *Phys. Rev. D*, 92:092008, 2015. DOI:10.1103/PhysRevD.92.092008.

[245] C. L. McGivern *et al.* Cross sections for ν_μ and $\overline{\nu}_\mu$ induced pion production on hydrocarbon in the few-GeV region using MINERvA. *Phys. Rev. D*, 94:052005, 2016. DOI:10.1103/PhysRevD.94.052005.

[246] O. Altinok *et al.* Measurement of ν_μ charged-current single π^0 production on hydrocarbon in the few-GeV region using MINERvA. *Phys. Rev. D*, 96:072003, 2017. DOI:10.1103/PhysRevD.96.072003.

[247] P. Stowell *et al.* Tuning the genie pion production model with MINERvA data. *Phys. Rev. D*, 100:072005, 2019. DOI:10.1103/PhysRevD.100.072005.

[248] B. Z. Kopeliovich *et al.* Nuclear shadowing in electro-weak interactions. *Prog. Part. Nucl. Phys.*, 68:314–372, 2013. DOI:10.1016/j.ppnp.2012.09.004.

[249] P. P. Allport *et al.* Observation of Shadowing of Neutrino and Anti-neutrino - Nucleus Interactions and Comparison With PCAC Predictions. *Phys. Lett. B*, 232:417, 1989. DOI:10.1016/0370-2693(89)90767-3.

[250] T. Katori. Meson Exchange Current (MEC) Models in Neutrino Interaction Generators, 2013. arXiv:1304.6014[nucl-th].

[251] B. Bourguille *et al.* Inclusive and exclusive neutrino-nucleus cross sections and the reconstruction of the interaction kinematics. *JHEP*, 2021(4), 2021. DOI:10.1007/jhep04(2021)004.

[252] C. Juszczak *et al.* Simulations from a new neutrino event generator. *Nucl. Phys. B Proc. Suppl.*, 159:211–216, 2006. DOI:10.1016/j.nuclphysbps.2006.08.069.

[253] A. Furmanski. *Charged-current Quasi-elastic-like neutrino interactions at the T2K experiment.* PhD thesis, The University of Warwick, 4 2015.

[254] M. J. Kuusela. *Uncertainty quantification in unfolding elementary particle spectra at the Large Hadron Collider*. PhD thesis, École Polytechnique Fédérale de Lausanne, Lausanne, 2016. DOI:10.5075/epfl-thesis-7118.

[255] A. P. Dempster *et al.* Maximum Likelihood from Incomplete Data via the EM Algorithm. *J. R. Stat. B*, 39(1):1–38, 1977. URL: http://www.jstor.org/stable/2984875.

[256] G. J. McLachlan *et al.* The EM Algorithm. Papers 2004,24, Berlin, 2004. URL: http://hdl.handle.net/10419/22198.

Appendix A

Nuclear target flux and 'daisy' reweight procedure

This appendix describes the calculation of the nuclear target flux and some details of the so-called 'daisy' reweight of the scintillator tracker to enable flux-independent comparisons between nuclear targets as discussed in Subsection 5.1.1. The procedure first appeared in Refs. [61,196] and has been extended to the antineutrino flux with MINERvA's combined flux constraint of (anti)neutrino-electron scattering and IMD for this work.

The antineutrino flux for each nuclear target (or combined nuclear targets of the same material) can be determined using the true information from the simulation as

$$\Phi(E_{\bar{\nu}_\mu}) = \frac{\text{Total } \bar{\nu}_\mu \text{ charged current events}(E_{\bar{\nu}_\mu})}{\sigma_{\text{avg}}(E_{\bar{\nu}_\mu}) N_{\text{atoms}} \text{POT}} \,. \tag{A.1}$$

Here, the numerator represents the true charged-current antineutrino interactions in a given nuclear target, $\sigma_{\text{avg}}(E_{\bar{\nu}_\mu})$ is a GENIE [42, 43] spline for the average cross-section on a given atom, and N_{atoms} denotes the number of atoms per cm^2 in the nuclear target. The flux is also normalised by the number of protons on target (POT) corresponding to the simulation. Similarly, the flux can be extracted in the individual 'daisy petals' of the scintillator tracker as shown in Figure A.1.

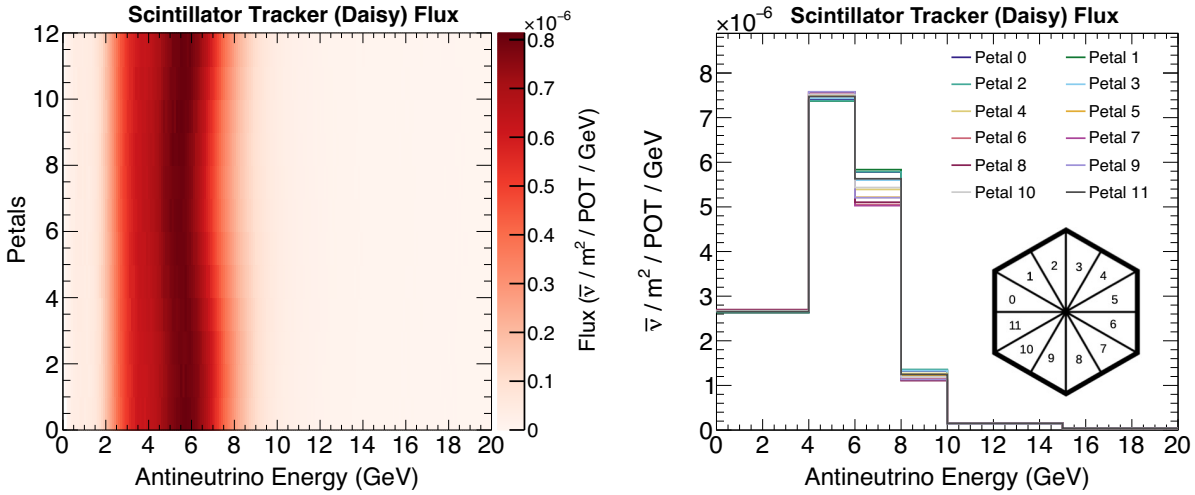

Figure A.1: Left: Two-dimensional heatmap of the scintillator tracker flux in the individual 'daisy petals' as a function of finely binned antineutrino energy. The color bar represents the flux intensity in a particular region. Right: One-dimensional projection of the scintillator tracker flux for each 'daisy petal' as a function of antineutrino energy, using the binning employed in the fitting procedure. The hexagon insert illustrates petal positions when looking downstream of the detector.

A regularised χ^2 fit is used to find a weight for each petal so that the linear combination of the 'daisy petals' fluxes matches the flux in the individual combinations of nuclear targets of the same material. This is defined as

$$\chi^2_{\text{reg}} = \frac{(N_{\text{target}} - \sum_i p_i N_i)^2}{\sigma^2_{\text{target}} + \sum_i p_i \sigma_i^2} + \lambda \sum_i \frac{N_i}{\sum_j N_j} (p_i - 1)^2 \,, \tag{A.2}$$

where the first term corresponds to the regular χ^2 calculation and the second term represents the regularisation term. N_{target} is the number of events (in a given bin of the nuclear target flux distribution), N_i is the number of events in a 'daisy petals' i, and p_i is the 'daisy petals' weight.

The regularisation term ensures that a preference is given to a solution with a small difference from the nominal weight of 1 and also enforces smoothness in the variation of the individual 'daisy petals' weights. A regularisation strength $\lambda = 100$ was found to work well for all combinations of nuclear targets of the same material by looking at the 'knee' of the L-curve of $\log \chi^2$ of the regularised solution versus λ as demonstrated in Figure A.2. This maintains the balance between the perfect fit (zero regularisation) and the smoothness of the solution (large regularisation).

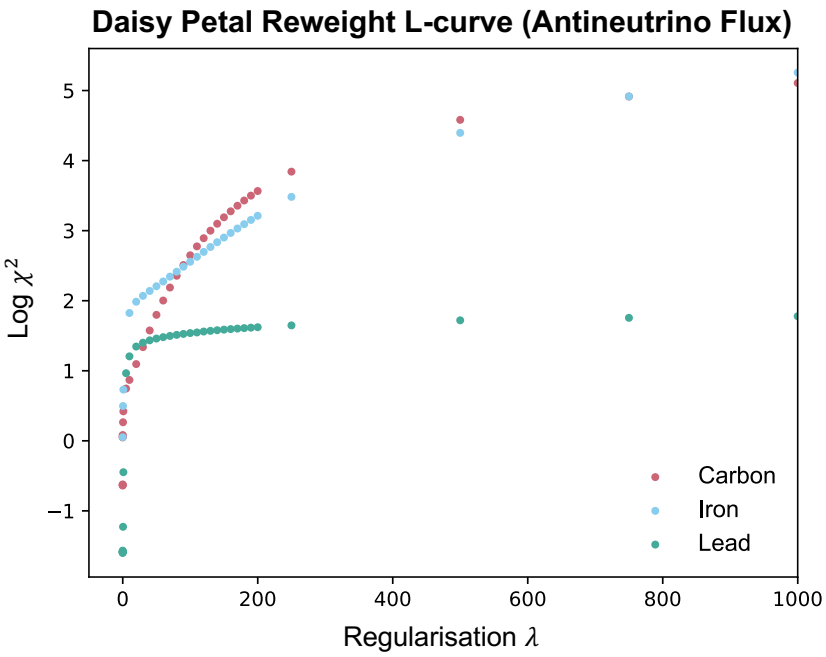

Figure A.2: L-curve of $\log \chi^2$ of the regularised solution versus λ for carbon, iron (combination of targets 2, 3, and 5), and lead (combination of targets 2–5). Note that different materials require different amounts of regularisation, but λ in the range of 50–100 provides a good enough $\log \chi^2$.

Figures A.3, A.4, and A.5 illustrate the nuclear target-to-scintillator (antineutrino) flux ratios both before and after applying a linear combination of the 'daisy petals' from the scintillator tracker to match the carbon, iron, and lead flux, respectively. The individual weights assigned to the 'daisy petals' are also shown. As expected, the distribution of 'daisy petal' weights reflects the transverse position of the individual target (or combined nuclear targets of the same material) within the detector. The statistical χ^2 of the nuclear target-to-scintillator (antineutrino) flux ratios both before and after the reweight are shown in Table A.1.

Note that the statistical errors on the fit are relatively large due to the petal-to-petal correlations. Therefore, the uncertainty on the fit is evaluated by re-extracting the weights for 50 Poisson-thrown universes around the central value of the flux. The overall error on the scale factor is calculated so the χ^2 of the flux ratio is equal to 1. However, the impact of the error from the 'daisy petal' reweight on the cross-section error is negligible.

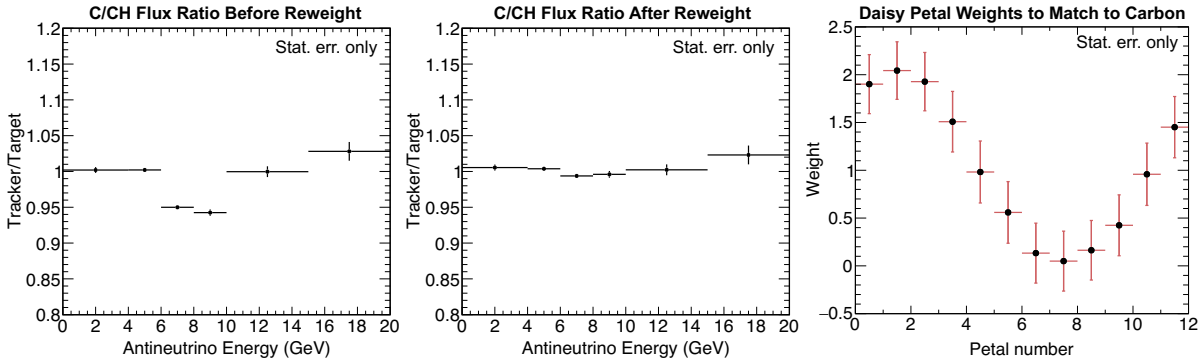

Figure A.3: Carbon-to-scintillator tracker flux ratio before (left) and after (centre) the reweight, and the individual 'daisy petal' weights to match the carbon flux (right).

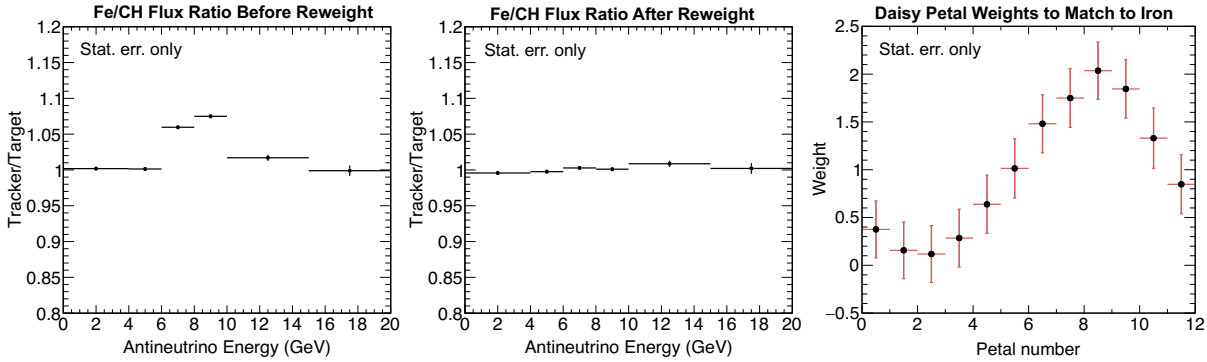

Figure A.4: Iron-to-scintillator tracker flux ratio before (left) and after (centre) the reweight, and the individual 'daisy petal' weights to match the iron flux (right).

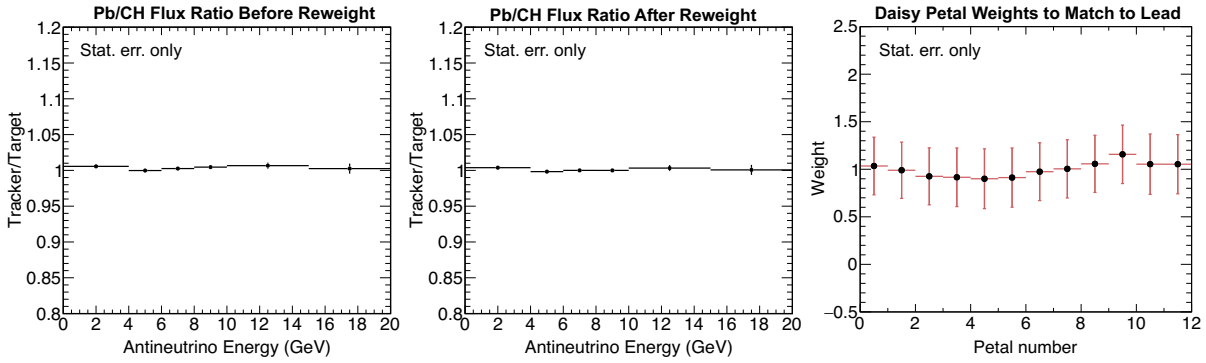

Figure A.5: Lead-to-scintillator tracker flux ratio before (left) and after (centre) the reweight, and the individual 'daisy petal' weights to match the lead flux (right).

Material	χ^2 before reweight	χ^2 after reweight
Carbon	101.11	2.30
Iron (Target 2, 3 and 5)	332.40	2.12
Lead (Target 2–5)	2.35	0.77

Table A.1: Statistical χ^2 of the nuclear target-to-scintillator flux ratios both before and after applying a linear combination of the 'daisy petals' from the scintillator tracker to match the carbon, iron, and lead flux, respectively.

Appendix B

Selected event distributions

Cut	Relative simulation sample left (%)		Relative data sample left (%)	
	Target 5 lead	Scintillator tracker	Target 5 lead	Scintillator tracker
1. Antimuon		65.6		44.5
2. 5σ curvature		94.6		95.5
3. MINOS fiducial		68.1		53.0
4. MINERvA fiducial		86.3		85.5
5. Dead channels		98.9		98.5
6. ML vertex		99.9		97.8
7. Target + material / Tracker	1.2	60.4	1.1	61.0
8. Antimuon energy	98.0	97.1	97.5	97.9
9. Antimuon angle	99.7	98.5	99.8	98.3

Table B.1: Relative simulation and data sample left after each reconstruction cut for target 5 lead and the scintillator tracker in the order listed in Section 7.1. Overall the data and the simulation relative % are similar except for the 'Antimuon' and 'MINOS fiducial' cuts. This is because the simulation does not model interactions in the ECAL and HCAL as mentioned in Chapter 5, whereas the data sample contains such events.

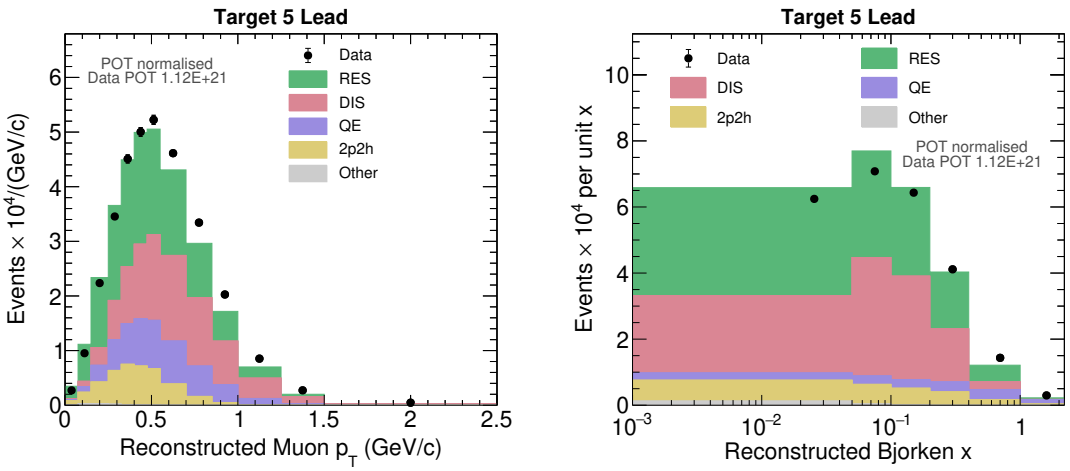

Figure B.1: Selected event distributions in target 5 lead for both antimuon p_{T} (left) and Bjorken x (right) with the simulation broken down into the various interaction channels stacked in the descending order of their contribution.

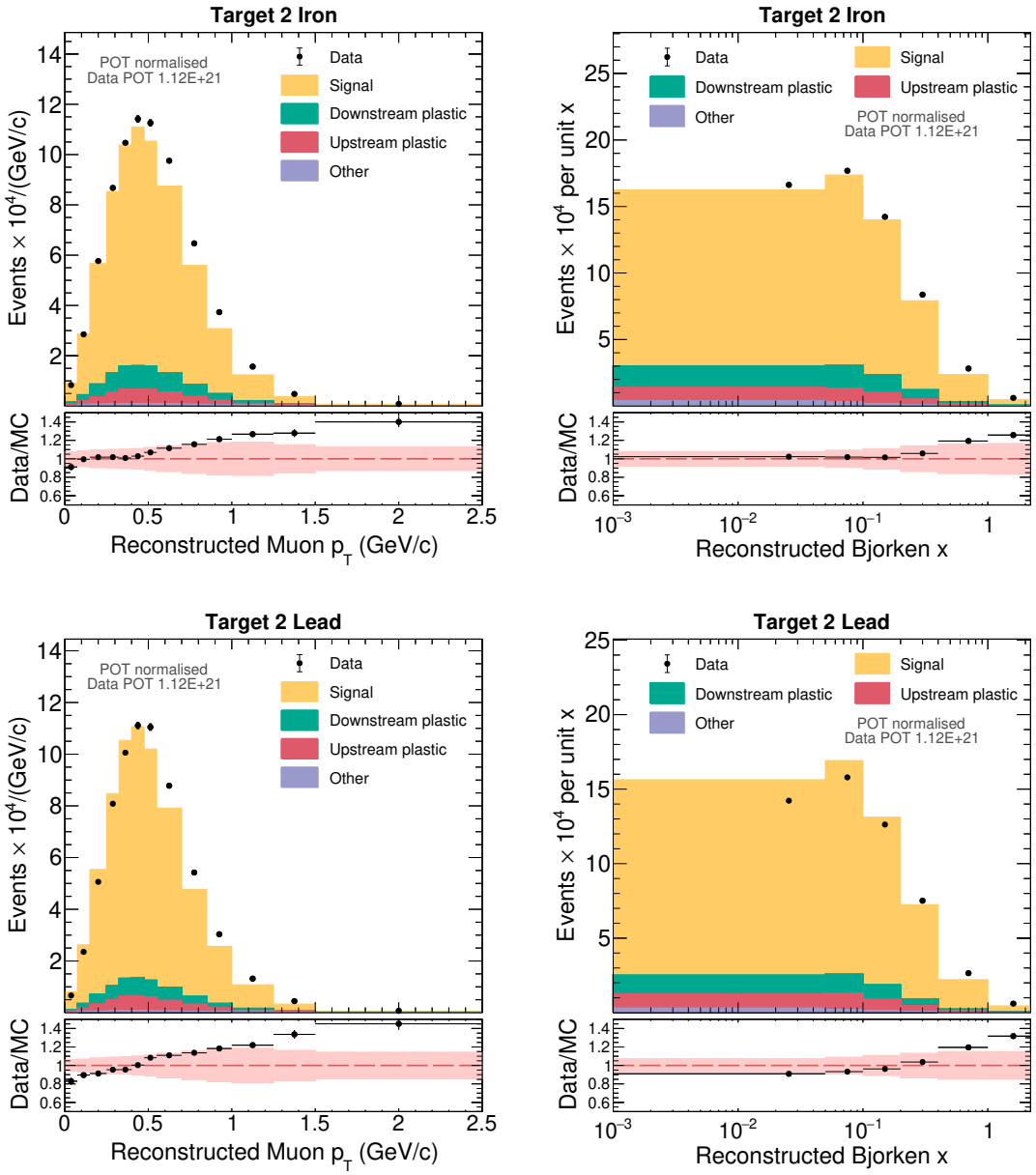

Figure B.2: Selected event distributions in target 2 iron (top panel) and target 2 lead (bottom panel) for both antimuon p_{T} (left) and Bjorken x (right). The top panel of each plot shows the black data points with their statistical uncertainty and the simulation broken down into the signal and various sources of background stacked in the descending order of their contribution. The bottom panel of each plot shows the data-to-simulation ratio with the statistical uncertainty on the black points and the systematic uncertainty represented by the solid band.

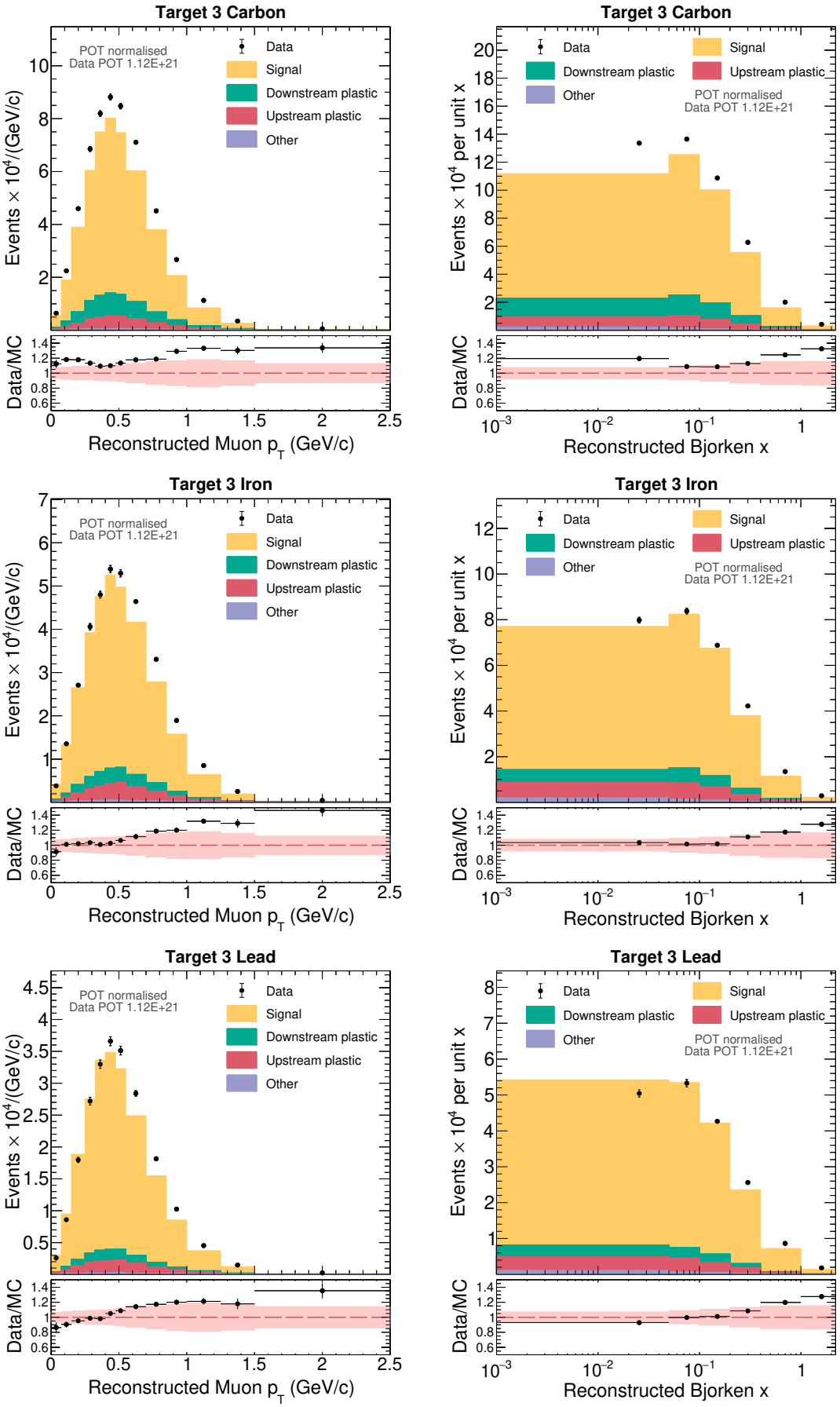

Figure B.3: Selected event distributions in target 3 carbon (top), target 3 iron (middle), and target 3 lead (bottom) for both antimuon p_{T} (left) and Bjorken x (right).

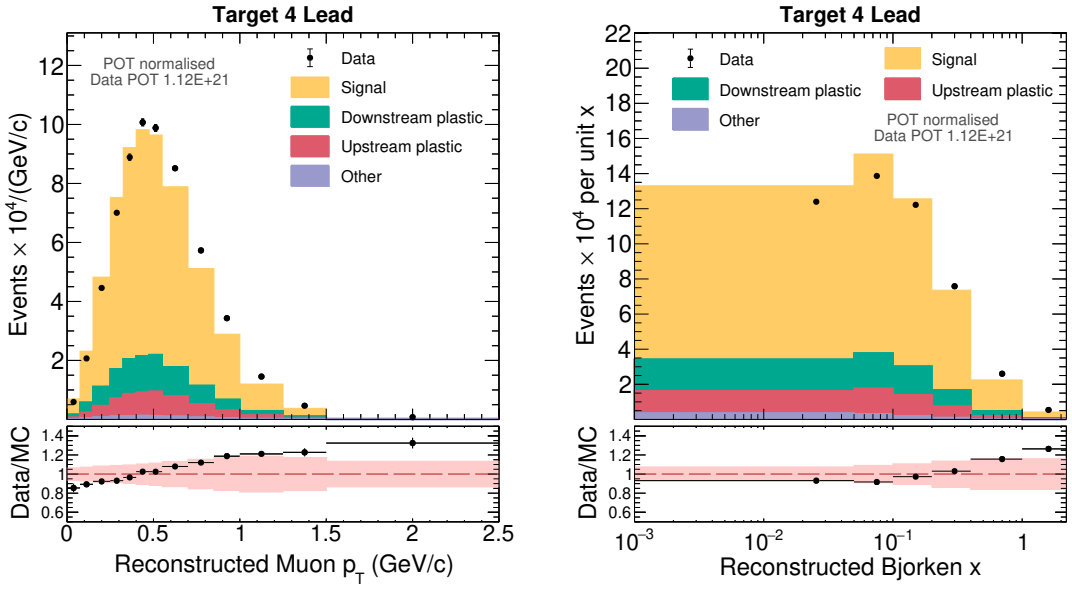

Figure B.4: Selected event distributions in target 4 lead for both antimuon p_{T} (left) and Bjorken x (right).

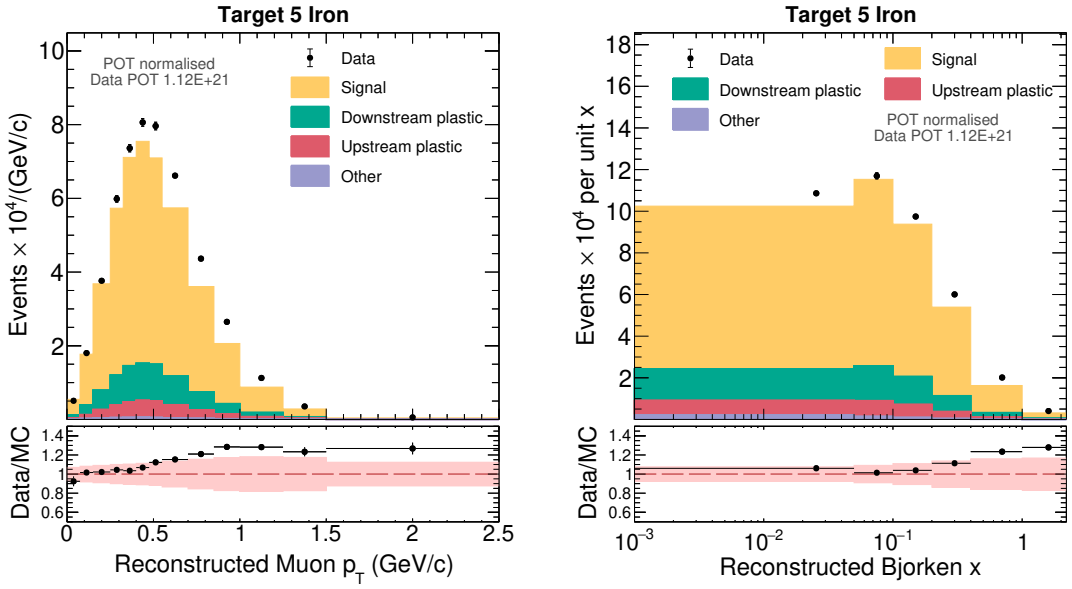

Figure B.5: Selected event distributions in target 5 iron for both antimuon p_{T} (left) and Bjorken x (right).

Appendix C

Plastic sidebands

This appendix presents additional plots relevant to the plastic sideband fit procedure described in Section 7.2. Specifically, it includes pre-fit and post-fit plots for the upstream lead target combination, as well as both upstream and downstream carbon and iron target combinations, in the reconstructed vertex plane, antimuon p_{T}, and Bjorken x.

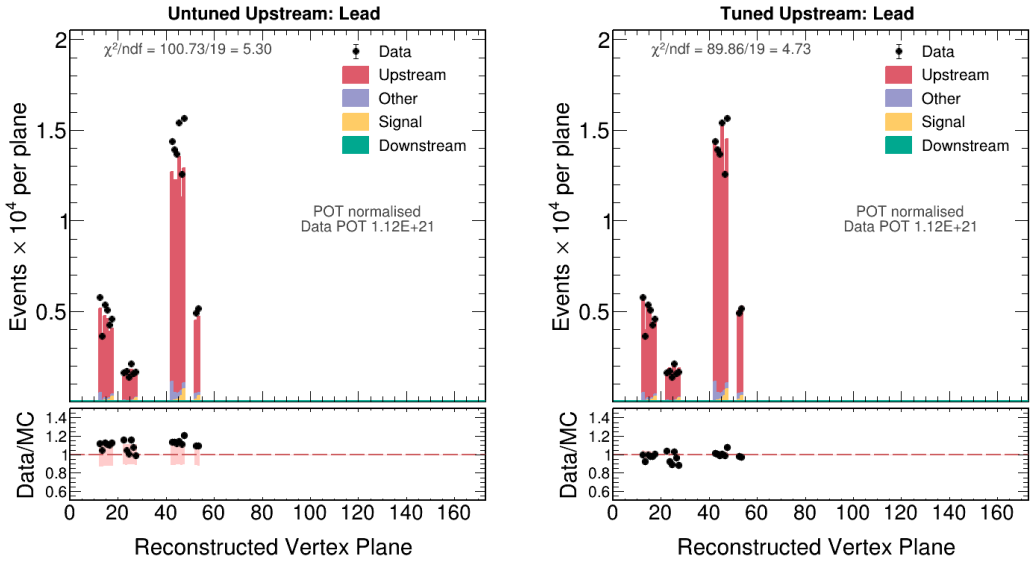

Figure C.1: Pre-fit (left) and post-fit distribution (right) of the plastic upstream of lead target combination in the fit variable, i.e. the vertex plane. The data points in the top panel carry the statistical uncertainty on the data. The bottom panel displays the data-to-simulation ratio, with the black points including the statistical uncertainty on the ratio and the pink band representing the systematic uncertainty on the simulation (as there are no systematic uncertainties present in the data). Note the constrained systematic uncertainty in the post-fit data-to-simulation ratio.

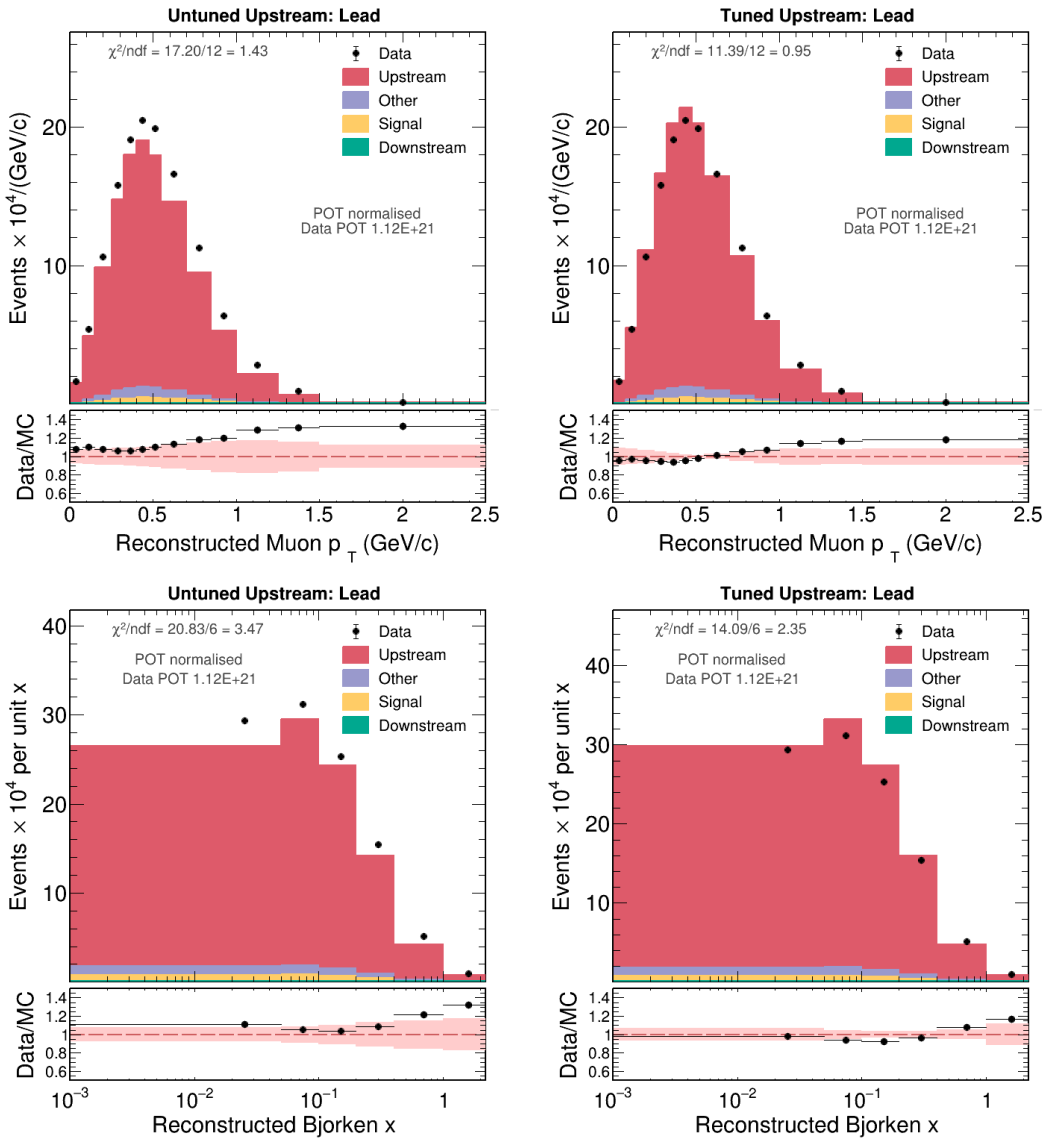

Figure C.2: Pre-fit distributions of plastic upstream of lead target combination in anti-muon p_{T} (top) and Bjorken x (bottom), along with the corresponding post-fit distributions (right) with applied scale factor.

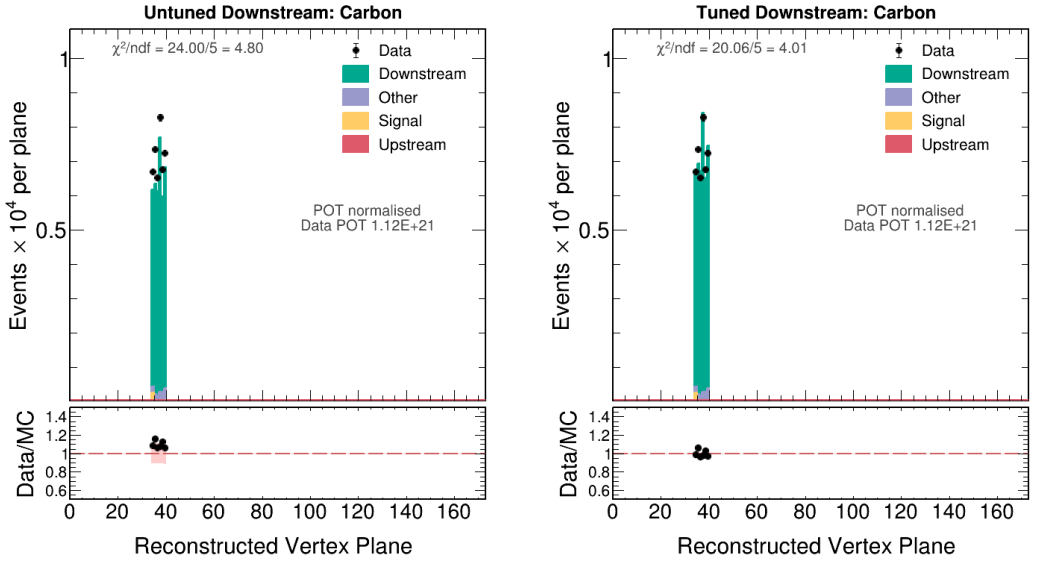

Figure C.3: Pre-fit (left) and post-fit distribution (right) of the plastic downstream of carbon target combination in the fit variable, i.e. the vertex plane.

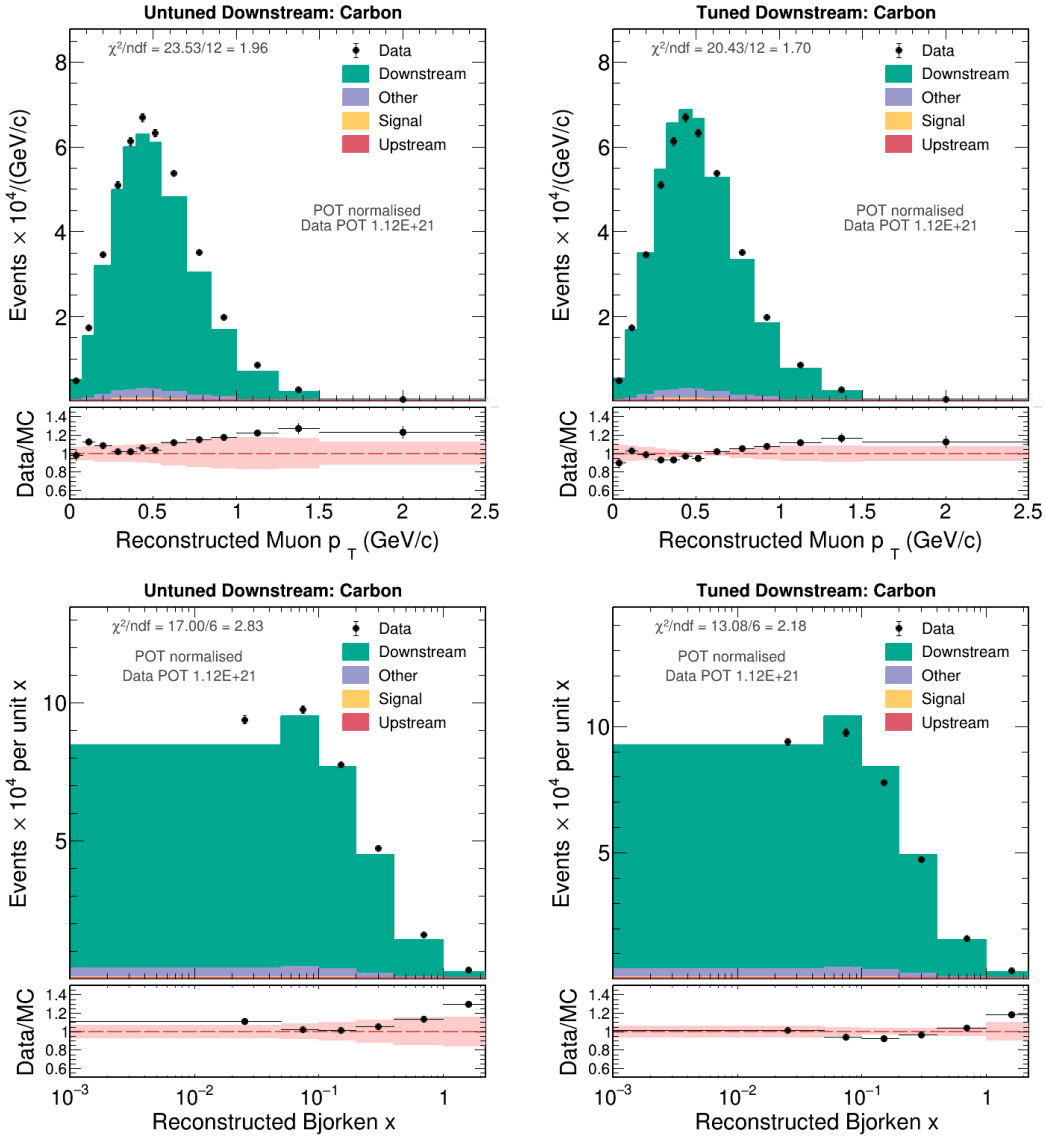

Figure C.4: Pre-fit distributions of plastic downstream of carbon target combination in antimuon p_{T} (top) and Bjorken x (bottom), along with the corresponding post-fit distributions (right) with applied scale factor.

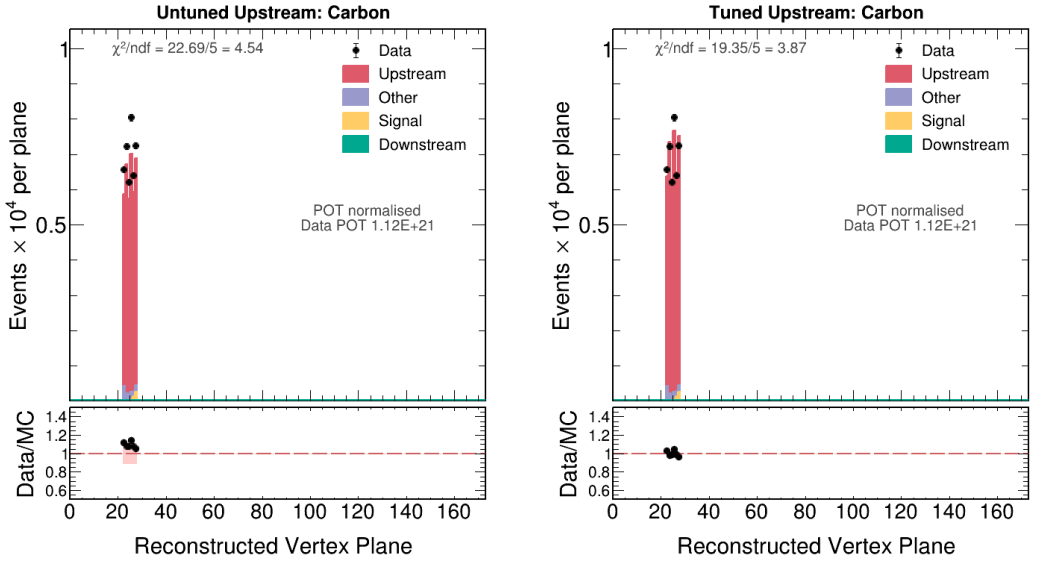

Figure C.5: Pre-fit (left) and post-fit distribution (right) of the plastic upstream of carbon target combination in the fit variable, i.e. the vertex plane.

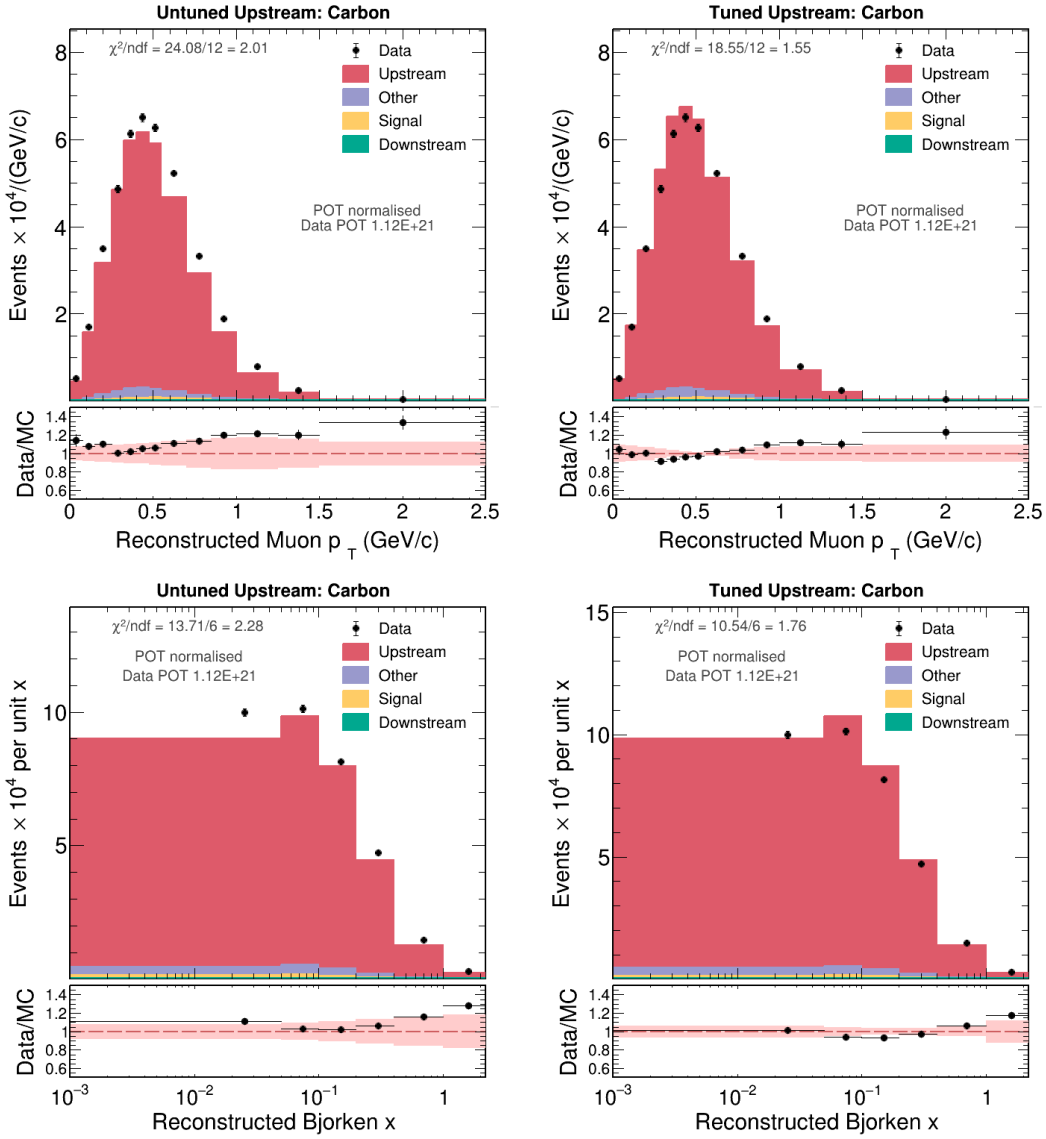

Figure C.6: Pre-fit distributions of plastic upstream of carbon target combination in antimuon p_{T} (top) and Bjorken x (bottom), along with the corresponding post-fit distributions (right) with applied scale factor.

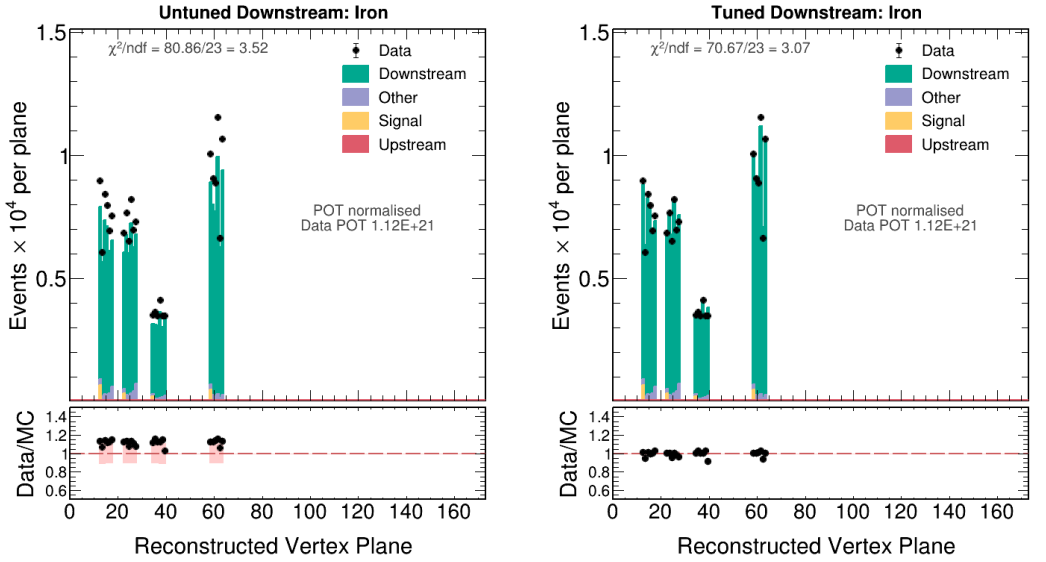

Figure C.7: Pre-fit (left) and post-fit distribution (right) of the plastic downstream of iron target combination in the fit variable, i.e. the vertex plane.

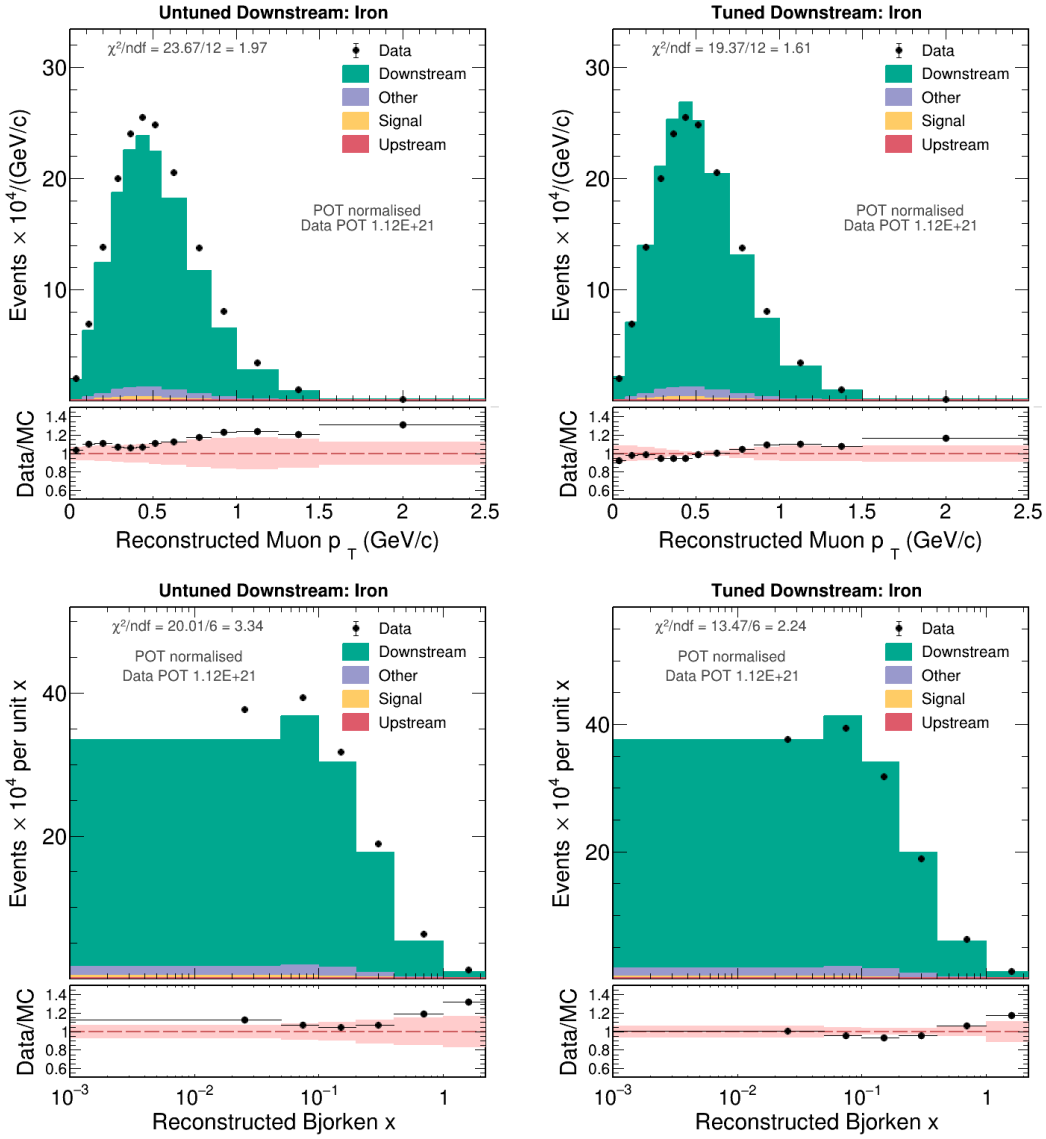

Figure C.8: Pre-fit distributions of plastic downstream of iron target combination in antimuon p_{T} (top) and Bjorken x (bottom), along with the corresponding post-fit distributions (right) with applied scale factor.

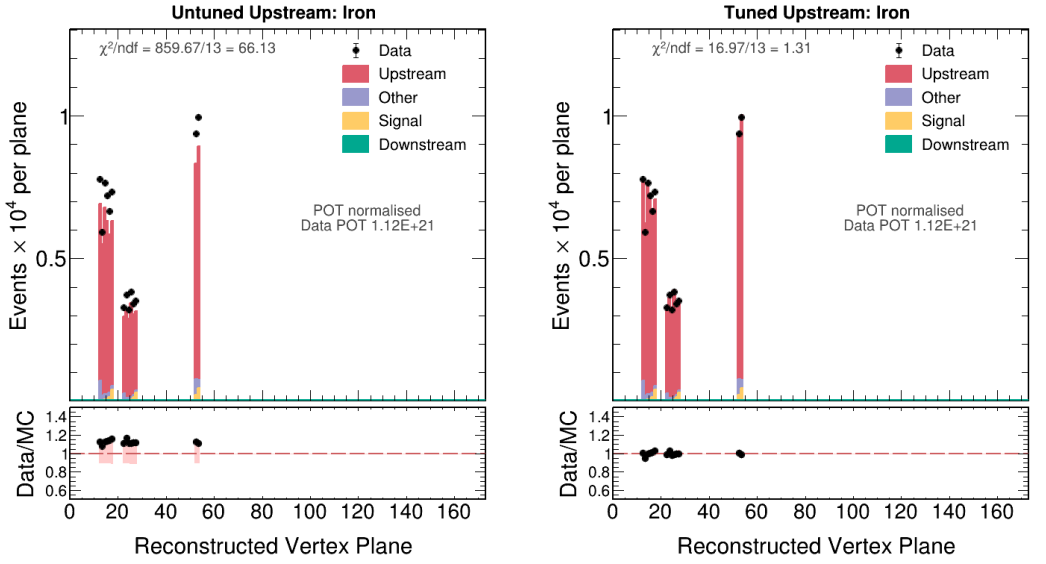

Figure C.9: Pre-fit (left) and post-fit distribution (right) of the plastic upstream of iron target combination in the fit variable, i.e. the vertex plane.

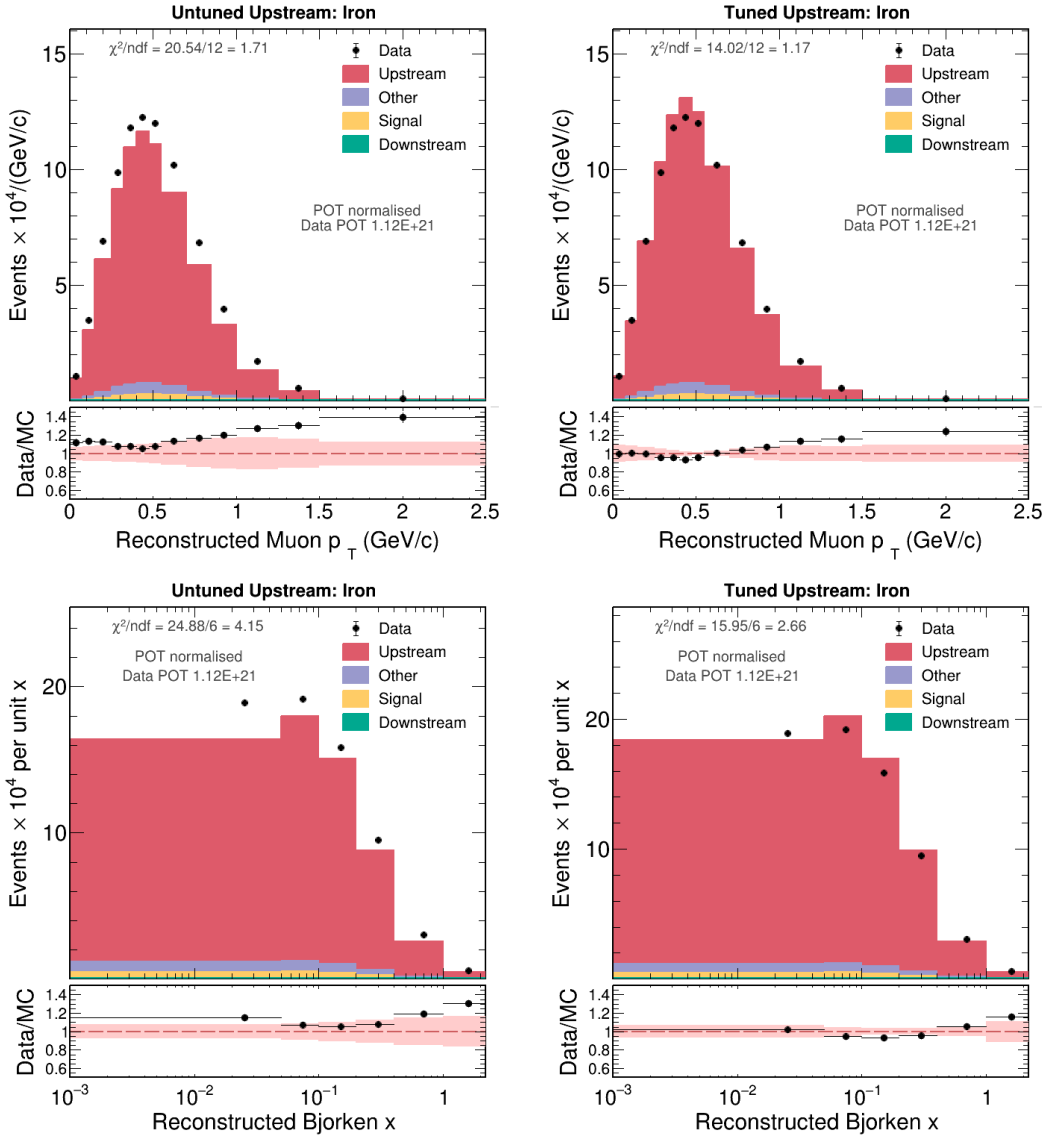

Figure C.10: Pre-fit distributions of plastic upstream of iron target combination in anti-muon p_{T} (top) and Bjorken x (bottom), along with the corresponding post-fit distributions (right) with applied scale factor.

Appendix D

Background-subtracted distributions

This appendix presents additional background-subtracted distributions not shown in Section 7.2, along with their associated fractional uncertainty breakdowns on the data. Specifically, it includes the background-subtracted distribution plots for target 2 iron and lead, target 3 carbon, iron, and lead, target 4 lead, and target 5 iron in both antimuon p_{T} and Bjorken x.

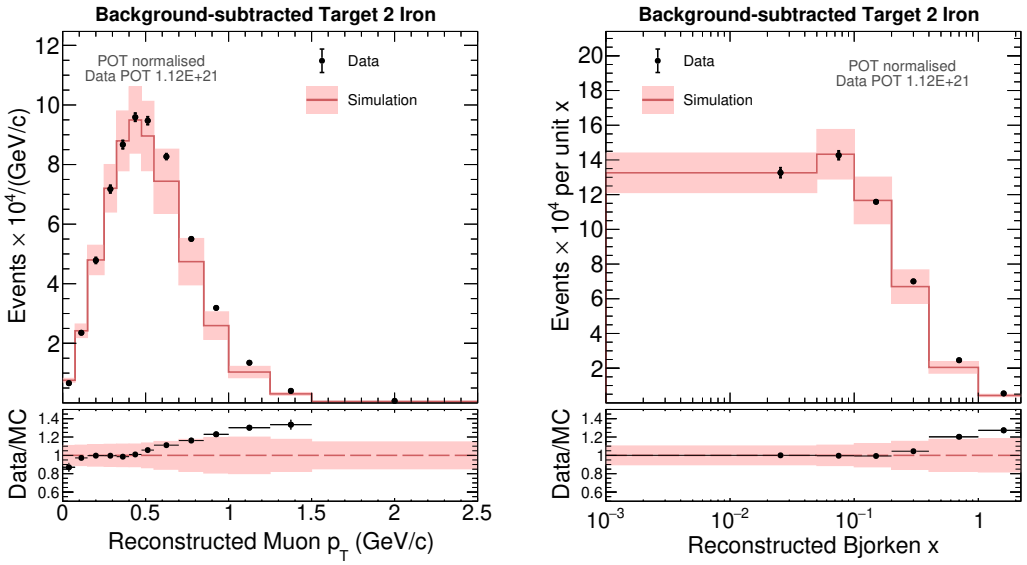

Figure D.1: Background-subtracted distributions in antimuon p_{T} (left) and Bjorken x (right) for target 2 iron. In the top panel, the pink band on the simulation represents both statistical and systematic uncertainties. The data points also carry both statistical (inner error bar) and systematic (outer error bar, which is the sum of statistical and systematic errors) uncertainties. The bottom panel of each plot displays the data-to-simulation ratio, with the pink band around 1 representing systematic uncertainties on both the data and the simulation, while the black points reflect the statistical uncertainty on the data-to-simulation ratio.

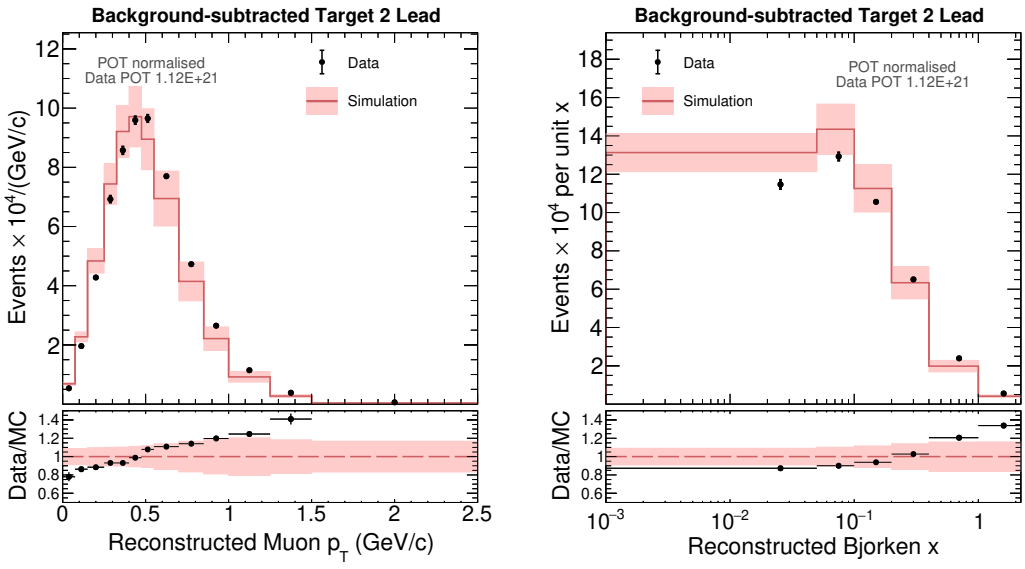

Figure D.2: Background-subtracted distributions in antimuon p_{T} (left) and Bjorken x (right) for target 2 lead.

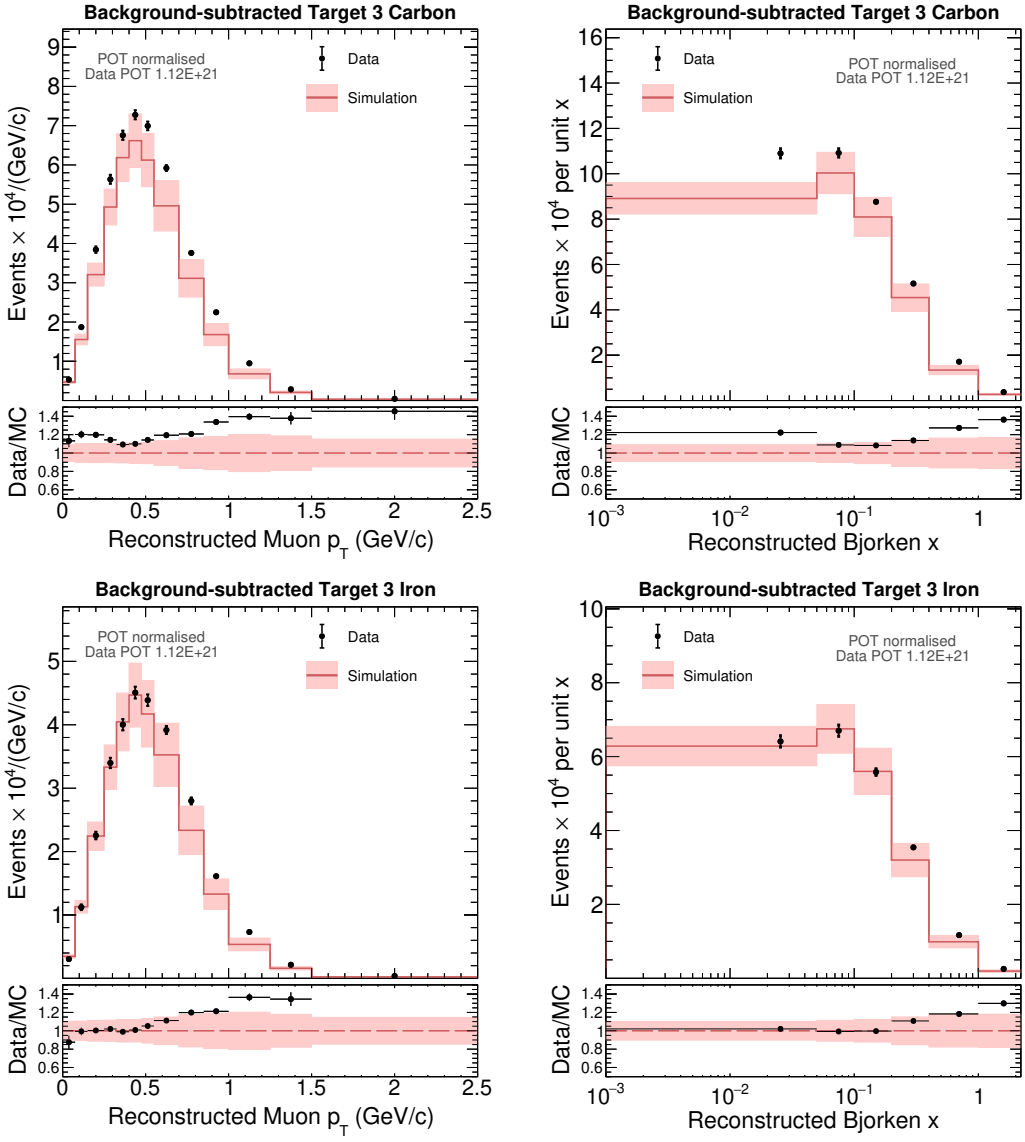

Figure D.3: Background-subtracted distributions in antimuon p_{T} (left panel) and Bjorken x (right panel) for target 3 carbon (top) and target 3 iron (bottom).

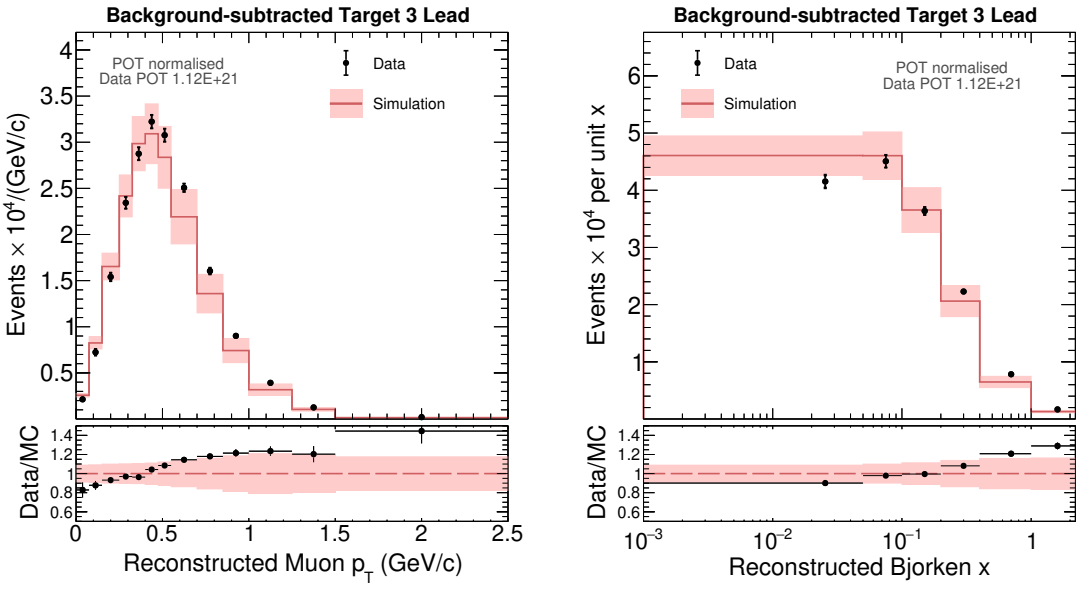

Figure D.4: Background-subtracted distributions in antimuon p_{T} (left) and Bjorken x (right) for target 3 lead.

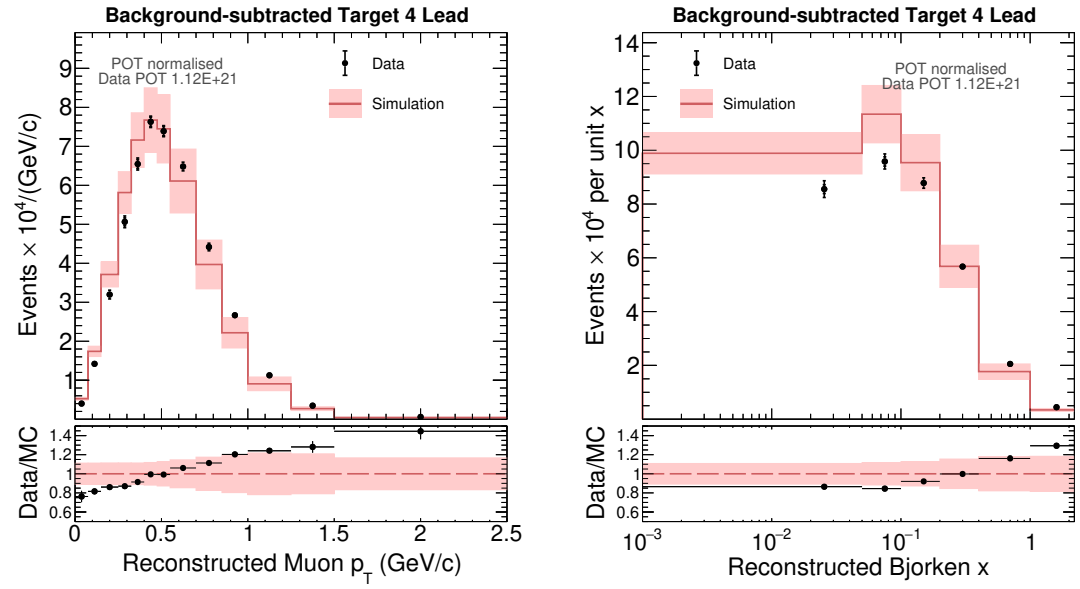

Figure D.5: Background-subtracted distributions in antimuon p_{T} (left) and Bjorken x (right) for target 4 lead.

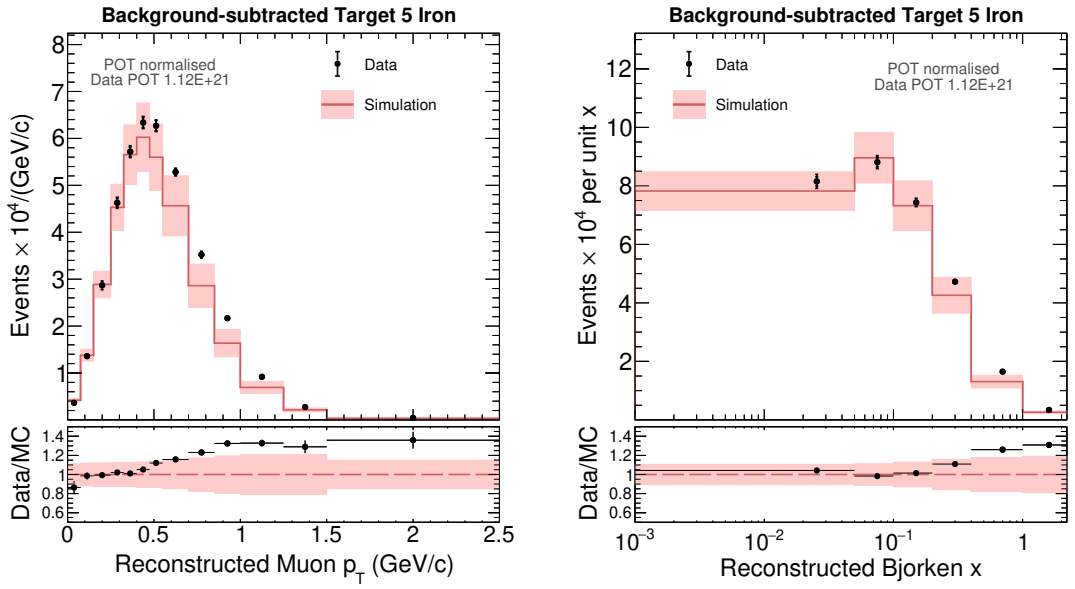

Figure D.6: Background-subtracted distributions in antimuon p_{T} (left) and Bjorken x (right) for target 5 iron.

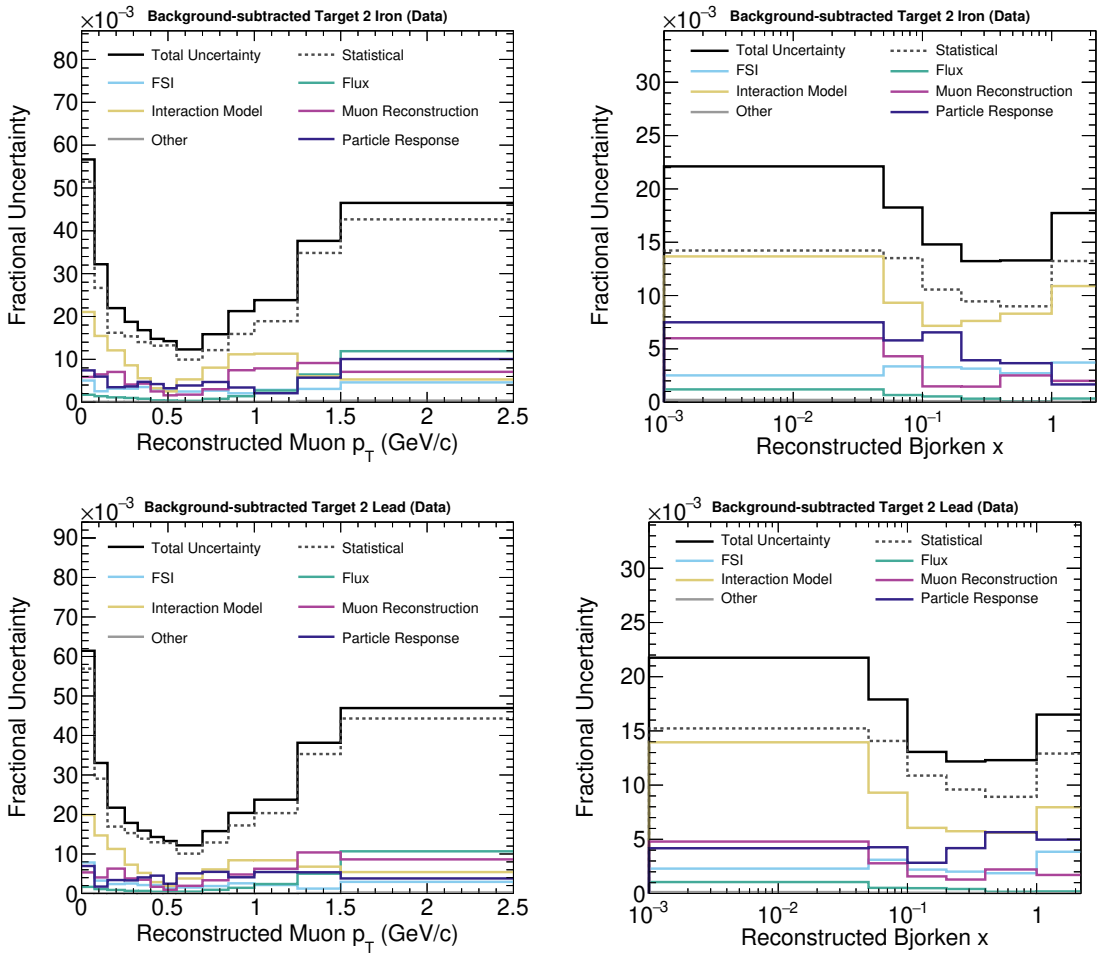

Figure D.7: Fractional uncertainty breakdowns on the background-subtracted data distributions in both p_{T} (left panel) and Bjorken x (right panel) for target 2 iron (top) and target 2 lead (bottom).

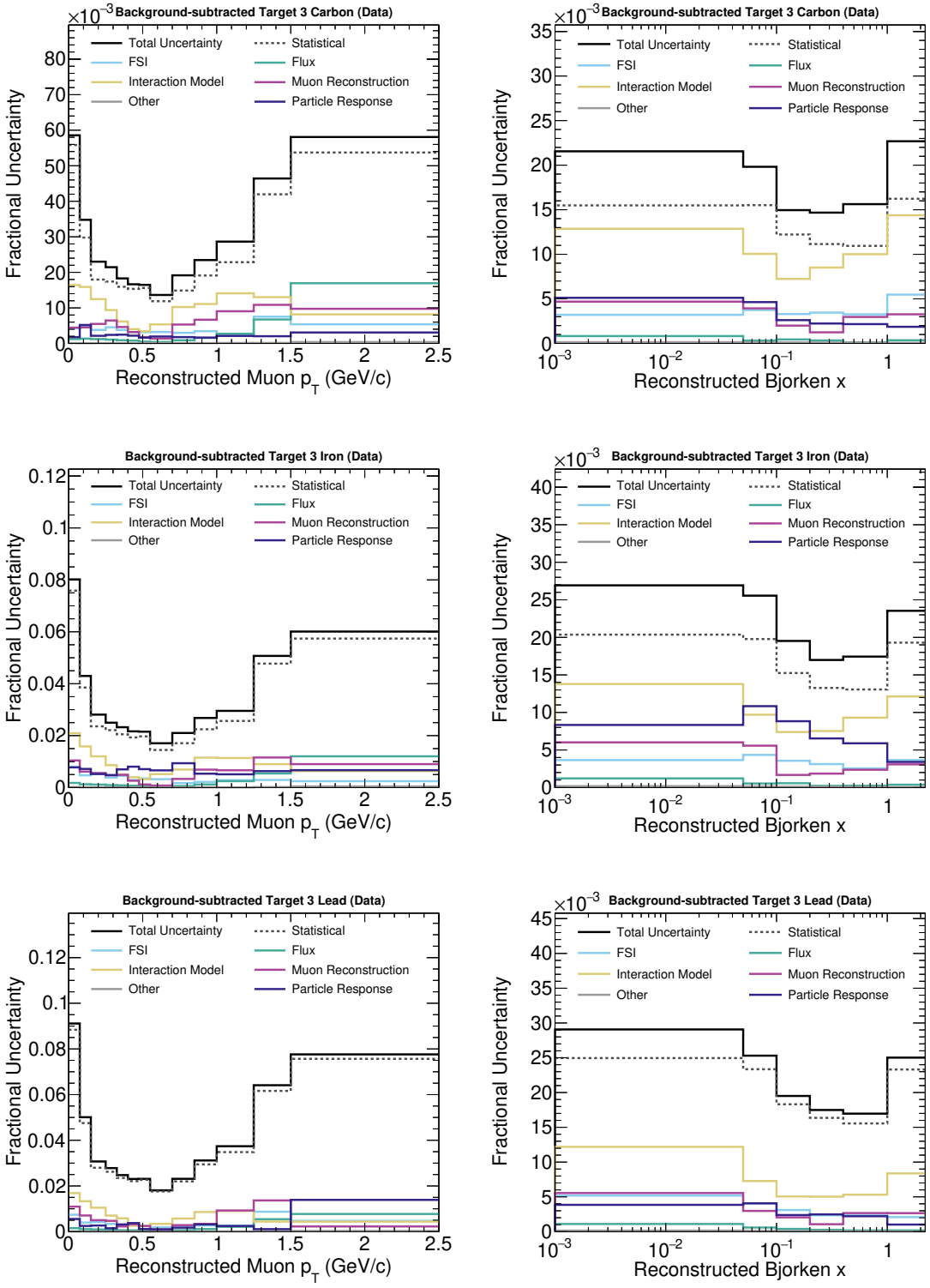

Figure D.8: Fractional uncertainty breakdowns on the background-subtracted data distributions in both p_{T} (left panel) and Bjorken x (right panel) for target 3 carbon (top), target 3 iron (middle), and target 3 lead (bottom).

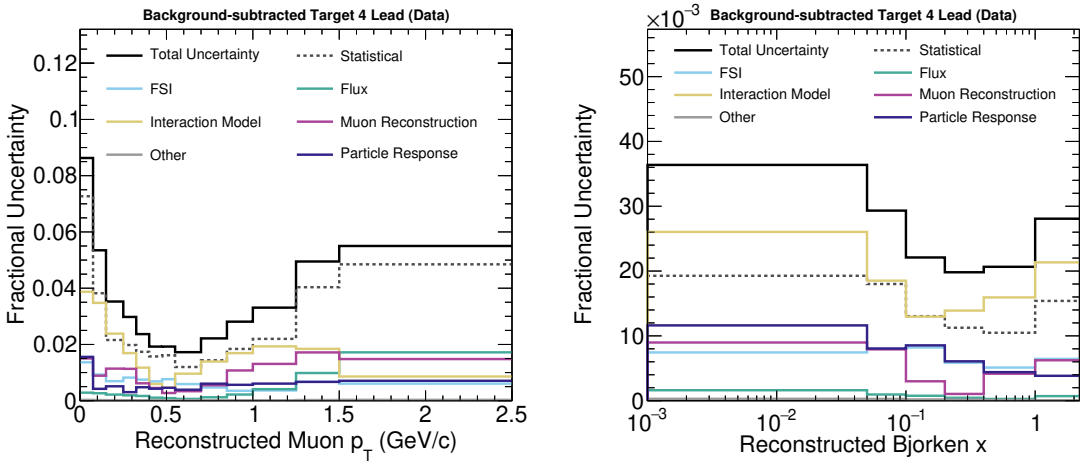

Figure D.9: Fractional uncertainty breakdowns on the background-subtracted data distributions in both p_{T} (left panel) and Bjorken x (right panel) for target 4 lead.

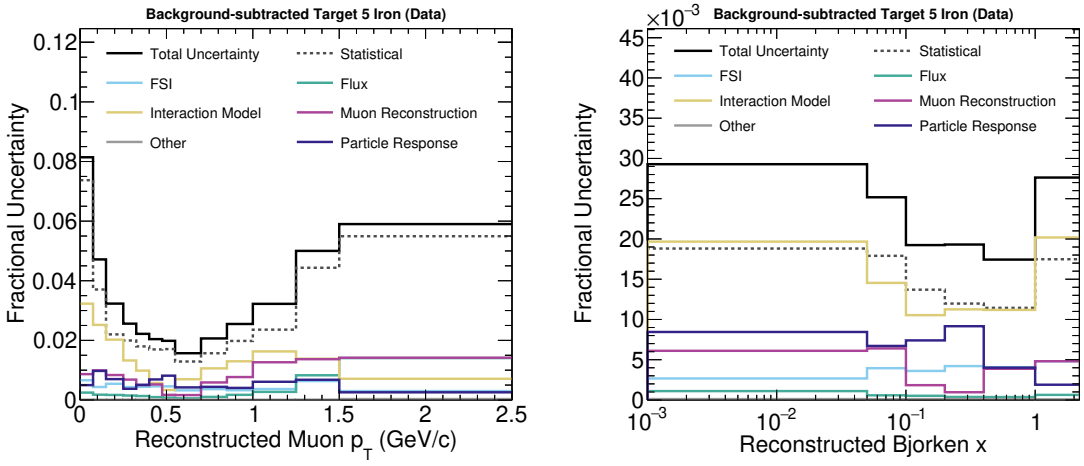

Figure D.10: Fractional uncertainty breakdowns on the background-subtracted data distributions in both p_{T} (left panel) and Bjorken x (right panel) for target 5 iron.

Appendix E

Row-normalised migration matrices

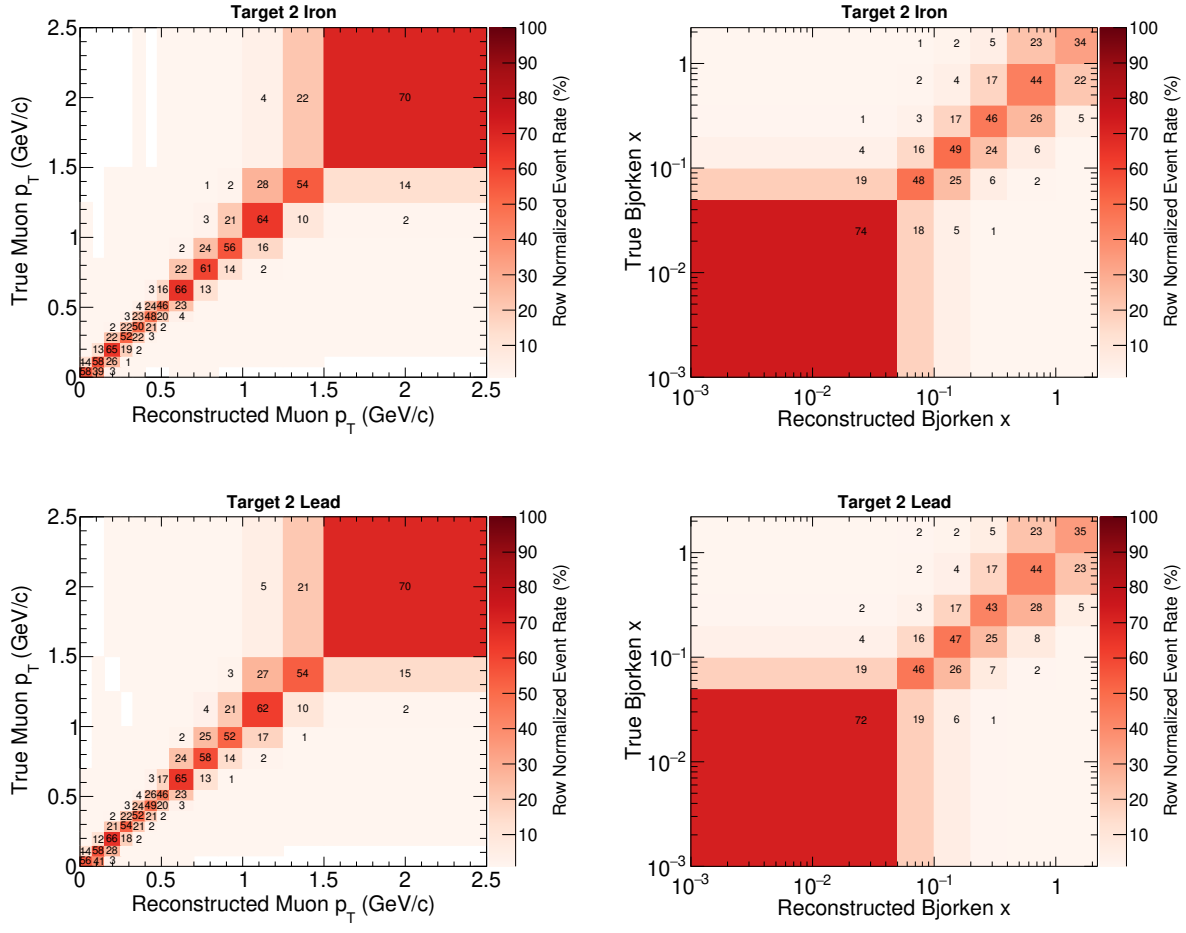

Figure E.1: Row-normalised migration matrices for target 2 iron (top panel) and target 2 lead (bottom panel) in both p_{T} (left) and Bjorken x (right).

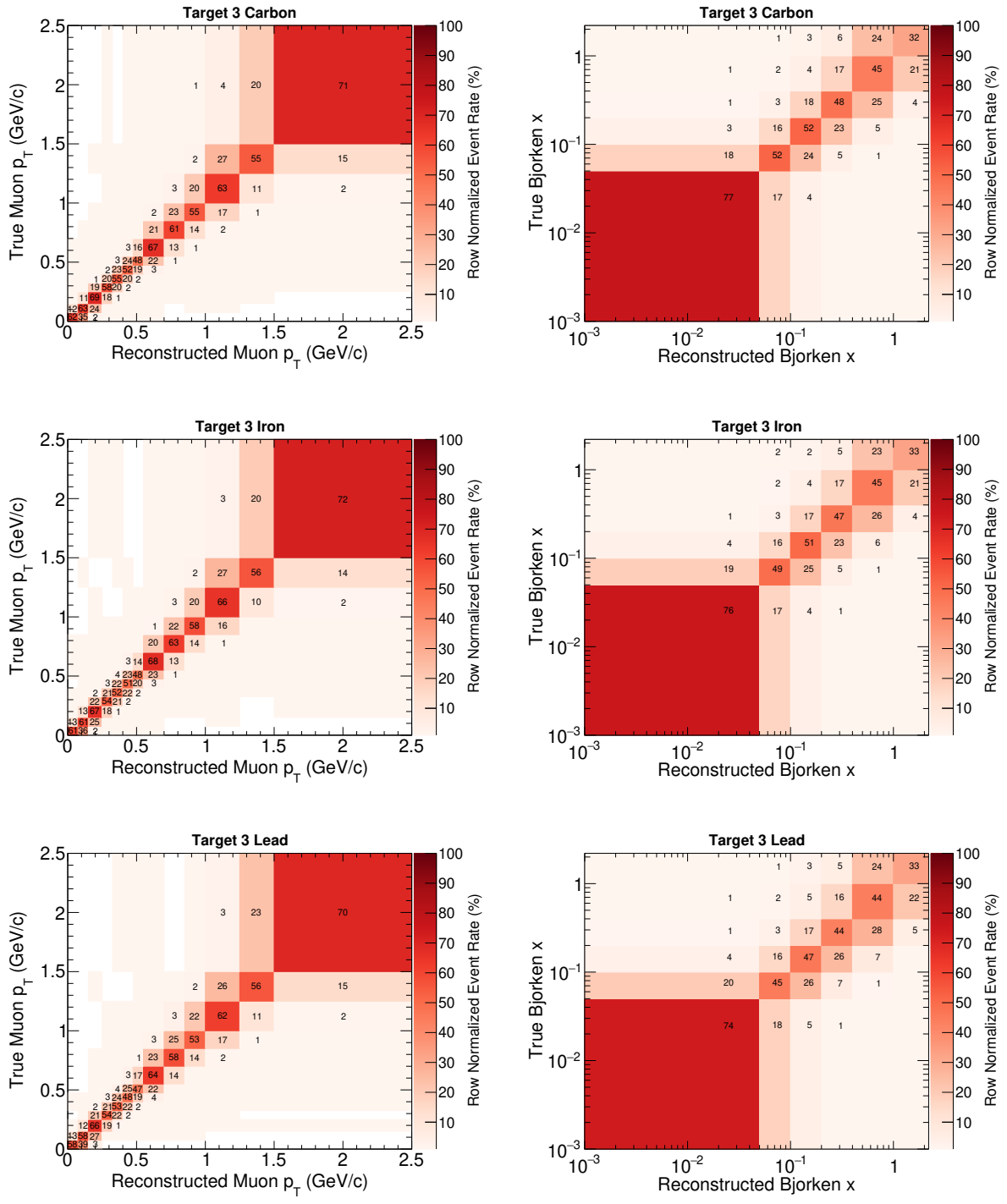

Figure E.2: Row-normalised migration matrices for target 3 carbon (top panel), target 3 iron (middle panel) and target 3 lead (bottom panel) in both p_T (left) and Bjorken x (right).

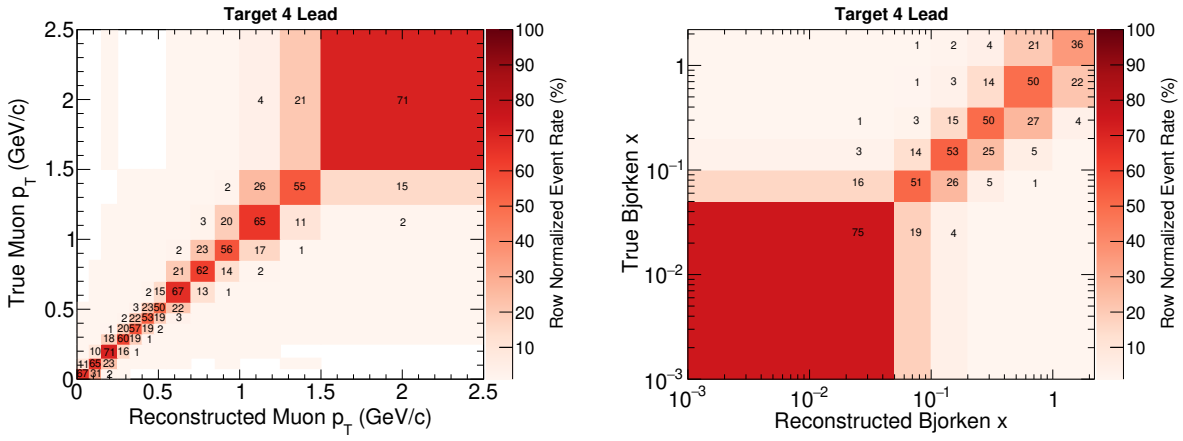

Figure E.3: Row-normalised migration matrices for target 4 lead in both p_{T} (left) and Bjorken x (right).

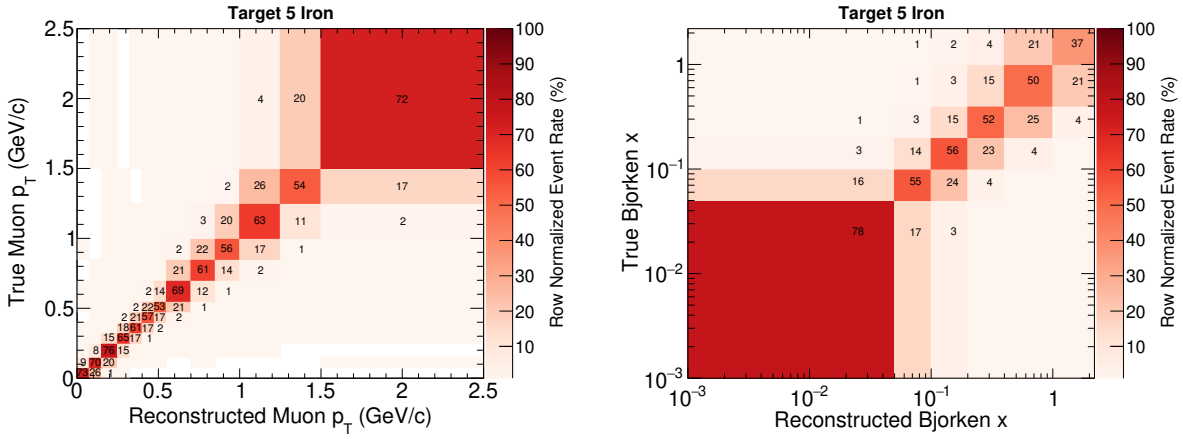

Figure E.4: Row-normalised migration matrices for target 5 iron in both p_{T} (left) and Bjorken x (right).

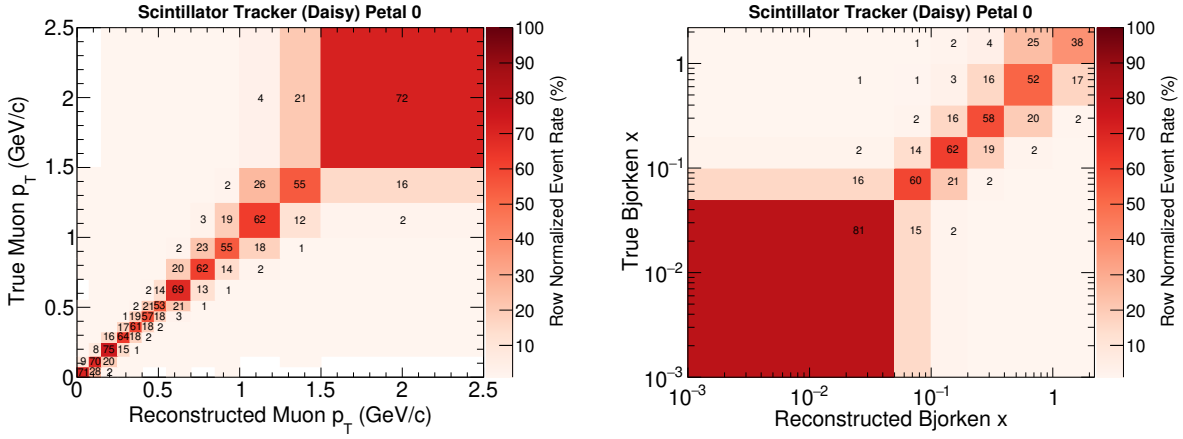

Figure E.5: Row-normalised migration matrices for the 'daisy petal' 0 of the scintillator tracker in both p_{T} (left) and Bjorken x (right).

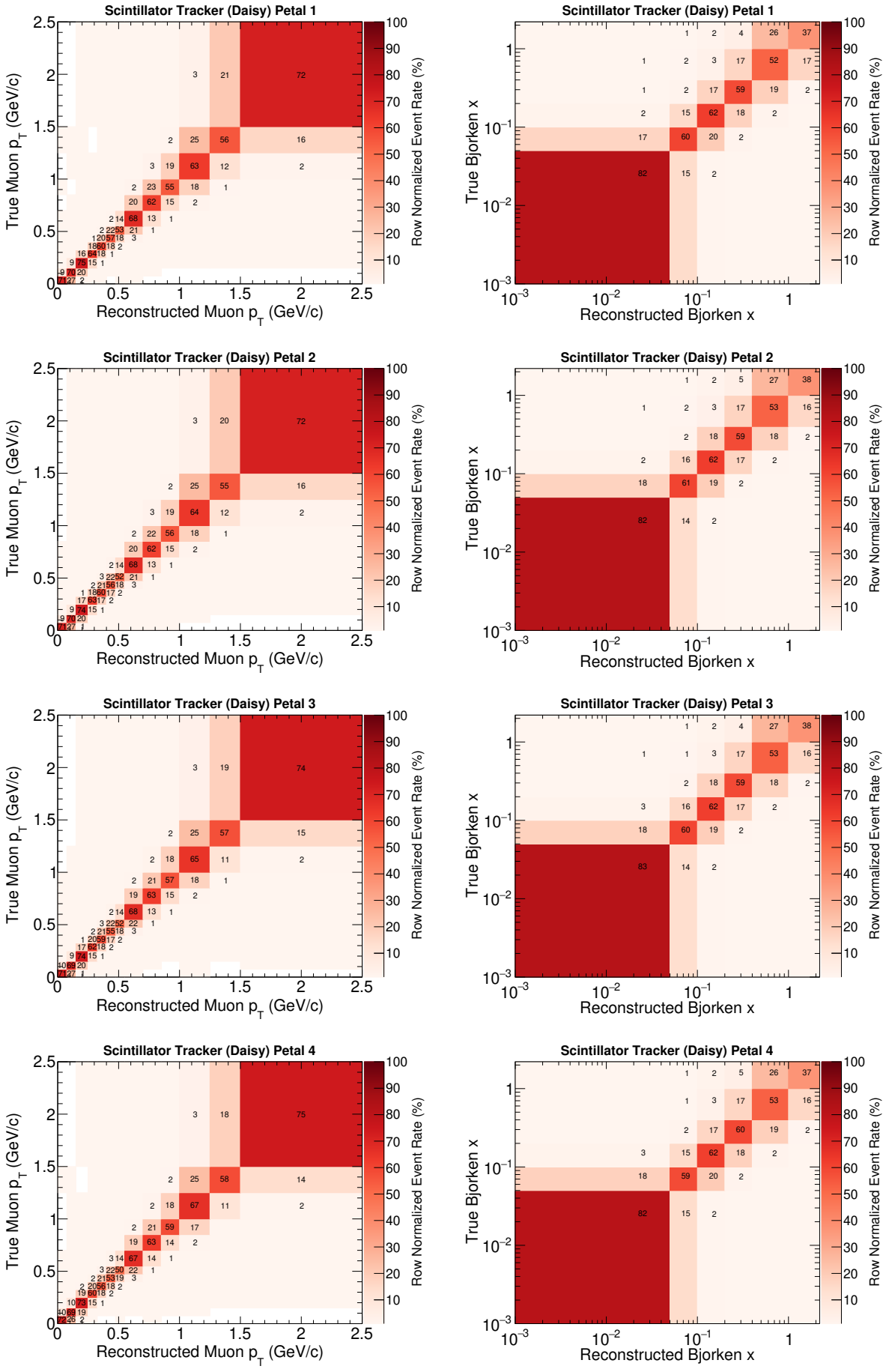

Figure E.6: Row-normalised migration matrices for 'daisy petals' 1–4 of the scintillator tracker in both p_{T} (left) and Bjorken x (right).

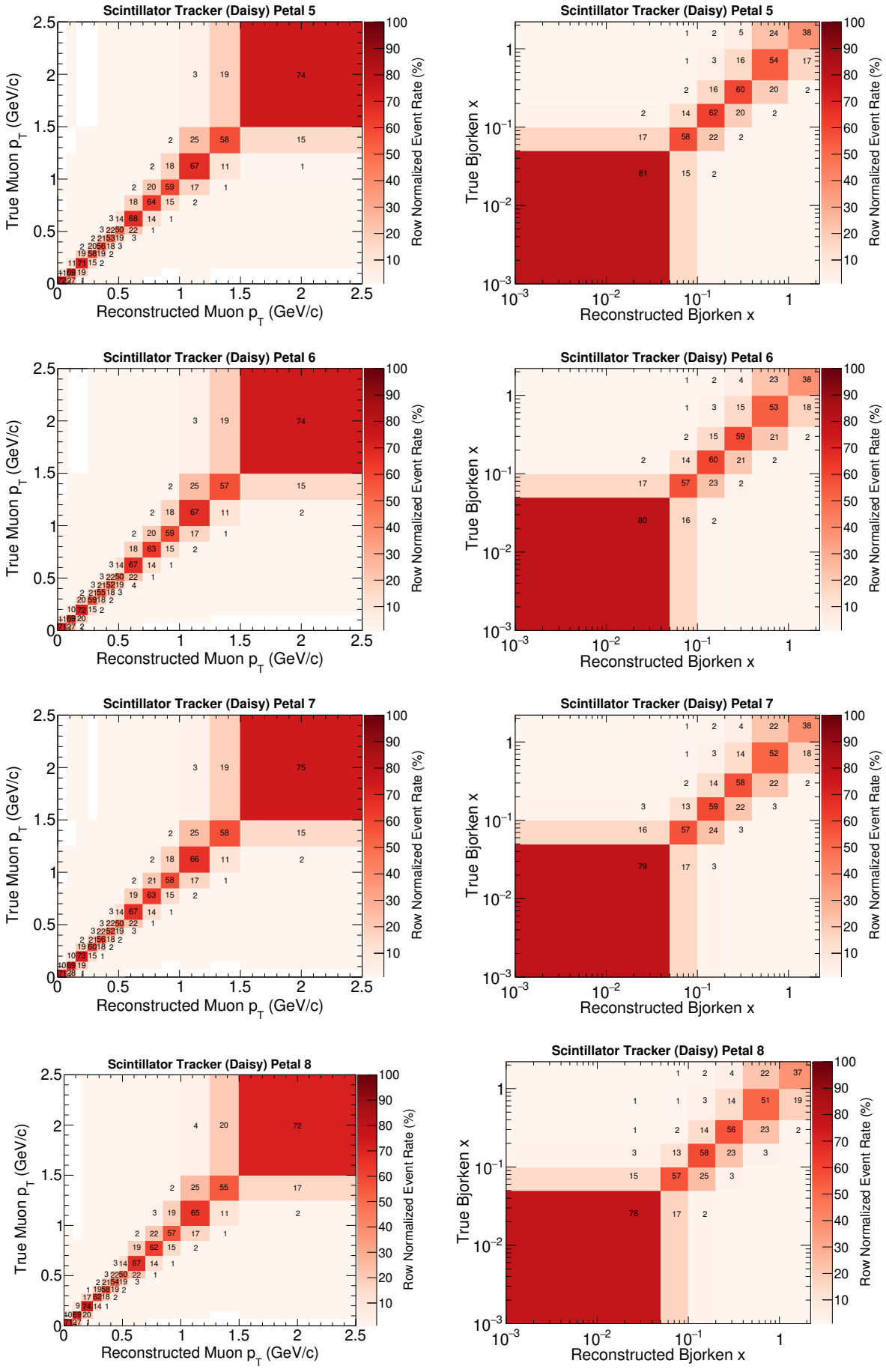

Figure E.7: Row-normalised migration matrices for 'daisy petals' 5–8 of the scintillator tracker in both p_{T} (left) and Bjorken x (right).

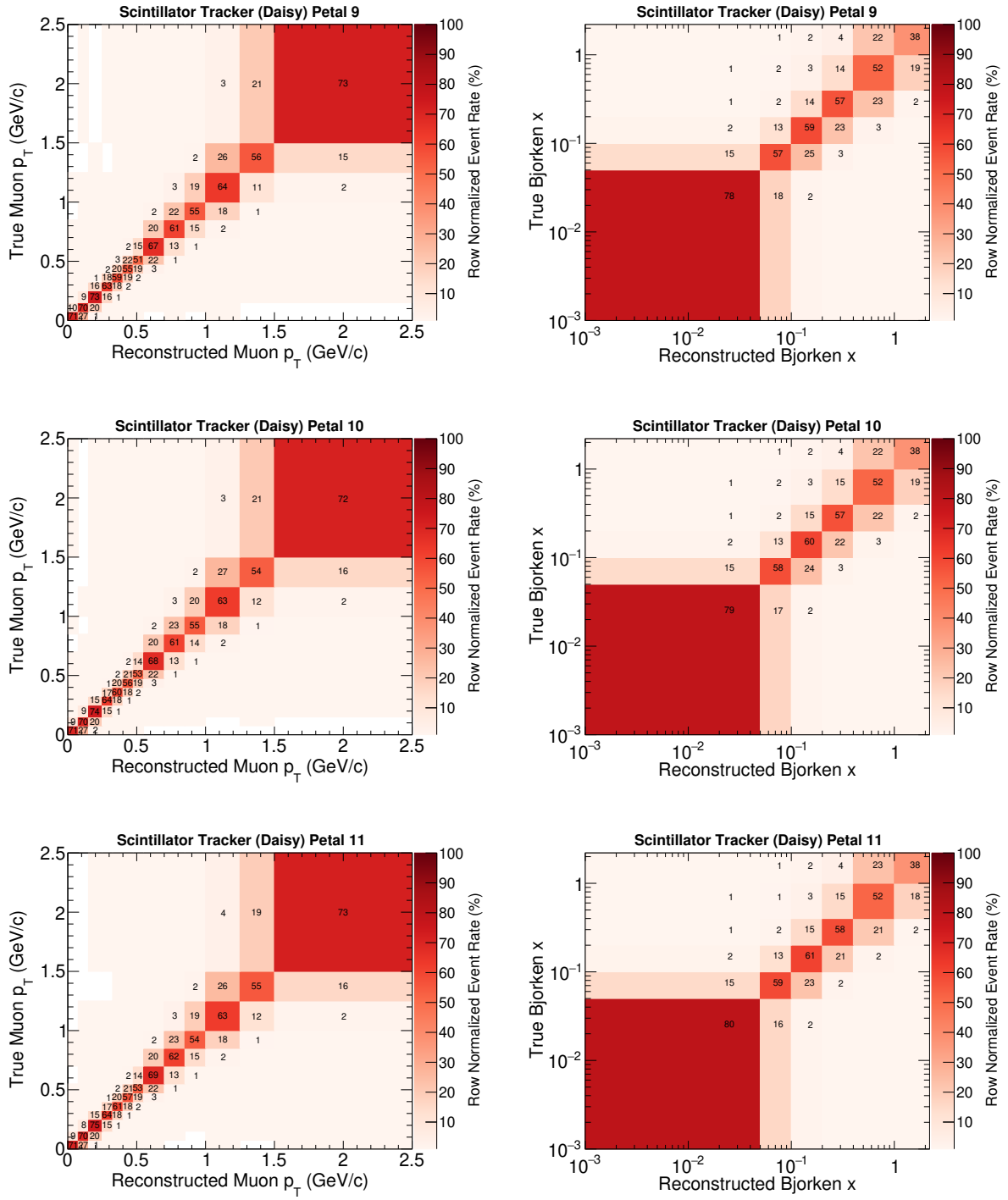

Figure E.8: Row-normalised migration matrices for 'daisy petals' 9–11 of the scintillator tracker in both p_T (left) and Bjorken x (right).

Appendix F

Regularised D'Agostini iterative unfolding

This appendix describes my understanding of the derivation and implementation of the regularised D'Agostini iterative unfolding algorithm, particularly the origin of the Equation 7.3, based on References [227,228,254]. The reasons for the smearing of reconstructed distributions and the needs to reverse this process are discussed in Section 7.3.

The number of events of a reconstructed distribution $\boldsymbol{y}$ in a particular bin j can be related to the number of events of a true distribution $\boldsymbol{\lambda}$ in the bin α via a migration matrix $U_{j\alpha}$ such as

$$y_j = \sum_{\alpha} U_{j\alpha}\lambda_{\alpha}, \tag{F.1}$$

where the migration matrix $U_{j\alpha}$ corresponds to

$$U_{j\alpha} = P(y \in \text{reco bin } j \mid \lambda \in \text{true bin } \alpha). \tag{F.2}$$

Here, y and λ are the events from the reconstructed distribution $\boldsymbol{y}$ and the true distribution $\boldsymbol{\lambda}$, respectively. Therefore, the Equation F.1 can be also thought of as the probability

that a y event belongs to the bin j,

$$P(y \in \text{reco bin } j) = \sum_{\alpha} P(y \in \text{reco bin } j \mid \lambda \in \text{true bin } \alpha) P(\lambda \in \text{true bin } \alpha). \quad \text{(F.3)}$$

To reverse the smearing of the reconstructed distribution as described in Section 7.3, the unfolding matrix $\tilde{U}_{j\alpha}$ can be expressed as

$$\tilde{U}_{j\alpha} = P(\lambda \in \text{true bin } \alpha \mid y \in \text{reco bin } j). \quad \text{(F.4)}$$

Applying the Bayes' theorem, this becomes

$$\tilde{U}_{j\alpha} = \frac{P(y \in \text{reco bin } j \mid \lambda \in \text{true bin } \alpha) P(\lambda \in \text{true bin } \alpha)}{P(y \in \text{reco bin } j)}. \quad \text{(F.5)}$$

Using the Equation F.3, the denominator of the unfolding matrix can be rewritten as

$$\tilde{U}_{j\alpha} = \frac{P(y \in \text{reco bin } j \mid \lambda \in \text{true bin } \alpha) P(\lambda \in \text{true bin } \alpha)}{\sum_{\beta} P(y \in \text{reco bin } j \mid \lambda \in \text{true bin } \beta) P(\lambda \in \text{true bin } \beta)}. \quad \text{(F.6)}$$

Taking into account that the conditional probability can be represented by the migration matrix from Equation F.2, the unfolding matrix is

$$\tilde{U}_{j\alpha} = \frac{U_{j\alpha} P(\lambda \in \text{true bin } \alpha)}{\sum_{\beta} U_{j\beta} P(\lambda \in \text{true bin } \beta)}, \quad \text{(F.7)}$$

The zeroth order probability of the true event λ in the bin α is the true event λ^0_α over the total of the observed events, i.e.

$$P^0(\lambda \in \text{true bin } \alpha) = \frac{\lambda^0_\alpha}{\sum_j y_j}, \quad \text{(F.8)}$$

and hence the unfolding migration matrix for the first iteration can be represented by

$$\tilde{U}_{j\alpha} = \frac{U_{j\alpha} \lambda^0_\alpha}{\sum_{\beta} U_{j\beta} \lambda^0_\beta}. \quad \text{(F.9)}$$

As discussed in Section 7.3, the zeroth order true distribution comes from the simulation prediction of the true distribution.

The unfolded truth can be expressed as

$$\lambda_\alpha = \frac{\sum_j P(\lambda \in \text{true bin } \alpha \mid y \in \text{reco bin } j)\ y_j}{\sum_i P(y \in \text{reco bin } i \mid \lambda \in \text{true bin } \alpha)}, \tag{F.10}$$

where the denominator represents the overall unfolding efficiency ϵ_α, which is the sum over the reconstructed bins i of the migration matrix in the Equation F.2,

$$\epsilon_\alpha = \sum_i P(y \in \text{reco bin } i \mid \lambda \in \text{true bin } \alpha) = \sum_i U_{i\alpha}. \tag{F.11}$$

The estimate of the true distribution after the first iteration is then given by substituting the Equation F.9 in the Equation F.10, i.e.

$$\lambda_\alpha = \frac{\lambda^0_\alpha}{\sum_i U_{i\alpha}} \sum_j \frac{U_{j\alpha} y_j}{\sum_\beta U_{j\beta} \lambda^0_\beta}. \tag{F.12}$$

This is valid for each iteration, as the true distribution $\boldsymbol{\lambda}$ is updated after each step with the new prediction. Finally, the $(k+1)$th iteration of the D'Agostini method can be determined by

$$\lambda^{(k+1)}_\alpha = \frac{\lambda^{(k)}_\alpha}{\sum_i U_{i\alpha}} \sum_j \frac{U_{j\alpha} y_j}{\sum_\beta U_{j\beta} \lambda^{(k)}_\beta}. \tag{F.13}$$

It is also important to note that this method was shown to be equivalent to the expectation–maximisation (EM) iteration algorithm [255] for finding the maximum likelihood estimator (MLE) of $\boldsymbol{\lambda}$ in the Poisson regression problem $\boldsymbol{y} \sim \text{Poission}(\boldsymbol{U\lambda})$, $\boldsymbol{\lambda} \geq 0$ as $k \to \infty$ [254, 256].

Appendix G

Unfolding studies

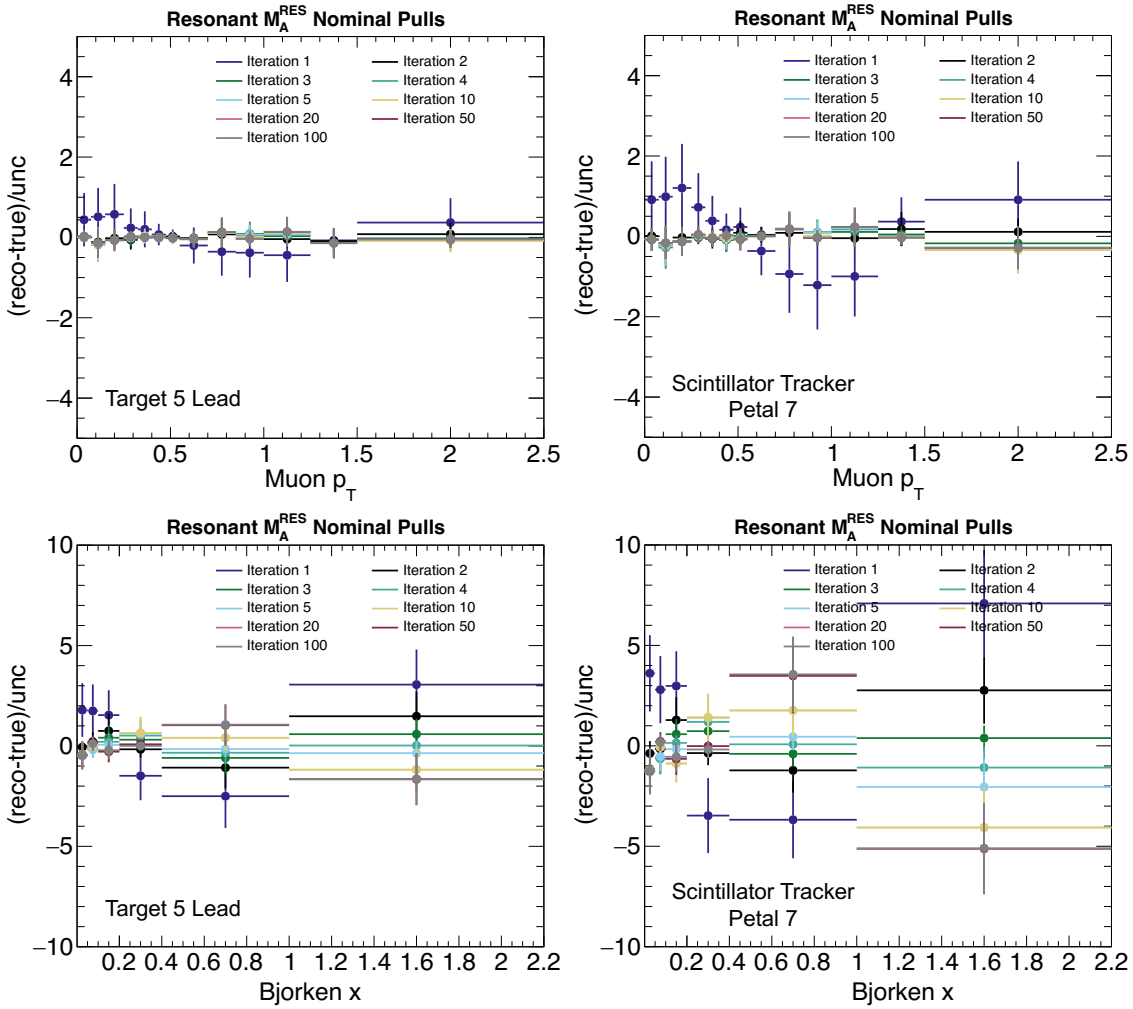

Figure G.1: Pull distributions for the 'Resonant M_A^{RES} nominal' warping study are presented for target 5 lead (left panel) and the scintillator tracker petal 7 (right panel) in both antimuon p_{T} (top) and Bjorken x (bottom). In the case of p_{T}, both pull distributions illustrate a reduction in bias with each iteration of the unfolding process. However, for the Bjorken x pull distribution, especially at high Bjorken x, there is an indication of some divergence, which prompted further investigation into potential model dependence.

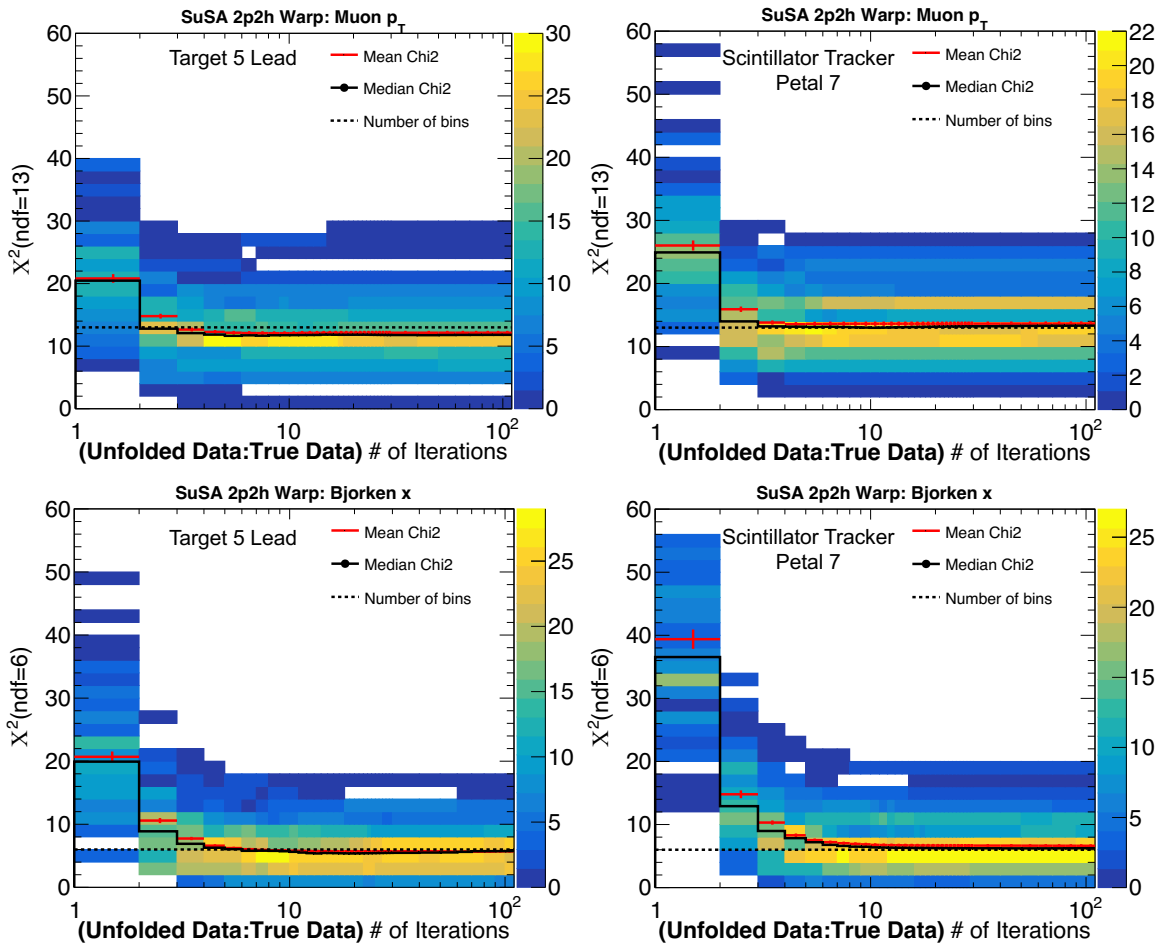

Figure G.2: The 'SuSA 2p2h' warping study conducted for target 5 lead (left panel) and the scintillator tracker petal 7 (right panel) in both antimuon p_{T} (top) and Bjorken x (bottom). Each heatmap displays the calculated χ^2 between the unfolded and true distribution of the warped model as a function of the number of iterations for each of the 100 Poisson throws. The solid lines represent the median and mean χ^2, while the dashed line indicates the number of bins or degrees of freedom (ndf). Both in p_{T} and Bjorken x, the median χ^2 stabilises at the ndf after several iterations indicating minimal bias.

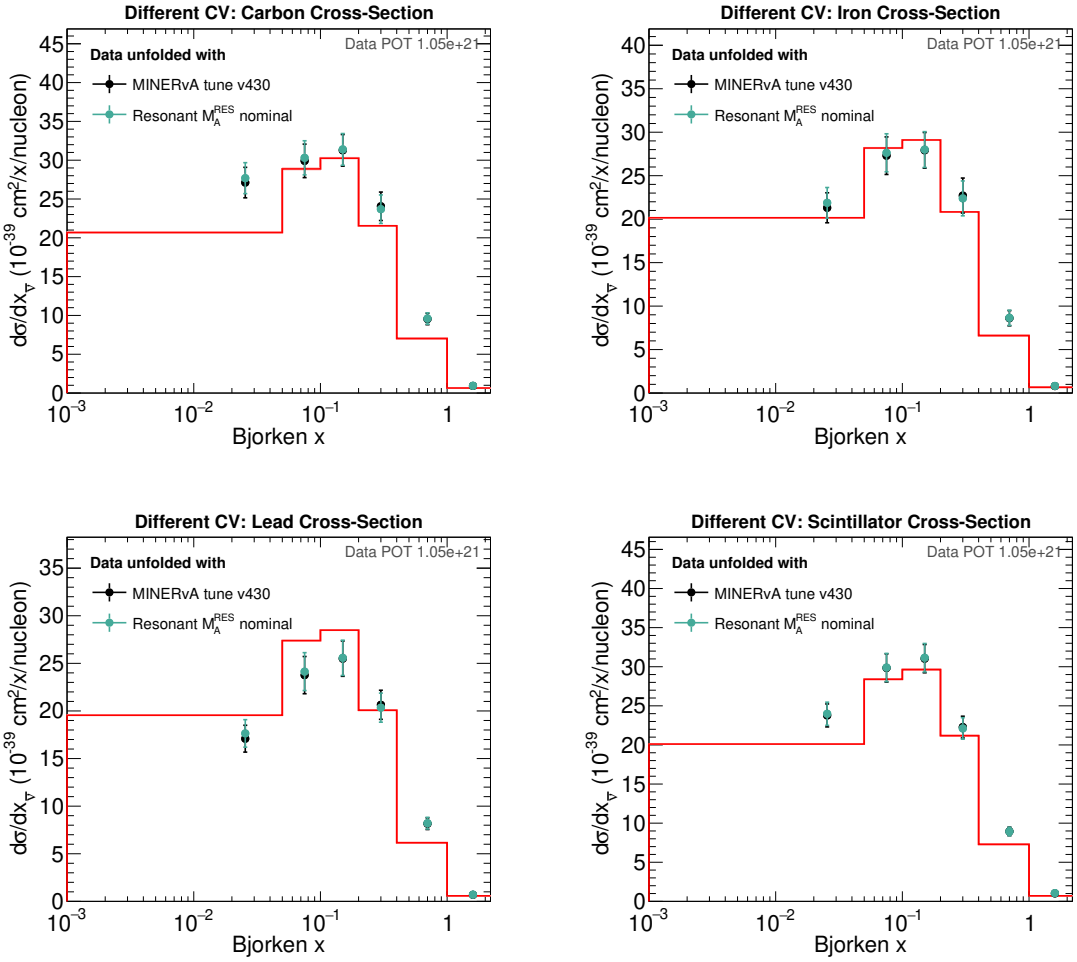

Figure G.3: Comparison of the data cross-section for carbon (top left), iron (top right), lead (bottom left) and scintillator (bottom right) as a function of Bjorken x extracted with the original simulation and 'Resonant M_A^{RES} nominal' central value to investigate potential model dependence.

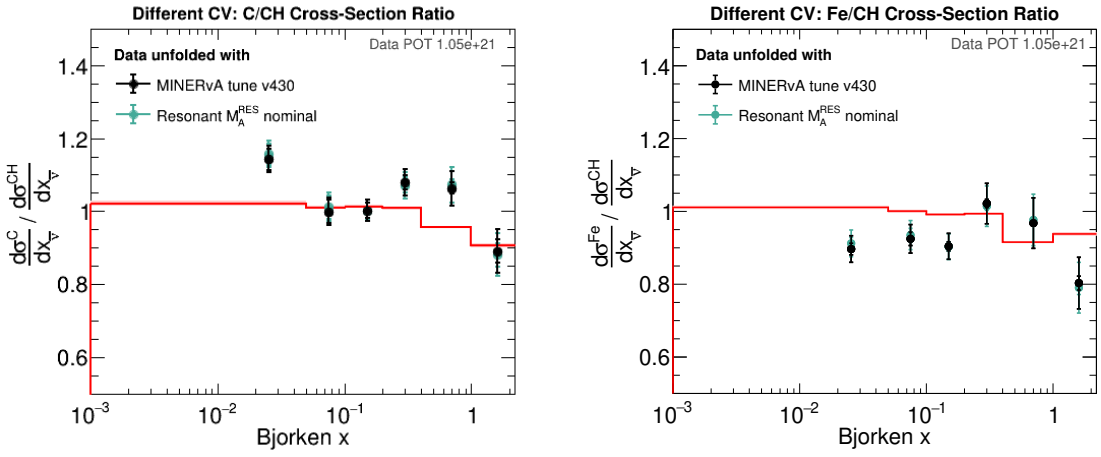

Figure G.4: Comparison of the carbon-to-scintillator (left) and iron-to-scintillator (right) data cross-section ratio as a function of Bjorken x extracted with the original simulation and 'Resonant M_A^{RES} nominal' central value. The central values of the data cross-section extracted using the warped model are encompassed by the total uncertainty (including the systematic, represented by the outer error bars) of the data cross-section extracted using the original simulation. This indicates that any potential model dependence is covered by the underlying uncertainty.

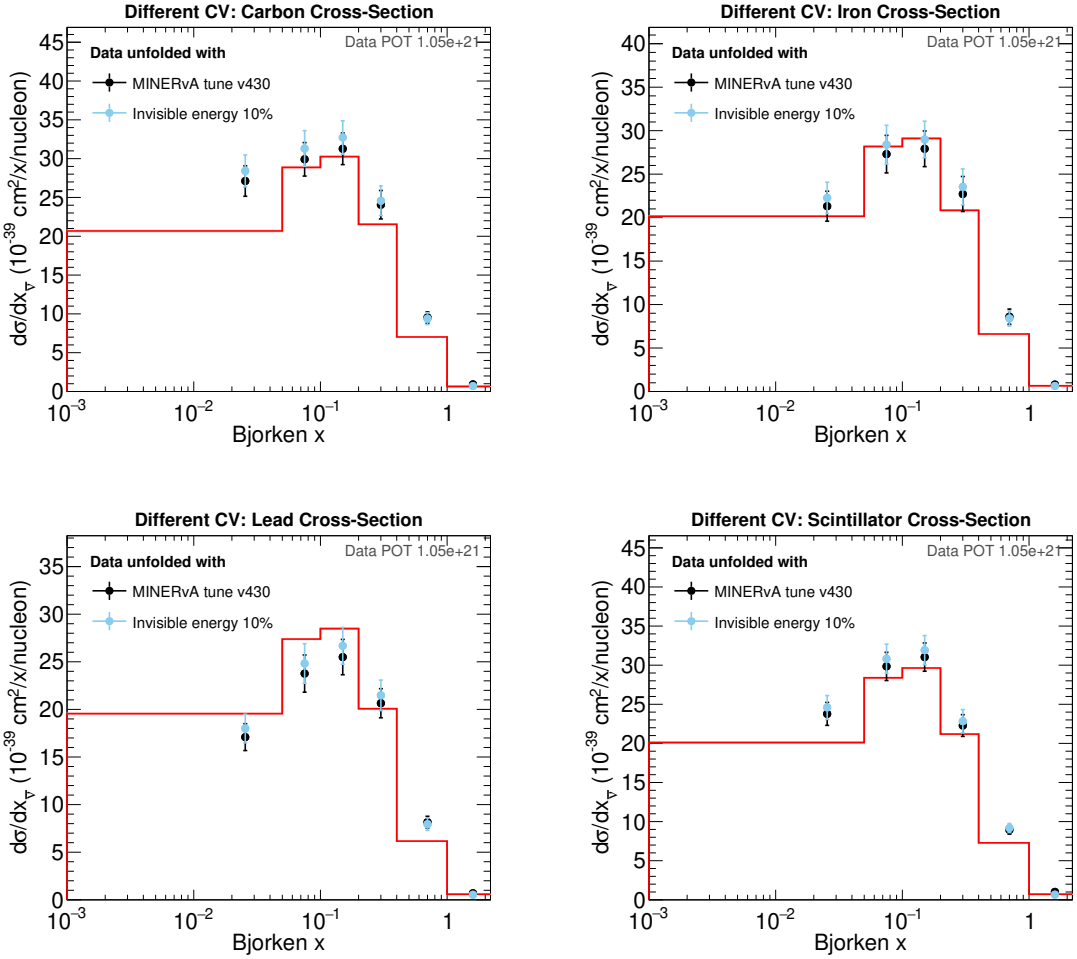

Figure G.5: Comparison of the data cross-section for carbon (top left), iron (top right), lead (bottom left) and scintillator (bottom right) as a function of Bjorken x extracted with the original simulation and 'Invisible energy 10%' central value to investigate model dependence arising from neutron modelling.

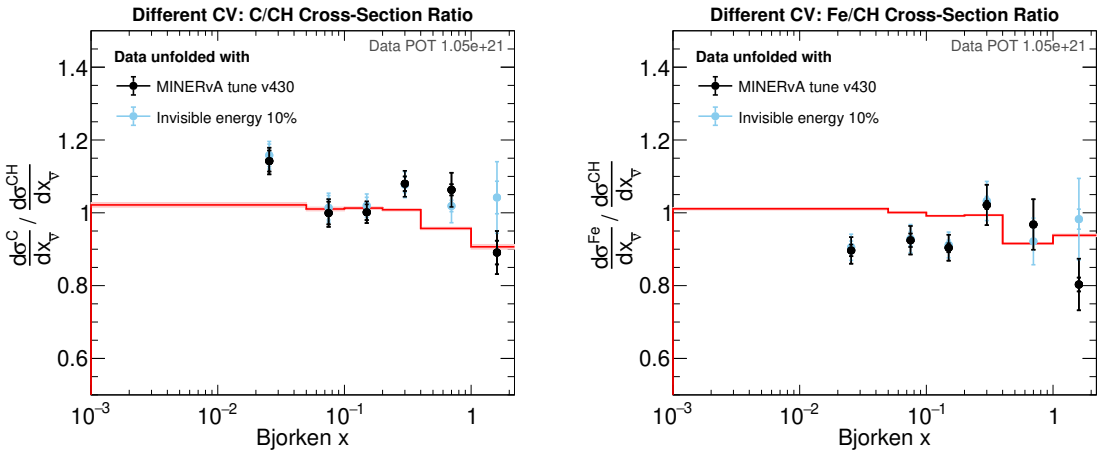

Figure G.6: Comparison of the carbon-to-scintillator (left) and iron-to-scintillator (right) data cross-section ratio as a function of Bjorken x extracted with the original simulation and 'Invisible energy 10%' central value to investigate model dependence arising from neutron modelling, revealing possible bias in the $x > 1$ bin.

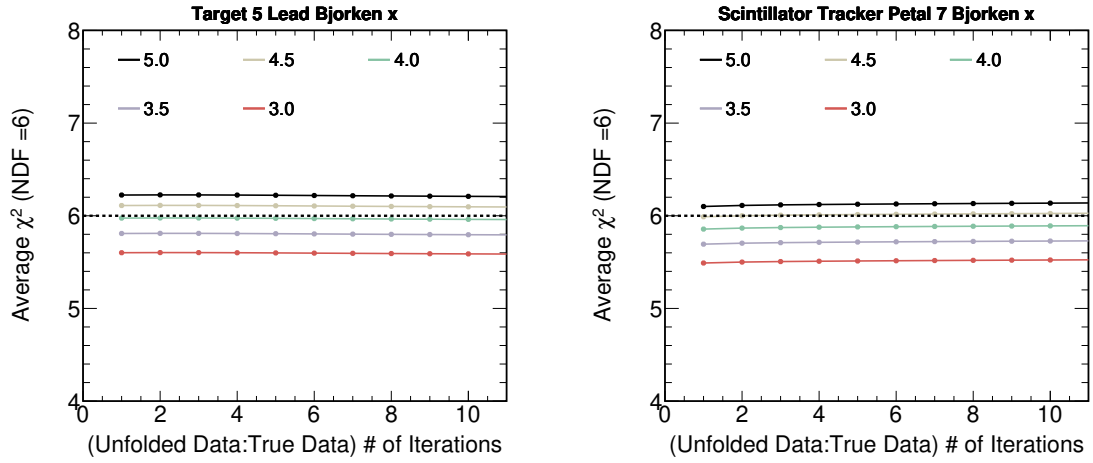

Figure G.7: Correction factor F to the statistical uncertainty of the unfolded sample due to finite size of the simulation in the migration matrix for target 5 lead and the scintillator tracker petal 7 in Bjorken x. The solid lines illustrate that at the selected number of iterations, i.e. 9 iterations, the calculated χ^2 between the unfolded and true simulation converges to the number of degrees of freedom (dashed line) for the F factor 4 and 4.5 for target 5 lead and the scintillator tracker petal 7 respectively.

Appendix H

Unfolded distributions

This appendix presents additional unfolded distributions not shown in Section 7.3, along with their associated fractional uncertainty breakdowns on the data. Specifically, it includes the unfolded distribution plots for target 2 iron and lead, target 3 carbon, iron, and lead, target 4 lead, and target 5 iron in both antimuon p_{T} and Bjorken x.

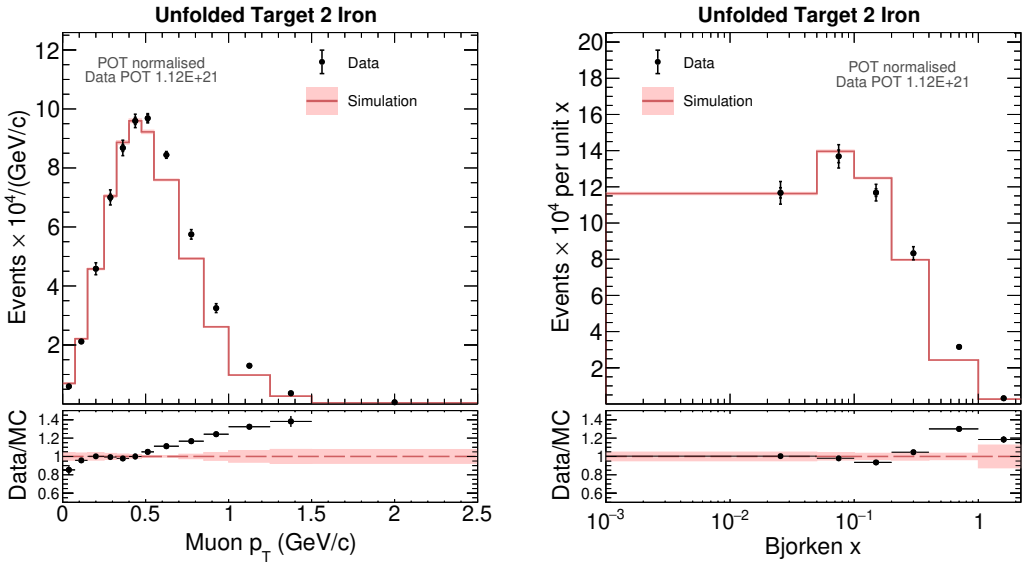

Figure H.1: Unfolded distributions in antimuon p_{T} (left) and Bjorken x (right) for target 2 iron. In the top panel, the pink band on the simulation represents the statistical uncertainty of the simulation. The data points carry both statistical (inner error bar) and systematic (outer error bar, which is the sum of statistical and systematic errors) uncertainties. The bottom panel of each plot displays the data-to-simulation ratio, with the pink band around 1 representing systematic uncertainty on the data, while the black points reflect the statistical uncertainty on the data-to-simulation ratio.

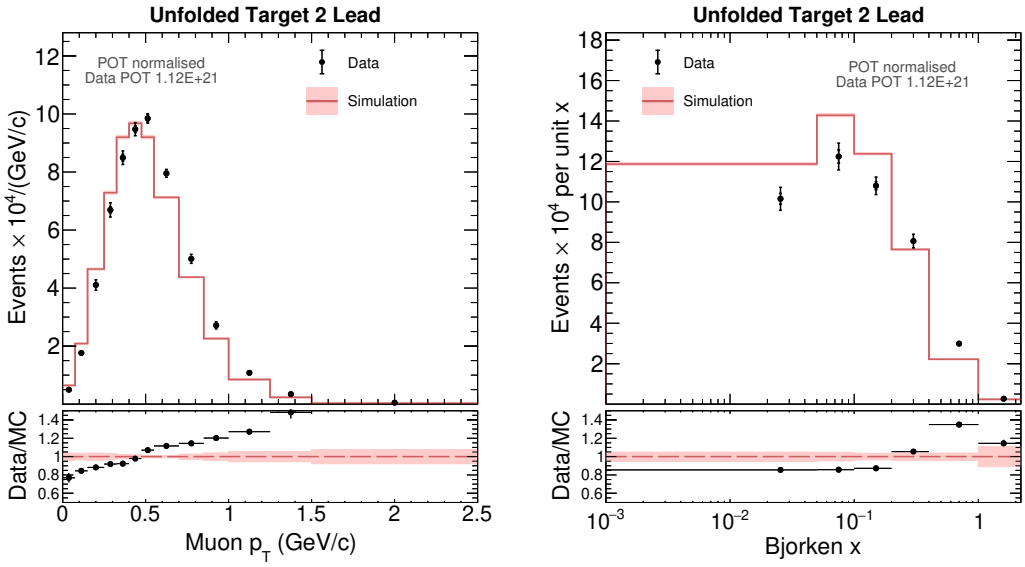

Figure H.2: Unfolded distributions in antimuon p_{T} (left) and Bjorken x (right) for target 2 lead.

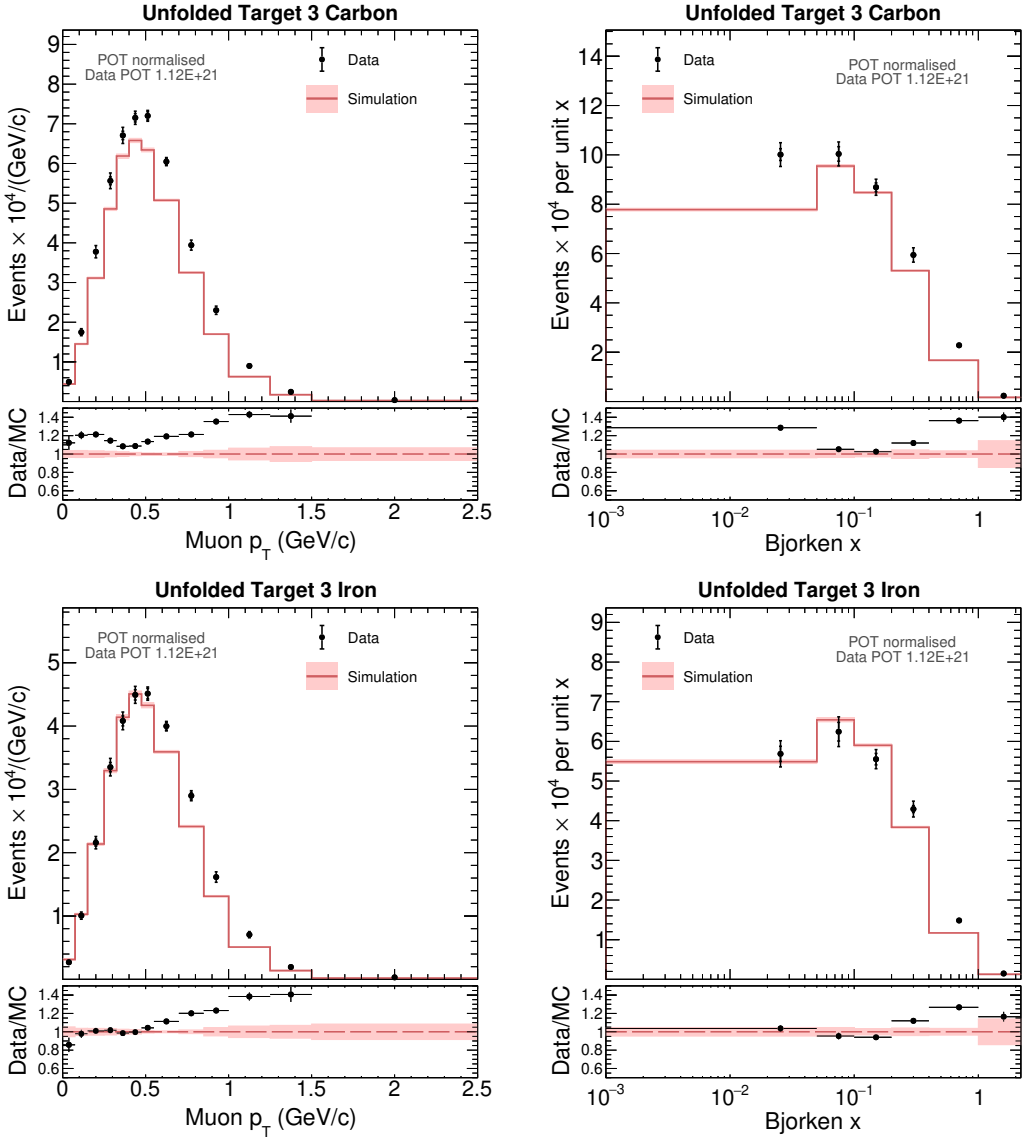

Figure H.3: Unfolded distributions in antimuon p_{T} (left panel) and Bjorken x (right panel) for target 3 carbon (top) and target 3 iron (bottom).

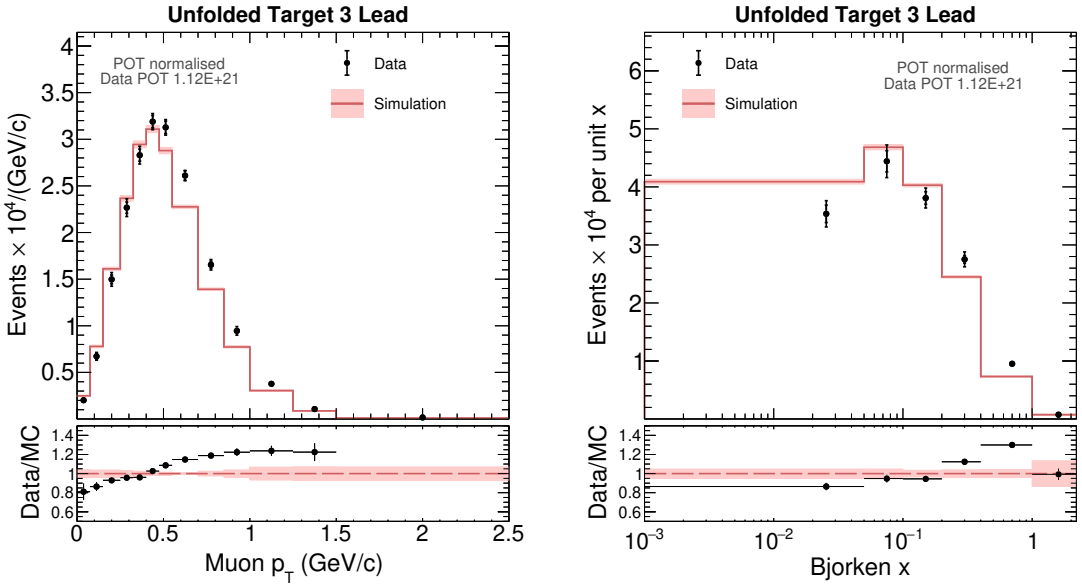

Figure H.4: Unfolded distributions in antimuon p_{T} (left) and Bjorken x (right) for target 3 lead.

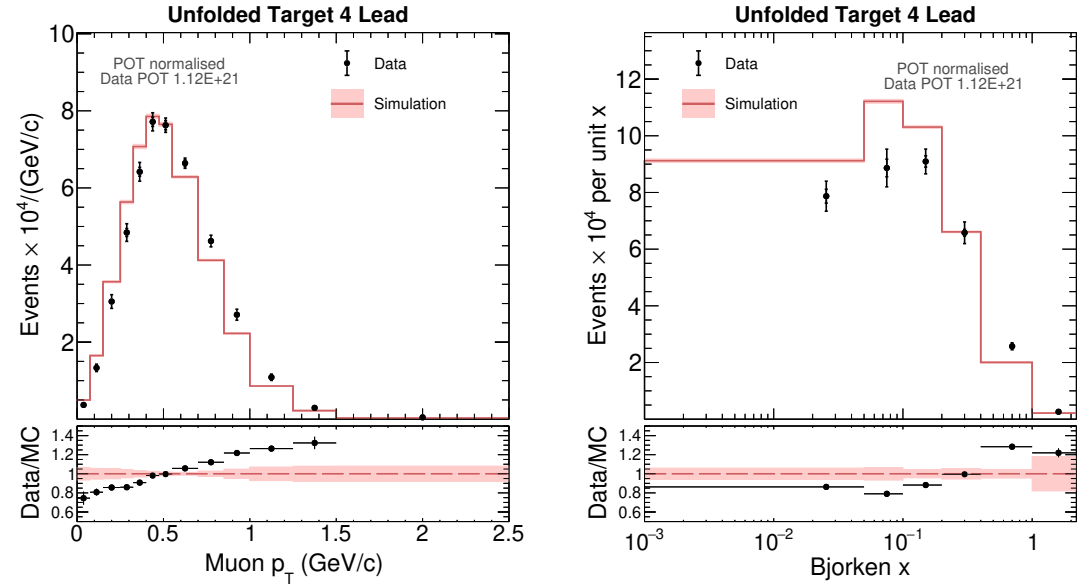

Figure H.5: Unfolded distributions in antimuon p_{T} (left) and Bjorken x (right) for target 4 lead.

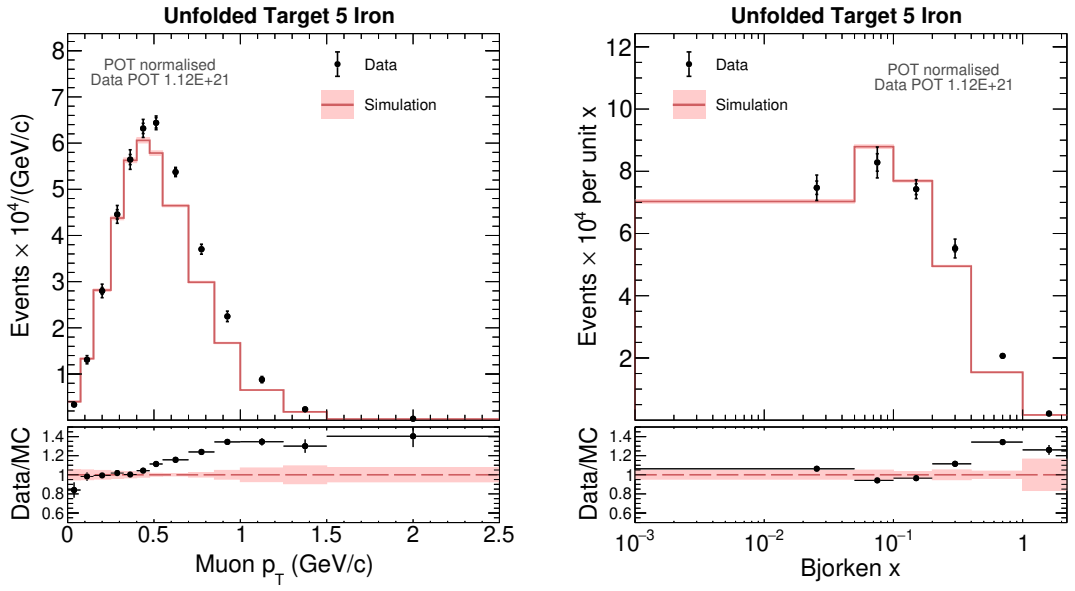

Figure H.6: Unfolded distributions in antimuon p_{T} (left) and Bjorken x (right) for target 5 iron.

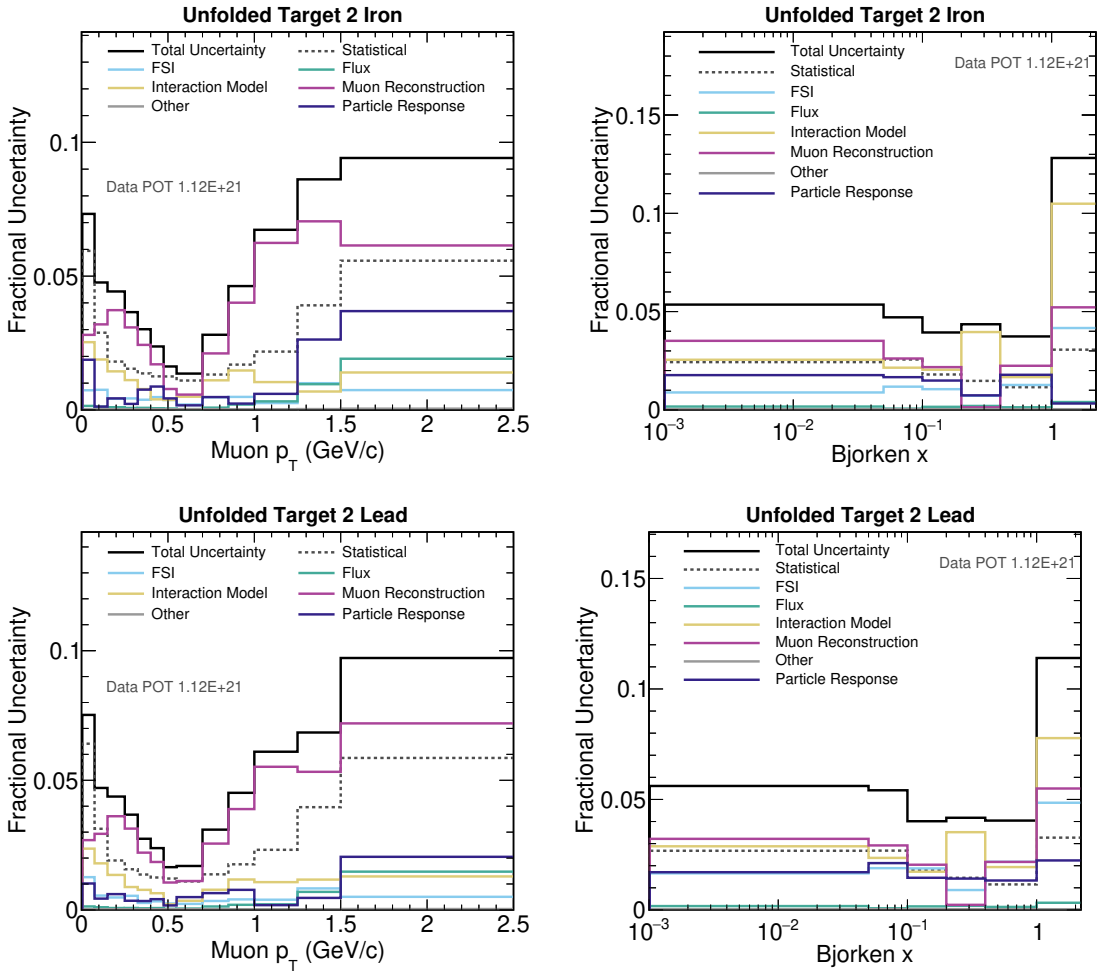

Figure H.7: Fractional uncertainty breakdowns on the unfolded data distributions in both p_{T} (left panel) and Bjorken x (right panel) for target 2 iron (top) and target 2 lead (bottom).

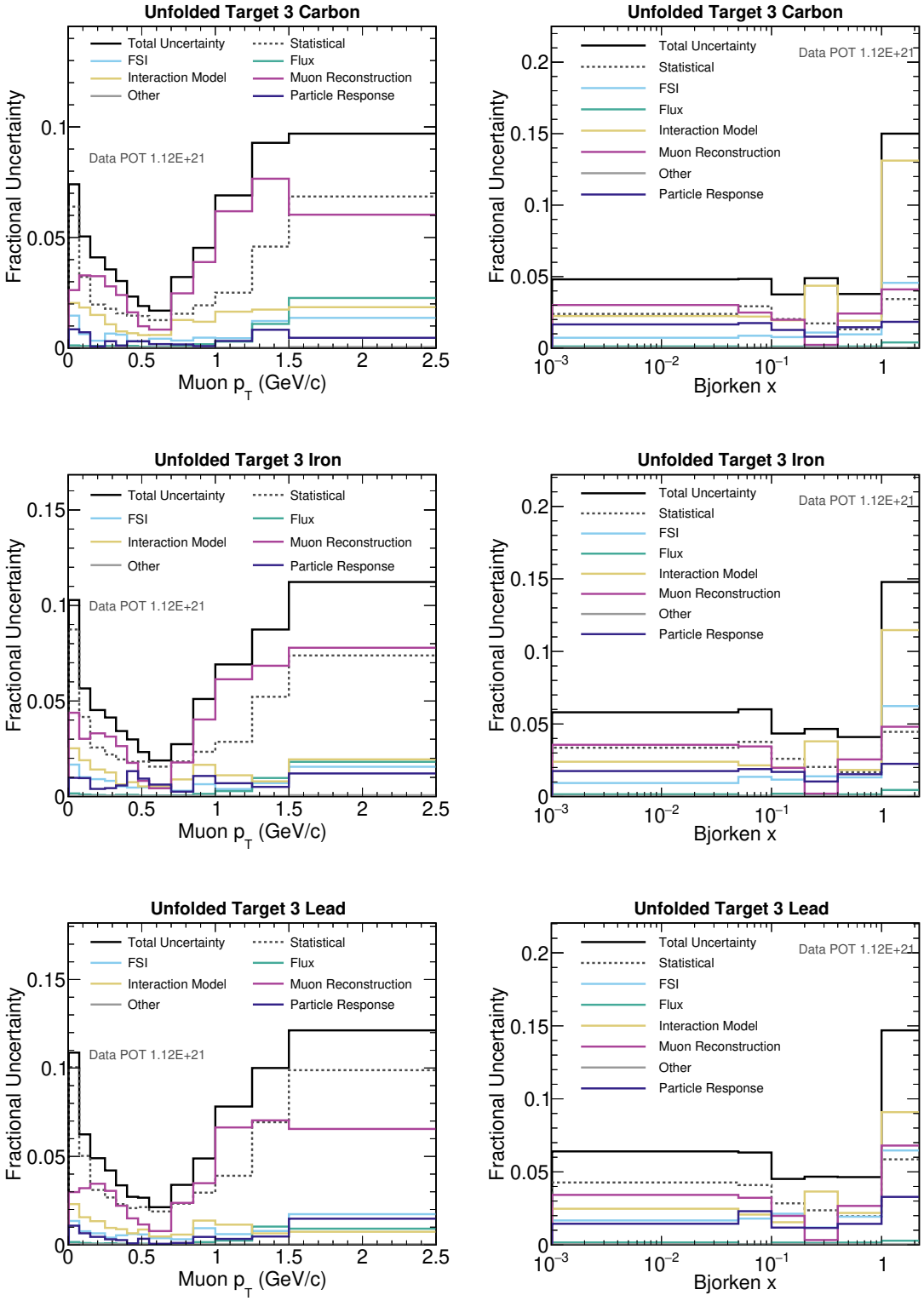

Figure H.8: Fractional uncertainty breakdowns on the unfolded data distributions in both p_{T} (left panel) and Bjorken x (right panel) for target 3 carbon (top), target 3 iron (middle), and target 3 lead (bottom).

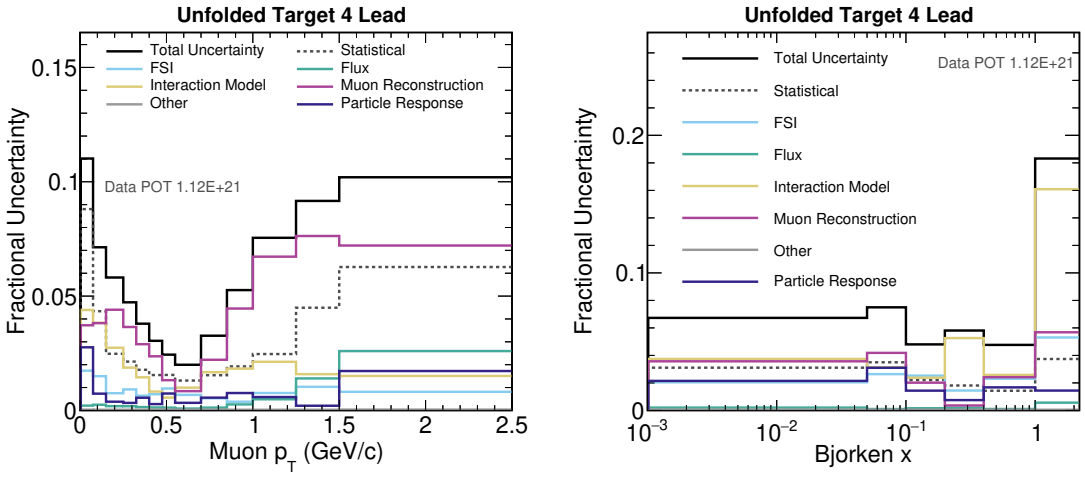

Figure H.9: Fractional uncertainty breakdowns on the unfolded data distributions in both p_{T} (left panel) and Bjorken x (right panel) for target 4 lead.

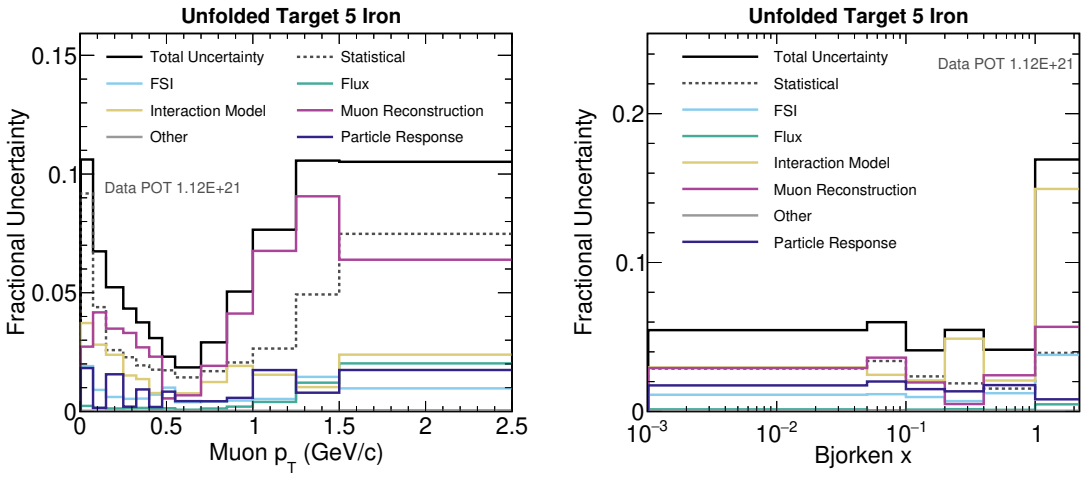

Figure H.10: Fractional uncertainty breakdowns on the unfolded data distributions in both p_{T} (left panel) and Bjorken x (right panel) for target 5 iron.

Appendix I

Efficiency distributions

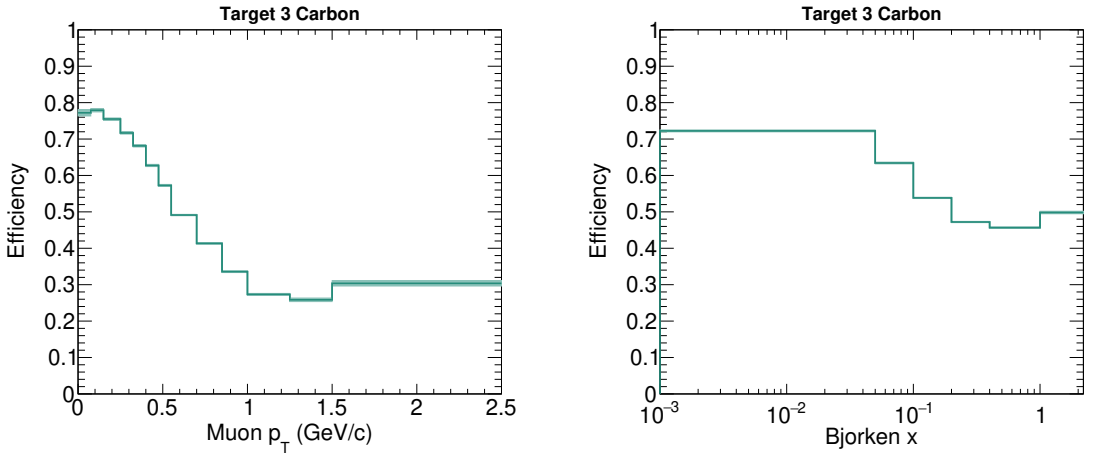

Figure I.1: Efficiency correction distributions for target 3 carbon as a function of p_{T} (left) and Bjorken x (right).

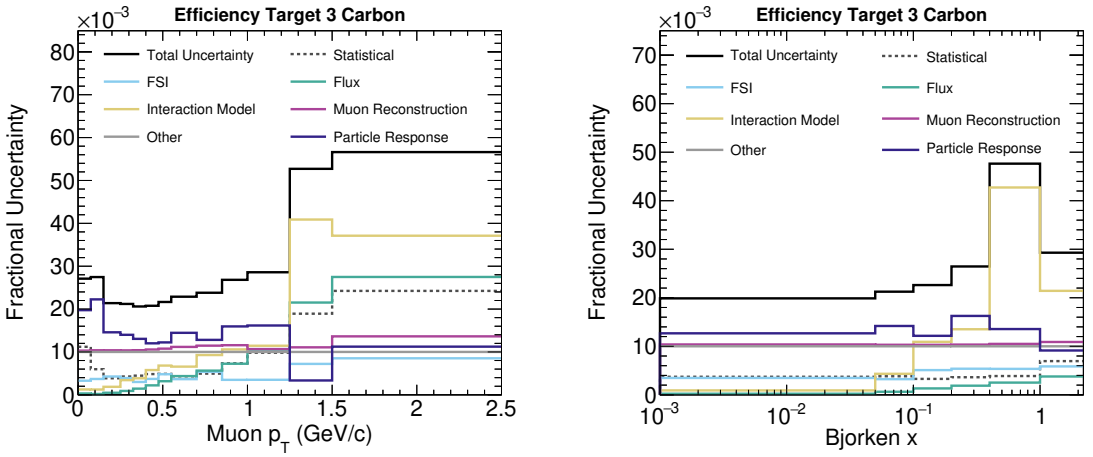

Figure I.2: Fractional uncertainty breakdown for the efficiency correction distributions for target 3 carbon as a function of p_{T} (left) and Bjorken x (right).

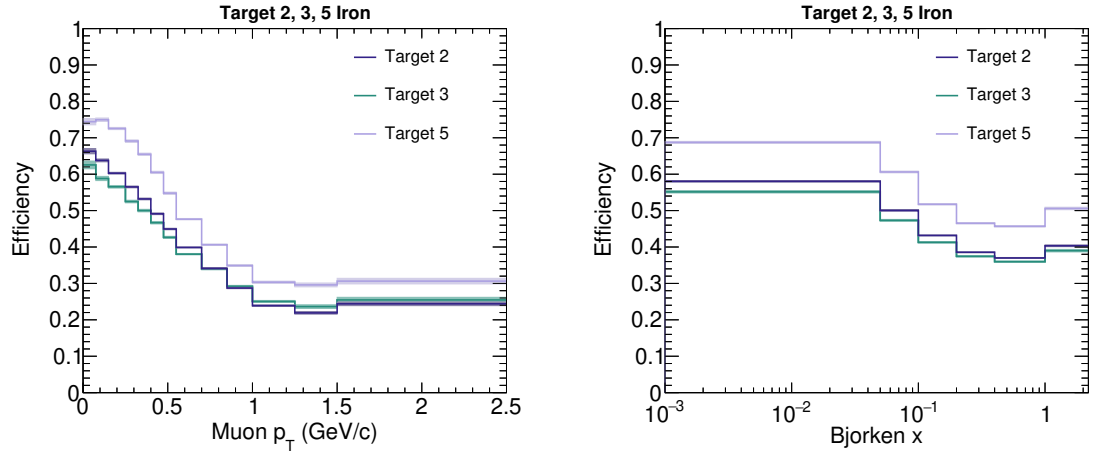

Figure I.3: Efficiency correction distributions for targets 2, 3, and 5 iron as a function of p_{T} (left) and Bjorken x (right).

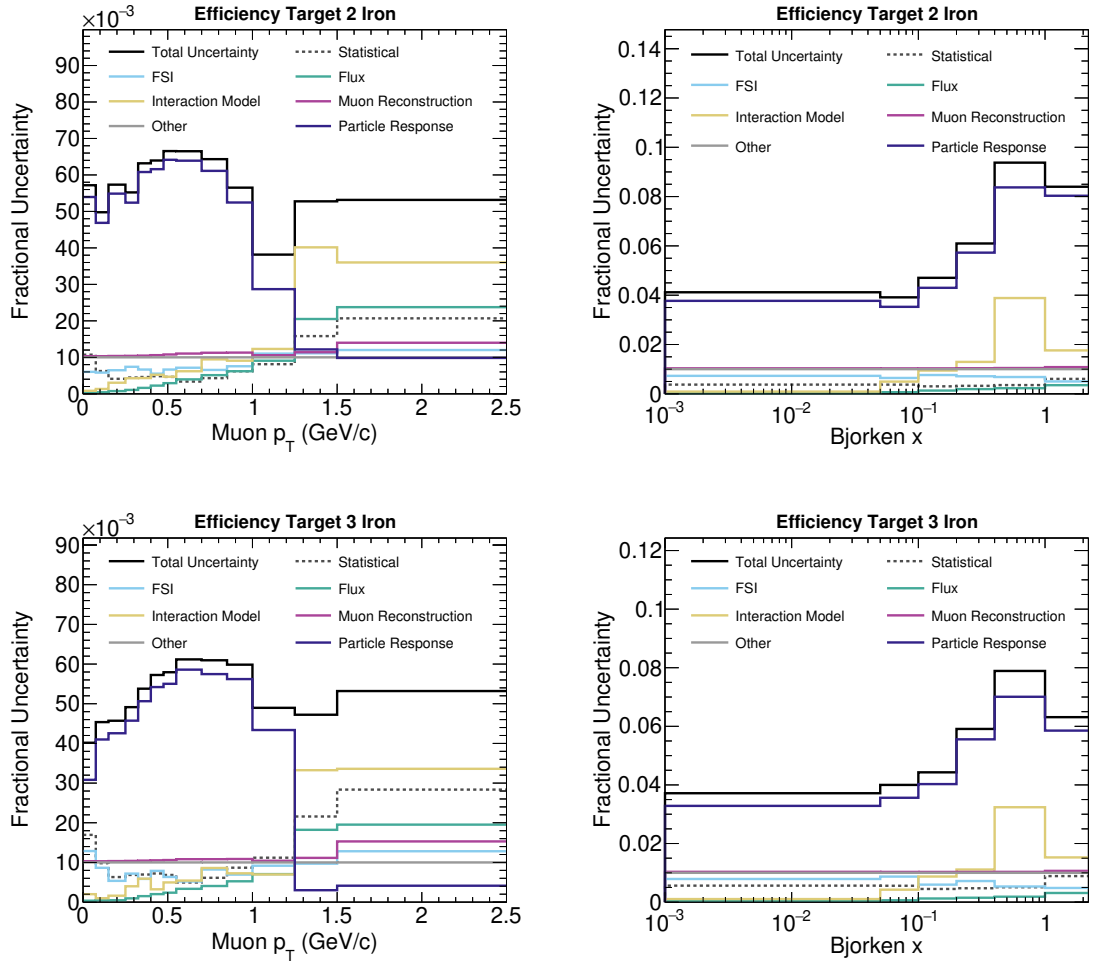

Figure I.4: Fractional uncertainty breakdown for the efficiency correction distributions for targets 2 and 3 iron as a function of p_{T} (left) and Bjorken x (right).

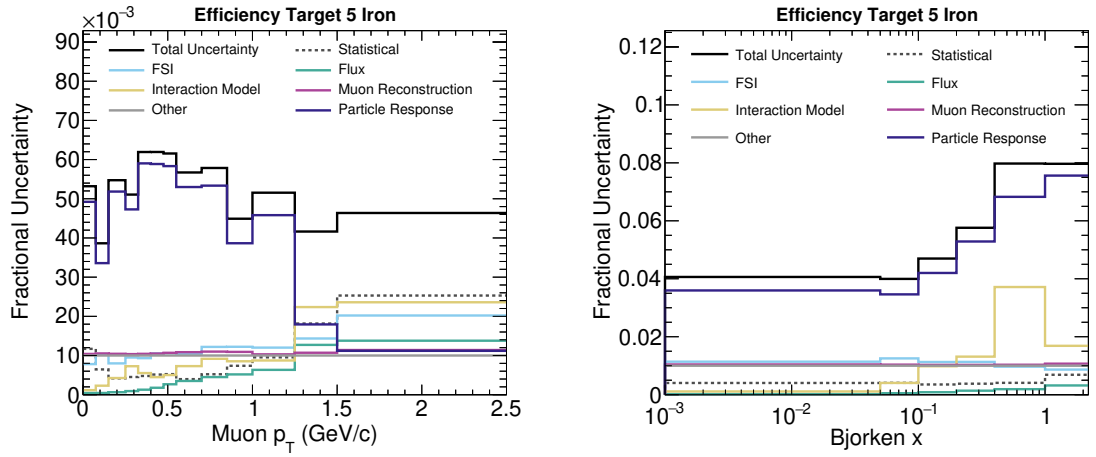

Figure I.5: Fractional uncertainty breakdown for the efficiency correction distributions for target 5 iron as a function of p_{T} (left) and Bjorken x (right).

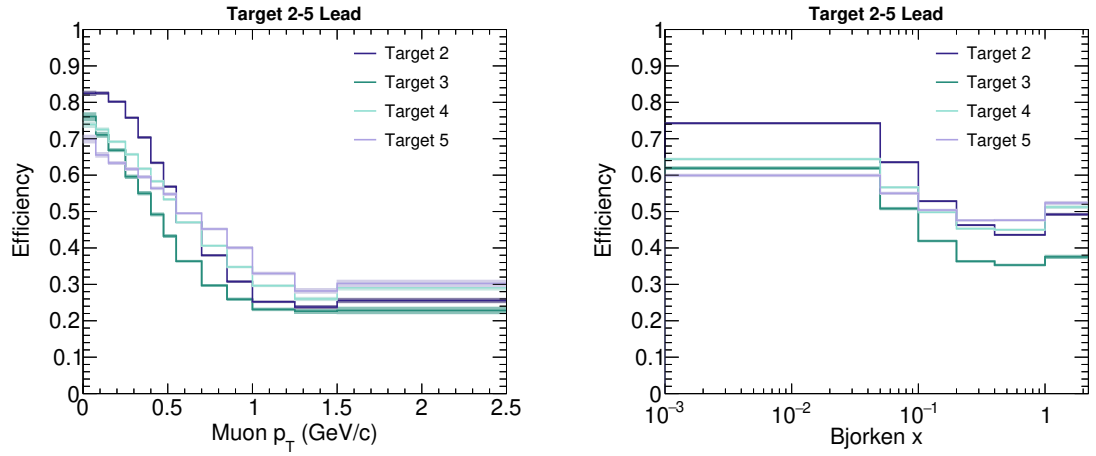

Figure I.6: Efficiency correction distributions for target 2–5 lead as a function of p_{T} (left) and Bjorken x (right).

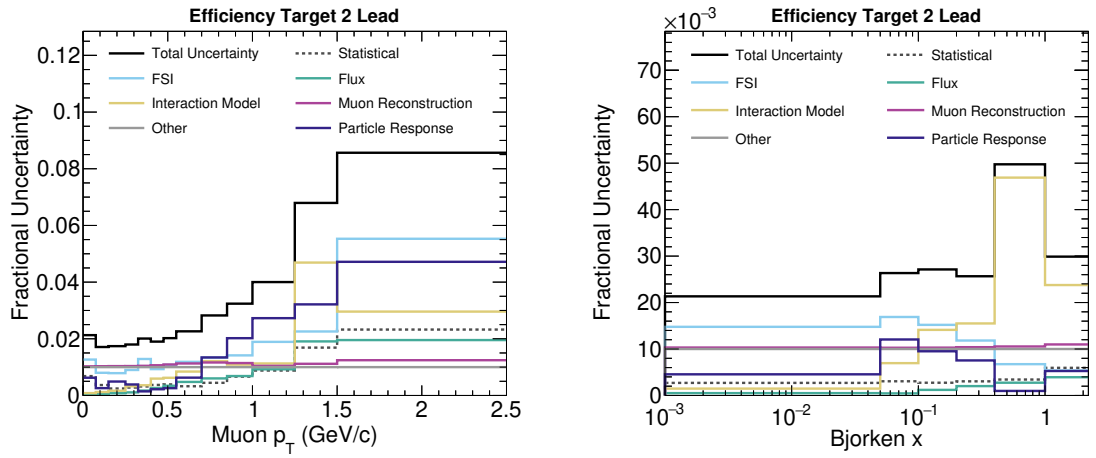

Figure I.7: Fractional uncertainty breakdown for the efficiency correction distributions for target 2 lead as a function of p_{T} (left) and Bjorken x (right).

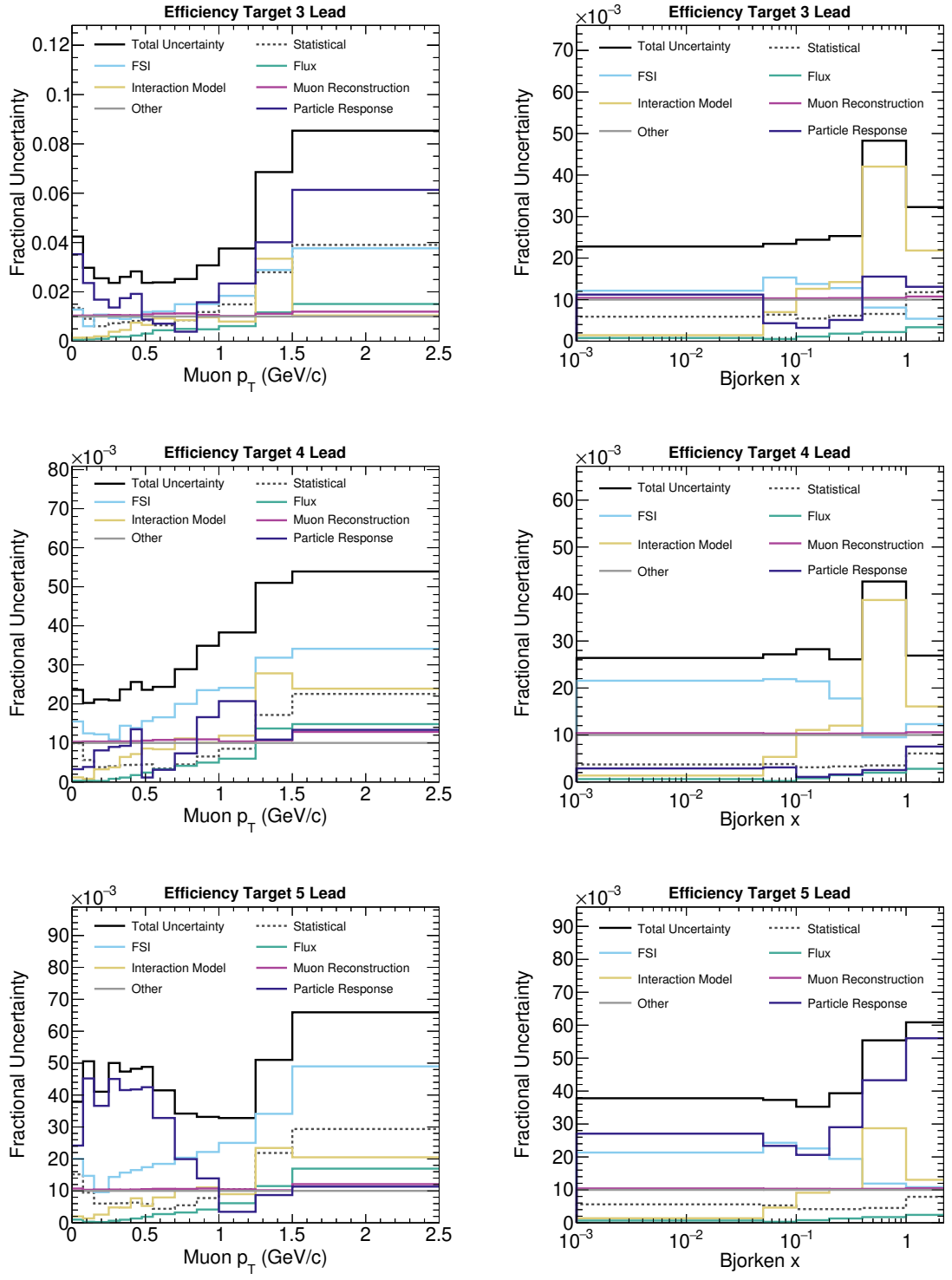

Figure I.8: Fractional uncertainty breakdown for the efficiency correction distributions for targets 3–5 lead as a function of p_{T} (left) and Bjorken x (right).

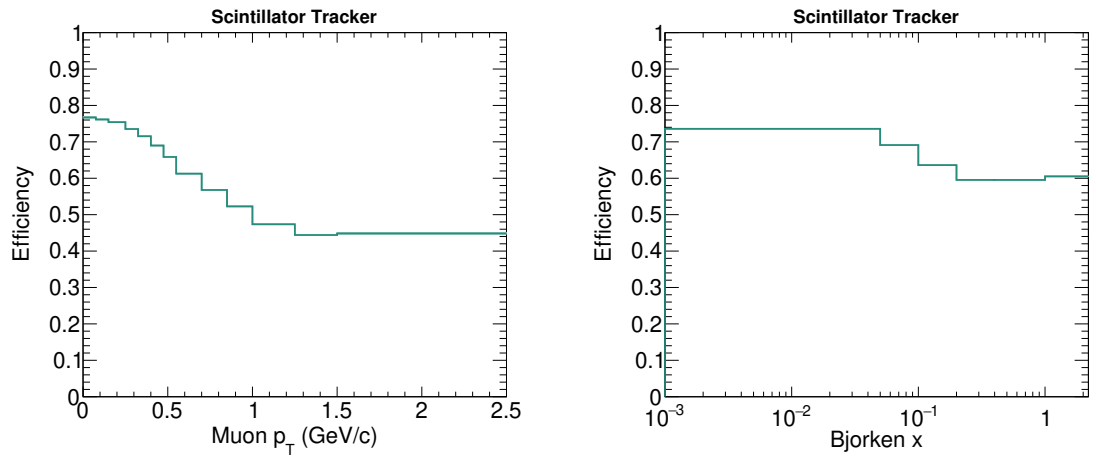

Figure I.9: Efficiency correction distributions for the scintillator tracker as a function of p_{T} (left) and Bjorken x (right).

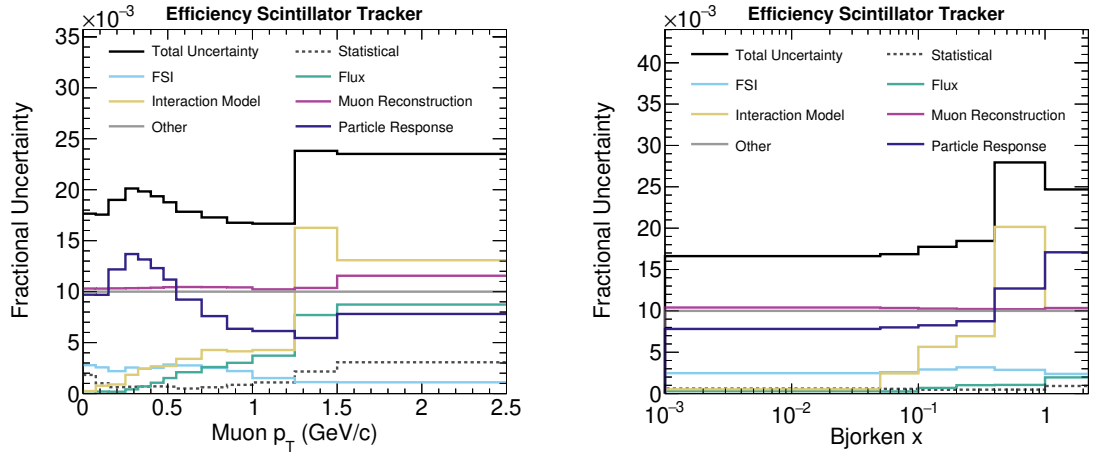

Figure I.10: Fractional uncertainty breakdown for the efficiency correction distributions for the scintillator tracker as a function of p_{T} (left) and Bjorken x (right).

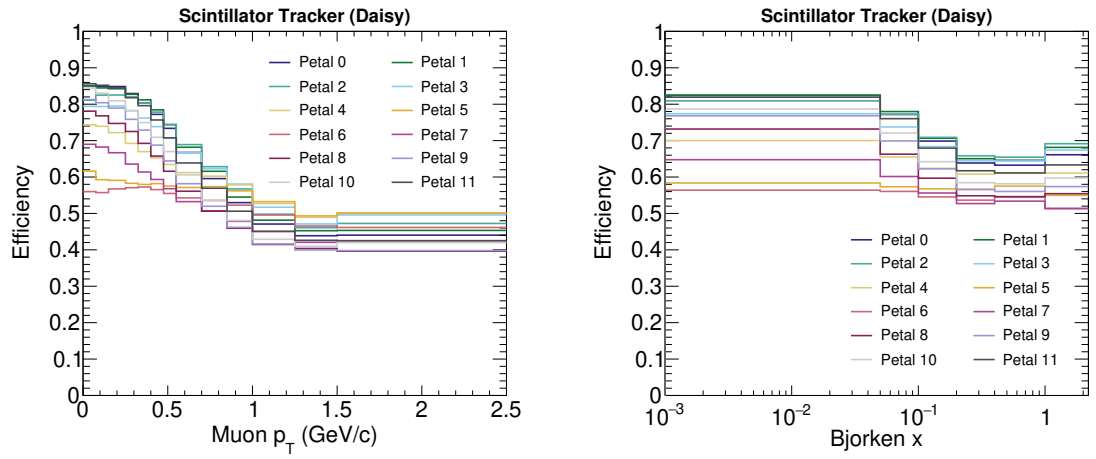

Figure I.11: Efficiency correction distributions for the scintillator tracker in 'daisy petals' as a function of p_{T} (left) and Bjorken x (right).

Appendix J

Efficiency-corrected distributions

This appendix presents the efficiency-corrected distributions per target and material combination not shown in Section 7.4, along with their associated fractional uncertainty breakdowns on the data. Furthermore, the efficiency-corrected distributions in p_{T} and Bjorken x combining targets 2, 3, and 5 iron are also included with their corresponding fractional uncertainties on the combined data distributions.

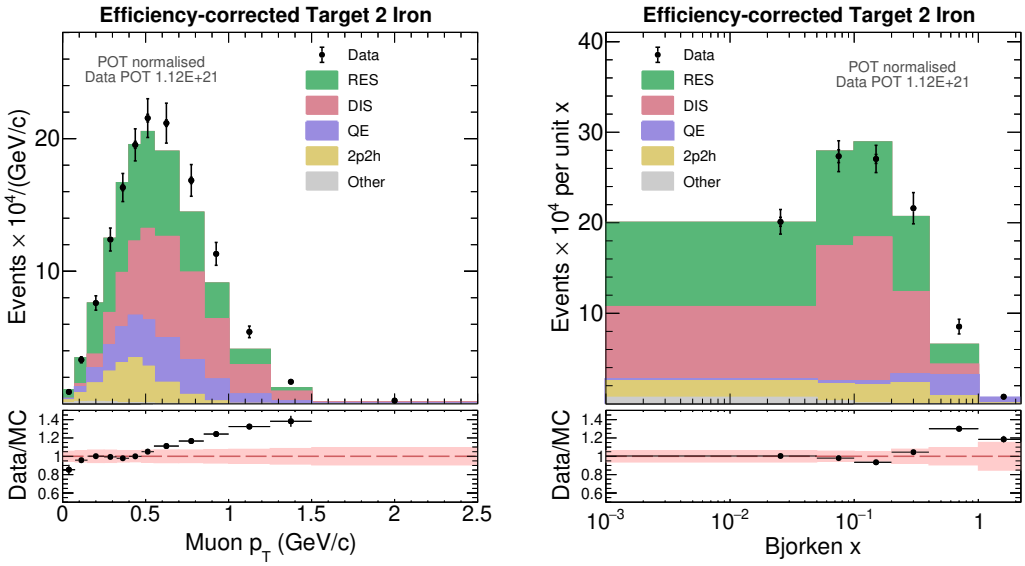

Figure J.1: Efficiency-corrected distributions in antimuon p_{T} (left) and Bjorken x (right) for target 2 iron with the simulation broken down into the various interaction channels stacked in the descending order of their contribution. In the top panel, the pink band on the simulation represents the statistical uncertainty of the simulation. The data points carry both statistical (inner error bar) and systematic (outer error bar, which is the sum of statistical and systematic errors) uncertainties. The bottom panel of each plot displays the data-to-simulation ratio, with the pink band around 1 representing systematic uncertainty on the data, while the black points reflect the statistical uncertainty on the data-to-simulation ratio.

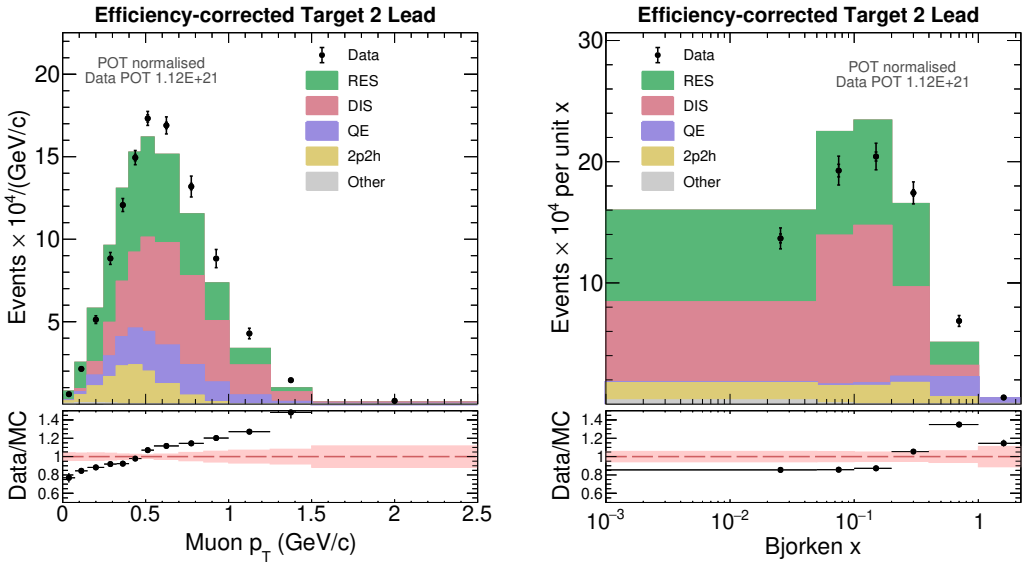

Figure J.2: Efficiency-corrected distributions in antimuon p_{T} (left) and Bjorken x (right) for target 2 lead.

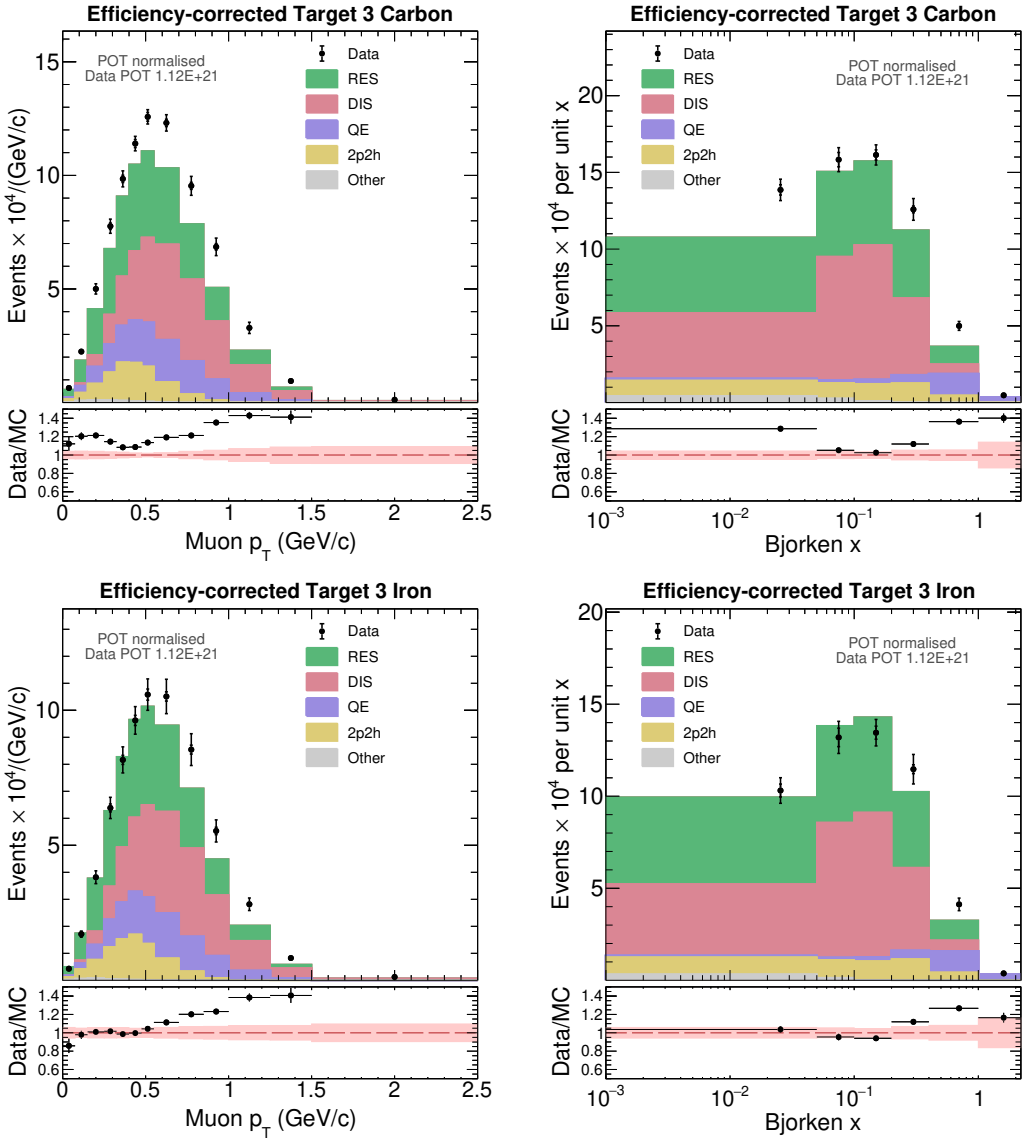

Figure J.3: Efficiency-corrected distributions in antimuon p_{T} (left panel) and Bjorken x (right panel) for target 3 carbon (top) and target 3 iron (bottom).

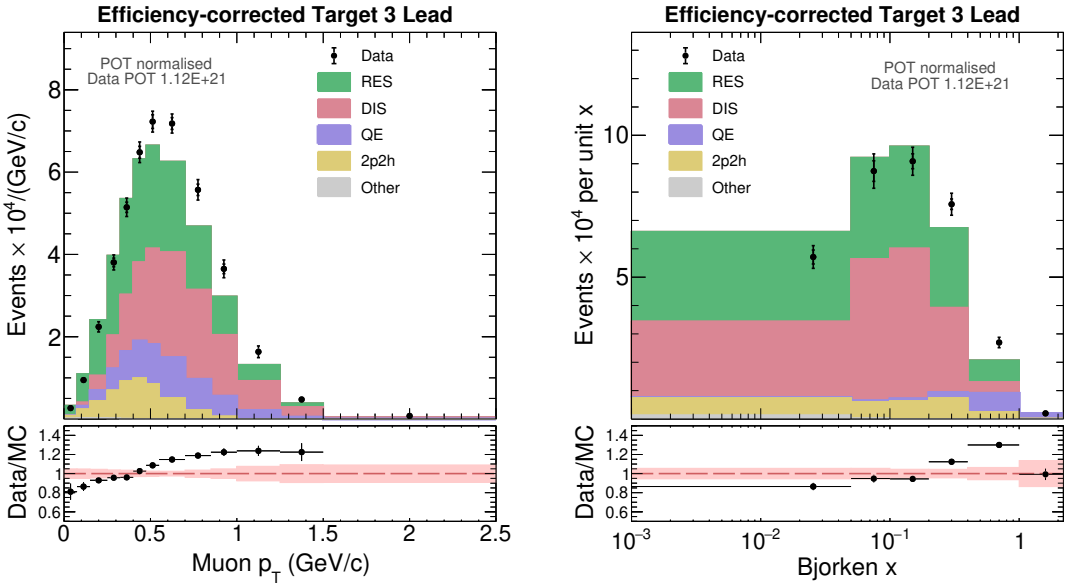

Figure J.4: Efficiency-corrected distributions in antimuon p_{T} (left) and Bjorken x (right) for target 3 lead.

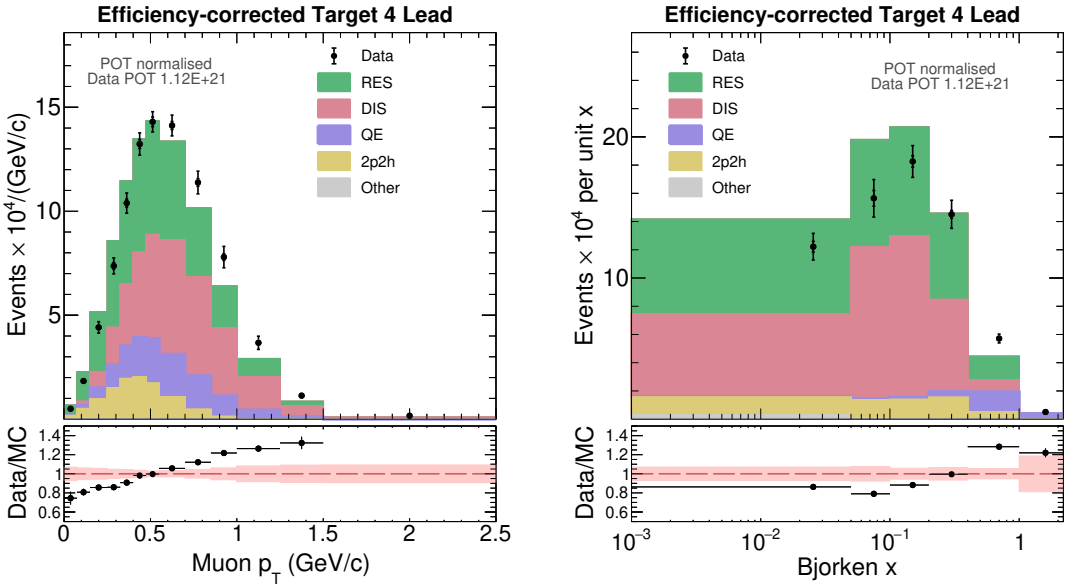

Figure J.5: Efficiency-corrected distributions in antimuon p_{T} (left) and Bjorken x (right) for target 4 lead.

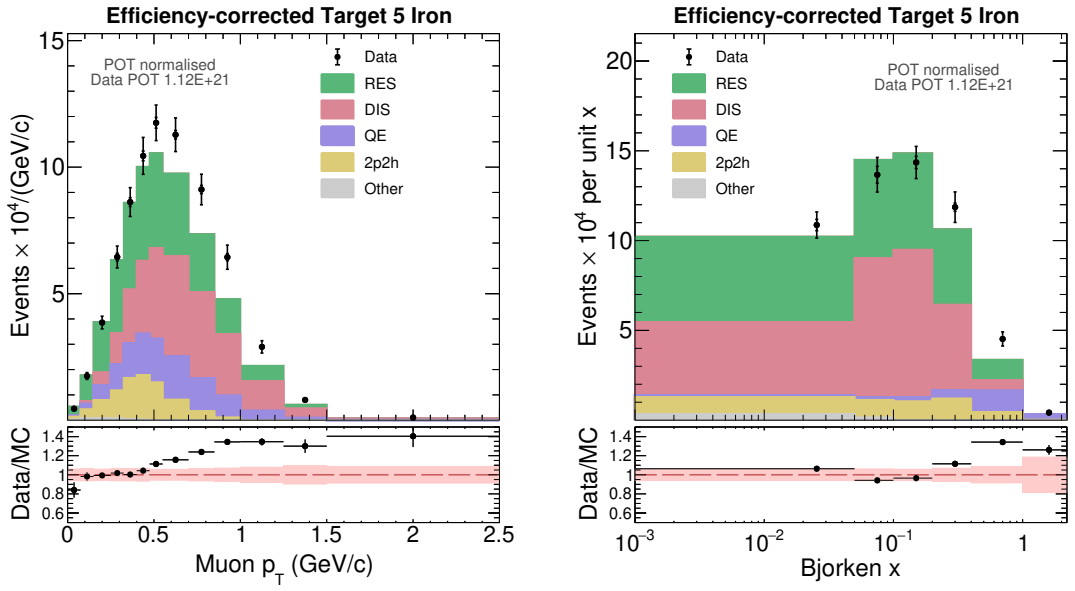

Figure J.6: Efficiency-corrected distributions in antimuon p_{T} (left) and Bjorken x (right) for target 5 iron.

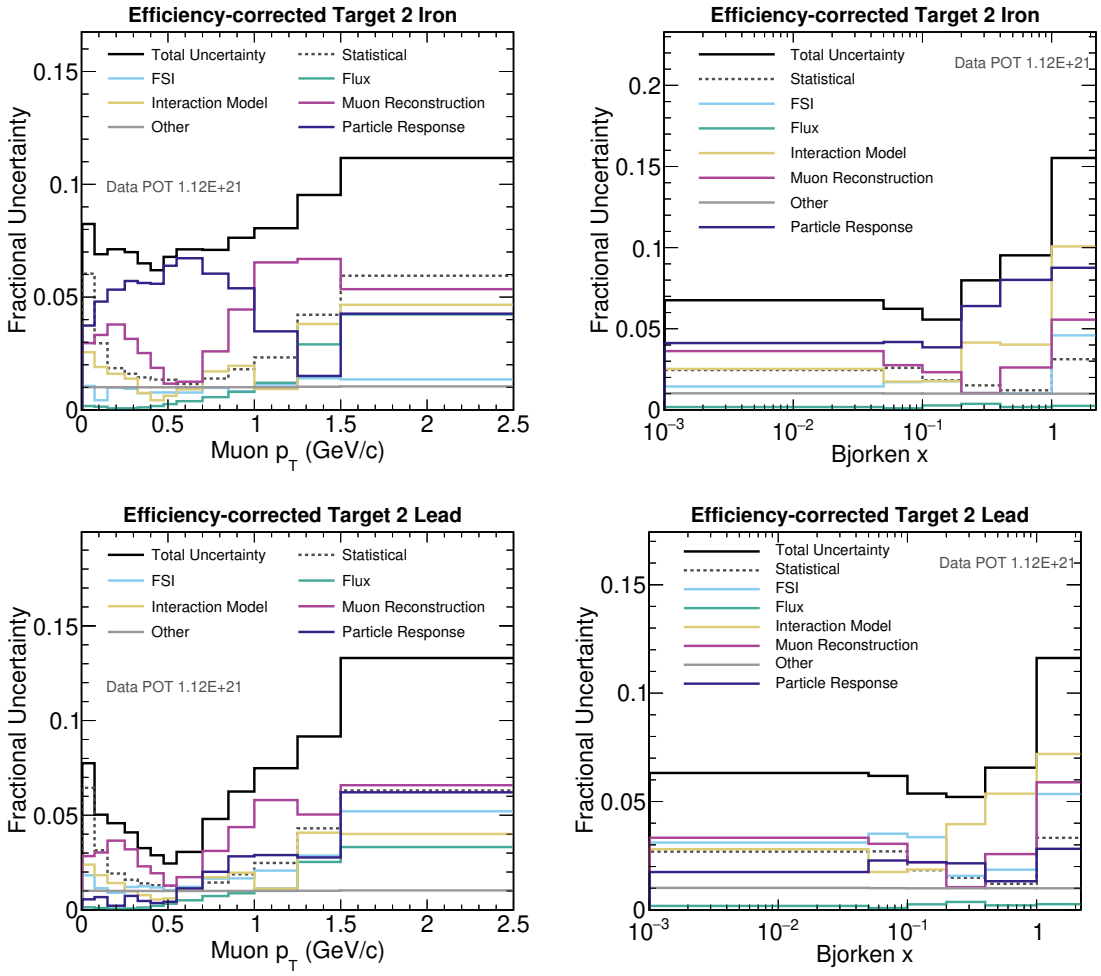

Figure J.7: Fractional uncertainty breakdowns on the efficiency-corrected data distributions in both p_{T} (left panel) and Bjorken x (right panel) for target 2 iron (top) and target 2 lead (bottom).

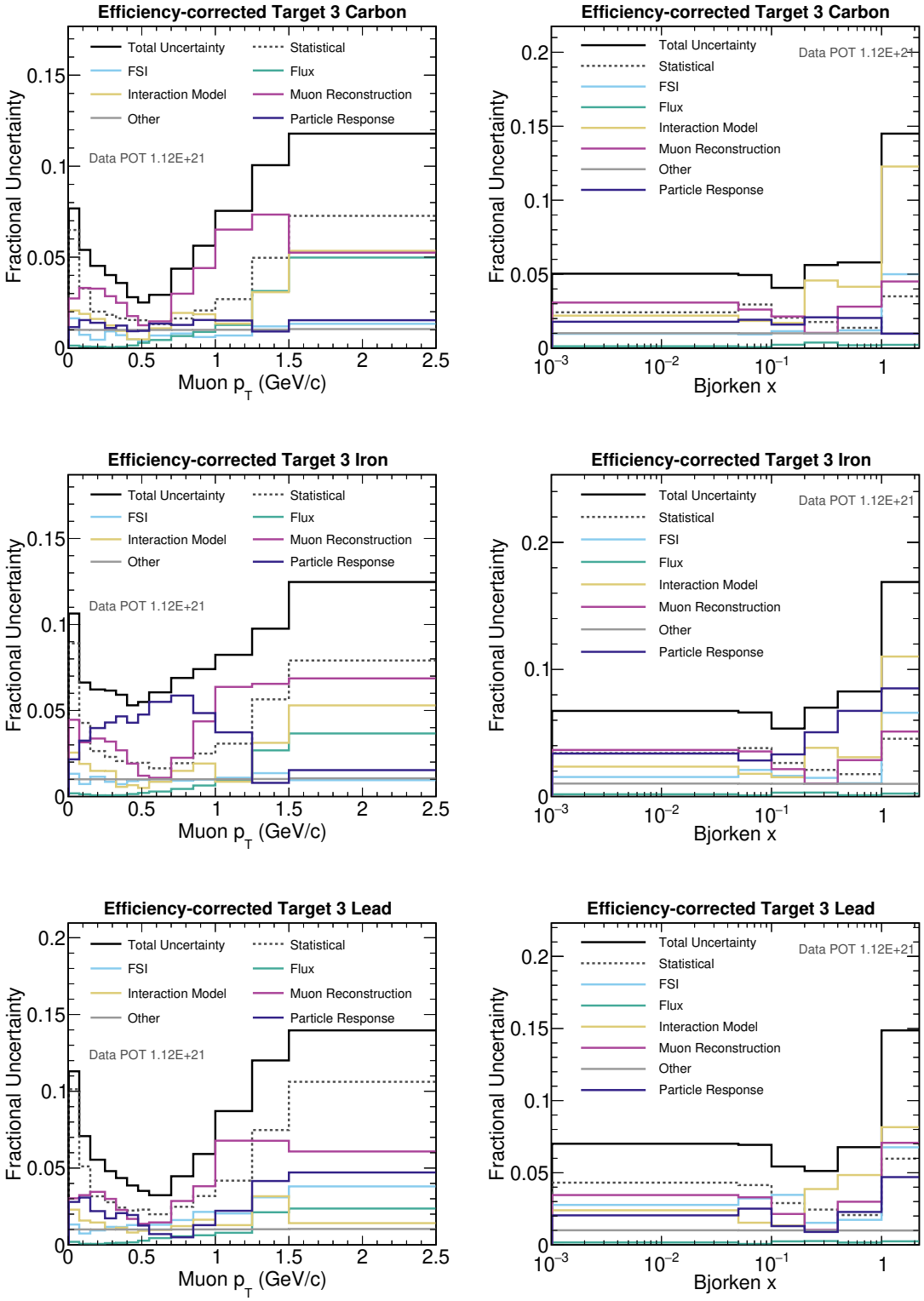

Figure J.8: Fractional uncertainty breakdowns on the efficiency-corrected data distributions in both p_{T} (left panel) and Bjorken x (right panel) for target 3 carbon (top), target 3 iron (middle), and target 3 lead (bottom).

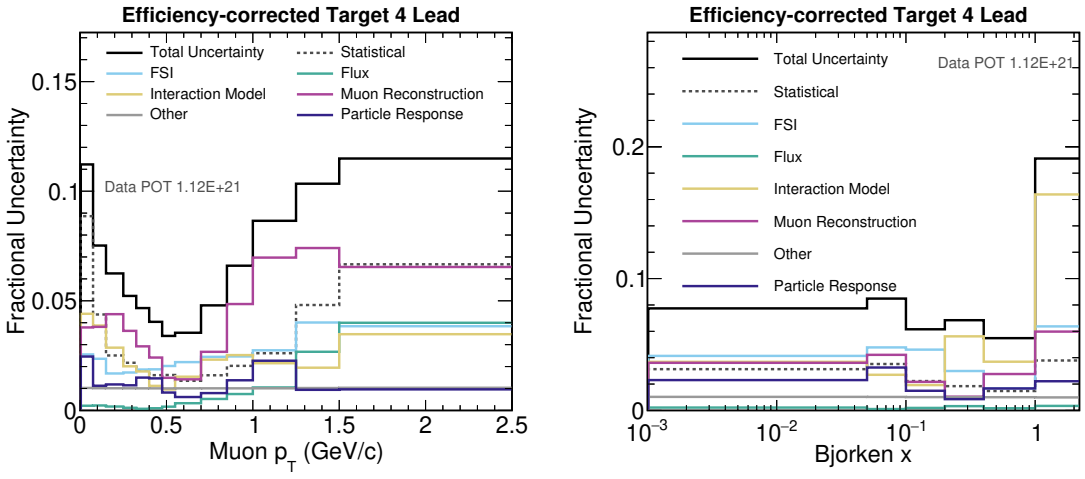

Figure J.9: Fractional uncertainty breakdowns on the efficiency-corrected data distributions in both p_{T} (left panel) and Bjorken x (right panel) for target 4 lead.

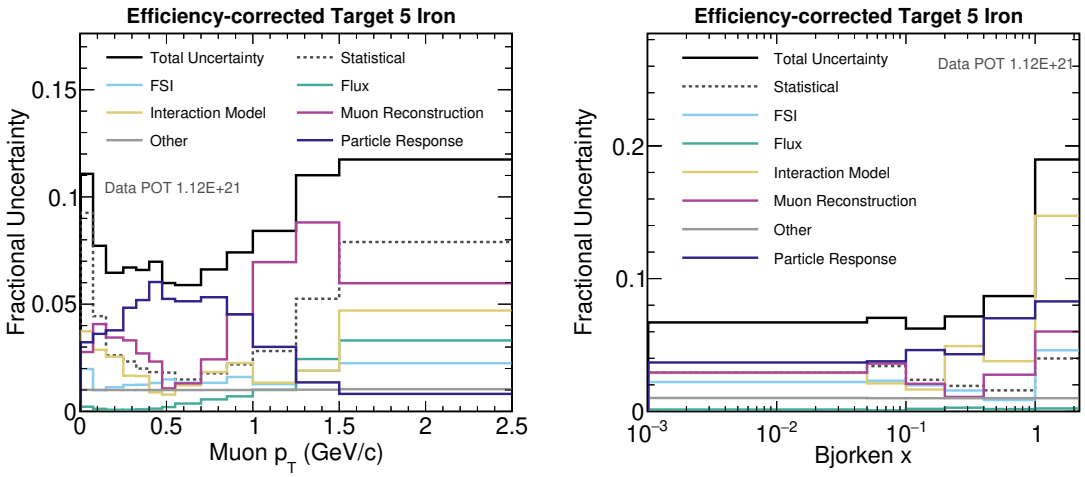

Figure J.10: Fractional uncertainty breakdowns on the efficiency-corrected data distributions in both p_{T} (left panel) and Bjorken x (right panel) for target 5 iron.

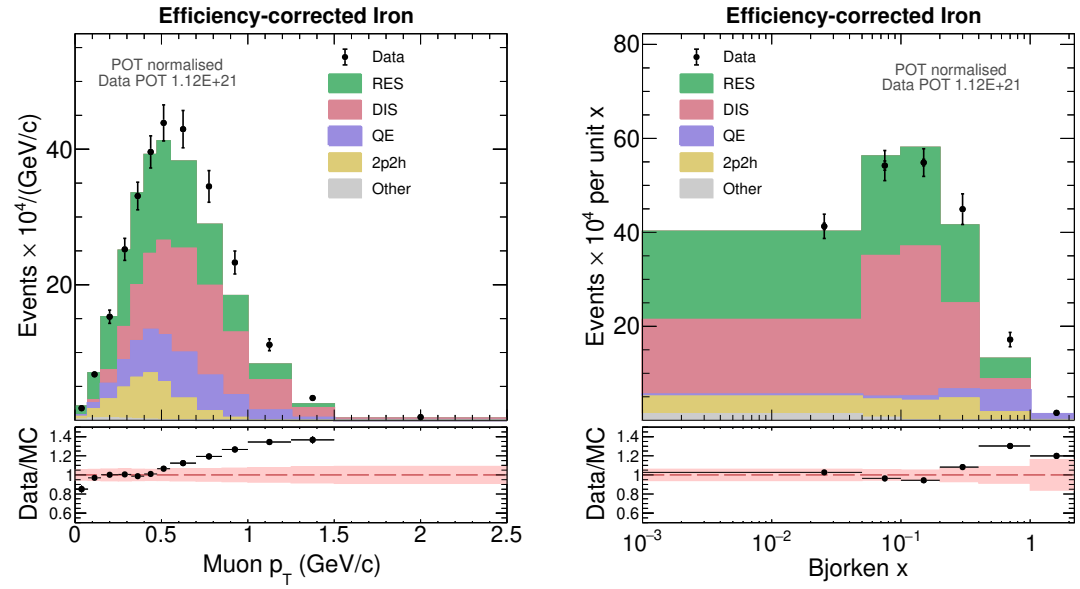

Figure J.11: Efficiency-corrected distributions in antimuon p_{T} (left) and Bjorken x (right) for combined iron, i.e. combined target 2, 3, and 5 iron.

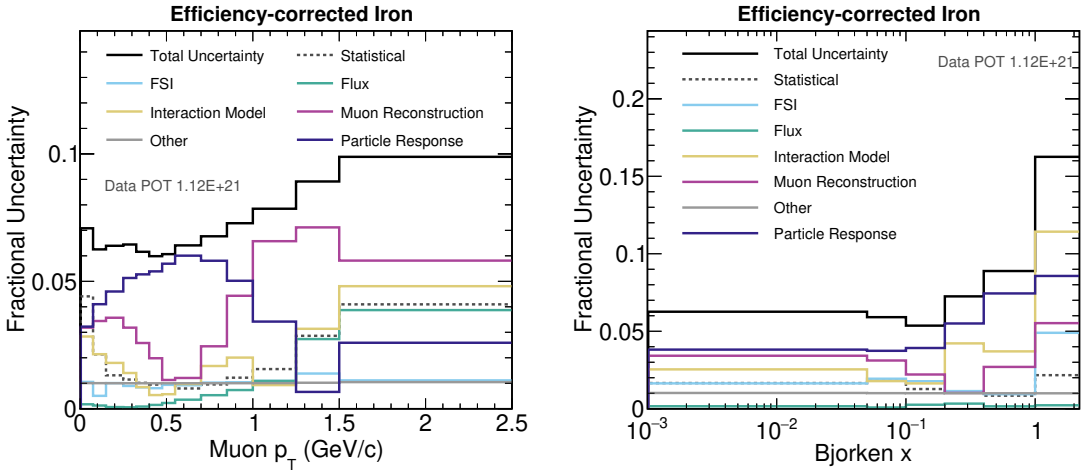

Figure J.12: Fractional uncertainty breakdowns on the efficiency-corrected data distributions in both p_{T} (left) and Bjorken x (right) for combined iron, i.e. combined target 2, 3, and 5 iron.

Appendix K

Fractional systematic uncertainties

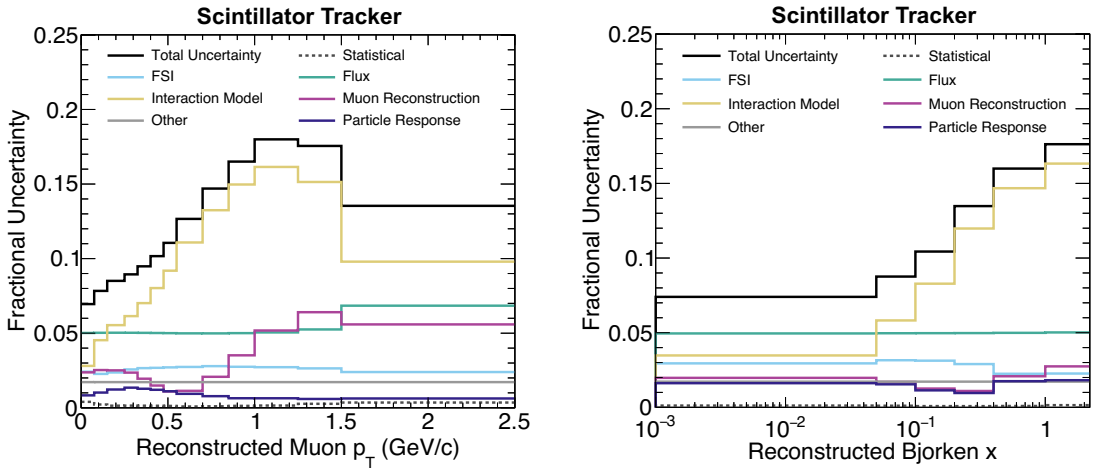

Figure K.1: Fractional uncertainty breakdown for the simulated event rate in both p_{T} (left) and Bjorken x (right) in the scintillator tracker.

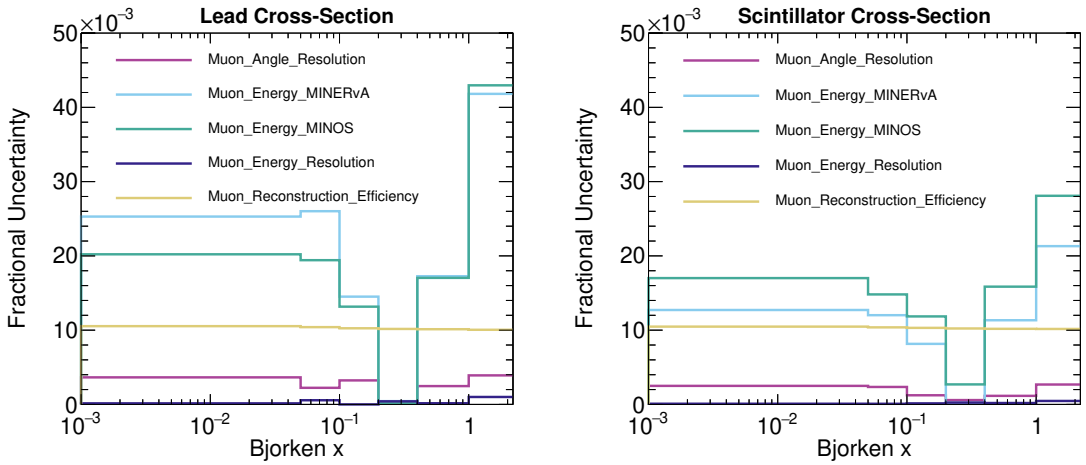

Figure K.2: Breakdown of various sources of uncertainty in the 'Muon Reconstruction' error band in the lead (left) and scintillator (right) differential cross-section in data in Bjorken x.

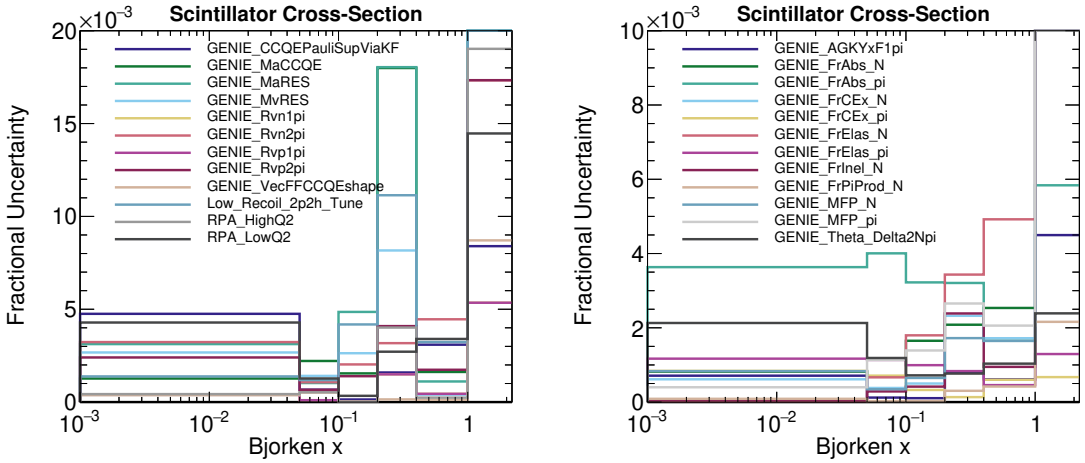

Figure K.3: Close-up of the breakdowns of various sources of uncertainty in the 'Interaction Model' (left) and the 'FSI' error band in the scintillator differential cross-section in data in Bjorken x.

Appendix L

MINERvA tune comparisons

This appendix presents the measured cross-section and cross-section ratio results compared to the various MINERvA tunes applied to the baseline GENIE 2.12.6 [42, 43]. These comparisons facilitate a broader understanding of this measurement in the context of other MINERvA results. The underlying simulation prediction corresponds to the MINERvA tune v4.3.0. In the comparisons, the baseline GENIE 2.12.6 is considered in addition to the so-called v1, v2 and v4 tunes based on different MINERvA results or reanalyses of other data. The characteristics of each tune are briefly reviewed below:

- **GENIE 2.12.6**: baseline GENIE prediction
- **MINERvA tune v1**: GENIE 2.12.6 + Valencia RPA suppression of the quasi-elastic interactions [104,197,198], enhanced 2p2h [111,113,197,199,200], and reduced non-resonant pion production [201]
- **MINERvA tune v2**: v1 + low Q^2 suppression based on MINERvA's low-energy pion production data and older bubble chamber data [247]
- **MINERvA tune v4**: v1 + full bubble chamber fit changing M_A^{RES} and charged-current resonant normalisation parameter [201]
- **MINERvA tune v4.3.0**: v4 + low Q^2 suppression based on MINERvA's medium energy charged-current $1\pi^+$ analysis [191]

Chapter 5 provides a detailed description of the specific modifications made to the baseline GENIE predictions to create the MINERvA tune v4.3.0.

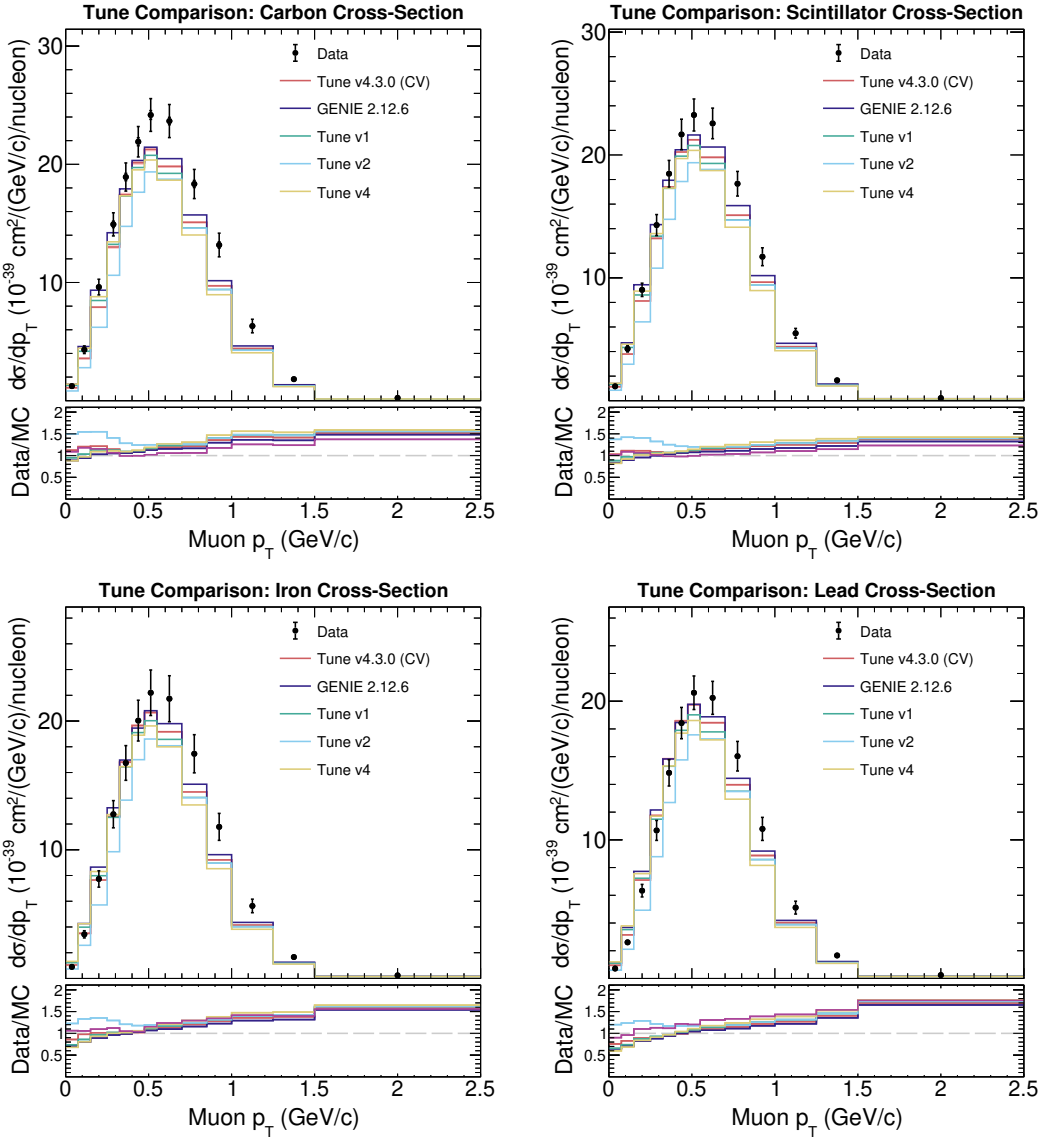

Figure L.1: Measured carbon, scintillator, iron, and lead (from left to right, top to bottom) cross-section as a function of antimuon p_{T} compared to the predictions from different MINERvA tunes. The inner error bar on the data indicates the statistical error while the outer error bar corresponds to the total, i.e. statistical + systematic, error.

Cross-section	MINERvA tune χ^2/ndf for p_{T} (ndf = 13)				
	CV	GENIE 2.12.6	v1	v2	v4
Carbon	2.64	2.12	2.12	4.88	2.93
Iron	3.04	9.30	7.06	4.81	11.48
Lead	6.22	18.20	15.72	2.62	24.86
Scintillator	10.35	42.07	24.89	39.29	51.82

Table L.1: Fully correlated χ^2/ndf calculated according to Equation 9.1 to assess the agreement between the measured data and the various MINERvA tunes for carbon, scintillator, iron, and lead cross-section in antimuon p_{T}.

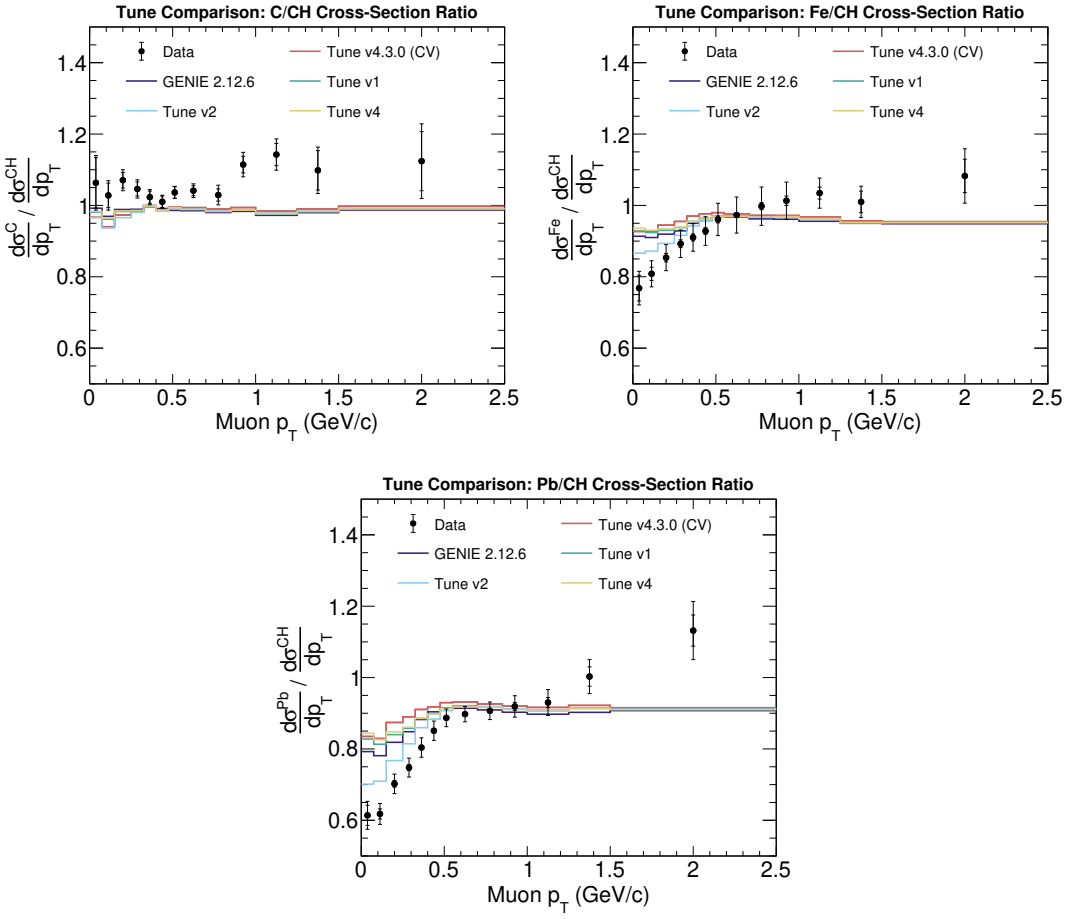

Figure L.2: Measured carbon-to-scintillator (top left), iron-to-scintillator (top right), and lead-to-scintillator (bottom) cross-section ratios in antimuon p_{T} compared to the predictions from different MINERvA tunes. The data is displayed with both the statistical (inner error bars) and the total (outer error bars) uncertainty.

Cross-section ratio	MINERvA tune χ^2/ndf for p_{T} (ndf = 13)				
	CV	GENIE 2.12.6	v1	v2	v4
C/CH	4.93	5.17	4.93	5.55	4.90
Fe/CH	2.35	2.17	2.39	1.33	2.61
Pb/CH	12.06	6.68	10.00	2.94	11.32

Table L.2: Fully correlated χ^2/ndf calculated according to Equation 9.1 to assess the agreement between the measured data and the various models in the cross-section ratios to scintillator for carbon, iron, and lead in antimuon p_{T}.

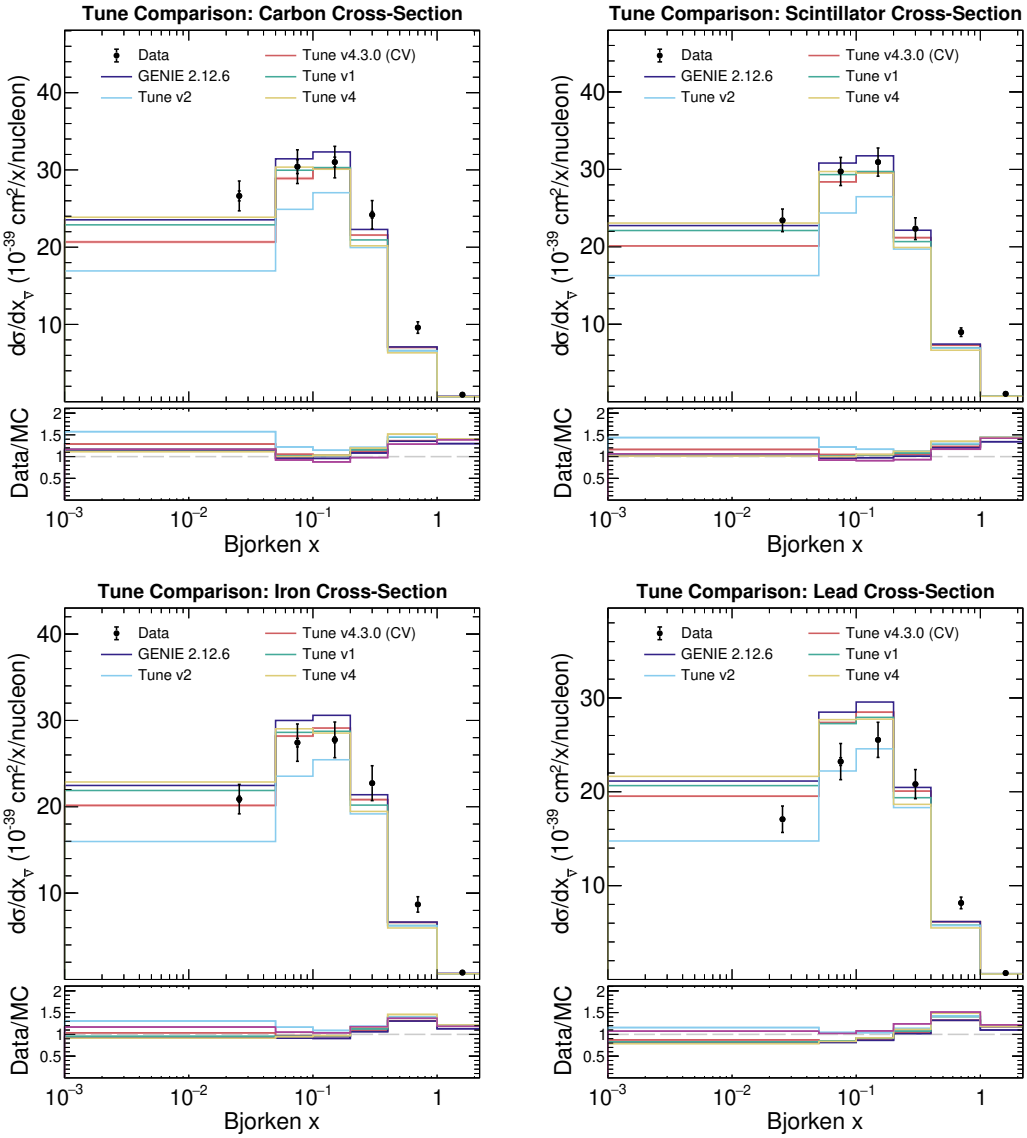

Figure L.3: Measured carbon, scintillator, iron, and lead (from left to right, top to bottom) cross-section as a function of Bjorken x compared to the predictions from different MINERvA tunes. The inner error bar on the data indicates the statistical error while the outer error bar corresponds to the total, i.e. statistical + systematic, error.

Cross-section	MINERvA tune χ^2/ndf for Bjorken x (ndf = 6)				
	CV	GENIE 2.12.6	v1	v2	v4
Carbon	5.34	4.87	4.56	7.50	5.08
Iron	3.50	4.34	3.80	4.92	5.47
Lead	4.46	6.57	7.77	4.93	11.90
Scintillator	17.22	10.19	6.47	30.38	6.09

Table L.3: Fully correlated χ^2/ndf calculated according to Equation 9.1 to assess the agreement between the measured data and the various MINERvA tunes for carbon, scintillator, iron, and lead cross-section in Bjorken x.

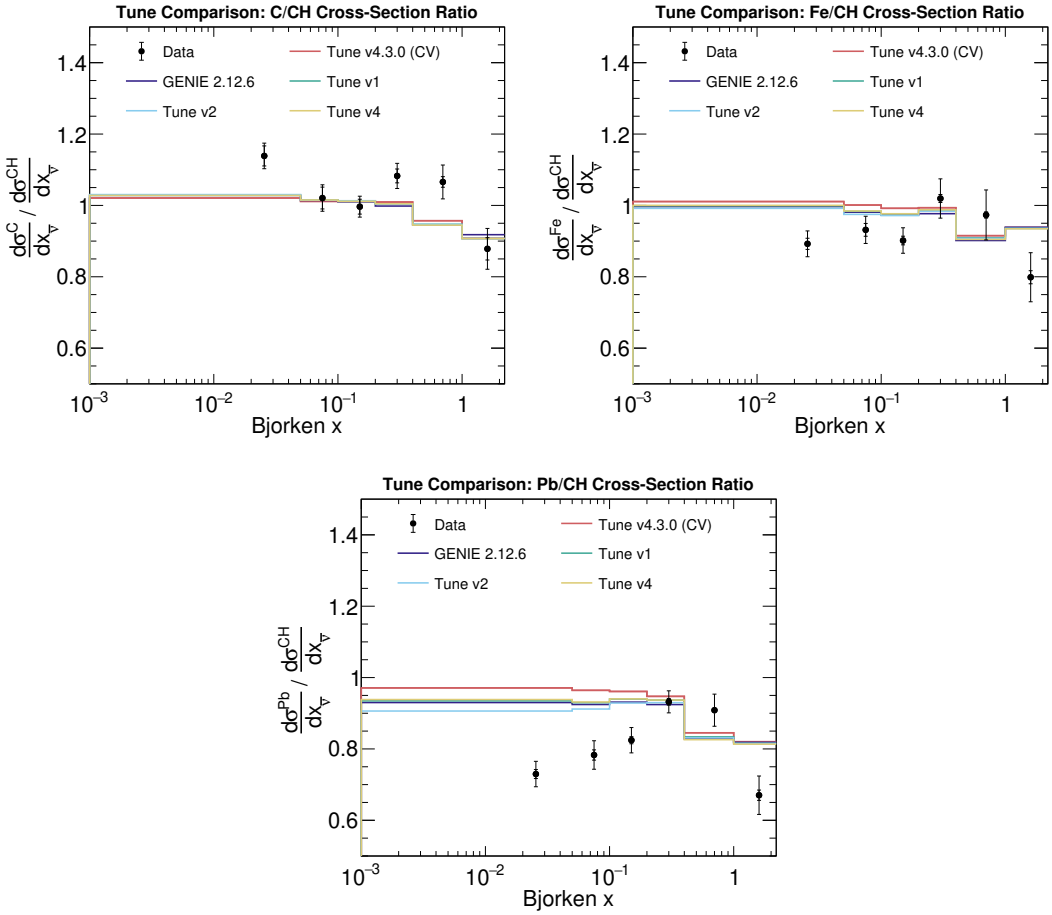

Figure L.4: Measured carbon-to-scintillator (top left), iron-to-scintillator (top right), and lead-to-scintillator (bottom) cross-section ratios in Bjorken x compared to the predictions from different MINERvA tunes. The data is displayed with both the statistical (inner error bars) and the total (outer error bars) uncertainty.

Cross-section ratio	MINERvA tune χ^2/ndf for Bjorken x (ndf = 6)				
	CV	GENIE 2.12.6	v1	v2	v4
C/CH	5.91	6.58	6.31	6.24	6.40
Fe/CH	6.28	6.08	5.72	5.45	5.80
Pb/CH	12.69	11.52	10.83	8.97	11.61

Table L.4: Fully correlated χ^2/ndf calculated according to Equation 9.1 to assess the agreement between the measured data and the various models in the cross-section ratios to scintillator for carbon, iron, and lead in Bjorken x.